Optical Coherence Tomography of the Eye

by

Michael Richard Hee

B.S., Electrical Engineering
Stanford University, 1990

S.M., Electrical Engineering and Computer Science
Massachusetts Institute of Technology, 1992

Submitted to the

DEPARTMENT OF ELECTRICAL ENGINEERING AND COMPUTER SCIENCE

in partial fulfillment of the requirements for the degree of

DOCTOR OF PHILOSOPHY IN ELECTRICAL ENGINEERING AND COMPUTER SCIENCE

at the

MASSACHUSETTS INSTITUTE OF TECHNOLOGY

February 1997

Signature of Author Michael R. Hee
Department of Electrical Engineering and Computer Science
December 3, 1996

Certified by James G. Fujimoto
Professor James G. Fujimoto
Thesis Supervisor

Accepted by
Arthur C. Smith
Chairperson, Department Committee on Graduate Students

Optical Coherence Tomography of the Eye

by

Michael Richard Hee

Submitted to the Department of Electrical Engineering and Computer Science

on December 3, 1996

in partial fulfillment of the requirements for the degree of

Doctor of Philosophy in Electrical Engineering and Computer Science

ABSTRACT

Optical Coherence Tomography (OCT) is a new technique for high-resolution, cross-sectional imaging of tissue in which the time-of-flight delay of light reflected from internal tissue structures is resolved with high precision using interferometry. Tomographic images are obtained which are analogous to those provided by ultrasound except that image contrast relies on differences in optical rather than acoustic properties of tissue. The use of light rather than sound enables higher resolution (10 μm) and non-contact imaging. A clinically viable high-sensitivity, fiber-optic based OCT instrument has been constructed based on engineering principles derived from optical communication theory. Computer algorithms have also been developed for quantitative image analysis and restoration.

OCT has been used to image patients with a variety of ocular diseases. In patients with macular pathology, OCT images have been correlated with conventional clinical examination and fluorescein angiography. Optical coherence tomograms are effective in staging macular holes, evaluating the vitreoretinal interface in eyes at risk for a macular hole, and providing a structural assessment of macular hole surgery. In eyes with central serous chorioretinopathy, OCT can evaluate sensory retinal separations undetected at the slit-lamp. Serial OCT images of macular edema are able to track both the progression of macular thickening and the resolution of macular edema following laser photocoagulation. In patients with diabetic retinopathy, measurements of macular thickness correlate with visual acuity and OCT is more sensitive to small changes in retinal thickness than slit-lamp biomicroscopy. OCT may provide a novel method of defining occult choroidal neovascular membranes in patients with age-related macular degeneration. OCT can also profile the thickness of the retinal nerve fiber layer with high resolution which is potentially important for the objective assessment of early glaucoma progression. OCT images have been correlated with visual field performance and optic nerve appearance in a cross-section of patients with various stages of glaucoma. These studies suggest that OCT has the potential to become an important diagnostic tool for the practicing ophthalmologist.

Thesis Supervisor: James G. Fujimoto
Professor of Electrical Engineering and Computer Science

To June and Mom and Dad

who are still waiting for me to finish . . .

ACKNOWLEDGEMENTS

The interaction between technology and medicine is vital for the continued improvement of medical care, and can simultaneously benefit the quality of the patient-doctor relationship, the caliber of preventive, diagnostic, and therapeutic treatment, and the economics of health care delivery. However, while the potential benefits are great, the chance for true success in the multidisciplinary field of engineering in medicine is rare. Since much of medicine necessarily depends on time-honored traditions and procedures, change comes slowly and with great effort.

Thus, I believe I have been incredibly fortunate to work on a project as productive as Optical Coherence Tomography (OCT). In retrospect, I feel that I could not have participated in this research during a more exciting time. I have experienced the absolutely stunning progression from the first ever OCT image *in vitro*, to the development of a clinically useful instrument which can influence a physician's decisions about patient treatment. The transition from laboratory to clinical practice has been exhilarating. It has been a privilege to be able to lay the groundwork for a fundamentally new technique which has the potential, at least, to revolutionize the care and study of the human eye.

The success of this multidisciplinary research has relied on the expertise of many individuals in a variety fields. I firmly believe that it is the collaborative interaction between MIT, the New England Eye Center (NEEC), and MIT Lincoln Laboratory which has provided the foundation for this project's success.

Jim Fujimoto has been my thesis advisor at MIT. He has provided me with opportunity, resources, and latitude to pursue this research. I am grateful for his guidance, mentorship, and support through all these years. Carmen Puliafito has provided both the resources of the NEEC and his patient population to support the clinical studies of macular disease in this thesis. Always the politician, he has almost single-handedly willed OCT onto the ophthalmic community. In the process, he has taught me something about politics as well. Eric Swanson of MIT Lincoln Laboratory designed the OCT electronics and is largely responsible for a clinical prototype which has operated successfully for over two years. He has either directly or indirectly taught me most of what I know about low-coherence interferometry. (He also showed me that Italy may not be the best place for a vacation). Joel Schuman has been leading the clinical studies of glaucoma at the NEEC. He continues to be an example of someone who manages to juggle the simultaneous demands of clinical practice, research, and family.

Joe Izatt helped out with the initial *in vitro* and *in vivo* studies of retinal and anterior eye imaging while he was a post-doc at MIT. He has one of the most positive laboratory attitudes that I have ever encountered and it was a pleasure working with him. David Huang came up with the idea of tomographic imaging with low-coherence interferometry while he was MD-PhD student in the Harvard-MIT program. He has blazed the way for a succession of MD-PhD students following him, including myself. Charles Lin participated in the first *in vitro* studies and in the initial clinical studies of patients while he was at the NEEC. He has since found his independence.

Carlton Wong has the distinction of being the first OCT technician and also one of the nicest people on the planet. He helped integrate OCT into routine clinical practice at the NEEC. He has also spent some time marketing the commercial OCT instrument for Humphrey Instruments. Jeffery Coker and Jason Wilkins, OCT technicians number two and three respectively, have actually imaged most of the patients which have been studied to date. Their independence and competence have

allowed me to finish this dissertation in a reasonable amount of time. Joe Szwartz, OCT technician number four, is the most recent addition to the OCT family. I wish him the best of luck in taking over things at the NEEC.

Back at MIT, Brett Bouma, Gary Tearney, Stephen Boppart, Mark Brezinsky, and Costas Pitris have been doing amazing things with OCT outside of the eye. Their work in scattering tissues will form the basis for the next generation of clinical studies in other organ systems. I thank Brett for an extremely careful reading of a draft of this thesis and for putting up with my fiber splicing demands. I only wish that I could have had the chance to work with him more so that I might learn some gems of ultrafast optics and physics. I thank Gary for finishing before I did (amazingly!) and for cleaning my desk when I happened to show up. I also thank him for missing more deadlines than me. The fact that he turned in his thesis before I turned in mine was one motivation for me to finish everything up. Stephen and I had a memorable trip to Texas in which he did most of the work. I wish both Steve and Costas luck as they plow through the rest of the HST program. Thanks to Boris Golubvic for convincing me to use FrameMaker to format this document which has saved me an immense amount of time.

At the NEEC, Jay Duker and Elias Reichel have provided the resources of their patient population and their clinical expertise in macular disease. Tamar Pedut-Kloizman, Caroline Baumal, Bryan Rutledge, and Lise Pieroth have undertaken some of the image and data analysis. Tamar and Lise continue to pursue research on glaucoma, and still put up with both my software and my unavailability. Ellen Hertzmark has been a statistical consultant on the project. I would also like to extend thanks to Tamar, Jeff, Jason, and Carlton for handling the monkey study which was an odious task.

Humphrey Instruments has been supportive in providing equipment and a revised design of the imaging optics. I wish them all the best in bringing the commercial OCT instrument to the ophthalmic community. The future success of OCT of ophthalmology depends in large part on their work.

John Wyatt and Erich Ippen have been official readers of this thesis. I thank them for their helpful suggestions and for letting me graduate. These are two of the most approachable and down-to-earth MIT professors in existence.

It is rare to find a project that simultaneously incorporates clinical investigation with active basic science research and technology development. I believe that OCT has and will continue to provide an environment where multidisciplinary research in engineering and medicine has the potential to produce extraordinary benefits in disease diagnosis, preventive care, and patient management in a variety of diverse clinical situations. I feel fortunate to have contributed to the project's success.

Hmmm. Maybe I'll actually finish this crazy combined degree program thing after all . . . .

CONTENTS

Chapter 1

INTRODUCTION

1.1 Overview

The human eye occupies a unique place in clinical medicine. Ocular disease and visual function impairment can have a devastating impact on a patient's quality of life. The unique and specialized anatomy of the eye provides a level of accessibility to internal structure not available in any other organ in the body. Both the anterior and posterior chambers of the eye are amenable to direct visual observation, facilitating the diagnosis of ocular pathology. The uninterrupted optic pathway to the posterior eye allows non-invasive inspection of nervous and vascular tissue, making the eye an important indicator of not only ophthalmic but also systemic vascular and neurological disease.

A basic ophthalmic exam relies on standardized visual function tests and slit-lamp observation to assess visual integrity and evaluate ocular manifestations of systemic disease. Current clinical evaluation often rests on direct and sometimes subjective visualization of ocular anatomy and reduced performance on visual function tests. In some cases, however, observable loss of visual function only occurs after irreversible microscopic changes in ocular anatomy. Micron scale high resolution tomographic imaging of the anterior and posterior eye would be a powerful diagnostic in these cases by providing quantitative evaluation of ocular microstructure and the potential for early diagnosis and treatment of disease before visual function loss. In the anterior segment, high resolution imaging would permit the evaluation of pathologies of the cornea, iris, lens, and anterior chamber angle. Accurate, non-invasive measurements of corneal curvature and thickness would also be useful in treatments where precise biometry is necessary, such as contact lens fitting, intraocular lens implant power calculation, and real-time monitoring of corneal refractive surgery. In the posterior segment, tomographic imaging of the retina and optic nerve head would allow quantitative evaluation and early treatment of degenerative retinal diseases such as open-angle glaucoma, macular degeneration, macular edema, retinal detachment, and macular hole.

This thesis describes Optical Coherence Tomography (OCT), a novel technique for non-contact, high-resolution, cross-sectional imaging of tissue. The design of a fiber-optic OCT system for real-time *in vivo* imaging of the human eye is developed. Computer algorithms for image acquisition, processing, and management are also discussed. Clinical applications of OCT in the diagnosis and management of a variety ocular diseases are explored in patients.

1.2 Conventional Ophthalmic Examination

The most important parameter in evaluating ocular disease is the visual acuity which provides an overall measure of ocular function. Localization of disease may then be established by history and physical examination of the eye. Conventional ophthalmic examination relies on direct observation of ocular structures. In ophthalmoscopy, intraocular structures are viewed directly under magnification. In angiography, intravenous fluorescent dye is used to highlight the structure and function of the retinal vasculature. The visual acuity is of primary value in evaluating central vision. Peripheral vision may be assessed quantitatively using automated or static perimetry techniques.

1.2.1 Slit-lamp and Indirect Biomicroscopy

Slit-lamp and indirect biomicroscopy remain the mainstay for physical examination of the intraocular anatomy. The slit-lamp is a tabletop binocular microscope with an adjustable slit-beam which provides a three-dimensional view of intraocular structures. The angle, width, length, and intensity of the slit illumination can be varied so that optical cross-sections may be studied. The slit-lamp is indispensable for examination of the anterior segment, including the cornea, iris, aqueous, and lens. Visualization of the iridocorneal junction may be accomplished with a slit-lamp by reflection through a goniolens or Goldmann lens.

Examination of the posterior segment structures such as the vitreous, retina and optic nerve is accomplished with direct or indirect ophthalmoscopy. The direct ophthalmoscope is a hand-held, monocular instrument which provides a 15x magnified view of the fundus. Because the direct ophthalmoscope is portable and does not require pupillary dilation, it is of primary value to the general physician.

The indirect ophthalmoscope, which is worn on the examiner's head, allows binocular viewing of an image of the retina which is formed through a hand held condensing lens placed in front of the eye. The primary advantages of indirect over direct ophthalmoscopy include a wider field-of-view and stereoscopic image formation. The principle of indirect ophthalmoscopy may also be used with slit-lamp biomicroscopy. In this technique, the adjustable magnification and slit-beam of the slit-lamp are used to examine an image of the retina formed in front of either a hand held condensing lens or a contact lens placed on the eye. Indirect biomicroscopy is the method of choice for high magnification, stereoscopic examination of the retina and optic nerve.

Fundus photography, which may be either monocular or stereo, is routinely performed to document changes in optic disc or retinal appearance associated with a variety of ophthalmic conditions. The principle is similar to indirect biomicroscopy except the condensing lens is mounted to the fundus camera, and a ring rather than a slit-beam of illumination is used. The ring provides equal illumination of the entire fundus and avoids back-reflections from ocular interfaces such as the cornea. Stereo images are typically used to evaluate optic disc cupping and neuroretinal rim area. A red-free filter may be employed to assess the reflection from the retinal nerve fiber layer.

1.2.2 Fluorescein Angiography

Fluorescein angiography involves systemic intravenous injection of fluorescein dye prior to fundus photography and is exceptionally useful in delineating vascular alterations such as aneurysm, neovascularization, ischemia, occlusion, hemorrhage, and edema. Sodium fluorescein is a hydrocarbon which absorbs light between 465 and 490 nm and fluoresces at a wavelength between 520 and 530 nm. Fundus photographs of this fluorescence taken at mul-

tiple time-points after intravenous injection of fluorescein provide information on vascular transit, leakage, staining, and blockage. Fluorescein angiography is the technique of choice in evaluating macular edema and age-related macular degeneration.

1.2.3 Visual Field Testing

Central vision is typically measured using the familiar Snellen chart and is a primary parameter in assessing evaluating the severity of ocular disease. Peripheral vision is most commonly tested using automated or static perimetry. Test lights of various brightness and size are displayed at different locations within the visual field. Numerical scores are produced which correspond to the threshold sensitivity of each test location. These scores may be statistically compared with previous tests to assess the probability of change. Characteristic losses in peripheral vision occur in glaucoma, and are important in the diagnosis of this disease.

1.3 Other Ocular Imaging Techniques

While direct observation of the fundus using direct and indirect ophthalmoscopy remains the primary means of assessing retinal anatomy, several other imaging techniques are being developed or are already routinely used in clinical practice to provide supporting or more objective information on retinal structure and function.

1.3.1 Retinal Imaging Techniques

Fluorescein angiography is limited in its ability to localize the growth of new blood vessels in the choroid (also known as choroidal neovascularization) secondary to age-related macular degeneration. Indocyanine green (ICG) is an alternative fluorescent dye which has several advantages over fluorescein for angiography of the choroid. These properties include absorption and emission in the near infrared range (805 and 835 nm respectively) and a high protein binding capacity which reduces the leakage of dye from choroidal vessels. These advantages permit better penetration and imaging through the pigmented layers of the fundus as well as through serosanguinous fluid and hemorrhage. Recent advances in this field have combined digital imaging technology with ICG angiography to make this technique clinically useful in defining neovascular membranes which would otherwise be occult on fluorescein angiography [1-3].

A and B-scan ultrasonography are currently employed in the evaluation of intraocular masses and tumors, the assessment of corneal thickness in keratorefractive surgeries, and the measurement of axial eye length for intraocular lens implant power calculations. A-scan ultrasound provides a uniaxial profile of acoustic reflectivity versus longitudinal depth into tissue. Ultrasound B-scan provides a cross-sectional image of tissue which is created from a series of separate A-scans. Ultrasonic imaging of the retina can be valuable in situations such as intraocular tumor or vitreous hemorrhage where the direct optical path to the retina is occluded. In typical clinical instruments, the depth resolution of ultrasound is limited by the wavelength of sound in ocular tissue to about 150 μm [4]. Recent advances in high-frequency ultrasound have reduced the minimum resolution to about 20 μm, but with a penetration depth limited to the first 4 mm of the anterior segment [5, 6]. Ultrasonic imaging also requires physical contact between the eye and the ultrasonic transducer or saline immersion of the eye.

The objective evaluation of retinal thickness is difficult with ophthalmoscopy but is essential to the management of macular edema. The Retinal Thickness Analyzer is a device which uses the principle of optical triangulation to provide a quantitative measurement of retinal thickening [7-10]. Laser light which is obliquely incident on a single point on the retina is

assumed to be reflected predominantly from both the vitreoretinal interface and the sensory retina/retinal pigment epithelium interface. The distance between the two reflected beams is measured and is proportional to the retinal thickness. Topographic images of retinal thickness may be constructed by analyzing an array of points on the retina, which then can be displayed as a wire-frame or false-color image. The reproducibility of measurements varies between 20 and 30 μm [7].

By applying laser confocal imaging to the eye, scanning laser ophthalmoscopy (SLO) and scanning laser tomography (SLT) can accurately profile changes in the contour of the fundus surface and quantify cupping of the optic disc with micron scale lateral resolution [11-13]. Direct depth resolved tomographic imaging of the fundus is limited by ocular aberrations and the numerical aperture available through the pupil to about 300 μm accuracy. In the macula, the SLO has been investigated for imaging of macular holes, cystoid macular edema, and choroidal neovascularization [14]; however, its primary use has been in the imaging of optic nerve head structure. The SLO will be discussed in more detail in the following Section.

1.3.2 Optic Nerve Head Imaging Techniques

Changes in the appearance of the optic disc have been traditionally associated with the onset of glaucoma. Loss of retinal nerve fibers in this disease causes distinct changes such as increased cupping and a reduction in the neuroretinal rim area which are traditionally assessed with indirect biomicroscopy, stereo fundus photography, and red-free photography. The interpretation of optic disc cupping and neuroretinal rim area with these techniques, however, is subjective and often extremely variable even among experienced observers. Despite this variability, it is the optic nerve head appearance, along with visual field examination and intraocular pressure which defines the presence of glaucoma. Several optic nerve head imaging techniques have been developed in an attempt to provide a more objective measurement of these parameters [15].

The principle of raster stereography has been used to reconstruct the surface profile of the optic nerve head. In a device called the Glaucoma-Scope, twenty-five parallel horizontal lines are projected onto the optic nerve head with an infrared light source and recorded by a video camera. The curvature of these lines is proportional to the depth of the nerve head. A reference point must be selected by the operator who also outlines the disc margin and the position of retinal vessels. Depth measurements are computed and reported on a grid where each pixel has an area of 75×100 μm. The cup-to-disc area and neuroretinal rim area are automatically calculated by assuming that the border of the cup lies 120 μm below the disc margin. The mean standard deviation of depth measurements for each pixel is approximately 15 μm [16-18].

Scanning laser ophthalmoscopy applies the classical principle of confocal microscopy to imaging of the eye [11-13]. A laser beam is scanned over the retina while a pinhole aperture allows only light reflected from a focal plane to reach the detector. Image contrast is increased because out-of-plane reflections are eliminated by the pinhole. Since the probe beam is scanned over the retina, only a small portion of the pupil is used for illumination leaving the majority for collection. The fundus can be imaged with light levels that are far below conventional indirect ophthalmoscopy and dilation of the pupil is not required. High scan rates may be attained using a rotating polygon mirror and commercial instruments can acquire a complete retinal image in approximately one second. Multiple images at different depths within the retina are also possible giving volumetric information on retinal reflectivity. A typical dataset in a commercial instrument consists of 32 images at different depths each consisting of 256×256 pixels. Cup-to-disc ratios, neuroretinal rim areas, and volumetric information can be automatically computed from these images after the operator outlines the disc margin. The

depth resolution is determined by the confocal parameter of the illumination beam which is limited by ocular aberrations and the entrance pupil of the eye to approximately 300 μm. The transverse resolution is similarly limited to about 10 μm.

1.3.3 Retinal Nerve Fiber Layer Imaging Techniques

Optic nerve head imaging instruments have been successful in providing objective measurements of parameters such as cup-to-disc ratios and neuroretinal rim area. In glaucoma, however, changes optic nerve head appearance may occur only after irreversible damage to the retinal nerve fiber layer. The primary cause of vision loss in glaucoma is ganglion cell atrophy. Changes in the appearance of the optic nerve head are only secondary to the loss of nerve fibers. Atrophy of up to half of the retinal nerve fiber layer may occur before clinically detectable changes in optic nerve appearance or visual field performance. The conventional clinical technique of evaluating the nerve fiber layer by examination or photography with red-free light is also very subjective. The SLO has been used in the two manners described below for enhanced imaging of the nerve fiber layer. Both of these methods rely on the relative birefringence of the nerve fiber layer compared to the remainder of the neurosensory retina.

Although the axial or confocal resolution of the SLO is much larger than the thickness of the retinal nerve fiber layer, the high transverse resolution of the instrument may be used to image the characteristic surface striations in the nerve fiber layer in a manner superior to conventional red-free fundus photography. Additionally, polarization differential contrast imaging may be employed to enhance images by taking advantage of the birefringence in the nerve fiber layer. In this technique, two SLO images acquired with illumination in orthogonal polarizations are subtracted to enhance birefringent features [11].

A Fourier ellipsometer [19] coupled to an SLO can also completely characterize the polarization state of reflected light [20]. An image of polarization retardation created in this manner can indirectly provide information on NFL thickness under the assumptions that (1) the nerve fiber layer is the major intraretinal source of birefringence, (2) most of the illumination light is reflected from the outer retina and double-passes the nerve fiber layer, and (3) the nerve fiber layer birefringence is homogenous [21]. While the cornea is known to be a biaxial medium with a total birefringence significantly larger than the nerve fiber layer birefringence [22], a polarimeter is available which incorporates a proprietary device to compensate for birefringent tissues anterior to the retina. The coefficient of variation (standard deviation divided by the mean) describing the reproducibility of this method for measurements of NFL thickness is about 4.5% for a ring of measurements concentric with the disc margin [23].

1.4 Optical Coherence Tomography

Optical coherence tomography (OCT) is a new technique for micron scale resolution cross-sectional imaging of ocular and other biological tissue [24-26]. OCT is similar to B-scan ultrasonic imaging, except that image contrast relies on differences in optical rather than acoustic backscattering characteristics of tissue. In OCT, low-coherence optical interferometry is used to resolve the position of reflective or optical backscattering sites within a sample. Two-dimensional tomographic images of a thin, optical slice of tissue may be obtained with approximately 10 μm longitudinal and lateral resolution. Optical heterodyne detection and the application of noise-reduction techniques originally developed for efficient optical communication achieve a sensitivity to reflected light as small or smaller than 10^{-10} of the incident optical power. OCT is non-contact, non-invasive, and has superior resolution to conventional clinical ultrasound. Unlike confocal imaging, the axial resolution of OCT is not

limited by the pupil aperture and ocular aberrations. OCT may be implemented in a compact, low-cost, fiber-optic based interferometer that is easily coupled to existing ophthalmic instrumentation.

1.4.1 Historical Overview

Optical time-of-flight ranging measurements were first demonstrated in biological tissue by Fujimoto *et al.* [27] in 1986. The time delay of femtosecond pulses of light reflected from intraocular structures was ascertained by correlating the reflected pulses with pulses from a reference optical delay line using second harmonic generation. In this technique, the temporal width of each pulse determined the axial resolution of the technique. Thus, pulse durations on the order of 30 femtoseconds would be required for distance resolutions on the order of 10 μm.

It was subsequently realized that the technique of low-coherence interferometry could also provide the equivalent of femtosecond time resolution without the need for a cumbersome modelocked laser source. Low-coherence reflectometry was originally conceived in 1987 as a technique for nondestructive characterization of optical waveguides and fiber devices [28-32]. The technique was an alternative to optical time-domain reflectometry whereby light with a short temporal coherence was used instead of short pulses of light to provide axial distance resolution. Thus, a continuous wave source with a large spectral bandwidth and a correspondingly short coherence length could be used to achieve a distance resolution on the order of 10 μm. While the concept of white light interferometry was not new, it was the emergence of the superluminescent light emitting diode (SLD) in the 1980s which made low-coherence reflectometry practical in a fiber-optic setup [33]. The SLD provided a compact, low-cost, continuous-wavelength light source with a low temporal coherence but a high degree of spatial coherence which was necessary to produce high contrast interference fringes.

In biological tissue, interferometry with partially coherent light was first applied to biological tissue by Fercher *et al.* in 1988 to make measurements of human axial eye length *in vivo* [34]. Continuous profiles of optical reflectivity versus depth using low-coherence interferometry were first obtained with measurements of corneal thickness and incision depth *in vitro* using a SLD and a Michelson interferometer [35]. In 1991, Huang *et al.* [24, 25] proposed OCT as a two-dimensional extension of low-coherence interferometry. The essential concept was analogous to ultrasonography: the acquisition of a number of uniaxial reflectivity profiles, or A-scans, in a sequence of locations across the tissue, which then could be displayed side-by-side to form a tomographic, or B-scan image. In this seminal paper, the authors demonstrated the first *in vitro* OCT images of the human retina and coronary arterial wall, suggesting the potential of OCT as a completely new biological imaging modality in both transparent and scattering media.

Early on, biological motion was a major limiting factor preventing real-time *in vivo* imaging with OCT. A high-speed low-coherence interferometer was developed which could acquire a single A-scan of reflectivity versus distance of the cornea and lens *in vivo* [36]. An interferometric system in which the effect of axial eye motion could be minimized by eliminating the use of an absolute reference distance was also demonstrated [37-41].

The first *in vivo* OCT images were obtained by the Fujimoto group in 1993. The data acquisition speed of the low-coherence interferometer was increased and scanning optics were coupled to a standard slit-lamp biomicroscope to produce real-time images of the living human retina [42]. Retinal imaging was also being pursued by Fercher *et al.* who acquired a low-coherence tomogram by manually translating the subject's fixation for A-scan comprising the image [43]. Because of the optical accessibility of various ocular structures, cross-sectional

imaging of the anterior eye [44] and retina [45, 46] were initially emphasized as potential clinical applications. More recently, the imaging of organ systems other than the eye has also generated clinical interest, both with single A-scan low-coherence interferometry [47-50] and with OCT [51-56].

1.4.2 Scope of Thesis

This thesis describes the further development of OCT into a new, clinically useful imaging modality for ophthalmology. The research is the product of an ongoing collaboration between James G. Fujimoto of the Massachusetts Institute of Technology, Carmen A. Puliafito and Joel S. Schuman of the New England Eye Center, Tufts University School of Medicine, and Eric A. Swanson of MIT Lincoln Laboratory. The result is a prototype OCT system which an ophthalmic technician is able to use to provide a clinical assessment of a variety of ocular diseases.

The scope of this thesis spans technology development through preliminary clinical trials in three main phases: (1) the transition from *in vitro* to *in vivo* imaging, involving the development of an optical system to deliver the OCT probe beam to the retina, and an increased data acquisition rate to reduce the effect of eye movements; (2) the transition from *in vivo* imaging in a laboratory environment to *in vivo* imaging of patients with ocular diseases, involving the construction of a robust system with a simultaneous view of the OCT probe beam on the fundus and a real-time display of the OCT image in progress, and the development of image processing techniques for the rapid display and analysis of multiple images; and (3) clinical trials with patients, involving the development of examination protocols and studies of a variety of ocular diseases to determine indications for the applicability of OCT. The work includes the contribution of many individuals, detailed in the Acknowledgments, whose different fields of expertise were essential to the success of this project.

The thesis is correspondingly organized into technical and clinical sections. Chapters 2 through 4 describe the optical, electronic, and image processing technology behind OCT. The optical principles of low-coherence interferometry and its associated system electronics are described in Chapter 2. The determinants of axial resolution, image acquisition time, and detection sensitivity for weak reflections are discussed. Chapter 3 covers the optics of the eye, and the optical imaging system used to scan the OCT probe beam across the retina. The transverse resolution and field-of-view of the system are described and the effects of patient positioning and ocular ametropia are analyzed. Image processing techniques and different methods of extracting and displaying quantitative information obtained from the OCT images are discussed in Chapter 4.

Chapters 5 through 7 explore the application of OCT to the diagnosis and management of ocular disease. Chapter 5 provides an overview of the morphological features of healthy and diseased eyes which are evident on OCT imaging. Selected macular diseases such as idiopathic macular hole, central serous chorioretinopathy, diabetic retinopathy and macular edema, and age-related macular degeneration are discussed in detail in Chapter 6. Chapter 7 focuses on the use of OCT for the quantitative measurement of retinal nerve fiber layer thickness in glaucoma. Finally, Chapter 8 discusses the scalability of the resolution, acquisition speed, and dynamic range of OCT in the eye in the context of the fundamental limit of tissue damage thresholds in the retina.

Chapter 2

LOW-COHERENCE INTERFEROMETRY

2.1 Introduction

This Chapter describes low-coherence interferometry, the technique which forms the basis for axial ranging in OCT. The inverse relationship between the spectral bandwidth of the light source and the axial resolution of the system is derived for media with and without dispersion. The detection and filtering electronics are also discussed, including their fundamental noise characteristics.

2.2 System Overview

A schematic diagram of the OCT system is shown in Figure 2-1. Low-coherence light from a superluminescent diode (SLD) source is coupled into a fiber-optic Michelson interferometer. The 843 nm light is divided at a fiber coupler into reference and sample paths. Light retroreflected from a variable distance reference mirror is recombined in the coupler with light backscattered from the patient's eye. Time-of-flight information is contained in the interference signal between the reference and sample beams, which is detected by a photodiode followed by signal processing electronics and computer data acquisition.

A single axial profile, or A-scan of optical reflectivity versus distance in the eye is obtained by rapidly translating the reference arm mirror and synchronously recording the magnitude of the resulting interference signal. Interference fringes are only evident when the reference arm distance matches the length of a reflective path through the eye to within the source coherence length. Thus, the coherence length, which is a fundamental property of the light source, determines the axial ranging resolution. Cross-sectional, or B-scan tomograms are constructed from a sequence of A-scans which are obtained by repetitively translating the reference mirror while scanning the probe beam across the retina. A typical B-scan OCT of the retina containing 100 longitudinal A-scans is acquired in 2.5 seconds.

The scanning and imaging optics are fitted onto a conventional slit-lamp biomicroscope. Two orthogonally mounted scanning mirrors provide lateral beam positioning on the retina. Retinal tomography is performed in a manner similar to indirect ophthalmoscopy, whereby a condensing lens mounted on the slit-lamp in front of the eye is used to relay an image of the retina onto the slit-lamp image plane. Computer control and data acquisition enable arbitrary scanning patterns on the retina and provide a real-time display of the OCT in progress. An infrared sensitive CCD camera attached to the slit-lamp provides a video image of the scanning OCT probe beam on the fundus, and permits the position of each tomogram

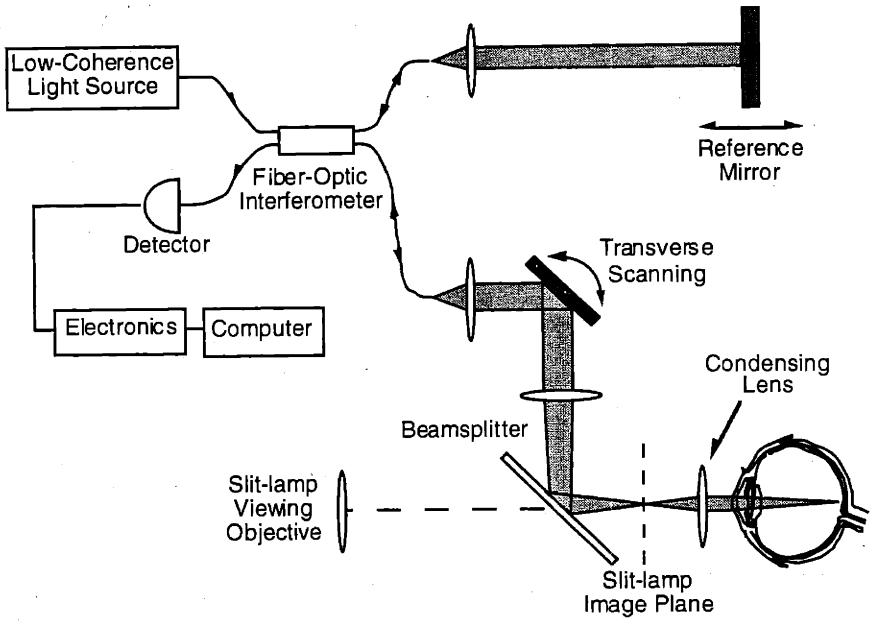

FIGURE 2-1. Schematic of the OCT system.

on the retina to be documented. Alternatively, direct slit-lamp observation of the fundus and probe beam may be accomplished with a visible aiming laser coupled into the interferometer which provides a visible spot coincident with the infrared probe beam on the retina.

This Chapter describes the fiber-optic low-coherence interferometer and the detection electronics which form the basis of the OCT system. The scanning and imaging optics as well as optical models of the eye, which are specific to ophthalmic applications of OCT, will be described in Chapter 3.

2.3 Interferometer and Axial Resolution

This Section describes the principle of low-coherence interferometry which allows the position of reflective boundaries within the eye to be precisely located. A Fourier transform relationship between the spectrum of the light source and the longitudinal point spread function or axial resolution of the interferometer is developed. The coherence-length of the light source, which defines the optimal axial resolution, is shown to be inversely related to the source spectral bandwidth in a dispersion free medium. Chromatic dispersion degrades this resolution by broadening the axial point spread function in direct analogy to the case of short pulse propagation through dispersive media.

2.3.1 Interferometer with Coherent Light

Consider the simplified schematic of the Michelson interferometer shown in Figure 2-2 where the eye has been replaced by a mirror in the sample arm of the interferometer. Light from the source is divided at a beamsplitter into reference and sample beams. Light reflected from the reference and sample mirrors is recombined at the same beamsplitter and incident on a detector. The reference and sample mirrors are positioned at distances l_R and l_S from the

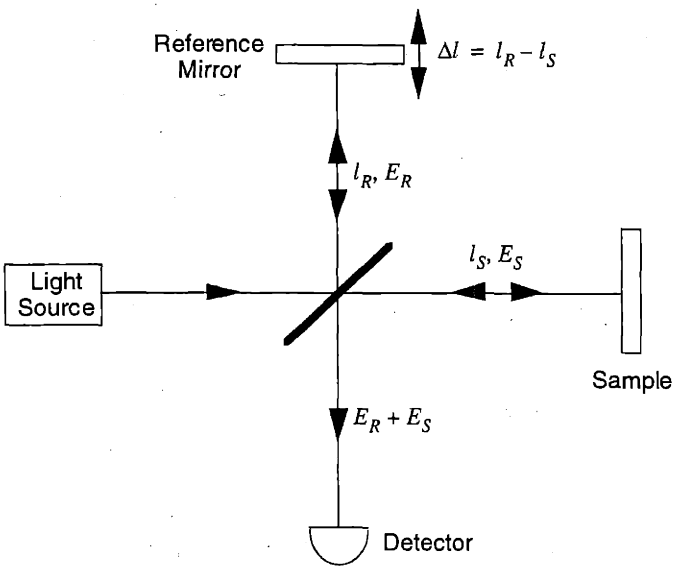

FIGURE 2-2. The Michelson interferometer.

beamsplitter respectively. If the light source is perfectly coherent (*i.e.* monochromatic), then reflection from the reference and sample mirrors produces a sum of two monochromatic electric field components E_S and E_R at the detector. These fields may be expressed by the phasors

$$E_R = A_R e^{-j(2\beta_R l_R - \omega t)} \quad \text{and} \quad E_S = A_S e^{-j(2\beta_S l_S - \omega t)} \tag{2.1}$$

where ω is the optical frequency of the light source and β is the propagation constant. The factors of two multiplying the propagation constants β_R and β_S arise from the roundtrip propagation of light to and from the reference and sample mirrors.

Note that E_R and E_S represent the field components in the interferometer *after* reflection and recombination at the beamsplitter, which eliminates the necessity of considering the split ratio and phase-shift of the beamsplitter. In general, the time averaged photocurrent I at the detector is given by

$$I = \langle \frac{\eta e}{h\nu} \cdot \frac{|E_R + E_S|^2}{2\eta_0} \rangle \tag{2.2}$$

where η is the detector quantum efficiency, e is the electronic charge, $h\nu$ is the photon energy, and η_0 is the intrinsic impedance of free space. For monochromatic fields, Equation (2.2) can be written

$$I = \frac{\eta e}{h\nu} \cdot \frac{1}{\eta_0} \left[\frac{1}{2}|A_R|^2 + \frac{1}{2}|A_S|^2 + \text{real}\{E_S E_R^*\} \right] \tag{2.3}$$

where the term

$$\text{real}\{E_S E_R^*\} = A_R A_S \cos(2\beta_R l_R - 2\beta_S l_S) \tag{2.4}$$

describes the variation of the photocurrent with the positions of the reference and sample mirrors. In free space, the propagation constants are equal for both the reference and sample fields, giving $\beta_R = \beta_S = 2\pi/\lambda$ and

$$\text{real}\{E_S E_R^*\} = A_R A_S \cos\left(2\pi \cdot \frac{\Delta l}{\lambda/2}\right) \tag{2.5}$$

where $\Delta l = l_S - l_R$ is the mismatch in distance between the reference and sample beam paths. Equation (2.5) shows that the photocurrent contains a sinusoidally varying term representing the interference between the reference and sample fields. The interference has a period of $\lambda/2$ relative to the length mismatch Δl.

Since all of the interference information is contained in the real part of the cross-spectral term $E_R E_S^*$, subsequent analysis of interferometer in the case of a low-coherence light source will focus on calculating this term only.

2.3.2 Interferometer with Low-Coherence Light

A low-coherence light source consists of a finite bandwidth of frequencies rather than just a single frequency. The analysis in Section 2.3.2 can be extended to account for partially coherent light by integrating the cross-spectral term $E_R E_S^*$ over the harmonic content of the light source. We allow the reference and sample fields to be functions of frequency:

$$\begin{aligned} E_R(\omega) &= A_R(\omega) e^{-j[2\beta_R(\omega) l_R - \omega t]} \\ E_S(\omega) &= A_S(\omega) e^{-j[2\beta_S(\omega) l_S - \omega t]} \end{aligned} \tag{2.6}$$

The interference signal at the photodetector is proportional to the sum of the interference due to each monochromatic plane wave component, according to

$$I \propto \text{real}\left\{\int_{-\infty}^{\infty} E_R(\omega) E_S(\omega)^* \frac{d\omega}{2\pi}\right\} = \text{real}\left\{\int_{-\infty}^{\infty} S(\omega) e^{-j\Delta\phi(\omega)} \frac{d\omega}{2\pi}\right\} \tag{2.7}$$

where we have used the definitions

$$S(\omega) = A_R(\omega) A_S(\omega)^* \tag{2.8}$$

and

$$\Delta\phi(\omega) = 2\beta_S(\omega) l_S - 2\beta_R(\omega) l_R. \tag{2.9}$$

If the sample and reference arm fields have the same spectral components as the light source (*i.e.* if the reflectors in each arm and the fiber beamsplitter are spectrally uniform), then $S(\omega)$ is essentially equivalent to the power spectrum of the light source. $\Delta\phi(\omega)$ expresses the phase

mismatch at the detector of each frequency component. We will show that Equation (2.7) expresses a fundamental inverse Fourier transform relation between the source spectrum and the detector photocurrent.

2.3.3 Non-Dispersive Medium

Consider the case where the sample and reference arms consist of a uniform, linear, and non-dispersive material. Let the spectrum of the light source $S(\omega-\omega_0)$ be bandlimited with a center frequency of ω_0. We assume the propagation constants β in each arm are equal, and rewrite them as first-order Taylor expansions around the center frequency:

$$\beta_S(\omega) = \beta_R(\omega) = \beta(\omega_0) + \beta'(\omega_0)(\omega-\omega_0). \tag{2.10}$$

Then, the phase mismatch $\Delta\phi(\omega)$ in Equation (2.9) is solely determined by the length mismatch $\Delta l = l_S - l_R$ between the reference and sample arms through

$$\Delta\phi(\omega) = \beta(\omega_0)\cdot 2\Delta l + \beta'(\omega_0)(\omega-\omega_0)\cdot 2\Delta l. \tag{2.11}$$

The integral over the power spectral density in Equation (2.7) becomes

$$I \propto \text{real}\left\{ e^{-j\omega_0\Delta\tau_p}\int_{-\infty}^{\infty} S(\omega-\omega_0)e^{-j(\omega-\omega_0)\Delta\tau_g}\frac{d(\omega-\omega_0)}{2\pi}\right\} \tag{2.12}$$

where the phase delay mismatch $\Delta\tau_p$ and the group delay mismatch $\Delta\tau_g$ are defined as

$$\Delta\tau_p = \frac{\beta(\omega_0)}{\omega_0}\cdot 2\Delta l = \frac{2\Delta l}{v_p} \tag{2.13}$$

$$\Delta\tau_g = \beta'(\omega_0)\cdot 2\Delta l = \frac{2\Delta l}{v_g}. \tag{2.14}$$

Thus, $v_p = \omega_0/\beta(\omega_0)$ corresponds to the center frequency phase velocity and $v_g = 1/\beta'(\omega_0)$ is the group velocity. Equation (2.12) is basically a statement of the familiar Wiener-Khintchine theorem: the autocorrelation function is equal to the inverse Fourier transform of the power spectral density. Equations (2.12) through (2.14) show that the interferometric term of the photocurrent consists of a carrier and an envelope. The carrier oscillates with increasing path length mismatch $2\Delta l$ at a spatial frequency of $\beta(\omega_0)$. The envelope, which determines the axial point spread function of the interferometer, is essentially the inverse Fourier transform of the source power spectrum $S(\omega-\omega_0)$.

Gaussian Power Spectrum and Non-Dispersive Medium

Assume that the light source has a Gaussian power spectral density given by

$$S(\omega-\omega_0) = \sqrt{\frac{2\pi}{\sigma_\omega^2}}e^{-\frac{(\omega-\omega_0)^2}{2\sigma_\omega^2}} \tag{2.15}$$

which has been normalized to unit power

$$\int_{-\infty}^{\infty} S(\omega)\frac{d\omega}{2\pi} = 1 \tag{2.16}$$

and where ω_0 is defined as the center frequency, and $2\sigma_\omega$ is the standard deviation power spectral bandwidth (radians/second). Substitution of this power spectrum into Equation (2.12) gives the interferometric photocurrent

$$I \propto e^{-\frac{\Delta\tau_g}{2\sigma_\tau^2}} e^{-j\omega_0\Delta\tau_p} \tag{2.17}$$

where the real{} notation has been discarded for convenience. The photocurrent contains a Gaussian envelope with a characteristic standard deviation temporal width $2\sigma_\tau$ (seconds) which is inversely proportional to the power spectral bandwidth:

$$2\sigma_\tau = \frac{2}{\sigma_\omega}. \tag{2.18}$$

Note that $\sigma_\tau\sigma_\omega = 1$ (*i.e.* the time/frequency uncertainty relation is minimized for a Gaussian waveform). The envelope falls off quickly with increasing group delay mismatch $\Delta\tau_g$ and is modulated by interference fringes which oscillate with increasing phase delay mismatch $\Delta\tau_p$. Thus, Equation (2.17) defines the axial resolving properties of the OCT system. The detector only sees interference fringes when the reference and sample arm lengths are matched so that the group delay mismatch falls within the Gaussian envelope:

$$-\sigma_\tau < \beta'(\omega_0) \cdot 2\Delta l < \sigma_\tau. \tag{2.19}$$

The standard deviation axial resolution, or width of the axial point spread function (*i.e.* the $\pm\sigma_\tau$ width of the Gaussian envelope in units of length mismatch Δl) is, from Equations (2.14), (2.18) and (2.19),

$$\Delta l_{SD} = \frac{1}{\beta'(\omega_0)\sigma_\omega} = \frac{v_g}{\sigma_\omega}. \tag{2.20}$$

For propagation in free space, both the phase velocity and group velocity equal the speed of light c, and Equation (2.20) reduces to

$$\Delta l_{SD} = \frac{c}{\sigma_\omega} \tag{2.21}$$

showing that the axial resolution is inversely proportional to the bandwidth.

For measurements of bandwidth and resolution, a full-width at half-maximum (FWHM) criteria is more convenient than a standard deviation measure. For a Gaussian with standard deviation σ, the FWHM equals $2\sigma\sqrt{2\ln 2}$. Thus, for the interferometer in free space, the FWHM resolution Δl_{FWHM} is related to the FWHM wavelength bandwidth $\Delta\lambda$ for a Gaussian source by

$$\Delta l_{FWHM} = \frac{2\ln 2}{\pi} \cdot \frac{\lambda_0^2}{\Delta\lambda} \tag{2.22}$$

where λ_0 is the center wavelength.

2.3.4 Group Velocity Dispersion

Group velocity dispersion (GVD) causes different frequencies to propagate with nonlinearly related velocities. A short pulse in dispersive media will broaden if significant dispersion is present. In analogy to the short pulse case, the interferometric autocorrelation (*i.e.* the axial point spread function) will also broaden if the there is significant GVD mismatch between reference and sample arms. Both the fiber-optics and the sample may have significant GVD.

To include GVD in the analysis, the propagation constants β_R and β_S are Taylor expanded to second order around the center frequency ω_0:

$$\beta(\omega) = \beta(\omega_0) + \beta'(\omega_0)(\omega-\omega_0) + \frac{1}{2}\beta''(\omega_0)(\omega-\omega_0)^2 . \tag{2.23}$$

We assume that a GVD mismatch exists in a length L of the sample and reference paths. The frequency dependent phase mismatch from Equation (2.9) is then

$$\Delta\phi(\omega) = \beta(\omega_0)\cdot 2\Delta l + \beta'(\omega_0)(\omega-\omega_0)\cdot 2\Delta l + \frac{1}{2}\Delta\beta''(\omega_0)(\omega-\omega_0)^2 \cdot 2L \tag{2.24}$$

where Δl is defined as before, and $\Delta\beta''(\omega_0) = \beta_S''(\omega_0) - \beta_R''(\omega_0)$ is the GVD mismatch between the reference and sample paths. Note that only the difference in GVD between the two interferometer arms enters Equation (2.24). Thus, the deleterious effects of dispersion may be decreased by equalizing the GVD in both interferometer arms.

Inserting $\Delta\phi(\omega)$ into the propagation equation (2.7) gives the photocurrent

$$I \propto e^{-j\omega_0\Delta\tau_p}\int_{-\infty}^{\infty} S(\omega-\omega_0)e^{-j\frac{1}{2}\Delta\beta''(\omega_0)(\omega-\omega_0)^2\cdot 2L} e^{-j(\omega-\omega_0)\Delta\tau_g}\frac{d(\omega-\omega_0)}{2\pi} \tag{2.25}$$

where the phase delay mismatch $\Delta\tau_p$ and group delay mismatch $\Delta\tau_g$ have been defined in Equations (2.13) and (2.14). Again the real{} notation has been dropped for convenience. The GVD mismatch multiplies the source power spectral density $S(\omega-\omega_0)$ in a frequency dependent quadratic phase term. The interferometric signal looks like a short pulse, with Fourier transform $S(\omega-\omega_0)$ which propagates through a length L of dispersive medium with second order dispersion equal to the difference in GVD between the interferometer arms. Thus, just as a short pulse broadens and chirps after propagation through a dispersive medium, the interferometric signal should also broaden and chirp due to GVD mismatch in the two interferometer arms.

Gaussian Power Spectrum and Dispersive Medium

To establish the analogy further, assume that the source has a Gaussian power spectral density according to Equation (2.15). Then, after substitution into Equation (2.25), we obtain a modulated interferometric signal with a complex Gaussian envelope described by

$$I \propto \frac{\sigma_\tau}{\Gamma(2L)} e^{-\frac{\Delta\tau_g^2}{2\Gamma(2L)^2}} e^{-j\omega_0\Delta\tau_p} \tag{2.26}$$

where σ_τ is the standard deviation half-width from Equation (2.18). The characteristic width of the axial point spread function in the presence of dispersion $\Gamma(2L)$ is a complex parameter which depends both on the roundtrip length of GVD mismatch $2L$ and σ_τ via

$$\Gamma(2L)^2 = \sigma_\tau^2 + j\Delta\beta''(\omega_0) \cdot 2L. \tag{2.27}$$

The real and imaginary components of $1/\Gamma(2L)^2$ describe the broadening and chirping of the interferometric signal respectively, and are

$$\frac{1}{\Gamma(2L)^2} = \frac{\sigma_\tau^2}{\sigma_\tau^4 + \tau_{critical}^4} - j\frac{\tau_{critical}^2}{\sigma_\tau^4 + \tau_{critical}^4} \tag{2.28}$$

where we have defined the dispersion parameter

$$\tau_{critical} = \sqrt{\Delta\beta''(\omega_0) \cdot 2L}. \tag{2.29}$$

Substituting the expression for $1/\Gamma(2L)^2$ into Equation (2.26), we discover that the Gaussian envelope is broadened to the new standard deviation width $2\tilde{\sigma}_\tau$:

$$2\tilde{\sigma}_\tau = 2\sigma_\tau\sqrt{1 + \left(\frac{\tau_{critical}}{\sigma_\tau}\right)^4}. \tag{2.30}$$

The broadening factor becomes appreciable when the magnitude of the dispersion parameter $\tau_{critical}$ becomes greater than the unbroadened standard deviation temporal width σ_τ. For a typical fused silica fiber at 800 nm, $\beta'' = 350\ \text{fs}^2/\text{cm}$. For a typical resolution achieved by OCT, $\Delta l_{FWHM} = 10\ \mu\text{m}$, implying $\sigma_\tau = 28\ \text{fs}$. Thus, dispersive broadening becomes a factor if the fiber arm lengths are mismatched by at least $L \approx 1\ \text{cm}$. The potential for dispersive broadening within the eye is discussed in Section 3.2.7.

The chirping of the interferometric signal with increasing path length mismatch Δl may be described by differentiating the phase in the exponent of Equation (2.26), leading to

$$k = \frac{d\phi}{d\Delta l} = 2\beta(\omega_0) - \frac{\tau_{critical}^2}{\sigma_\tau^4 + \tau_{critical}^4} \cdot 4\Delta\beta'(\omega_0)^2 \cdot \Delta l \tag{2.31}$$

where k describes the spatial frequency of the interference fringes versus the distance measure Δl. For example, in the positive dispersion mismatch regime $\Delta\beta''(\omega_0) > 0$, as the reference arm path length is increased, Δl decreases, the wavenumber k increases, and interference fringes occur at the detector more often. It is important to note that GVD changes the phase, but not the bandwidth of the interference signal.

Dispersion mismatch also degrades the peak height of the interferometric envelope which reduces the system dynamic range. The degradation in the photocurrent amplitude is described by the multiplicative factor

$$\frac{\sigma_\tau}{|\Gamma(2L)|} = \frac{1}{\left[1 + \left(\frac{\tau_{critical}}{\sigma_\tau}\right)^4\right]^{1/4}}. \tag{2.32}$$

The reduction of the signal amplitude peak scales as the square-root of the broadening. Assuming the dynamic range is measured in terms of reflected optical power, which is proportional to photocurrent power, then the loss in dynamic range scales linearly with the broadening.

2.3.5 Non-Gaussian Light Sources

If the light source has a non-Gaussian spectrum, then several abnormalities in the axial point spread function may occur which can be predicted using the inverse Fourier transform relation in Equation (2.12).

Spectral Modulation

Modulation or ripples in the light source spectrum can cause echoes to appear in the axial point spread function. Assume that we may write the modulated spectrum $S_m(\omega)$ as a function of an ideal, unmodulated spectrum $S(\omega)$ in the form

$$S_m(\omega) = S(\omega)\left[1 + \frac{M}{2}\cos\left(\omega\frac{\lambda_0^2}{c\lambda_m}\right)\right] \tag{2.33}$$

where λ_0 is the center wavelength, M is the ratio of the peak-to-peak modulation height to the average spectral height and λ_m is the approximate modulation period measured in the wavelength domain. Then by the inverse Fourier transform relation in Equation (2.12) for a non-dispersive medium, the photocurrent will consist of a main peak situated at $\Delta l = 0$ and two side peaks or echoes with a height of $M/4$ relative to the main peak situated at

$$\Delta l = \pm\frac{\lambda_0^2}{2\lambda_m}\cdot\frac{v_g}{c}. \tag{2.34}$$

Equation (2.34) reduces to $\Delta l = \pm\lambda_0^2/(2\lambda_m)$ in free space.

Superluminescent diode light sources often contain variable amounts of spectral modulation. A typical retinal image contains a dynamic range of 45 dB. For the echoes from spectral modulation to be greater than 45 dB below the largest reflection, the modulation M needs to be less than approximately 2% to submerge the echoes below the noise floor of the image.

Blindness

Blindness occurs if the tails of the axial point spread function are sufficiently broad to prevent the observation of a weak reflection placed next to a strong reflection [57]. The effect is a function of the light source spectrum according to the inverse Fourier transform relationship in Equation (2.12). If the source has a Gaussian spectrum, then the axial point spread function is also Gaussian and its tails decay exponentially with the squared path length mismatch between reference and sample arms. However, if the source is non-Gaussian, then significant tails in the axial point spread function may occur. A Lorentzian line shape, for example, will only decay exponentially with the linear path length mismatch.

2.4 Detection Electronics

Section 2.3 showed that the interferometric photocurrent consists of an axial point spread function envelope superimposed on a carrier frequency. An electrical circuit is used to extract the envelope of the detected signal in a manner similar to the demodulation of AM radio signals. In the actual OCT system, the reference mirror oscillates rapidly and travels at a velocity v_s during scanning. Therefore, the axial point spread function, which is a function of the path length mismatch Δl, is mapped into a function of time by the change of variables $\Delta l = -v_s t$ (where time $t = 0$ occurs when the two path lengths are matched, and t increases as the reference mirror is translated farther from the beamsplitter). From Equation (2.13), the resulting electrical signal has a carrier frequency of

$$\tilde{\omega}_D = \frac{2v_s}{v_p} \cdot \omega_0 \tag{2.35}$$

where ω_0 is, as before, the center frequency of the source spectrum, and the tilda denotes the electronic frequency counterpart of the corresponding optical frequency. If free space propagation is assumed, then Equation (2.35) simplifies to

$$\tilde{f}_D = \frac{2v_s}{\lambda_0}. \tag{2.36}$$

The carrier frequency $\tilde{f}_D$ can also be interpreted as the Doppler shift caused by the moving reference mirror which creates a beat frequency at the photodetector after mixing with unshifted light returning from the sample mirror.

To extract this signal, the detection circuit consists of three main elements in succession after the photodetector, shown in Figure 2-3: (1) a transimpedance amplifier with a gain of R which converts the interferometric photocurrent into a voltage; (2) a band-pass filter with a transfer function $H_{bp}(s)$ centered at the carrier frequency $\tilde{f}_D$ which separates the actual interferometric signal from the DC photocurrent and noise; and (3) an amplitude demodulator which extracts the envelope of the interferometric signal. The envelope is subsequently digitized and stored on a computer. As will be discussed later, the amplitude demodulator may be realized by mixing or by envelope detection. Mixing involves multiplication of the interferometric signal by a sinusoidal reference at the carrier frequency followed by low-pass filtering. Envelope detection entails some sort of rectification, for example, square-law detection, followed by low-pass filtering.

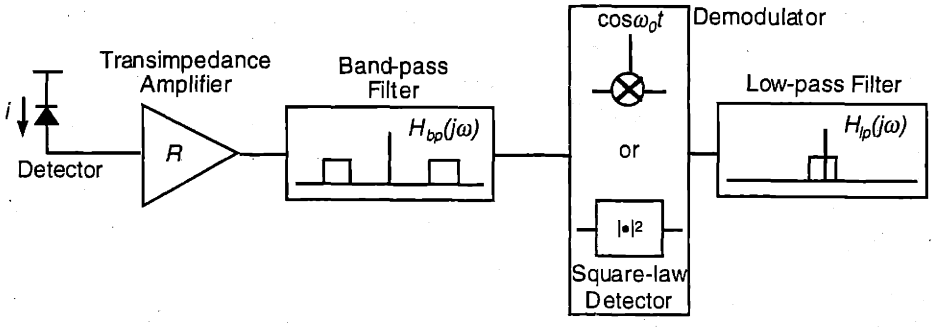

FIGURE 2-3. Block diagram of OCT electronics.

2.4.1 Correspondence Between Optical and Electrical Frequency

A one-to-one mapping may be established between the source power spectrum in the optical frequency domain and the interferometric photocurrent in the electrical frequency domain. Consider $\phi(\omega)$ given by Equation (2.23) for the case of dispersive media. If we define a linear transformation $T(\omega)$ between optical frequencies ω and electrical frequencies $\tilde{\omega}$ such that

$$\tilde{\omega} = T(\omega) = \frac{2\nu_s}{\nu_g}\left[\omega - \omega_0\left(\frac{\nu_g}{\nu_p} - 1\right)\right] \tag{2.37}$$

then Equation (2.35) is automatically satisfied, and the phase mismatch term in Equation (2.24) can be rewritten as

$$\Delta\phi(\omega) = \Phi(\tilde{\omega}) - \tilde{\omega}t\,. \tag{2.38}$$

In Equation (2.38), $\tilde{\omega}t$ contains the entire linear component of the frequency dependence and

$$\Phi(\tilde{\omega}) = \frac{1}{2}\left[\Delta\beta''(\omega_0)\cdot 2L\right]\left[\frac{\nu_g}{2\nu_s}(\tilde{\omega} - \tilde{\omega}_D)\right]^2 \tag{2.39}$$

contains the quadratic phase variation. The propagation Equation (2.7) then reduces to an inverse Fourier transform relation between the time and electrical frequency domains, described by

$$I \propto \frac{\nu_g}{2\nu_s}\int_{-\infty}^{\infty} S[T^{-1}(\tilde{\omega})]e^{-j\Phi(\tilde{\omega})}e^{j\tilde{\omega}t}\frac{d\tilde{\omega}}{2\pi} = \frac{\nu_g}{2\nu_s}\mathcal{F}^{-1}\left\{S[T^{-1}(\tilde{\omega})]e^{-j\Phi(\tilde{\omega})}\right\}. \tag{2.40}$$

The Fourier transform $\mathcal{F}\{I\}$ of the photocurrent from the time domain t to the electrical frequency domain $\tilde{\omega}$ simply reverses the inverse transform in Equation (2.40):

$$\mathcal{F}\{I\} \propto \frac{\nu_g}{2\nu_s}S[T^{-1}(\tilde{\omega})]e^{-j\Phi(\tilde{\omega})}. \tag{2.41}$$

Equation (2.41) shows that the frequency domain representation of the photocurrent is simply a shifted and scaled version of the light source power spectrum which is multiplied by a quadratic phase factor that accounts for dispersion. In other words, in the case of non-dispersive propagation, the shape of the frequency domain representation of the electronic signal is exactly the shape of the light source power spectrum. The mapping of optical frequencies f to electrical frequencies $\tilde{f}$ is given by Equation (2.37) which, for the case of free space propagation, reduces to

$$\tilde{f} = \frac{2v_s}{\lambda}. \tag{2.42}$$

where we have written the optical frequencies in terms of optical wavelengths λ. Note that Equation (2.42) holds for not only the Doppler shift frequency $\tilde{f}_D$ corresponding to the center optical wavelength λ_0, but also for the other optical wavelengths within the source spectral bandwidth as well.

Equation (2.37) is particularly useful for calculating the bandwidth and quality factor of the photocurrent from the bandwidth and quality factor of the source spectrum because the mapping is independent of both the specific shape of the source spectrum and the particular definition of bandwidth. If $\Delta\tilde{f}$, Δf and $\Delta\lambda$ are arbitrary but equivalent measures of electrical frequency bandwidth, optical frequency bandwidth, and optical wavelength bandwidth respectively, then

$$\Delta\tilde{f} = \frac{2v_s}{v_g}\Delta f \approx \frac{2v_s}{v_g}\cdot\frac{c}{\lambda_0^2}\Delta\lambda \tag{2.43}$$

where λ_0 is the center optical wavelength. In free space, Equation (2.43) becomes

$$\Delta\tilde{f} \approx \frac{2v_s}{\lambda_0^2}\Delta\lambda. \tag{2.44}$$

Note that the scaling factor in Equation (2.43) is the ratio between the roundtrip mirror velocity $2v_s$ and the optical group velocity v_g. Since the scaling factor is constant, the mapping is linear, and the scaling factor cancels out of any ratios. Therefore, the quality factor Q in the optical and electrical domains is identical and is given by the simple relations

$$\frac{1}{Q} = \frac{\Delta\tilde{f}}{\tilde{f}_D} = \frac{\Delta f}{f_0} \approx \frac{\Delta\lambda}{\lambda_0}. \tag{2.45}$$

where the subscript 0 denotes the center optical frequency or optical wavelength, and the subscript D indicates the center (Doppler shift) electronic frequency. Equation (2.45) approximately gives the Q desired for the band-pass filter in terms of the wavelength bandwidth $\Delta\lambda$ of the light source.

2.4.2 Transimpedance Amplifier

The photodetector is followed by a transimpedance amplifier, shown in Figure 2-4, which converts the photocurrent i into an output voltage v. For low frequencies, the output

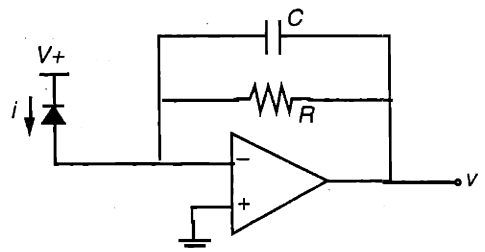

FIGURE 2-4. Transimpedance amplifier.

voltage is simply

$$v = iR. \tag{2.46}$$

The capacitance C in parallel with the feedback resistance is necessary for amplifier stability and causes the amplifier to roll off at 20 dB/decade above the dominant pole at

$$\omega_c = \frac{1}{RC}. \tag{2.47}$$

2.4.3 Band-pass Filter

A band-pass filter follows the transimpedance amplifier (after a simple single pole RC circuit which removes the DC photocurrent) to separate the bandlimited interferometric signal from noise. The filter is designed with a center frequency $\tilde{f}_D$ and quality factor Q given by Equations (2.36) and (2.45) respectively. In the discussions below, the tilda indicating electrical frequencies will be dropped. Both an active and a passive filter were used.

Active Sallen and Key Cascade Filter

The active band-pass filter was used for carrier frequencies below 100 kHz. For higher frequencies, the filter was limited by the slew rate of the operational amplifier and a passive network filter needed to be employed. The band-pass filter was created by cascading a low-pass followed by a high-pass Sallen and Key biquad filter [Sallen, 1955 #42].

Figure 2-5 depicts the low-pass Sallen and Key filter in a unity gain configuration. The transfer function is given by the standard second-order form

$$H(s) = \frac{V_o(s)}{V_i(s)} = \frac{\omega_n^2}{s^2 + \frac{\omega_n}{Q}s + \omega_n^2} \tag{2.48}$$

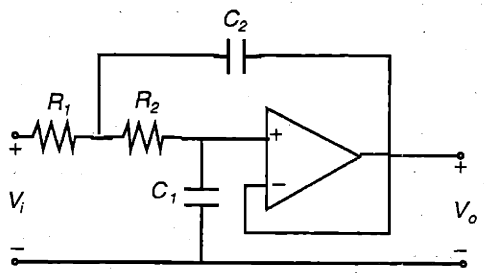

FIGURE 2-5. Sallen and Key low-pass filter.

where the undamped natural frequency ω_n is

$$\omega_n = \frac{1}{\sqrt{R_1 R_2 C_1 C_2}} \tag{2.49}$$

and the quality factor Q is

$$Q = \frac{1}{2\zeta} = \frac{\sqrt{R_1 R_2}}{R_1 + R_2} \cdot \sqrt{\frac{C_2}{C_1}}. \tag{2.50}$$

The two design parameters ω_n and Q are functions of four variables. The design equations may be simplified by setting $R = R_1 = R_2$. In this case, Equations (2.49) and (2.50) become

$$\omega_n = \frac{1}{R\sqrt{C_1 C_2}} \tag{2.51}$$

and

$$Q = \frac{1}{2}\sqrt{\frac{C_2}{C_1}}. \tag{2.52}$$

The resonance frequency ω_n is chosen to be equal to the signal carrier frequency ω_D. In practice the quality factor Q is chosen to be smaller than the value given by Equation (2.45) so that the filter bandwidth is larger than the signal bandwidth. A filter bandwidth which is too narrow will widen the signal in time and arbitrarily limit the axial point spread function. Section 2.6 will show that a filter bandwidth which is too large will let in more noise and reduce the minimum detectable reflectivity or dynamic range of the system.

The unity gain Sallen and Key high-pass filter is exactly the dual of the low-pass filter except resistors are interchanged with capacitors (Figure 2-6). The high-pass transfer function is

$$H(s) = \frac{V_o(s)}{V_i(s)} = \frac{\omega_n^2 s^2}{s^2 + \frac{\omega_n}{Q}s + \omega_n^2} \tag{2.53}$$

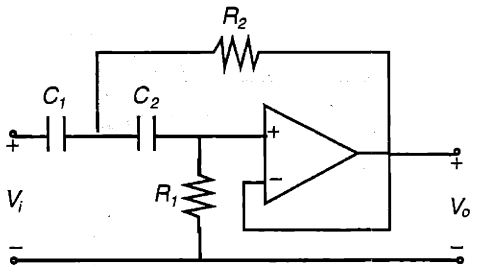

FIGURE 2-6. Sallen and Key high-pass filter.

where

$$\omega_n = \frac{1}{C\sqrt{R_1 R_2}} \tag{2.54}$$

and

$$Q = \frac{1}{2\zeta} = \frac{1}{2}\sqrt{\frac{R_1}{R_2}} \tag{2.55}$$

using the simplification $C = C_1 = C_2$. The resonant frequency and quality factor are chosen to match those for the low-pass filter. In practice, the component values for both filters must be measured carefully since small variations can displace the two resonance frequencies and effectively broaden the bandwidth.

The band-pass filter $H_{bp}(s)$ created by the cascade of the low-pass and high-pass filter has two sets of pole pairs at

$$p_{1,2} = -\frac{\omega_n}{2Q} \pm j\omega_n\sqrt{1 - \frac{1}{4Q^2}}. \tag{2.56}$$

Thus, the frequency response rolls off at 40 dB/decade in both directions outside of the resonance peak.

Passive Network Butterworth Filter

A passive network band-pass filter was designed for high-frequency operation using the standard techniques for broadband matching network synthesis. The problem is formulated as follows in relation to Figure 2-7: given a Thevenin equivalent voltage source defined by V_t and R_t, synthesize a lossless two-port network which is matched to the load impedance R_2 and has the desired transfer function power gain characteristic $|H(j\omega)|^2 = |V_2(j\omega)/V_t(j\omega)|^2$.

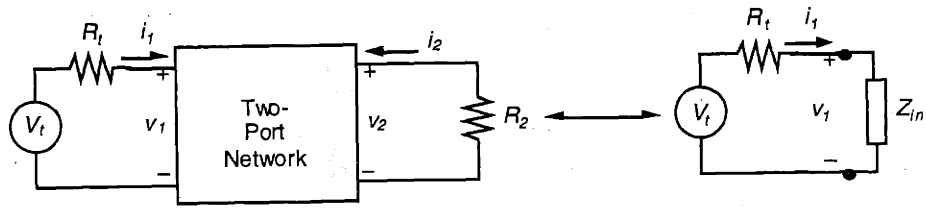

FIGURE 2-7. Network synthesis problem.

The solution to the general problem has been explored in detail [58] and only a brief outline of the problem using resistive termination will be given here. In general, one first computes the reflection coefficient $\rho(s)$ which is a measure of the power reflected back to the source by the equivalent input impedance $Z_{in}(s)$. The ratio $|\rho(s)|^2$ of the reflected to the total power is related to ratio $|H(s)|^2$ of the transmitted to the total power by

$$|\rho(s)|^2 = 1 - |H(s)|^2 . \tag{2.57}$$

The reflection coefficient may also be expressed in terms of the equivalent input impedance of the two-port:

$$\rho(s) = \frac{Z_{in}(s) - R_t}{Z_{in}(s) + R_t} . \tag{2.58}$$

Therefore, the equivalent input impedance $Z_{in}(s)$ may be found from the desired power gain characteristic by the prudent (*i.e.* minimum phase) choice of poles and zeros in the factorization of Equation (2.57). Once the input impedance is found, a two-port network with resistive termination can be synthesized by the process of Cauer ladder development to match this impedance.

It can be shown that an LC ladder can always be obtained to match a purely resistive source and load and achieve the n^{th} order Butterworth low-pass characteristic given by

$$|H(j\omega)|^2 = \frac{K}{1 + \left(\frac{j\omega}{j\omega_c}\right)^{2n}} . \tag{2.59}$$

The Butterworth filter with DC gain K and low-pass cutoff ω_c is maximally flat in the passband and has evenly spaced poles placed in the LHP on a circle centered at the frequency origin. Furthermore, explicit formulas exist for the element values of the LC ladder, shown in Figure 2-8, which simplifies the design process. (An odd order filter is realized by removing the terminating capacitor).

To realize a Butterworth filter of order n given R_t and R_2, first compute the gain parameter α from

$$\alpha^n = \frac{X-1}{X+1} \quad \text{where} \quad X = \begin{cases} R_2/R_t & \text{for } R_2 > R_t \\ R_t/R_2 & \text{for } R_t > R_2 \end{cases} . \tag{2.60}$$

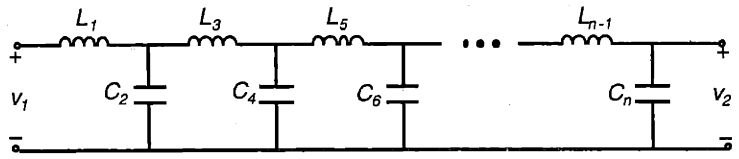

FIGURE 2-8. LC ladder network of order n.

The Butterworth DC gain is then determined by $K = 1 - \alpha^{2n}$. The capacitor and inductor element values may be calculated in a recursive fashion:

$$L_1 = \frac{2R_t \sin\frac{\pi}{2n}}{(1-\alpha)\omega_c} \tag{2.61}$$

$$C_m = \frac{A_m}{\omega_c^2 L_{m-1}} \tag{2.62}$$

$$L_m = \frac{A_m}{\omega_c^2 C_{m-1}} \tag{2.63}$$

where the recursion parameter A_m is defined as

$$A_m = \frac{4\sin\left[\frac{(2m-3)\pi}{2n}\right]\sin\left[\frac{(2m-1)\pi}{2n}\right]}{1-2\alpha\cos\left[\frac{(2m-2)\pi}{2n}\right]+\alpha^2}. \tag{2.64}$$

If the source and load resistances are equal, then $\alpha = 0$ and Equations (2.61) through (2.64) simplify to the following non-recursive definitions:

$$L_m = \frac{2R_t}{\omega_c}\sin\left[\frac{(2m-1)\pi}{2n}\right] \tag{2.65}$$

$$C_m = \frac{2}{R_t\omega_c}\sin\left[\frac{(2m-1)\pi}{2n}\right]. \tag{2.66}$$

To realize a band-pass filter with low-pass cutoff ω_1 and high-pass cutoff ω_2, one first designs a normalized, prototype low-pass filter with a cut-off of frequency of $\omega_c = 1$ radians/second. The following frequency transformation is then used to warp the filter from the low-pass domain s, with a pass band of $-1 \leftrightarrow 1$ radians/second, to the band-pass domain $\tilde{s}$, with pass bands $\omega_1 \leftrightarrow \omega_2$ and $-\omega_2 \leftrightarrow -\omega_1$:

$$s = \frac{\omega_m}{B}\left[\frac{\tilde{s}}{\omega_m} + \frac{\omega_m}{\tilde{s}}\right]. \tag{2.67}$$

We have defined $B = \omega_2 - \omega_1$ as the desired band-pass filter bandwidth and $\omega_m = \omega_1\omega_2$ as the mid-band (geometric mean) frequency. It is straightforward to verify that the transformation described by Equation (2.67) involves replacing inductors in the prototypical filter (Figure 2-8) by an inductor and a capacitor in series, and replacing capacitors in the prototypical filter by an inductor and a capacitor in parallel. The necessary component values for this low-pass to band-pass frequency warping are shown in Figure 2-9. Resistors remain unchanged. The low-pass to band-pass frequency warping process doubles the number of poles in the system.

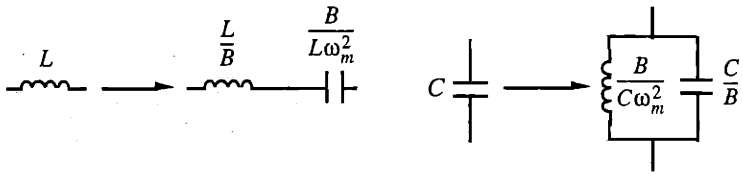

FIGURE 2-9. Low-pass to band-pass frequency warping.

A second order prototypical Butterworth low-pass filter which was transformed into a four-pole band-pass filter was implemented in the OCT system (Figure 2-10). The design

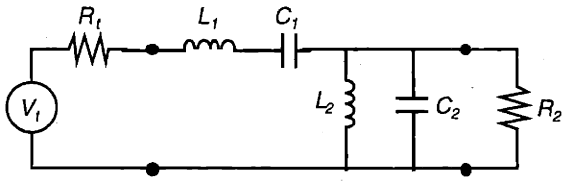

FIGURE 2-10. Second-order Butterworth band-pass filter.

parameters were a center frequency of 400 kHz and a quality factor of 10. The condition of equal input and output impedances was used, since in practice it is easy to match resistive impedances with operational amplifiers. (For a simple inverting or non-inverting operational amplifier circuit, the input impedance equals the value of the input resistor, and the output impedance is usually negligible). For $R_t = R_2 = 5\ \text{k}\Omega$, the following component values were obtained using the procedure described above: $L_1 = 28.1$ mH, $C_1 = 5.64$ pF, $L_2 = 141\mu$H, and $C_2 = 1.13$ nF. The frequency response of the resulting band-pass filter is shown in Figure 2-11. The filter has two zeros located at the origin and a two complex pole pairs located at

$$\begin{aligned} p_{1,2} &= -0.092 \pm j2.60 \\ p_{3,4} &= -0.086 \pm j2.42 \end{aligned} \qquad \text{rad/s} \times 10^6. \tag{2.68}$$

Thus, the frequency response rolls off at 40 db/decade in both directions off the main peak.

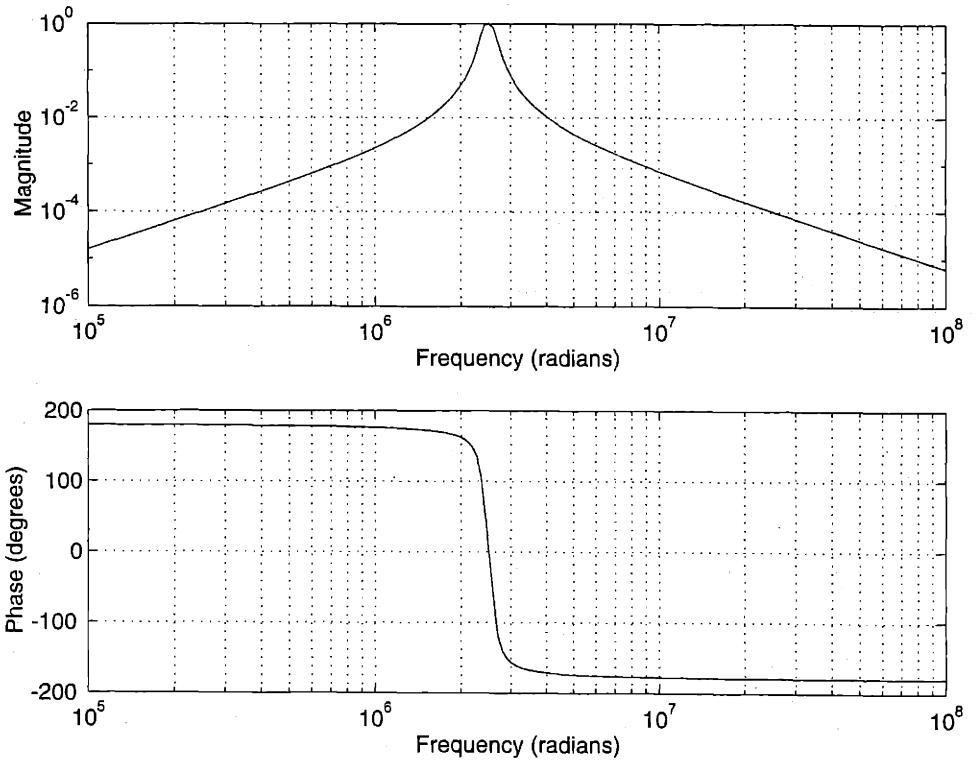

FIGURE 2-11. Frequency response of Butterworth band-pass filter.

2.4.4 Demodulation

Amplitude demodulation may occur either by mixing or envelope detection. Both models will be briefly introduced here so that noise propagation through the electronics can be understood for both methods.

Mixing

Demodulation by mixing entails multiplication with a reference sinusoidal signal of the correct phase followed by low-pass filtering. Mixing is easily implemented using a lock-in amplifier. The reference frequency is chosen to match the Doppler shift carrier frequency ω_D, and the bandwidth of the low-pass filter is chosen to be slightly larger than approximately one-half the signal bandwidth $\Delta\omega$. In a typical lock-in amplifier, a single-pole RC time constant is used, giving a low-pass transfer function

$$H_{lp}(s) = \frac{H_0}{RCs + 1} \tag{2.69}$$

with a bandwidth of $1/RC$ radians/second.

The phase of the reference sine wave must be locked to the phase of the signal for adequate demodulation. If this is not possible, then the signal can be divided and correlated simultaneously in quadrature (*i.e.* with both a sine and a cosine). The sum of the squares of the two quadrature components accurately gives the signal power independent of the actual phase.

Envelope Detection

Envelope detection occurs by rectification followed by low-pass filtering. A single chip implementation may be used which can provide either a linear or a logarithmic output. The AD637 High Precision Wideband RMS-to-DC Converter (Analog Devices) was used in the current system. For ease of calculation, the performance of the chip can be modeled by a single-pole low-pass transfer function (*e.g.* Equation (2.69)) operating on the square of the input voltage.

Envelope detection is more advantageous than mixing when the phase or frequency of the carrier has nonlinear variations (for example due to non-linear sweeping of the reference mirror).

2.5 Noise Sources

The sensitivity of the OCT system is very important since the retina is poorly reflective and often images must be acquired under conditions of media opacity (such as cataracts) and poor alignment. This Section will review thermal noise, shot noise, and excess intensity noise which are the dominant sources of noise which affect the OCT electronics.

The noise sources below may be described by wide-sense stationary (WSS) stochastic processes. A WSS stochastic process $p(t)$ has a constant mean

$$E\{p(t)\} = \langle p(t) \rangle = m_p \tag{2.70}$$

and a statistical autocorrelation

$$R_p(t_1, t_2) = E\{p(t_1)p(t_2)\} = \langle p(t_1)p(t_2) \rangle \tag{2.71}$$

which is a function of $\tau = t_2 - t_1$ alone. A description of the frequency content a WSS stochastic process is given by the power spectral density

$$S_p(\omega) = \int_{-\infty}^{\infty} R_p(\tau) e^{-j\omega t} d\tau \tag{2.72}$$

which is simply the Fourier transform of the statistical autocorrelation.

The power spectral density $S_p(\omega)$ is defined for both positive and negative frequencies and is a real and even function of ω by definition. In practice, however, only positive fre-

quencies are measured. For convenience we define a positive frequency or single-sided power spectral density

$$S_p^+(\omega) = S_p(\omega) + S_p(-\omega) = 2S_p(\omega) \tag{2.73}$$

which is valid for $\omega \geq 0$ and allows comparison of theory with experiment.

2.5.1 Thermal Noise

Thermal noise arises from random particle motion due to the thermal energy of a system. In electrical circuits, resistors are the only passive elements which exchange energy with the environment. Thus, thermal noise is associated with the transfer of energy and the temperature equilibrium established between a resistor and its surroundings. A noisy resistor may be modeled as the parallel combination of an ideal resistor with resistance R and a noisy current source i_n which represents the thermal noise or energy provided by the environment [59-62]. The noise current is approximated by zero-mean white noise with a double-sided power spectral density

$$S_{i_n}(\omega) = \frac{2kT}{R} \tag{2.74}$$

where T is the temperature and k is Boltzmann's constant.

2.5.2 Shot Noise

Shot noise arises from current fluctuations due to the quantization of light and charge [59-62]. A photodetector will emit charge corresponding to a mean rate defined by the photocurrent; however, the time between specific emissions will be random. The photon arrival and electron emission times may be described by a Poisson distributed random variable. It can be shown that the shot noise associated with any photocurrent $\langle i \rangle$ is a white noise process with mean $\langle i \rangle$ and double-sided power spectral density

$$S_{i_n}(\omega) = e\langle i \rangle . \tag{2.75}$$

The shot noise power is proportional to the electronic charge and the square root of the photocurrent power $\langle i \rangle^2$.

2.5.3 Excess Intensity Noise and Amplified Spontaneous Emission

Excess intensity noise includes any noise source whose power spectral density scales linearly with the mean photocurrent power $\langle i \rangle^2$. Examples include fluctuations in optical power from the source and from the mechanical motion of optical mounts. With a superluminescent diode source using heterodyne detection, amplified spontaneous emission (ASE) also results in noise which scales linearly with the photocurrent power. The spectral density of excess intensity noise and ASE noise may be approximated as white over the frequency band of interest and may be modeled as

$$S_{i_n}(\omega) = e\gamma\langle i \rangle^2 \tag{2.76}$$

where the noise parameter γ must usually be determined by experiment.

2.6 Sensitivity and Noise

This Section will give expressions for the expected sensitivity of the OCT system considering the noise sources described in Section 2.5. The sensitivity is a measure of the minimum detectable reflectivity of the OCT system. The sensitivity, or signal-to-noise ratio (SNR) for any system is defined simply as the signal power P_{signal} divided by the noise process variance $\text{var}\{n(t)\}$. If the noise process is zero-mean WSS, then

$$SNR = \frac{P_{signal}}{\text{var}\{n(t)\}} = \frac{P_{signal}}{R_n(0)} = \frac{P_{signal}}{\int_{-\infty}^{\infty} S_n(\omega)\frac{d\omega}{2\pi}} \tag{2.77}$$

which shows that the SNR is equal to the signal power divided by the mean noise power, where the noise power is the integral of its power spectral density $S_n(\omega)$ over all frequencies.

The signal-to-noise ratio will be derived below by propagating the various sources of noise described in Section 2.5 through the detection electronics described in Section 2.4. In the shot noise limit, the noise power is dominated by the shot noise of the reference beam, also termed the local oscillator. The signal power is given by the correlation of the power reflected from the sample with the power in the local oscillator. Weak reflections from within the eye are therefore multiplied by the local oscillator field to create a relatively strong interference signal at the detector. In this manner, a relatively high SNR may be achieved. Figure 2-12 displays the variables used for the noise processes, power spectral densities, and noise equivalent bandwidths at various points in the system and will be helpful in the subsequent sections.

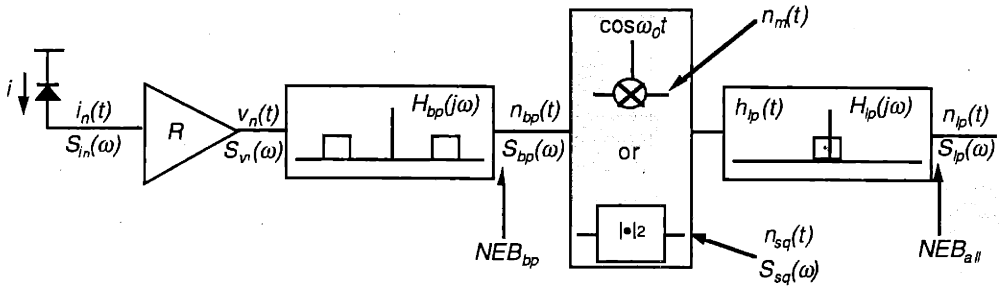

FIGURE 2-12. Noise variable definitions.

2.6.1 Photodetection Noise

From Equation (2.3), the photodetector current is the sum of the DC power $P_R = |A_R|^2/2\eta_0$ returning from the reference path, the DC power $P_S = |A_S|^2/2\eta_0$ returning from the sample, and an interference term $\text{real}\{E_S E_R^*\}$ from the correlation of the signal and the local oscillator:

$$I = \frac{\eta e}{h\nu}\cdot\left[P_R + P_S + \frac{1}{\eta_0}\text{real}\{E_S E_R^*\}\right] + i_{dark} \tag{2.78}$$

We have also added a term i_{dark} which represents the dark current of the photodiode. As we have seen, the signal power is completely contained within the term real$\{E_S E_R^*\}$ which is separated from the DC components P_R and P_S by band-pass filtering and demodulation. The filtering and demodulation steps, however, do not eliminate the noise associated with these components, which may exist at all frequencies.

Both shot noise (Equation (2.75)) and excess intensity noise (Equation (2.76)) contribute to the photocurrent noise $i_n(t)$ which can propagate through the detection electronics. Therefore, the power spectral density $S_{i_n}(\omega)$ of this noise may be expressed as the sum of these two uncorrelated components:

$$S_{i_n}(\omega) = e\langle i\rangle + e\gamma\langle i\rangle^2 \tag{2.79}$$

where $\langle i\rangle$ is the mean photocurrent and contains contributions from the local oscillator beam, the sample beam, the signal, and the dark current.

2.6.2 Transimpedance Amplifier Noise

At the input to the transimpedance amplifier (Figure 2-4), thermal noise (Equation (2.74)) from the feedback gain resistor R is added to the photocurrent noise. Since all the noise sources are uncorrelated, the power spectral density of the noise current becomes

$$S_{i_n}(\omega) = e\langle i\rangle + e\gamma\langle i\rangle^2 + \frac{2kT}{R}. \tag{2.80}$$

At the output of the transimpedance amplifier, the noise current $n_i(t)$ is transformed into a voltage $n_v(t)$ with a gain of R. Since the variance scales as R^2, the spectral density $S_{v_n}(\omega)$ of the output noise voltage is

$$S_{v_n}(\omega) = e\langle i\rangle R^2 + e\gamma\langle i\rangle^2 R^2 + 2kTR. \tag{2.81}$$

Equation (2.81) can also be written in terms of the mean output voltage $\langle v\rangle = \langle i\rangle R$ as

$$S_{v_n}(\omega) = e\langle v\rangle R + e\gamma\langle v\rangle^2 + 2kTR = q \tag{2.82}$$

where a new variable q has been defined as the representing the amplitude of the noise spectral density, which is constant across all frequencies. Equation (2.82) is useful because the voltage output of the transimpedance amplifier is more conveniently measured than the photocurrent.

2.6.3 Band-Pass Filter Noise Equivalent Bandwidth

Let the band-pass filter have an impulse response $h_{bp}(t)$ and a transfer function $H_{bp}(s)$ given by one of the design procedures detailed in Section 2.4.3. The noise input to this filter is given by Equation (2.82). Since the input noise is white with a constant spectral density, the output noise will be colored, or shaped according to the characteristics of the filter.

Using the standard results for a WSS stochastic process through a linear time invariant filter, we obtain the power spectral density $S_{bp}(\omega)$ of the noise process $n_{bp}(t)$ at the output of the filter:

$$S_{bp}(\omega) = q|H_{bp}(j\omega)|^2. \tag{2.83}$$

The corresponding autocorrelation $R_{BP}(\tau)$ may be found by taking the inverse Fourier transform:

$$R_{bp}(\tau) = q\int_{-\infty}^{\infty} |H_{bp}(j\omega)|^2 e^{j\omega\tau}\frac{d\omega}{2\pi}. \tag{2.84}$$

The noise variance at the band-pass filter output is

$$var\{n_{bp}(t)\} = R_{bp}(0) = q\int_{-\infty}^{\infty} |H_{bp}(j\omega)|^2\frac{d\omega}{2\pi} = 2q\int_{0}^{\infty} |H_{bp}(j\omega)|^2\frac{d\omega}{2\pi} = 2q \cdot NEB_{bp} \tag{2.85}$$

where the noise equivalent bandwidth (NEB) of the band-pass filter is defined above and is a geometric measure of the how much noise passes through the filter. The factor of two arises because the NEB is defined for positive frequencies only. Note that the band-passed noise has zero mean, since the DC gain of the filter is zero.

2.6.4 Noise Equivalent Bandwidth for Demodulation by Mixing

The noise process $n_{bp}(t)$ at the output of the band-pass filter is then input to the demodulator. The NEB and resulting signal-to-noise ratio (SNR) of demodulation by mixing will be considered below and in Section 2.6.5. Demodulation by envelope detection will be considered separately in Section 2.6.6.

The discussion of the noise characteristics after demodulation by mixing is involved because the noise is not a WSS process after correlation with $\cos\omega_D t$. The demodulated noise process, however, is WSS. Therefore, the noise must be propagated through both the sinusoidal correlator and the low-pass filter in one step to compute the final power spectral density. Let

$$n_m(t) = n_{bp}(t)\cos\omega_D t \tag{2.86}$$

be the noise process after mixing with a frequency ω_D, and $n_{lp}(t)$ be describe the final demodulated signal after low-pass filtering $n_m(t)$ with system function $H_{lp}(s)$ and impulse response $h_{lp}(t)$. Since

$$E\{n_m(t)\} = E\{n_{bp}(t)\}\cos\omega_D t = 0, \tag{2.87}$$

the output noise process $n_{lp}(t)$ will also be zero-mean after low-pass filtering. Thus, the output noise covariance is equal to the output noise autocorrelation $R_{lp}(t_1, t_2)$ and the noise variance may be computed from

$$\text{var}\{n_{lp}(t)\} = R_{lp}(t_1, t_2)\big|_{t_1 = t_2 = t} = E\{n_{lp}(t_1)n_{lp}(t_2)\}\big|_{t_1 = t_2 = t}. \tag{2.88}$$

The demodulated noise process $n_{lp}(t)$ is related to the input noise process $n_{bp}(t)$ at the output of the band-pass filter by mixing with $\cos\omega_D t$ and subsequent convolution with the low-pass impulse response $h_{lp}(t)$:

$$n_{lp}(t) = \int_{-\infty}^{\infty} n_{bp}(\tau)\cos\omega_D\tau \cdot h_{lp}(t-\tau)d\tau . \tag{2.89}$$

Substituting Equation (2.89) into right-hand side of Equation (2.88) twice, and evaluating the expectation, we arrive at an expression for the noise autocorrelation $R_{lp}(t_1, t_2)$ after mixing and low-pass filtering in terms of the WSS autocorrelation $R_{bp}(\tau)$ of the noise at the output of the band-pass filter:

$$R_{lp}(t_1, t_2) = \int_{-\infty}^{\infty}\int_{-\infty}^{\infty} R_{bp}(\tau-\mu)\cdot\cos\omega_D\tau\cdot h_{lp}(t_1-\tau)\cdot\cos\omega_D\mu\cdot h_{lp}(t_2-\mu)\cdot d\mu d\tau . \tag{2.90}$$

Inserting the expression for $R_{bp}(\tau)$ in Equation (2.84) into Equation (2.90) and splitting up the complex exponential contained in Equation (2.84) gives

$$R_{lp}(t_1, t_2) = q\int_{-\infty}^{\infty} |H_{bp}(j\omega)|^2 \cdot X_{lp}(\omega, t_1)\cdot Y_{lp}(\omega, t_2)\cdot\frac{d\omega}{2\pi} \tag{2.91}$$

where

$$X_{lp}(\omega, t_1) = \int_{-\infty}^{\infty} h_{lp}(t_1-\tau)\cos\omega_D\tau\cdot e^{j\omega\tau}d\tau \tag{2.92}$$

and

$$Y_{lp}(\omega, t_2) = \int_{-\infty}^{\infty} h_{lp}(t_2-\mu)\cos\omega_D\mu\cdot e^{-j\omega\mu}d\mu . \tag{2.93}$$

Equations (2.92) and (2.93) are essentially Fourier transform relations operating on the modulated and time-shifted low-pass impulse response $h_{lp}(t)$. Therefore, $X_{lp}(\omega, t_1)$ and $Y_{lp}(\omega, t_2)$ are related to the low-pass frequency response $H_{lp}(j\omega)$. The time-shifts cause a t-dependent multiplicative phase factor in the frequency domain while the modulation causes a shift in the center frequency of the low-pass filter from 0 to ω_D radians/second. Note also that $Y_{lp}(\omega, t)$ is the complex conjugate of $X_{lp}(\omega, t)$. Evaluating the Fourier transforms in Equations (2.92) and (2.93) and taking their product, we find

$$X_{lp}(\omega, t_1)Y_{lp}(\omega, t_2) = \frac{e^{j(\omega+\omega_D)\zeta}}{4}|H_{lp}(j\omega+j\omega_D)|^2 + \frac{e^{j(\omega-\omega_D)\zeta}}{4}|H_{lp}(j\omega-j\omega_D)|^2 \tag{2.94}$$

where $\zeta = t_1 - t_2$, and we have used that fact that $H_{lp}(j(\omega+\omega_D))H_{lp}(j(\omega-\omega_D)) = 0$ for ω_D sufficiently greater than the bandwidth of the low-pass filter to cancel out any cross-factors.

Substitution of Equation (2.94) into Equation (2.91) leads, after change of variables, to the following inverse Fourier transform:

$$R_{lp}(\zeta) = \frac{q}{4}\int_{-\infty}^{\infty} |H_{lp}(j\omega)|^2 \cdot \left[|H_{bp}(j\omega + j\omega_D)|^2 + |H_{bp}(j\omega - j\omega_D)|^2 \right] \cdot e^{j\omega\zeta} \cdot \frac{d\omega}{2\pi}. \tag{2.95}$$

The noise autocorrelation $R_{lp}(\zeta)$ after mixing and low-pass filtering is a function of $\zeta = t_1 - t_2$ only and not t_1 and t_2 independently. Therefore, $R_{lp}(\zeta)$ is WSS and has a power spectral density $S_{lp}(\omega)$ given by the Fourier transform of Equation (2.95).

Thus, the power spectral density $S_{lp}(\omega)$ of the demodulated noise is simply

$$S_{lp}(\omega) = \frac{q}{4}\left\{ |H_{lp}(j\omega)|^2 \cdot \left[|H_{bp}(j\omega + j\omega_D)|^2 + |H_{bp}(j\omega - j\omega_D)|^2 \right] \right\}. \tag{2.96}$$

Equation (2.96) shows that the band-pass filter transfer function is modulated to the frequency origin, where it is multiplied by the low-pass transfer function. Note that the sidebands of the modulated band-pass filter at $\pm\omega_D$ do not appear in the final spectrum because of the multiplication with $|H_{lp}(j\omega)|^2$.

The variance of the noise after mixing and low-pass filtering is computed from the integral of (2.96) over all frequencies:

$$\mathrm{var}\{n_{lp}(t)\} = \frac{q}{2} \cdot \int_{-\infty}^{\infty} |H_{lp}(j\omega)|^2 \cdot \frac{1}{2}\left[|H_{bp}(j\omega + j\omega_D)|^2 + |H_{bp}(j\omega - j\omega_D)|^2 \right] \cdot \frac{d\omega}{2\pi} \tag{2.97}$$

Equation (2.97) gives the appealing result that the noise power of the entire circuit looks like half the noise which would result from the band-pass and low-pass filter in succession, because the band-pass filter acts as if it were shifted to the frequency origin by the correlation with $\cos\omega_D t$. The factor of two noise reduction results from neglecting the sideband of the modulated band-pass filter. Note that the mixing also causes a factor of two reduction in the signal power for the same reason. In general, we will neglect this factor of two in both the noise and the signal so that the signal-to-noise calculation is independent of the technique used for demodulation. Therefore, the NEB of the entire circuit for demodulation by mixing will be defined as

$$NEB_{all} = \int_{0}^{\infty} |H_{lp}(j\omega)|^2 \cdot \frac{1}{2}\left[|H_{bp}(j\omega + j\omega_D)|^2 + |H_{bp}(j\omega - j\omega_D)|^2 \right] \cdot \frac{d\omega}{2\pi} \tag{2.98}$$

so that

$$\mathrm{var}\{n_{lp}(t)\} = 2q \cdot NEB_{all} \tag{2.99}$$

holds regardless of the method of demodulation used. Thus, the NEB of the entire filtering and demodulation circuit looks like the NEB of the product of the low-pass and band-pass filters, if the band-pass filter were translated in frequency down to the origin. Thus, for ideal rectangular filters, the system NEB is determined by the NEB of the filter with the narrower bandwidth.

2.6.5 Signal-to-Noise Ratio for Demodulation by Mixing

The signal-to-noise ratio or sensitivity of OCT is defined by Equation (2.77) and describes the minimum detectable reflection. To use Equation (2.77), we define the signal power P_{signal} to be the peak voltage squared at the output of the filtering and demodulation circuit. While other definitions could have been used (*e.g.* the typical definition of signal energy is the integral of the signal squared over time), this particular definition was easily compared with experimental results.

To determine the output signal power, we begin by propagating the interferometric signal through the detection and demodulation electronics. Let $\tilde{S}(\omega)$ be the spectrum of the electronic signal defined by the optical to electronic frequency mapping in Equation (2.37) and normalized to unit power. Let $\bar{P}_S$ and $\bar{P}_R$ be the time averaged optical powers returning from a perfectly reflective sample and the reference mirror respectively *after* recombination at the beamsplitter. The signal current waveform $s_i(t)$ after photodetection is given by the inverse Fourier transform of the signal spectrum:

$$s_i(t) = \frac{\eta e}{h\nu} \cdot \sqrt{\bar{P}_S \bar{P}_R} \int_{-\infty}^{\infty} \tilde{S}(\omega) e^{j\omega t} \frac{d\omega}{2\pi}. \tag{2.100}$$

where η is the quantum efficiency of the photodetector, e is the electronic charge, and $h\nu$ is the photon energy. The transimpedance amplifier converts the current $s_i(t)$ into a voltage $s_v(t)$ with a gain of R, producing

$$s_v(t) = \frac{\eta e}{h\nu} \cdot R\sqrt{\bar{P}_S \bar{P}_R} \int_{-\infty}^{\infty} \tilde{S}(\omega) e^{j\omega t} \frac{d\omega}{2\pi}. \tag{2.101}$$

Band-pass filtering the signal $s_v(t)$ with the transfer function $H_{bp}(j\omega)$ gives

$$s_{bp}(t) = \frac{\eta e}{h\nu} \cdot R\sqrt{\bar{P}_S \bar{P}_R} \int_{-\infty}^{\infty} \tilde{S}(\omega) H_{bp}(j\omega) e^{j\omega t} \frac{d\omega}{2\pi}. \tag{2.102}$$

We model the demodulation of the band-passed filtered signal $s_{bp}(t)$ as a frequency shift from the carrier frequency ω_D to the origin followed by low-pass filtering. The impact of factors of two from correlation with $\cos\omega_D t$ in the case of demodulation by mixing are accounted for in the description of the noise equivalent bandwidth as explained in Section 2.6.4. Thus, for the arbitrary demodulator, the output signal $s_{lp}(t)$ is

$$s_{lp}(t) = \frac{\eta e}{h\nu} \cdot R\sqrt{\bar{P}_S \bar{P}_R} \cdot \int_{-\infty}^{\infty} \tilde{S}_{out}(\omega) e^{j\omega t} \frac{d\omega}{2\pi} \tag{2.103}$$

where $\tilde{S}_{out}(\omega)$ is the band-passed and demodulated normalized spectrum at the output of the electronics:

$$\tilde{S}_{out}(\omega) = \left[\tilde{S}(\omega + \omega_D) H_{bp}(j\omega + j\omega_D) + \tilde{S}(\omega - \omega_D) H_{bp}(j\omega - j\omega_D)\right] H_{lp}(j\omega). \tag{2.104}$$

Assuming that the group delays of the band-pass and low-pass filters are zero, the signal peak occurs at $t = 0$ for an approximately Gaussian spectrum. (If the group-delays are non-zero then we need to evaluate at a different time). Therefore, the signal power as defined above is

$$P_{signal} = s_{lp}(0)^2 = \left(\frac{\eta e}{h\nu}\right)^2 \cdot R^2 \bar{P}_S \bar{P}_R \cdot \left[\int_{-\infty}^{\infty} \tilde{S}_{out}(\omega)\frac{d\omega}{2\pi}\right]^2 \tag{2.105}$$

which is proportional to the product of the reference and sample powers.

The noise variance is given by $2q \cdot NEB$ where the q is the amplitude of the white noise input to the band-pass filter defined in Equation (2.82) and NEB is the noise-equivalent bandwidth defined in Equation (2.98) for demodulation by mixing. In the shot noise limit, the white noise amplitude q is dominated by the shot noise from light reflected from the reference mirror. Section 2.7.1 will discuss the design considerations so that this limit may be achieved in practice. In the shot noise limit, the noise variance after filtering and demodulation is

$$\text{var}\{n_{lp}(t)\} = \frac{\eta e}{h\nu} \cdot 2e\bar{P}_R R^2 \cdot NEB \tag{2.106}$$

Therefore, the signal-to-noise ratio in the shot noise limit is obtained by substituting Equations (2.105) and (2.106) into Equation (2.77), resulting in

$$SNR = \frac{P_{signal}}{\text{var}\{n_{lp}(t)\}} = \frac{\eta}{h\nu} \cdot \frac{\bar{P}_S}{2 \cdot NEB} \cdot \left[\int_{-\infty}^{\infty} \tilde{S}_{out}(\omega)\frac{d\omega}{2\pi}\right]^2. \tag{2.107}$$

The integral in Equation (2.106) effectively describes the gain of the demodulation and filtering circuit. The gain will be less than one if either the band-pass filter bandwidth or the low-pass filter bandwidth is less than the signal bandwidth. If the filters are designed properly and normalized to unit gain, then the SNR in Equation (2.107) may be simplified to

$$SNR = \frac{\eta}{h\nu} \cdot \frac{\bar{P}_S}{2 \cdot NEB}. \tag{2.108}$$

In the shot noise limit, the dynamic range does not depend on the reference arm power $\bar{P}_R$. The SNR scales linearly with the power $\bar{P}_S$ returning from a perfectly reflective sample and is inversely proportional to the noise equivalent measure of the detection bandwidth. Section 2.7.2 will discuss how Equation (2.108) leads to design trade-offs between power, image acquisition time, and dynamic range.

2.6.6 Signal-to-Noise Ratio for Demodulation by Envelope Detection

Demodulation by envelope detection may be modeled as square-law detection followed by low-pass filtering as described in Section 2.4.4. Since the square-law detector is a non-linear device, the output noise power will in general depend on both the input signal and input noise power. Thus, a simple expression for the NEB which depends only on the input noise cannot be derived as in the case of demodulation by mixing.

Autocorrelation and Power Spectral Density for Square-Law Detection

Let $y(t) = [s(t) + n(t)]^2$ define the output of the square-law detector before low-pass filtering where $s(t)$ is the input signal and $n(t) = n_{bp}(t)$ is the input noise. The autocorrelation $R_y(\tau)$ of the output process can be written

$$R_y(\tau) = E\left\{\left[s(t) + n(t)\right]^2\left[s(t+\tau) + n(t+\tau)\right]^2\right\} = R_{s\times s}(\tau) + R_{s\times n}(\tau) + R_{n\times n}(\tau) \qquad (2.109)$$

where

$$R_{s\times s}(\tau) = R_{s^2}(\tau) = E\left\{s^2(t)s^2(t+\tau)\right\} \qquad (2.110)$$

is a term due to the interaction between the signal $s(t)$ with itself,

$$R_{s\times n}(\tau) = 4R_s(\tau)R_n(\tau) + 2R_s(0)R_n(0) \qquad (2.111)$$

is a term due to the interaction between the signal $s(t)$ with the noise $n(t)$, and

$$R_{n\times n}(\tau) = R_{n^2}(\tau) = E\left\{n^2(t)n^2(t+\tau)\right\} \qquad (2.112)$$

is due to the interaction between noise $n(t)$ with itself. Of these terms, only the $s\times s$ term relates to the desired signal output; the $s\times n$ and $n\times n$ terms both contribute to the output noise. The spectral density $S_y(\omega)$ of the square-law detector output is similarly defined:

$$S_y(\omega) = S_{s\times s}(\omega) + S_{s\times n}(\omega) + S_{n\times n}(\omega). \qquad (2.113)$$

We will evaluate each of the three terms in Equations (2.109) and (2.113). To evaluate the $n\times n$ terms, we assume that the noise $n_{bp}(t)$ after band-pass filtering has Gaussian statistics. This can be shown to be exactly the limiting case of Poisson distributed shot noise after transformation by a linear system with time constants much longer than the average distance between the Poisson arrivals [62]. This condition is satisfied for OCT since the photon arrival rate is much greater than the maximum cutoff frequency of the band-pass filter. Thus, $n_{bp}(t) = n(t)$ may be adequately approximated as zero-mean Gaussian process with an autocorrelation given by Equation (2.84). Under this assumption, the following "moment factoring" relation between four jointly distributed zero-mean Gaussian random variables a, b, c, and d:

$$E\{abcd\} = E\{ab\}E\{cd\} + E\{ac\}E\{bd\} + E\{ad\}E\{bc\}. \qquad (2.114)$$

Since $n(t)$ and $n(t+\tau)$ are also jointly Gaussian by the assumption of Gaussian statistics, direct comparison with Equation (2.114) yields

$$R_{n\times n}(\tau) = [R_n(0)]^2 + 2[R_n(\tau)]^2 \qquad (2.115)$$

where $R_n(\tau)$ is the autocorrelation of the input noise process. The power spectral density $S_{n\times n}(\omega)$ corresponding to the autocorrelation $R_{n\times n}(\tau)$ is the Fourier transform of Equation (2.115):

$$S_{n\times n}(\omega) = 2\pi\left[R_n(0)\right]^2 \cdot \delta(\omega) + \frac{1}{\pi}\left[S_n(\omega) \otimes S_n(\omega)\right] \quad . \tag{2.116}$$

The evaluation of the $s\times s$ and $s\times n$ terms in Equation (2.109) depends on the specific form of the signal $s(t)$. To proceed, we assume that the input signal is a randomly amplitude modulated sine wave:

$$s(t) = p(t)\cos(\omega_D t + \theta) \tag{2.117}$$

where $p(t)$ is the modulating envelope (or axial reflectivity profile as a function of depth), ω_D is the electronic carrier frequency determined by the Doppler shift of the scanning reference mirror, and θ is a uniformly distributed random phase. In this case, the autocorrelation of the input signal $R_s(\tau)$ is simply

$$R_s(\tau) = \frac{1}{2}R_p(\tau)\cos(\omega_D\tau) \tag{2.118}$$

where we have introduced $R_p(\tau)$ as the autocorrelation of the modulating envelope.

With the definitions in Equations (2.117) and (2.118), the $s\times s$ terms can be calculated from Equation (2.110) and are given by

$$R_{s\times s}(\tau) = \frac{1}{8}R_{p^2}(\tau)\left[1 + 2\cos(2\omega_D\tau)\right] \tag{2.119}$$

and

$$S_{s\times s}(\omega) = \frac{1}{4}S_{p^2}(\omega) + \frac{1}{16}\left[S_{p^2}(\omega - 2\omega_D) + S_{p^2}(\omega + 2\omega_D)\right] \tag{2.120}$$

where $R_{p^2}(\tau)$ and $S_{p^2}(\omega)$ are the autocorrelation and power spectral density respectively of the squared modulating process $p^2(t)$.

In a similar fashion, the $s\times n$ terms describing the nonlinear interaction between the signal and the noise are

$$R_{s\times n}(\tau) = 2R_p(\tau)R_n(\tau)\cos(\omega_D\tau) + R_p(0)R_n(0) \tag{2.121}$$

and

$$S_{s\times n}(\omega) = \frac{1}{2\pi}\left\{\left[S_n(\omega - \omega_0) + S_n(\omega + \omega_0)\right] \otimes S_p(\omega)\right\} + 2\pi R_p(\tau)R_n(\tau) \cdot \delta(\omega) \,. \tag{2.122}$$

Low-Pass Filtering After Square-Law Detection

An estimate of the squared envelope $p^2(t)$ may be obtained from the output $y(t)$ of the square-law device by low-pass filtering. Equation (2.120) shows that the spectrum $S_{p^2}(\omega)$ of the signal envelope resides in the $s \times s$ signal term. A low-pass filter with a bandwidth equal to twice the signal bandwidth B of $p(t)$ will retrieve the following components of the $s \times s$, $s \times n$, and $n \times n$ spectral densities:

$$S_{s \times s}(\omega) \rightarrow \frac{1}{4} S_{p^2}(\omega), \tag{2.123}$$

$$S_{s \times n}(\omega) \rightarrow \frac{1}{2\pi} \left\{ \left[S_n(\omega - \omega_D) + S_n(\omega + \omega_D) \right] \otimes S_p(\omega) \right\}, \tag{2.124}$$

and

$$S_{n \times n}(\omega) \rightarrow \frac{1}{\pi} \left[S_n(\omega) \otimes S_n(\omega) \right]. \tag{2.125}$$

DC terms (δ functions) have been neglected in Equations (2.123) through (2.125) because they just produce a constant offset at the output.

Signal-to-Noise Ratio for Square-Law Detection

For an optimal rectangular low-pass filter with bandwidth $2B$, the signal power at the output of the low-pass filter is, from Equation (2.123),

$$P_{signal} = \int_{-\infty}^{\infty} \frac{1}{4} S_{p^2}(\omega) \frac{d\omega}{2\pi} = \frac{1}{4} R_{p^2}(0). \tag{2.126}$$

If the band-pass filter bandwidth is also optimally chosen to equal B, then Equations (2.123) through (2.125) also represent spectra with bandwidths of $2B$. In this case, the noise power at the output of the low-pass filter may be similarly calculated by integrating the sum of Equations (2.124) and (2.125), producing

$$P_{noise} = [R_n(0)]^2 + R_n(0) R_p(0). \tag{2.127}$$

The SNR at the output of the low-pass filter is then given by the ratio of Equations (2.126) and (2.127):

$$SNR_{out} = \frac{1}{4} \cdot \frac{R_{p^2}(0)}{[R_n(0)]^2 + R_n(0) R_p(0)} \tag{2.128}$$

It is more instructive to consider the output SNR as a function of the SNR at the input to the square-law detector (but after band-pass filtering). From Equation (2.118), the input SNR is given by

$$SNR_{in} = \frac{R_s(0)}{R_n(0)} = \frac{1}{2} \cdot \frac{R_p(0)}{R_n(0)}. \tag{2.129}$$

Therefore, the output SNR in Equation (2.128) can be rewritten as

$$SNR_{out} = \kappa \cdot \frac{(SNR_{in})^2}{1 + 2 \cdot SNR_{in}} \tag{2.130}$$

where

$$\kappa = \frac{R_{p^2}(0)}{[R_p(0)]^2} = \frac{E\{p^4(t)\}}{E^2\{p^2(t)\}}. \tag{2.131}$$

Note that κ is a function only of the form of the probability distribution of the signal envelope. Equation (2.130) shows that for an input SNR which is substantially greater than one, the output SNR is linearly dependent on the input, and is given by

$$SNR_{out} \approx \frac{\kappa}{2} \cdot SNR_{in}. \tag{2.132}$$

Thus, for large signal-to-noise ratios, the output SNR is linearly dependent on the input SNR, and therefore demodulation by square-law detection is similar to demodulation by mixing. However, the carrier is not required to have a constant phase in square-law detection. This property is advantageous when the velocity of reference mirror is not perfectly linear. In this case, square-law detection is relatively insensitive to small variations in the phase of the Doppler shift or carrier frequency which can cause problems for coherent demodulation.

2.7 Design Issues

2.7.1 Design for Shot Noise Limited Sensitivity

Equation (2.82) shows that the noise after photodetection and amplification may be represented as a zero-mean, white, WSS stochastic process which contains contributions from shot noise, thermal noise, and excess intensity noise. Quantum limited operation is attained only when the shot noise dominates the other sources of noise. In the shot noise limit, described by Equation (2.108), the detection sensitivity is approximately two photons per resolution element.

It is possible to design the system for shot noise limited sensitivity by using a spectrum analyzer to measure the noise $v_n(t)$ at the output of the transimpedance amplifier. Since the spectrum analyzer combines positive and negative frequencies, it effectively measures (from Equation (2.82)) the positive frequency power spectral density

$$S^+_{v_n}(\omega) = 2e\langle v\rangle R + 2e\gamma\langle v\rangle^2 + 4kTR = 2q \tag{2.133}$$

which contains, from left to right, the white noise contributions from shot noise, excess intensity noise, and thermal noise.

The transimpedance gain R and the reference arm power $\langle v \rangle$ are chosen so that the shot noise term is greater than the excess intensity noise and thermal noise. To ensure that shot noise eclipses the thermal noise, we require $2e\langle v \rangle R > 4kTR$, or

$$\langle v \rangle > \frac{2kT}{e} \approx 0.05 \text{ V} \quad \text{for} \quad T = 300°\text{K}. \tag{2.134}$$

This limit defines the absolute minimum reference arm power. Thus, in the absence of excess intensity noise or amplified spontaneous emission noise, whenever the DC output of the reference arm power is greater than 50 mV, the system will be shot noise limited. The gain R must be chosen so that the shot noise dominates the excess intensity noise, or

$$R > \gamma(v). \tag{2.135}$$

The upper limit on R is determined by the transimpedance amplifier stability and roll-off frequency in Equation (2.47). Ideally the gain R should be as large as possible and the reference arm power $\langle v \rangle$ should be as small as possible to minimize the excess intensity and amplified spontaneous emission noise (Section 2.5.3).

In practice, to construct the detector circuit, R is chosen before $\langle v \rangle$. Since the excess intensity noise parameter γ is usually unknown, given R, the optimal value of $\langle v \rangle$ must be determined experimentally. The procedure is to successively attenuate the reference arm power $\langle v \rangle$ and examine the noise spectral density on the spectrum analyzer until the white component equals the predicted shot noise value $2e\langle v \rangle R$. Attenuation of the reference arm intensity reduces the excess noise as the square $\langle v \rangle^2$ of the intensity, but only affects the shot noise component linearly with $\langle v \rangle$. If $\langle v \rangle$ needs to be decreased below the thermal noise limit of 0.05 V, then the amplifier gain R should be increased, and the procedure repeated. If increasing R places the transimpedance amplifier roll-off frequency below the signal bandwidth, then other methods of reducing the excess intensity noise need to be considered, such as dual-balanced detection [59, 63].

2.7.2 Trade-off Between Resolution, Power, Speed, and Sensitivity

The four fundamental design issues for OCT are the optical power, the acquisition speed, signal-to-noise ratio, and the axial resolution. Equation (2.108) establishes the linear relation between the signal-to-noise, optical power incident on the sample, and noise equivalent bandwidth of the electronics:

$$\frac{SNR \cdot NEB}{\bar{P}_S} = \text{constant}. \tag{2.136}$$

The NEB, however, is essentially equal to the electronic bandwidth $\Delta\tilde{f}$ used for detection of the interferometric signal. The electrical bandwidth is linearly related to the reference mirror scanning velocity v_s and the wavelength bandwidth $\Delta\lambda$ of the light source by Equation (2.44). Therefore, we have

$$NEB \approx \Delta\tilde{f} \propto v_s \cdot \Delta\lambda. \tag{2.137}$$

The axial resolution Δl is inversely proportional to the spectral bandwidth $\Delta\lambda$ of the light source, as seen in Equations (2.21) and (2.22), so that we also may write

$$NEB \approx \Delta\tilde{f} \propto \frac{v_s}{\Delta l}. \tag{2.138}$$

By combining Equations (2.136) and (2.138), we obtain the fundamental relation between the four design parameters:

$$\frac{SNR \cdot v_s}{\bar{P}_S \cdot \Delta l} = \text{constant}. \tag{2.139}$$

Equation (2.139), which is linear in all its parameters, expresses the basic idea that "you can't get something for nothing," and allows the major design issues to be easily considered in relation to one another.

The limitations expressed by Equation (2.139) may be intuitively understood with an alternative interpretation of Equation (2.108). The minimum detectable reflectivity R_{min} is equal to the reciprocal of the SNR. Equation (2.108) can then be rewritten as

$$\frac{2}{\eta} = \frac{P_s R_{min}/NEB}{h\nu}. \tag{2.140}$$

In Equation (2.140), the quantity $P_s R_{min}$ is equal to the power reflected from a minimally detectable point within the sample. The quantity $1/NEB$ is the inverse detection bandwidth, or equivalently, the time spent observing each resolution element within the sample. From Equation (2.138) it is evident that this observation time is proportional to the longitudinal resolution Δl divided by the scanning velocity v_s. The right-hand side numerator $P_s R_{min}/NEB$ is therefore equal to the optical energy which returns from a minimally detectable resolution element during the observation period. By dividing this quantity by the photon energy $h\nu$, we obtain the number of photons returning from the resolution element. Equation (2.140) shows that the number of returning photons must equal to or larger than $2/\eta$ in order to be detected. This requirement ensures that a minimum of one photon is detected by the photodetector, since, on average, only half of the reflected photons return to the detector through the beamsplitter and the probability that each returning photon is converted into a unit of electric charge is η.

The preceeding discussion shows that the shot noise limit is directly related to the quantization of light. In summary, at least one (but actually $2/\eta$) photons need to be received for each resolution element in the OCT image in order for that resolution element to have a detectable reflectivity. Increased sensitivity may be obtained only be either increasing the number of incident photons, increasing the size of the resolution element, or increasing the time spent observing each element.

Chapter 3

OCT IMAGING OPTICS AND THE EYE

3.1 Introduction

This Chapter reviews the eye as an optical system and introduces the imaging optics used by OCT for retinal imaging. An overview of the Gullstrand schematic eye is provided which is used for subsequent analysis of the imaging system. As currently implemented, OCT is interfaced to a standard slit-lamp biomicroscope. Therefore, the imaging concept is similar to that of indirect ophthalmoscopy. Expressions for magnification, field-of-view, and transverse resolution are derived. The effects of axial positioning error and ametropia are also discussed.

3.2 The Eye as an Optical System

The Gullstrand schematic eye is the natural starting point for any discussion of the eye as a optical system [64, 65]. The simplified and reduced schematic eyes are presented below with expressions for the entrance and exit pupils. Changes during accommodation, myopia, hyperopia, and aphakia are discussed as they are clinically relevant to imaging patients.

3.2.1 Complete Gullstrand Schematic Eye

The two major refractive elements of the eye are the cornea and crystalline lens (Figure 3-1). The cornea and lens are separated by the aqueous humor ($n_{aq} = 1.336$) and the vitreous body ($n_{vi} = 1.336$) separates the lens from the retina. An adjustable aperture is formed

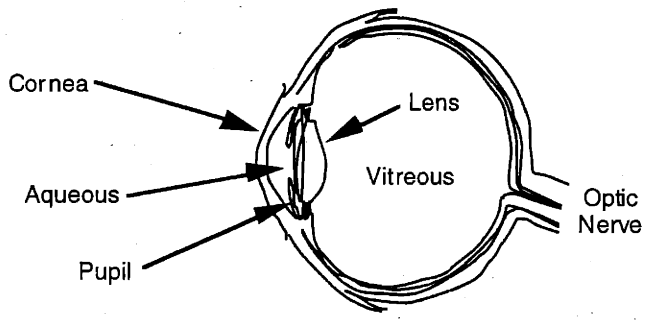

FIGURE 3-1. Optical elements of the eye.

by the pupil. The refractive elements are positioned along the optical axis of the eye which is situated approximately 4 to 5 degrees nasal to and 1 degree superior to the fovea.

The anterior surface of the cornea has a radius of curvature $r_{co,a} = 7.7$ mm. The posterior surface is slightly steeper ($r_{co,p} = 6.8$ mm). The cornea has a central thickness of $t_{co} = 0.5$ mm and its index of refraction is $n_{co} = 1.376$. The power of the anterior surface is thus

$$F_{co,a} = \frac{n_{co} - n_{air}}{r_{co,a}} = 48.83 \text{ D}. \tag{3.1}$$

The power of the posterior corneal surface is similarly

$$F_{co,p} = \frac{n_{aq} - n_{co}}{r_{co,p}} = -5.88 \text{ D}. \tag{3.2}$$

The power of the equivalent thick lens created by both the anterior and posterior corneal surfaces is

$$F_{co} = F_{co,a} + F_{co,p} - \frac{t_{co}}{n_{co}} F_{co,a} F_{co,p} = 43.05 \text{ D}. \tag{3.3}$$

The crystalline lens is optically more complex because its refractive index increases towards the center and changes in the lens are responsible for accommodating the eye. The anterior surface of the lens is positioned approximately 3.6 mm behind the posterior corneal surface. In the original (No. 1) schematic eye, the cyrstalline lens is represented by a central biconvex core surrounded by a larger biconvex lens. The refractive index of the core lens is 1.406 and its radii of curvature are 7.911 mm and -5.76 mm. The larger surrounding lens has a refractive index of 1.386 and radii of curvature of 10.00 mm and -6.0 mm. The equivalent power of the combination of these two biconvex elements is 19.11 D.

3.2.2 Simplified Gullstrand Eye

For most practical purposes, the corneal thickness is negligible and it is not necessary to consider inhomogeneities within the crystalline lens. The simplified or No. 2 Gullstrand eye consists of a single curved refractive surface representing the effects of both corneal surfaces and a homogenous lens consisting of two biconvex refracting surfaces (Figure 3-2). Three materials are considered present: the aqueous, lens and vitreous. Table 3-1 details the radii of curvature and equivalent powers for the components of this eye. The equivalent power of the eye is 59.60 D when unaccommodated. Most of the refractive power is due to the cornea, which is more than twice as powerful as the unaccommodated lens.

The two principle planes lie within the anterior chamber and are only separated by 0.28 mm. Calculations using this (as well as any other) model are reduced to the familiar thin lens formula if distances are measured from the two principle planes and are divided by the local refractive index. In other words, the retinal image distance for an object placed in front of the eye is given by

$$L_i = L_o + F_{eye} \tag{3.4}$$

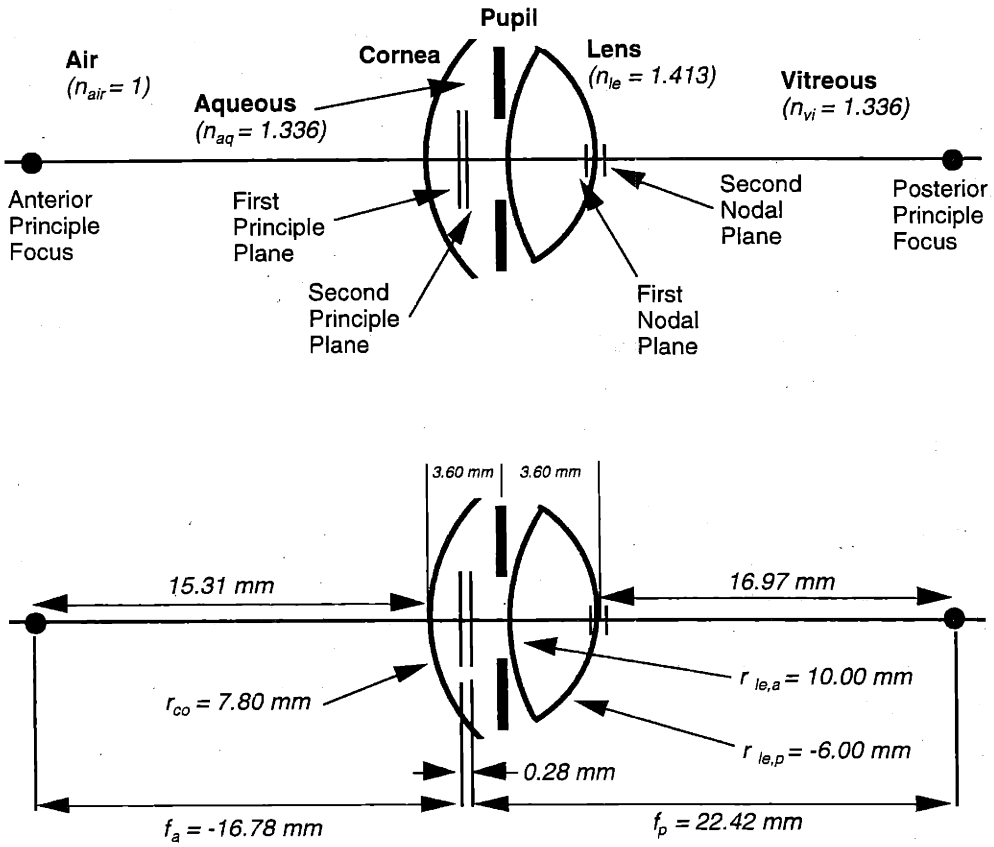

FIGURE 3-2. Simplified Gullstrand schematic eye (to scale) [64].

where F_{eye} is the equivalent power of the (accommodated) entire eye, and the reduced vergences (inverse distances) are defined as

$$L_o = \frac{n_{air}}{l_o} \quad \text{and} \quad L_i = \frac{n_{vi}}{l_i}. \tag{3.5}$$

The object and image distances l_o and l_i are measured from the first and second principle planes respectively and are positive in the direction of light propagation for real images. The transverse magnification m is given by

$$m = \frac{L_o}{L_i} = \frac{l_i}{l_o} \cdot \frac{n_{air}}{n_{vi}}. \tag{3.6}$$

		Unaccommodated	Accommodated 8.62 D
Radius of Curvature	Cornea	r_{co} = 7.80 mm	r_{co} = 7.80 mm
	Anterior Lens	$r_{le,a}$ = 10.00 mm	$r_{le,a}$ = 5.00 mm
	Posterior Lens	$r_{le,p}$ = −6.00 mm	$r_{le,p}$ = −5.00 mm
Power	Cornea	F_{co} = 43.08 D	F_{co} = 43.08 D
	Anterior Lens	$F_{le,a}$ = 7.70 D	$F_{le,a}$ = 15.40 D
	Posterior Lens	$F_{le,p}$ = 12.83 D	$F_{le,p}$ = 15.40 D
Equivalent Power	Lens	F_{le} = 20.28 D	F_{le} = 30.13 D
	Eye	F_{eye} = 59.60 D	F_{eye} = 68.22 D
Focal Lengths from Principle Planes	Anterior	f_a = −16.78 mm	f_a = −14.66 mm
	Posterior	f_p = 22.42 mm	f_p = 19.58 mm

TABLE 3-1. Components of the simplified Gullstrand schematic eye [64].

3.2.3 Entrance and Exit Pupils

Light entering the eye is apertured by the entrance pupil, defined as the image of the real pupil created by refraction from the cornea (Figure 3-3). In the simplified schematic eye,

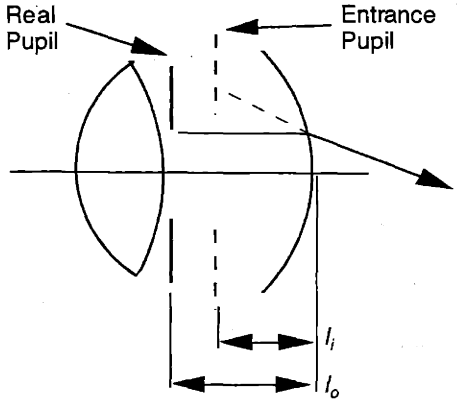

FIGURE 3-3. Entrance pupil in the simplified schematic eye.

the cornea is represented by a single spherical surface with refractive power $F_{co} = 43.08$ D. The position of the entrance pupil relative to the cornea is given by

$$l_i = \frac{n_{air}}{L_i} = \frac{n_{air}}{L_o + F_{co}} = \frac{n_{air}}{n_{aq}/l_o + F_{co}} = -3.05 \text{ mm} \tag{3.7}$$

for a real pupil placed at $l_o = -3.60$ mm relative to the cornea. The apparent position of the entrance pupil is 0.55 mm in front of the real pupil. The magnification of the entrance pupil relative to the real pupil is $m = L_o/L_i = 1.15$.

The exit pupil is defined as the image of the real pupil formed after propagation through the lens. If the real pupil is assumed to coincide with the anterior lens surface, then refraction only occurs at the posterior lens surface (Figure 3-4). If the lens thickness is 3.60

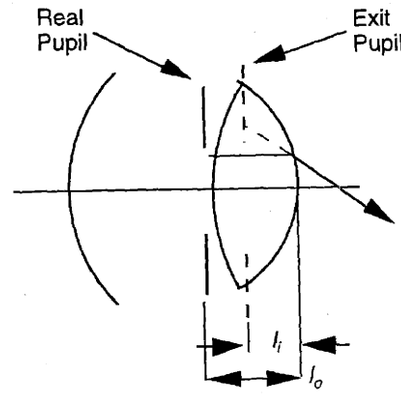

FIGURE 3-4. Exit pupil in the simplified schematic eye.

mm, then in analogy to Equation (3.7), the position of the exit pupil relative to the posterior lens surface is

$$l_i = \frac{n_{vi}}{n_{le}/l_o + F_{le,p}} = -3.52 \text{ mm} \tag{3.8}$$

with a magnification $m = 1.03$. Thus, the exit pupil is located 0.08 mm behind the real pupil.

3.2.4 Reduced Gullstrand Eye

The cornea and lens may combined into a single refractive element with power F_{eye} to further simplify calculations (Figure 3-5). This simplification is possible because the first and second principle planes are separated by a relatively small distance. This is the standard 60 D eye commonly seen in the literature in which air is separated from the vitreous by a single spherical refractive surface of radius $r = 5.55$ mm. The refracting surface is considered to lie 1.67 mm behind the actual corneal surface, which is approximately the location of the first and second principle planes in the simplified eye.

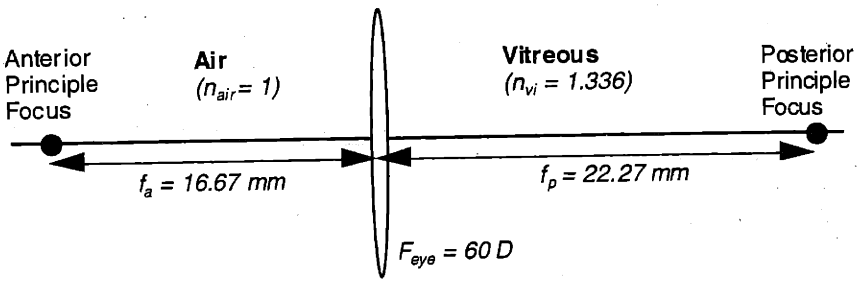

FIGURE 3-5. Reduced Gullstrand eye.

3.2.5 Accommodation

Accommodation to focus on a near object occurs mainly by an increase in curvature in the anterior lens surface (which moves slightly forward) and a smaller increase in curvature in the posterior lens surface (Table 3-1). The thickness of the lens increases by approximately 0.4 mm for the maximum 8.62 D shift considered in Table 3-1. The equivalent power of an ideal eye can vary from 59.60 D to 68.22 D.

3.2.6 Ametropia

The unaccommodated *emmetropic* eye focuses parallel rays of light onto a single point on the retina. *Ametropia* occurs when the refractive power of the eye is not matched to the axial eye length. Thus, the unaccommodated ametropic eye does not focus parallel rays entering the eye onto the retina. If the image of an object placed at infinity falls anterior to the retina, the eye is *myopic*; if the image falls posterior to the retina the eye is *hyperopic*.

Ocular ametropia is characterized by the *principle point refraction A* which is defined as the vergence (reciprocal distance) of the *far point* in the unaccomodated eye. The far point is defined as the location at which an unaccomodated eye will focus an object so its image falls directly on the retina. Thus, the far point and the retina are conjugate image planes. Figure 3-6 depicts the far point and the sign of the principle point refraction for emmetropia, myopia, and hyperopia. Let a be defined as the distance from far point to the principle plane of the eye measured in the direction of light propagation. By definition, the principle point refraction is given by $A = 1/a$ and is expressed in diopters.

In emmetropia, the unaccommodated eye focuses parallel rays of light; therefore the far point is located at infinity and the principle point refraction is zero. In myopia, parallel rays are focused anterior to the retina--only diverging rays are correctly focused at the retina. Therefore, the far point is located in front of the eye and the principle point refraction is negative. In hyperopia, parallel rays are focused behind the retina--converging rays are required for imaging at the retina. Therefore, the far point is virtual and located behind the eye, and the principle point refraction is positive.

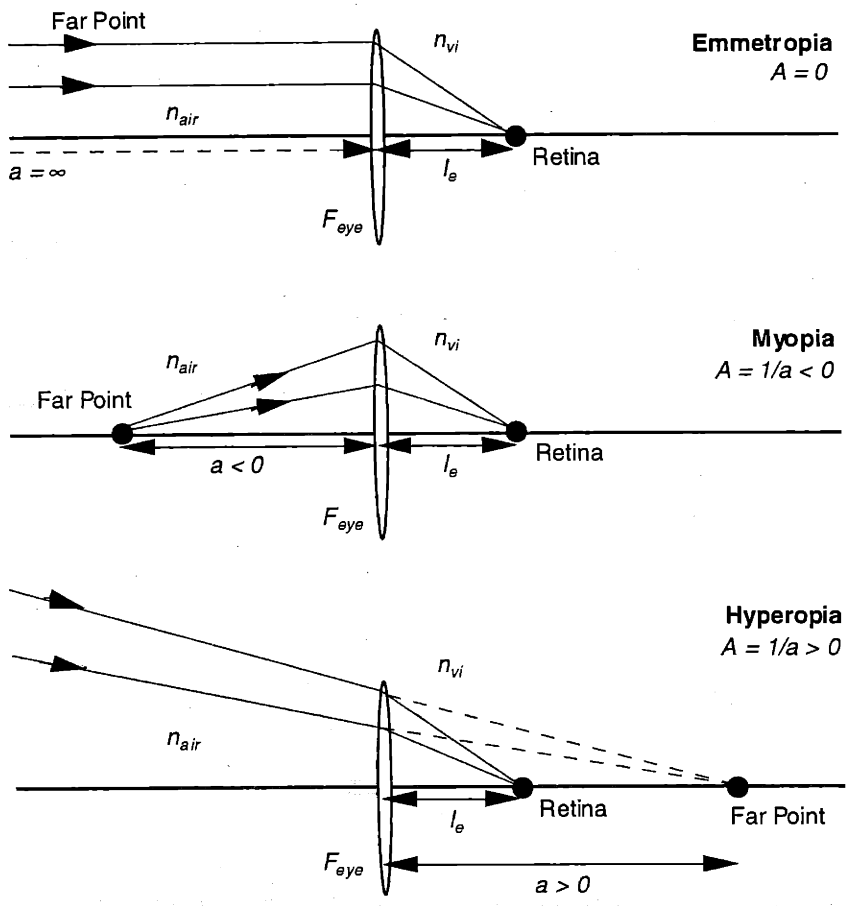

FIGURE 3-6. Principle point refraction.

If l_e is the distance from the principle plane of the eye to the retina (*i.e.* the axial eye length minus the separation between the cornea and the principle plane) and F_{eye} is the optical power of the cornea and lens, then the principle point refraction can be computed from the thin lens formula given in Equation (3.4):

$$A + F_{eye} = \frac{n_{vi}}{l_e}. \tag{3.9}$$

The principle point refraction is thus the difference between the reduced retinal vergence and the refractive power of the eye.

Correction of ametropia may be accomplished by placing a spectacle lens of refractive power A in front of the eye so that the posterior focal point of the lens coincides with the far point Alternatively, a contact lens may be used to increase the corneal refractive power by A diopters.

The aphakic eye is an important example since many patients require OCT examination after cataract extraction. After removal of the lens, the simplified Gullstrand eye is reduced to only a spherical refracting surface with power $F_{co} = 43.08$ D. The first and sec-

ond principle planes coincide at the corneal surface; therefore the axial eye length is l_e = 24.16 mm. The principle point refraction is thus $A = n_{vi}/l_e - F_{co}$ = 12.22 D showing that the eye is hyperopic.

3.2.7 Ocular Dispersion

A mismatch in group velocity dispersion between the reference and sample paths of the interferometer has the potential to degrade the axial point spread function, especially if very short coherence lengths are involved (see Section 2.3.4). Therefore, propagation through the eye itself can lead to reduced axial resolution. Estimating the group velocity dispersion in the human eye is difficult because the ocular media contains many tissues and most experimental measurements of refractive index have used only a few visible wavelengths in vertebrate eyes.

To obtain an order of magnitude approximation of the dispersion in the eye, we use the following empirically derived formula proposed by Cornu [66] for the refractive index $n(\lambda)$ in a variety of transparent media:

$$n(\lambda) = N + \frac{K}{(\lambda - D)}. \tag{3.10}$$

where N, K and D are constants that must be determined from a series of experimental measurements. The general expressions for the group delay $\beta'(\omega)$ and group velocity dispersion $\beta''(\omega)$ in terms of the index of refraction $n(\lambda)$ as a function of wavelength may be derived by successive differentiation of the propagation constant $\beta(\omega)$:

$$\beta(\omega) = \frac{2\pi}{\lambda} n \tag{3.11}$$

$$\beta'(\omega) = \frac{n}{c} - \frac{\lambda}{c} \cdot \frac{\partial n}{\partial \lambda} \tag{3.12}$$

$$\beta''(\omega) = \frac{\lambda^3}{2\pi c^2} \cdot \frac{\partial^2 n}{\partial \lambda^2}. \tag{3.13}$$

To compute the GVD we differentiate Equation (3.10) twice and plug into Equation (3.13), producing

$$\beta''(\omega) = \frac{\lambda^3}{2\pi c^2} \cdot \frac{2K}{(\lambda - D)^3} = \frac{K}{\pi c^2} \cdot \left(\frac{\lambda}{\lambda - D}\right)^3. \tag{3.14}$$

The parameters of the Cornu equation (3.10) were then fit (using MATLAB "curvefitnl") to selected data of Sivak and Mandelman [67], who experimentally measured the refractive indices of various ocular media in eight vertebrate species at four wavelengths (Table 3-2). The only human tissue measured was the lens, so cow ocular media was selected for the vitreous, aqueous, and cornea. Since the vitreous was most likely to be the largest contributor to dispersion (due to its length), data from the pig and chicken were also included for this tissue to estimate the interspecies variability. The dispersion parameter $\beta''(\omega)$ was then calculated for each of these tissues at the OCT operating wavelength of 840 nm and for comparison at 590 nm (where the refractive index data was known to be valid) (Table 3-3). Table 3-3 also shows the total roundtrip dispersion $\beta''(\omega) \cdot 2L$ of these tissues by using the average human dimen-

Ocular Media	Species	Measured Refractive Index				Fit to Cornu Equation		
		440 nm	486 nm	590 nm	650 nm	N	K (nm)	D (nm)
Vitreous	Cow	1.3391	1.3372	1.3337	1.3320	1.3704	23.067	-288.41
	Pig	1.3399	1.3375	1.3339	1.3322	1.3183	8.3015	55.416
	Chicken	1.3389	1.3370	1.3335	1.3321	1.3164	10.755	-38.571
Lens	Human	1.4155	1.4100	1.4015	1.3983	1.3734	12.717	137.79
Aqueous	Cow	1.3399	1.3377	1.3339	1.3323	1.3160	10.683	-7.7348
Cornea	Cow	1.3794	1.3748	1.3699	1.3680	1.3598	3.0096	285.93

TABLE 3-2. Refractive index of vertebrate ocular media.

Ocular Media	Length in Human (mm)	Species	Dispersion (fs^2/cm)		Roundtrip Dispersion using Human Length (fs^2)	
			590 nm	840 nm	590 nm	840 nm
Vitreous	17	Cow	247	336	841	1144
		Pig	395	360	1342	1225
		Chicken	315	332	1070	1130
Lens	3.6	Human	999	770	719	554
Aqueous	3.6	Cow	363	368	262	265
Cornea	0.5	Cow	778	371	78	37

TABLE 3-3. Dispersion in vertebrate ocular media.

sions of the Gullstrand eye. Observe that the vitreous has the largest total dispersion, and the lens has the greatest dispersion per unit length. Note that the variation between species for vitreal dispersion is small.

An estimate of the dispersion in the human eye at 840 nm can by calculated by summing these values (using the average value for the vitreous), leading to the result:

$$\beta''(\omega) \cdot 2L \approx 2000 \text{ fs}^2 \quad \text{at} \quad \lambda = 840 \text{ nm}. \tag{3.15}$$

Note that this parameter neglects propagation through the retina and choroid. The critical dispersion parameter for the eye, defined by Equation (2.29), is $\tau_{critical} = 45$ fs. Therefore, dispersion becomes an issue when $\sigma_\tau = 45$ fs, or when the FWHM width of the axial point spread function is $\Delta l_{FWHM} < 16$ μm. Using these parameters in Equation (2.30), we see that a FWHM axial resolution of 16 μm will be dispersively broadened to 23 μm, a resolution of 10

μm will be broadened to 28 μm, and a resolution of 5 μm will be broadened to 52 μm. Thus, dispersive broadening within the eye will be of particular concern for future high-resolution OCT instruments and dispersive compensation will most likely be required.

3.2.8 Ocular Aberrations

The human eye is not a diffraction limited system. For large pupil diameters, ocular aberrations limit the minimum focused spot size on the retina, even for monochromatic illumination. Coma and other third-order aberrations, rather than spherical or fourth order aberrations, appear to place the dominant limitation on the resolving power of the eye. Ocular aberrations are of interest for OCT and related techniques such as scanning laser ophthalmoscopy [12, 13] because they provide the ultimate limit on the achievable transverse resolution for imaging.

Several studies have attempted to estimate the modulation transfer function (MTF) or complete optical transfer function (OTF) of the eye. In the double-pass method, a point or a line source is imaged onto the retina and light reflected out of the eye is imaged a second time and used to compute the MTF for a single pass through the ocular optics [68-70]. In the interferometric method, the MTF is estimated from the ratio of subject's contrast sensitivity to interference fringes which are not blurred by the ocular optics [70]. In the aberroscope method, a square grid is projected onto a subject's retina and either the subject sketches the appearance of the grid which is distorted by ocular aberrations [71], or the grid itself is photographed on the retina for a more objective assessment [72].

Both the double-pass and the aberroscope methods can provide an estimate of the wave aberration function of the eye (*i.e.* the complex pupil function), which can be used to estimate the diffraction limited pupil size. The critical pupil diameter may be defined using the Marechal criterion as the maximum diameter at which the root-mean-square deviation of the wave front is less than $1/14$ of the optical wavelength [71]. The studies which report a critical pupil diameter show considerable variation between individual subjects. The largest series, performed in 55 eyes using a subjective aberroscope method, reveals an average diffraction-limited diameter of approximately 3 mm with an individual variation ranging between 2 and 4.5 mm [71]. Other studies report that the average optimal pupil size varies between 2 and 3.5 mm [73, 74]. Thus, the minimum spot diameter on the retina may be achieved with approximately a 3 mm diameter beam incident on the eye.

3.3 OCT Imaging Optics

The fiber-optic interferometer is interfaced to a conventional slit-lamp biomicroscope so that the examiner can view the OCT probe beam as it scans across the fundus during image acquisition (Figure 3-7). The principle of indirect ophthalmoscopy is used whereby a condensing lens placed in front of the eye brings an image of the retina out to the image plane of the slit-lamp. Unlike conventional indirect ophthalmoscopy, however, the condensing lens is mounted to the slit-lamp. Focusing is achieved by translating the condensing lens along its axis which compensates for difference in refractive power. A beamsplitter is used to integrate the ocular viewing path with the OCT beam path. A focusing lens placed in the OCT beam path ensures that the probe beam is brought to a focus at the image plane and at the retina. A pair of orthogonal scanning mirrors provides transverse beam positioning on the retina.

The reduced schematic eye is used for analysis of this optical system. Figure 3-8 shows both the reduced eye and the other optical elements in the OCT beam path including the fiber collimating lens, arranged linearly. The beam path is comprised of three telescopes. The first telescope, composed of the collimating lens and the focusing lens, images the fiber-

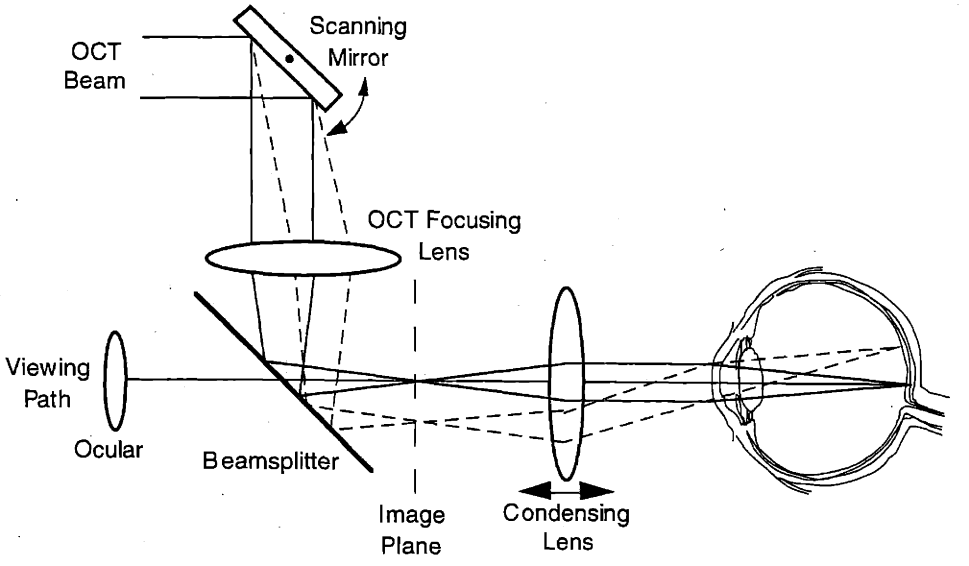

FIGURE 3-7. OCT imaging geometry.

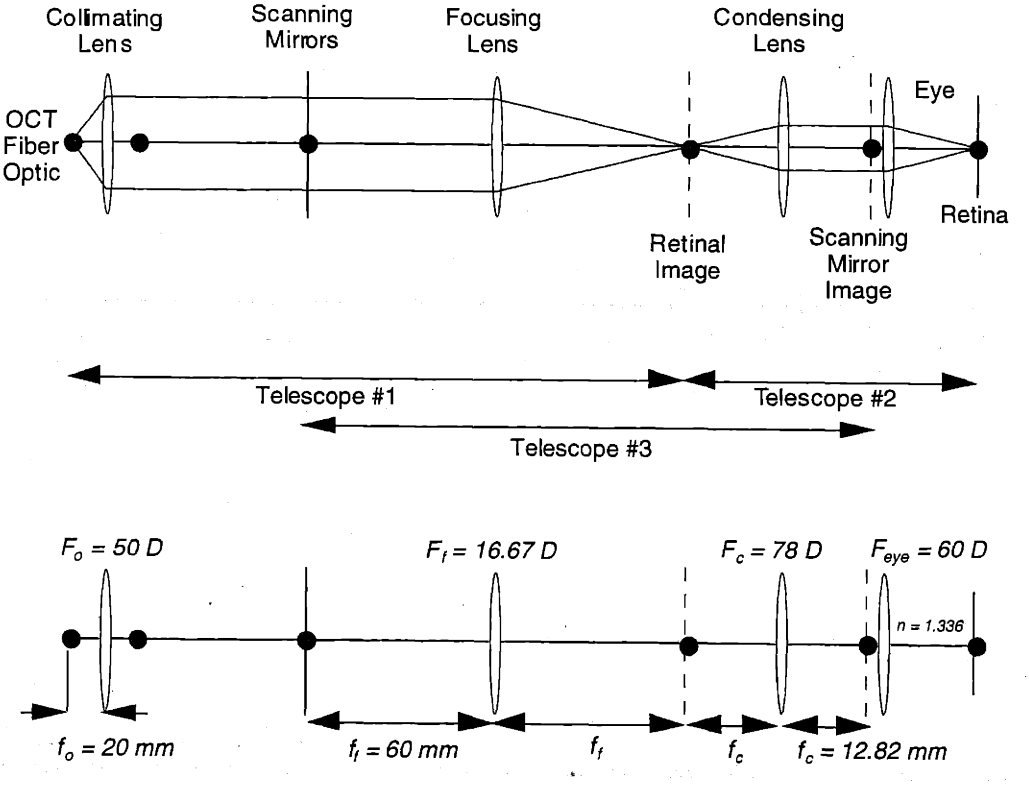

FIGURE 3-8. OCT beam path.

optic face onto the retinal image plane (which is also the slit-lamp image plane). The second telescope consists of the condensing lens and the eye. This telescope maps an image of the retina onto the retinal image plane. The third telescope is composed of the focusing lens and condensing lens, and images the scanning mirrors onto the pupil plane of the eye. Thus, two of the telescopes combine to image the fiber face onto the retina and the third telescope ensures that the scanning mirrors are not apertured by the entrance pupil of the eye.

3.4 Transverse Resolution and Confocal Parameter

3.4.1 Retinal Spot Size

The minimum achievable transverse resolution is equal to the probe beam spot diameter $2w_r$ on the retina. The spot size may be calculated simply (without resort to Gaussian beam propagation) by considering telescopes #1 and #2 in Figure 3-8, which image the fiber face first to the retinal image plane and then to the retina. For a beam diameter of $2w_0$ at the fiber face, the retinal spot diameter $2w_r$ is

$$2w_r = \frac{F_c}{F_{eye}} \cdot \frac{f_f}{f_o} \cdot 2w_0 \tag{3.16}$$

where lens focal lengths and powers are used interchangeably. If we assume that the initial spot size $2w_0$ is approximately equal to the single-mode fiber core diameter, then $2w_r$ = 20 μm for $2w_0$ = 5 μm. Using similar reasoning, the spot size at the retinal imaging plane would be $2w_i$ = 15 μm under these same conditions.

3.4.2 Beam Diameter at Pupil

The collimated beam diameter at the entrance pupil of the eye is very important since it is this pupil (and ocular aberration) which limits the minimum spot size achievable on the retina. The diameter of the beam $2w_p$ at the pupil is related to the diameter $2w_m$ at the location of the scanning mirrors by telescope #3 comprised of the focusing lens and condensing lens:

$$2w_p = \frac{1}{F_c f_f} \cdot 2w_m . \tag{3.17}$$

The $1/e$ beam diameter at the scanning mirror is given by Gaussian beam diffraction from the fiber face:

$$2w_m = \frac{2\lambda f_o}{\pi w_0} . \tag{3.18}$$

For a fiber core diameter of $2w_0$ = 5 μm and λ = 843 nm, the diameters at the mirror plane and pupil plane are $2w_m$ = 4.3 mm and $2w_p$ = 1.2 mm respectively.

A smaller spot size on the retina and better transverse resolution may be achieved by increasing the beam diameter at the pupil. For a given diameter $2w_p$ at the pupil, the retinal spot size is

$$2w_r = \frac{2\lambda}{\pi F_{eye} w_p} \tag{3.19}$$

assuming diffraction limited focusing by the eye. Thus a 4 mm beam at 843 nm may be used to produce a theoretical retinal spot size of 4.5 μm. In practice, however, ocular aberrations limit the minimum achievable spot size for larger beam diameters as described in Section 3.2.8.

3.4.3 Confocal Parameter

An additional constraint is the depth of focus of the probe beam at the retina which is determined by the confocal parameter. It is well known that the confocal parameter $2b_r$ is related to the square of the spot size:

$$2b_r = \frac{2\pi w_r^2}{\lambda}. \tag{3.20}$$

For the geometry in Figure 3-8 and λ = 843 nm, the probe beam is focused over a length $2b_r$ = 710 μm in the retina--between two and three times the nominal retinal thickness of 250 μm. This relatively large confocal parameter allows for easier axial alignment of the reference arm position and ensures that the beam is not defocused for pathologies in which the retinal thickness is significantly increased.

3.5 Magnification and Field-of-View

3.5.1 Magnification

To compute the transverse distances on the retina, the angular deviation of the scanning mirrors must be related to the angle subtended on the retina. Figure 1-8 illustrates the case for a perfectly aligned, emmetropic eye. In perfect alignment, the probe beam pivots in the pupil plane of the eye, minimizing any aperturing effect.

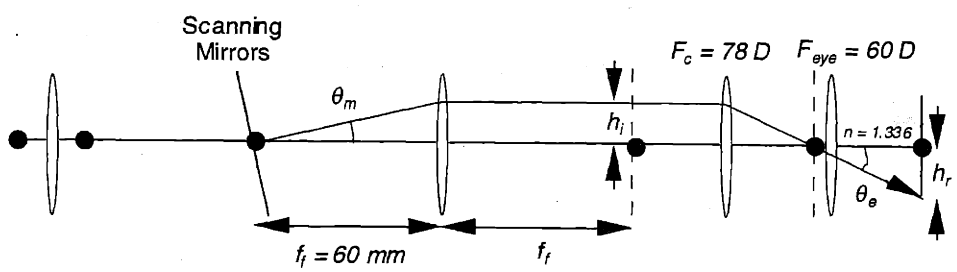

FIGURE 3-9. Magnification of scanning mirrors on retina.

The transverse position of the beam on the retina, h_r, is related to the position h_i in the retinal image plane by the telescope formed by the condensing lens and the eye:

$$h_r = -\frac{F_c}{F_{eye}} \cdot h_i. \tag{3.21}$$

Therefore the angles θ_e and θ_m are related by

$$\theta_e = \frac{h_r}{n_{vi}/F_{eye}} = -\frac{F_c}{n_{vi}} \cdot h_i = -\frac{F_c f_f}{n_{vi}} \cdot \theta_m \tag{3.22}$$

where the paraxial approximation $\theta \approx \tan\theta$ has been invoked. Numerical evaluation shows that $\theta_e = -3.50\theta_m$ for the lenses depicted in Figure 3-9.

Equation (3.22) shows that the angular deviation of the scanning mirrors in the pupil plane of the eye is scaled inversely by the magnification of the telescope which images the mirrors onto this plane. The angle is also reduced by the refractive index of the vitreous according to Snell's law. In this ideal situation, the optical power of the eye does not affect the magnification because the beam pivots through the center of the ideal eye's only refractive element.

The effects of eye positioning and refractive error on the magnification of the transverse scan will be investigated in Section 3.6.

3.5.2 Field-of-View

In the case of optimal alignment, the field-of-view, or maximum transverse scanning distance on the retina, of the OCT system is limited by the usable apertures of the focusing and condensing lenses. The entrance pupil of the eye has no effect in the ideal case because there is no transverse deviation of the scanning probe beam in this plane. From Equation (3.22), the angular field-of-view $2\theta_e$ is related to the maximum usable transverse beam position h_i between the focusing and condensing lens by

$$2\theta_e = \frac{F_c}{n_{vi}} \cdot 2h_i. \tag{3.23}$$

The field-of-view depends only on the power of the condensing lens F_c and the limiting aperture diameter $2h_i$. Higher power condensing lenses increase the field-of-view. However, the available working distance between the condensing lens and the eye is decreased since the pupil plane of the eye must be positioned at the focal plane of the condensing lens. According to Equation (3.16), the retinal spot size also scales inversely with increasing condensing lens power.

In the current implementation, the focusing lens has a diameter of 1″ and the condensing lens has a diameter of approximately 1.5″. Therefore the field-of-view is limited by the focusing lens. Assuming $2h_i \approx 2$ cm for the maximum usable lens diameter, then the field-of-view is $2\theta_e \approx 67°$ with a 78 D condensing lens. This is approximately four times the 15° distance between the fovea and optic disc in a normal human eye.

In practice, the field-of-view is often limited by the pupil due to deviations in the position of the eye relative to the slit-lamp along the optic axis (see Section 3.6.6 for more details).

3.6 Axial Eye Positioning and Ametropia

The analysis of the OCT system has so far assumed an ideal emmetropic eye which is perfectly positioned in front of the slit-lamp condensing lens. However, in actual practice, the axial distance between the slit-lamp and the eye is poorly controlled. In addition, many eyes are ametropic. To compensate for refractive errors and positioning, the axial position of the condensing lens may be varied by the examiner along the optical axis. This section will analyze the effect of misalignment and ametropia on OCT image formation, including transverse resolution, field-of-view, magnification, and distortion of the retinal curvature.

3.6.1 Non-Ideal Imaging Geometry

Since the fiber optic, collimating lens, scanning mirrors, and focusing lens in Figure 3-8 are fixed, analysis of the non-ideal imaging system can begin at the slit-lamp image plane. Figure 3-10 depicts the non-ideal imaging geometry.

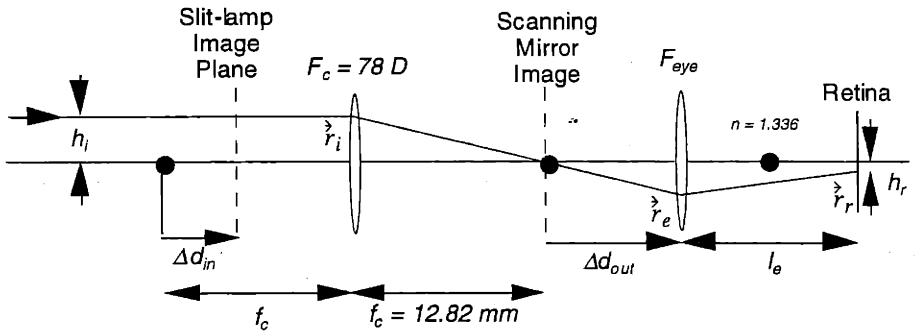

FIGURE 3-10. Non-ideal OCT imaging geometry.

The probe beam remains focused in the slit-lamp image plane by the telescope formed by the collimating lens and the focusing lens (not shown). The probe beam is also parallel to the optic axis in this plane due to the action of the focusing lens. The height of the probe beam with respect to the optic axis is given by $h_i = \theta_m f_f$ (Figure 3-9).

The condensing lens F_c is mobile along the optic axis. Thus, the slit-lamp image plane does not necessarily coincide with the focal plane of the condensing lens. The distance from the condensing lens anterior focal plane to the slit-lamp image plane is Δd_{in}, which is measured in the direction of light propagation (positive as shown). It is important to note that the image of the scanning mirrors remains at the posterior focal point of the condensing lens, independent of Δd_{in}, because the virtual object corresponding to the scanning mirrors lies at infinity due to the action of the focusing lens (Figure 3-9). The position of the eye is also allowed to vary relative to the condensing lens. Δd_{out} gives the distance from the posterior focal plane of the condensing lens to the refractive surface and pupil plane of the eye, also measured in the direction of light propagation (positive as shown).

Finally, the eye being imaged may be ametropic and the retina may not coincide with the eye's posterior focal plane. The ocular ametropia is described by the principle point refraction (Section 3.2.6) which is given by $A = n_{vi}/l_e - F_{eye}$. Both the axial length and the refractive power of the eye may differ from those in the Gullstrand eye.

3.6.2 Ray Matrices

The ABCD ray matrix formalism will be used to compute the beam height at the pupil and retina in terms of the parameters described above. Let

$$\vec{r}_i = h_i \begin{bmatrix} 1 \\ 0 \end{bmatrix} \tag{3.24}$$

describe the horizontal ray of height h_i incident on the condensing lens F_c due the angular deviation θ_m of the scanning mirrors. After propagation to the pupil plane through condensing lens F_c and through free space of length $f_c + \Delta d_{out}$, the ray becomes, at the entrance to the eye,

$$\vec{r}_e = \begin{bmatrix} 1 & f_c + \Delta d_{out} \\ 0 & 1 \end{bmatrix} \cdot \begin{bmatrix} 1 & 0 \\ -F_c & 1 \end{bmatrix} \cdot h_i \begin{bmatrix} 1 \\ 0 \end{bmatrix} = -h_i F_c \begin{bmatrix} \Delta d_{out} \\ 1 \end{bmatrix}. \tag{3.25}$$

The ray is then refracted by the eye, encounters an index boundary between air and vitreous, and propagates a distance l_e through the vitreous to the retina:

$$\vec{r}_r = -h_i F_c \cdot \begin{bmatrix} 1 & l_e \\ 0 & 1 \end{bmatrix} \cdot \begin{bmatrix} 1 & 0 \\ 0 & \frac{1}{n_{vi}} \end{bmatrix} \cdot \begin{bmatrix} 1 & 0 \\ -F_{eye} & 1 \end{bmatrix} \cdot \begin{bmatrix} \Delta d_{out} \\ 1 \end{bmatrix} = -\frac{h_i F_c}{n_{vi}} \cdot \begin{bmatrix} l_e(1 + A\Delta d_{out}) \\ 1 - F_{eye}\Delta d_{out} \end{bmatrix}. \tag{3.26}$$

The ray height at the retina depends both on the ocular ametropia and the axial eye length. Note that neither Equation (3.25) or Equation (3.26) depends on the separation Δd_{in} between the condensing lens and slit-lamp image plane.

For the reduced Gullstrand eye in perfect alignment, Equations (3.25) and (3.26) reduce to

$$\vec{r}_e = -h_i F_c \begin{bmatrix} 0 \\ 1 \end{bmatrix} \tag{3.27}$$

describing the ray at the entrance (pupil plane) of the eye and

$$\vec{r}_r = -\frac{h_i F_c}{n_{vi}} \begin{bmatrix} l_e \\ 1 \end{bmatrix} \tag{3.28}$$

describing the ray at the retina.

3.6.3 Magnification and Transverse Resolution

Equation (3.26) shows that the magnification on the retina of the scanning beam depends both on the optical power of the eye and the distance between the eye and the instrument. A similar relation is valid for the fundus camera [75]. The magnification m between the

retinal plane and slit-lamp image plane is found by dividing the height of the ray at the retina in Equation (3.26) by the height of the ray incident on the condensing lens (Equation (3.24)), which gives

$$m = -\frac{F_c}{n_{vi}} \cdot l_e(1 + A\Delta d_{out}) . \tag{3.29}$$

For an ideally positioned, Gullstrand eye, Equation (3.29) becomes

$$m_{ideal} = -\frac{F_c}{n_{vi}} \cdot l_{ideal} \tag{3.30}$$

where the ideal axial eye length from the reduced Gullstrand eye is $l_{ideal} = 22.27$ mm.

The relative magnification between the non-ideal case and the ideally positioned reduced Gullstrand eye is, by comparing Equation (3.29) with Equation (3.30),

$$\frac{m}{m_{ideal}} = \frac{l_e}{l_{ideal}} \cdot (1 + A\Delta d_{out}) \tag{3.31}$$

Equation (3.31) describes exactly the scaling of the probe beam spot size in the non-ideal relative to the ideal eye. Thus, the transverse resolution decreases (larger spot size) with increasing eye length l_e, increasing hyperopia ($A > 0$), and increasing positive distance Δd_{out} from the condensing lens. Equation (3.31) also the describes the necessary correction for refractive and positioning errors of transverse measurements extracted from the OCT image (see Section 3.6.5 for further details). Note that this correction is independent of the axial position for an emmetropic eye.

3.6.4 Focusing

In typical operation, the position of the condensing lens is adjusted along the optic axis until the retinal image is brought into focus at the slit-lamp image plane. The focused arrangement is diagrammed in Figure 3-11. The focused arrangement constrains the relation-

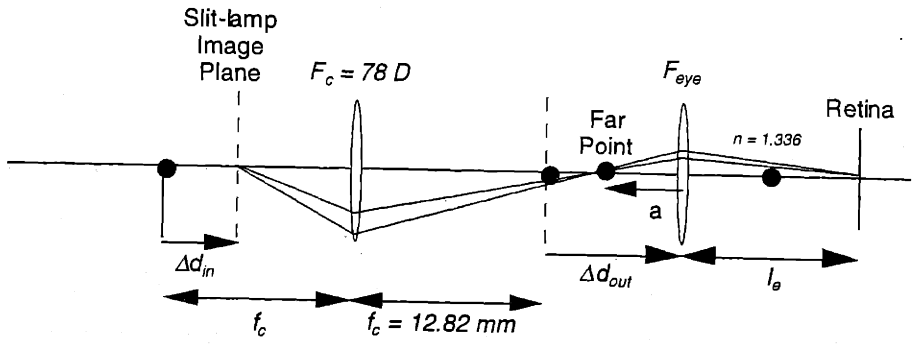

FIGURE 3-11. Focusing condition.

ship between the distance Δd_{in} between the condensing lens anterior focus and the slit-lamp image plane, the distance Δd_{out} between the condensing lens posterior focus and the eye, and the ocular ametropia A.

The retinal image in the unaccommodated eye, by definition, occurs at the far point a (Section 3.2.6), which defines the ocular ametropia A:

$$A = \frac{1}{a} = \frac{n_{vi}}{l_e} - F_{eye}. \tag{3.32}$$

The position of the condensing lens is constrained so that the far point and slit-lamp image plane are conjugate image planes. By Newton's relation, the product of the extrafocal distances in conjugate image planes is equal to the product of lens anterior and posterior focal lengths:

$$\Delta d_{in} \cdot (\Delta d_{out} + a) = \frac{1}{F_c^2}. \tag{3.33}$$

Combining Equations (3.32) and (3.33) leads to the focusing condition

$$\frac{1}{A} = \frac{1}{\Delta d_{in} F_c^2} - \Delta d_{out}. \tag{3.34}$$

Equation (3.34) can be used to calculate the maximum translation distance of the condensing lens required to image eyes with ametropia. Solving for Δd_{in} we have

$$\Delta d_{in} = \frac{1}{F_c^2 \cdot \left(\frac{1}{A} + \Delta d_{out}\right)} \approx \frac{A}{F_c^2} \tag{3.35}$$

where the approximation assumes that $|1/A| \gg |\Delta d_{out}|$. Since the examiner usually attempts to position the eye at the focal plane of the condensing lens, $|\Delta d_{out}|$ does not usually exceed 2 cm. Thus, the approximation only requires that $|A| \ll 50$ D.

In practice, the maximum ocular ametropia encountered is due to aphakia after cataract extraction (Section 3.2.6). In this case, the principle point refraction is $A = 12.22$ D and the required translational distance of the condensing lens from Equation (3.35) is approximately $\Delta d_{in} = 2$ mm. Higher power condensing lenses decrease the axial movement required for focusing.

3.6.5 Correction for Refractive Error

Transverse measurements extracted from OCT images must be scaled by the factor m/m_{ideal} from Equation (3.31) for ametropic and/or poorly positioned eyes. However, there are practical problems in measuring the values necessary to evaluate Equation (3.31). Only the ocular ametropia A is routinely measured in clinical practice. The axial eye length l_e can be measured with ultrasonography (and in the future OCT!), but is only routinely done for calculation of intraocular lens implant power after cataract extraction. It is very inconvenient to attempt to measure the distance between the patient's eye and the condensing lens posterior focus Δd_{out} since this parameter can vary during the imaging session.

However, by employing the focusing constraint in Equation (3.34), we can rewrite Equation (3.31) in terms of the distance Δd_{in} from the condensing lens anterior focus to the slit-lamp image plane:

$$\frac{m}{m_{ideal}} = \frac{l_e}{l_{ideal}} \cdot \frac{A}{\Delta d_{in} F_c^2}. \tag{3.36}$$

Since Δd_{in} only depends on the optical components, it could in principle be automatically measured and recorded for each OCT image by a sensor placed on the translation device of the condensing lens.

The distance between the principle plane of the eye and the retina, l_e, can be calculated either from ultrasonic measurements of axial eye length, or estimated from the principle point refraction [76, 77]. If the more accurate ultrasonic measurement is used, then

$$l_e \approx l_{ax} - 1.6 \text{ mm} \tag{3.37}$$

where l_{ax} is the axial eye distance from the anterior surface of the cornea to the retina as measured by ultrasound, and 1.6 mm is the approximate distance between the corneal surface and the principle plane of the eye (Figure 3-2). If the principle point refraction is used, then

$$l_e \approx \frac{n_{vi}}{A + F_{ideal}} \tag{3.38}$$

where $F_{ideal} = 60$ D is the power of the ideal Gullstrand eye. Equation (3.38) assumes that the entire refractive error is due to differences in eye length, rather than refractive power.

For practical purposes, a rough estimate of the relative magnification for ametropic eyes can be obtained by assuming that the eye is correctly positioned ($|A\Delta d_{out}| \ll 1$ is satisfied) and using the principle point refraction to estimate the axial eye length. With these assumptions, Equation (3.31) becomes

$$\frac{m}{m_{ideal}} \approx \frac{F_{ideal}}{A + F_{ideal}}. \tag{3.39}$$

For example, a myopic eye with a -4 D refractive error results in $m/m_{ideal} \approx 1.07$ using the approximation in Equation (3.39). The effect of axial positioning becomes apparent when the magnification error due to axial positioning is approximately half the error due to refraction alone (*i.e.* $A\Delta d_{out} \approx 0.04$) which results in $\Delta d_{out} \approx 1$ cm.

3.6.6 Field-of-View Limited by Pupil

If the image of the scanning mirrors does not coincide with the pupil plane of the eye ($\Delta d_{out} \neq 0$), then the field-of-view may also be limited by the pupil (instead of just the apertures of the focusing lens and condensing lens as described in Section 3.5.2). The height of scanning ray at the pupil is given by Equation (3.25). If this height is set to one-half the pupil diameter d_p then

$$\frac{d_p}{2} = -h_i F_c \Delta d_{out}. \tag{3.40}$$

Substituting Equation (3.40) into Equation (3.26), we find that the height of the ray at the retina is given by

$$h_r = \frac{d_p}{2n_{vi}} \cdot l_e\left(\frac{1}{\Delta d_{out}} + A\right). \tag{3.41}$$

The angular deviation between two such rays, one above and one below the optical axis is equal to the field-of-view:

$$2\theta_m = \frac{d_p}{n_{vi}} \cdot \left(\frac{1}{\Delta d_{out}} + A\right). \tag{3.42}$$

The field-of-view is proportional to the pupil diameter and scales inversely with the distance between the condensing lens and the eye. For an emmetropic eye with a 5 mm pupil diameter positioned 1 cm away from the condensing lens focal point, the field-of-view is $2\theta_m = 21°$.

Comparing Equation (3.42) with Equation (3.25), we find that the field-of-view is limited by the pupil when

$$d_p \cdot \left(\frac{1}{\Delta d_{out}} + A\right) \approx 2F_c h_i. \tag{3.43}$$

For an emmetropic eye with a 5 mm pupil, and a 78 D condensing lens limited by a 2 cm aperture diameter (see Section 3.5.2), the axial positioning error Δd_{out} must be less than 3 mm to avoid further aperturing by the pupil.

3.6.7 Beam Diameter at Pupil

After the OCT instrument has been focused, the slit-lamp image plane is conjugate to the far point of the retina (Figure 3-11). Therefore, the probe beam has a waist at the far point. The width of the beam waist at the far point is given by the width at the slit-lamp image plane multiplied by the magnification of the condensing lens. Using the telescope formed by the collimating objective and the focusing lens, the spot size $2w_i$ at the image plane is

$$2w_i = 2w_o \frac{f_f}{f_o}. \tag{3.44}$$

The magnification of the condensing lens is given by the ratio of image to object distances from the lens. Therefore, the beam waist diameter $2w_a$ at the far point is

$$2w_a = 2w_o \cdot \frac{f_f}{f_o} \cdot \frac{f_c + \Delta d_{out} + a}{f_c - \Delta d_{in}}. \tag{3.45}$$

The beam diameter $2w_p$ after propagation of the Gaussian beam from the far point to the pupil plane may be calculated from the standard formula

$$w_p^2 = w_a^2\left[1 + \left(\frac{\lambda a}{\pi w_a^2}\right)^2\right]. \tag{3.46}$$

For the far point distance a much larger than the confocal parameter, which is usually the case,

$$w_p \approx \frac{\lambda a}{\pi w_a}. \tag{3.47}$$

Equations (3.45) and (3.46) cannot be used in the emmetropic case ($a = \infty$). However, since the far point is at infinity, we know that the slit-lamp image plane must lie at the anterior focal plane of the condensing lens ($\Delta d_{in} = 0$). Therefore, the beam is collimated between the condensing lens and the eye and not affected by changes in Δd_{out}. Equations (3.17) and (3.18) then apply.

3.6.8 Retinal Curvature Distortion

Consider an ideal, emmetropic eye positioned such that the image of the scanning mirrors is placed in the pupil plane. The propagation distance of each ray from the scanning mirrors to the pupil plane image of the mirrors is equivalent and independent of the angular deviation of the mirrors. Although the peripheral rays have longer geometric paths compared to the central rays, these longer paths are balanced out by shorter distances through the lenses, which have a higher refractive index. The equidistant surface traced out by scanning is a circular arc, with radius of curvature equal to the posterior focal length of the eye. Ideally, this arc matches the radius of curvature of the retina, so the resulting OCT image is flat. A distortion of the retinal curvature, however, can occur if the image of the scanning mirrors does not fall on the center of the retinal radius of curvature. This may occur due to imperfect positioning of the eye along the optical axis, or to ocular ametropia.

To estimate the magnitude of this distortion, let r_s be the radius of curvature of the equidistant surface created by the scanning mirrors and r_r be the retinal radius of curvature. If the center of the retinal radius of curvature lies at the posterior principle plane of the eye, then $r_r = l_e$. The center of the equidistant curve traced out by the scanning mirrors is given by the image of the scanning mirrors in the eye formed by the refractive surface of the eye. The virtual object corresponding to this image is the image of the scanning mirrors which always lies at the anterior focal plane of the condensing lens. Let o be the distance from the refractive surface of the eye to the anterior focal plane of the condensing lens. We will use the sign convention that $o > 0$ in the direction of light propagation which means that $o = -\Delta d_{out}$ where Δd_{out} is defined in Figure 3-10. We define the image distance i as the distance between the refractive surface of the eye and the image of the scanning mirrors within the eye, again positive in the direction of light propagation. The scanning mirror radius of curvature is therefore related to the image distance by $r_s = r_r - i = l_e - i$.

Using the thin lens equation, we have

$$\frac{1}{o} + F_{eye} = \frac{n_{vi}}{i}. \tag{3.48}$$

which leads to

$$r_s = r_r - \frac{n_{vi}}{F_{eye} - \frac{1}{\Delta d_{out}}}. \tag{3.49}$$

There are four possible conditions relating r_s and r_r which are described below.

If $\Delta d_{out} = 0$, then the posterior focus of the condensing lens coincides with the refractive surface of the eye and the scanning mirror image is located at the center of the radius of curvature of the eye. Therefore, $r_s = r_r$, and the apparent retinal contour appears straight (Figure 3-12).

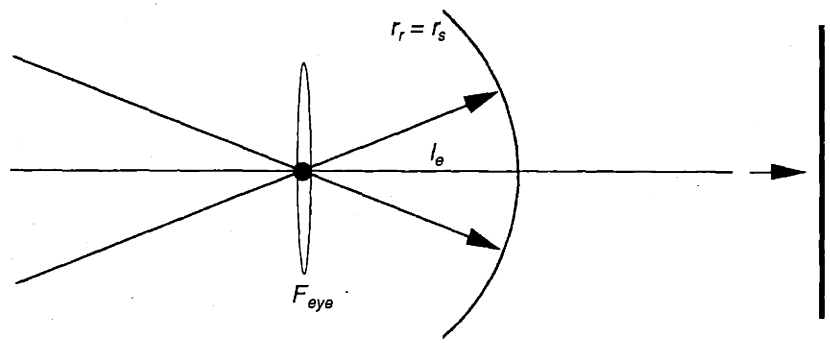

FIGURE 3-12. Scanning curvature equal to retinal curvature.

The condition $r_s > r_r$ occurs if the image I of the scanning mirrors is located anterior the refractive surface of the eye. This occurs if the condensing lens posterior focus O is located between anterior to the refractive surface of the eye and the anterior focus F of the eye, *i.e.* $0 < \Delta d_{out} < 1/F_{eye}$ (Figure 3-13). In this condition, the retinal surface is more curved then the scanning mirror surface and the retinal contour appears slightly curved (although less curved than the actual retinal curvature).

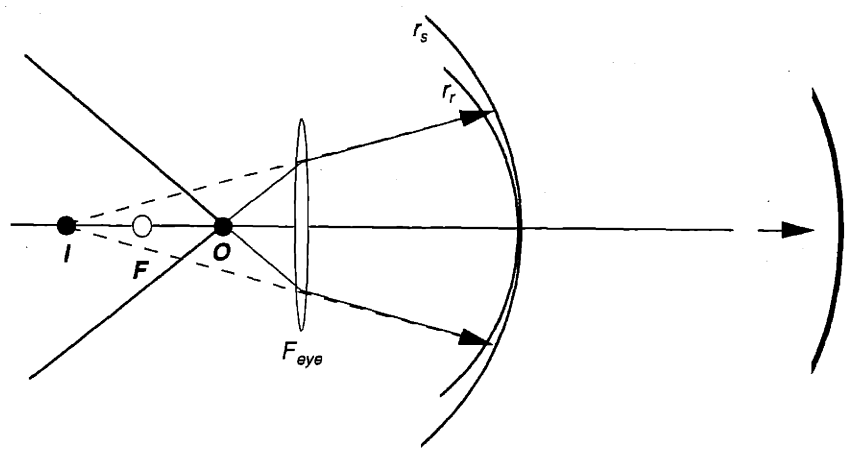

FIGURE 3-13. Scanning curvature greater than retinal curvature.

The condition $0 < r_s < r_r$ occurs if the image I of the scanning mirrors is located between the refractive surface of the eye and the retina. This occurs if

$$\begin{cases} \Delta d_{out} < 0 \text{ and } \Delta d_{out} < \dfrac{1}{A} \\ \text{or} \\ \Delta d_{out} > 0 \text{ and } \dfrac{1}{F_{eye}} > \Delta d_{out} > -\dfrac{1}{A} \end{cases} \tag{3.50}$$

where the principle point refraction (Section 3.2.6) is defined as $A = n_{vi}/r_r - F_{eye}$. Recall $A > 0$ (hyperopia) means that the posterior focus of the eye is located behind the retina, while $A < 0$ (myopia) means that the posterior focus is located in front of the retina. For an emmetropic eye ($A = 0$), the conditions in Equation (3.50) reduce to the condition $\Delta d_{out} < 0$, which occurs when the posterior focus of the condensing lens O is located within the eye (Figure 3-14). The apparent retinal curvature is flattened or even inverted.

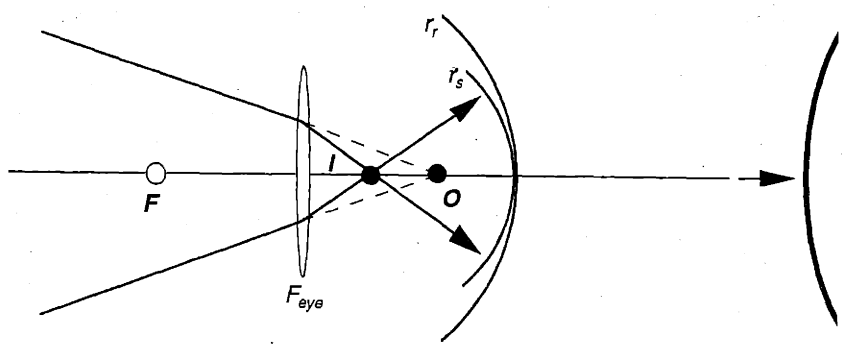

FIGURE 3-14. Scanning curvature less than retinal curvature.

If the image I of the scanning mirrors lies behind the retina, then the scanning curvature is negative ($r_s < 0$) and severe distortion of the retinal curvature results (Figure 3-15). This condition results if

$$\begin{cases} \Delta d_{out} > \dfrac{1}{F_{eye}} \text{ and } \begin{cases} A \geq 0 \\ \text{or} \\ A < 0 \text{ and } \Delta d_{out} < \dfrac{1}{A} \end{cases} \\ \text{or} \\ \Delta d_{out} < 0 \text{ and } |\Delta d_{out}| > \dfrac{1}{A} \end{cases} \tag{3.51}$$

For an emmetropic eye, Equation (3.51) may be rewritten as $\Delta d_{out} > 1/F_{eye}$, which says that the posterior focus of the condensing lens O must lie anterior to the anterior focus F of the eye.

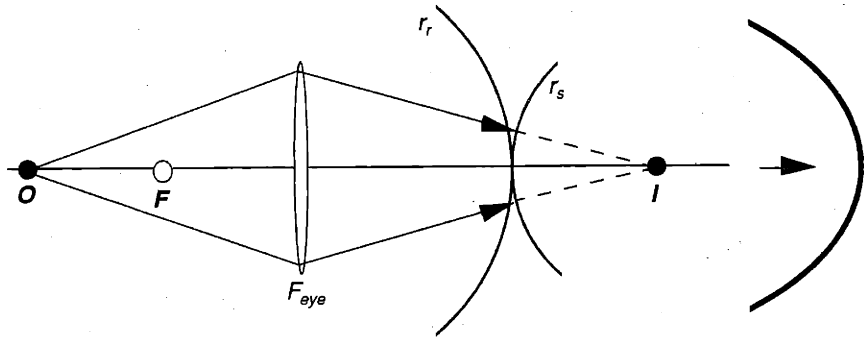

FIGURE 3-15. Negative scanning curvature.

The effective or apparent curvature of the OCT image r_{eff} is related to the scanning curvature r_s and the retinal curvature r_r by

$$\frac{1}{r_{eff}} = \frac{1}{r_r} - \frac{1}{r_s}. \tag{3.52}$$

After substitution using Equation (3.49), we find

$$r_{eff} = r_r + \frac{r_r^2}{n_{vi}}\left(\frac{1}{\Delta d_{out}} - F_{eye}\right) \tag{3.53}$$

which is valid for $r_s \neq r_r$. The condition depicted in Figure 3-13 occurs most often in practice, since it is relatively difficult to get too close to the eye due to the size of the condensing lens. Note that corneal surface is approximately 1.6 mm anterior to the principle plane of the eye (Figure 3-2). Thus, the anterior focus F for the reduced Gullstrand eye lies approximately 15 mm in front of the corneal surface. A greater than $1/F_{eye}$ = 16.67 mm positioning error would be necessary for the condition expressed in Figure 3-15 to occur in an emmetropic eye. This can occasionally occur in patients with very recessed eyes or protruding foreheads.

The effect of retinal curvature distortion is most noticeable for long transverse scans, for example those containing both the fovea and optic disc along the papillomacular axis. Consider such an OCT image in an emmetropic eye. Assume the image is centered on the optic axis (5° nasal to the fovea) and extends 15° nasally to cover 5° beyond the optic disc (which is located 15° nasal to the fovea). The edge of this scan spans an arc of 5.8 mm measured from the center of the optic axis. Now assume that the eye is located just 5 mm beyond the location of the posterior focus of the condensing lens (Δd_{out} = 5 mm). The effective radius of curvature from Equation (3.53) is r_{eff} = 74 mm (assuming $r_r = l_e = n_{vi}/F_{eye}$ and F_{eye} = 60 D). The effective span θ_{eff} of a 5.8 mm arc with 74 mm radius is 4.3°. The separa-

tion in axial distance between the optic axis and the end of the arc on the OCT image Δd_a is given by $\Delta d_a = r_{eff}(1 - \cos\theta_{eff}) = 230\ \mu m$ which is approximately the retinal thickness. Therefore, the curvature distortion will be immediately apparent on the image.

If the axial positioning error is increased to $\Delta d_{out} = 1\ cm$, then we have $r_{eff} = 37\ mm$, $\theta_{eff} = 9°$, and $\Delta d_a = 450\ \mu m$ which is quite a significant apparent curvature. With $\Delta d_{out} = 2\ cm$ in an emmetropic eye, the condition in Figure 3-15 unfortunately occurs. In this case, $r_{eff} = 19\ mm$, $\theta_{eff} = 18°$, and $\Delta d_a = 930\ \mu m$.

3.6.9 Retinal Thickness Distortion

The curvature distortion described in Section 3.6.8 also leads to distortions in the measurement of retinal thickness because the OCT probe beam has oblique incidence on the retinal surface. The geometry is shown in Figure 3-16. Assume the probe beam is inclined an

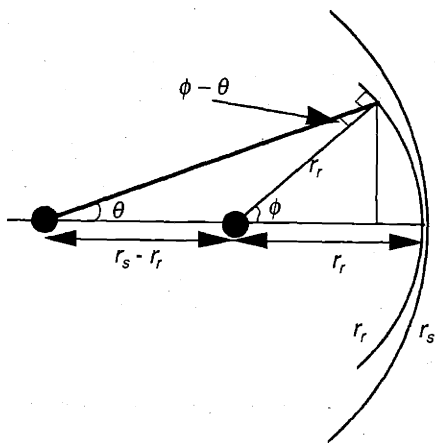

FIGURE 3-16. Oblique incidence due to curvature distortion.

angle θ from the optic axis and scanning in a radius r_s. If r_r is the actual retinal curvature, then the off-normal incidence angle of the probe beam on the retina is given by $\phi - \theta$ as shown. From the geometry, the angle θ is given by

$$\tan\theta = \frac{r_r \sin\phi}{r_s - r_r + r_r \cos\phi}. \tag{3.54}$$

Assuming small angles, the incidence angle of the OCT beam is then

$$\phi - \theta \approx \phi\left(1 - \frac{r_r}{r_s}\right). \tag{3.55}$$

A measurement of retinal thickness will be increased by the factor $1/\cos(\phi - \theta)$ from its actual value due to the oblique incidence.

Using the example in Section 3.6.8 (Δd_{out} = 5 mm and a reduced Gullstrand eye), we find that r_s = 32 mm and $\phi - \theta \approx 0.3\phi$. Therefore, a measurement of retinal thickness at the edge of a 15° length scan would be off by a factor of 1.004 (an error of approximately 1 μm assuming a 250 μm thick retina). If Δd_{out} = 1 cm, then r_s = 56 mm, $\phi - \theta \approx 0.6\phi$, and the same measurement would be off by a factor of 1.01 (an error of approximately 2.5 μm over 250 μm). These are relatively small errors. However, if the negative scanning curvature condition in Figure 3-15 is satisfied then larger errors are induced. For example, with Δd_{out} = 2 cm, we find r_s = −111 mm, $\phi - \theta \approx 1.2\phi$, and $1/\cos(\phi - \theta)$ = 1.05. This is a 13 μm error in retinal thickness at the edge of the scan and is approximately the same magnitude as the longitudinal resolution.

3.6.10 Scanning Mirror Separation

If the scanning mirrors are not placed exactly in the anterior focal plane of the focusing lens, then consideration of the telescope formed by the focusing lens and the condensing lens shows that the image of the scanning mirrors does not occur at the posterior focus of the condensing lens. This is a potential problem because an effective axial positioning error may occur in which the image of the scanning mirrors does not occur in the pupil plane of the eye even if the pupil plane is placed at the posterior focus of the condensing lens. In other words, Δd_{out} may be effectively non-zero, which could potentially disrupt the magnification, field-of-view, and image curvature as described above.

Thus, the dependence of scanning mirror image position on the actual position of the scanning mirrors is of concern, especially since it is impossible to place both orthogonal scanning mirrors at the anterior focus of the focusing lens. Let Δs_1 be the relative distance of the scanning mirrors from anterior focus of the focusing lens (in the direction of light propagation), and Δs_2 be the relative distance of the image at the output of the telescope measured from the posterior focus of the condensing lens. Applying Newton's relation twice in succession (Section 3.6.4) to both lenses, we find

$$\Delta s_2 = \left(\frac{1}{F_c f_f}\right)^2 \Delta s_1 . \tag{3.56}$$

In other words, the extrafocal output distance is related to extrafocal input distance by the square of the telescope magnification.

In the current implementation (F_c = 78 D and f_f = 60 mm), the magnification is less than one, and $\Delta s_2 \approx \Delta s_1/22$. Thus, with a 4 cm positioning error in at least one of the scanning mirrors, the axial deviation in the position of the image of the mirror is less than 2 mm. This deviation is certainly less than the manual positioning error of the distance between the eye and the condensing lens and can be neglected.

Chapter 4

IMAGE PROCESSING

4.1 Introduction

This Chapter develops the image processing algorithms used to display the false-color OCT images, remove the effects of eye motion in the axial direction, and to compute retinal and retinal nerve fiber layer thickness. The concept of acquiring multiple OCTs to generate topographic information on retinal and retinal nerve fiber layer thickness is also discussed.

4.2 Logarithmic Transformation

4.2.1 Color Table Mapping

The OCT images are displayed on a logarithmic scale of reflectivity which was chosen to offset the exponential attenuation of unscattered light propagating through tissue. The detector current is proportional to the field in the reference arm multiplied by the field in the sample arm, or equivalently the square root of the sample reflectivity. With a linear filtering and amplification circuit, the voltage read by the computer after the analog-to-digital converter is also proportional to the square root of reflectivity. To display the logarithm of sample reflectivity in false-color, the transformation

$$R = 10\log\left(\frac{V - offset}{SD}\right)^2 \tag{4.1}$$

is used, where R is the reflectivity expressed on a decibel (dB) scale, V is the measured detector voltage, $offset$ is the DC voltage bias of the filtering and amplification circuity, and SD is the standard deviation of the image background noise. Thus, the logarithmic scale of reflectivity is referenced to a noise variance of 0 dB. Reflectivities less than two standard deviations above the image background noise floor (*i.e.* $R < 20\log 2$ dB) are thresholded and set to $R = 20\log 2$ dB to maximize the color values available to real image data. In practice, the DC bias and the background noise floor are computed from the mean and standard deviation respectively of the first few lines in the image which are assumed to contain noise only.

The image color table is assigned to the reflectivity values using

$$I = \frac{R - 20\log 2}{\max(R) - 20\log 2} N \tag{4.2}$$

where I is the index into the color table, N is the number of color table entries, and $\max(R)$ is the maximum reflectivity value in the image. $\max(R)$ is interpreted as the signal-to-noise (SNR) ratio of the image and is displayed in the lower right corner of each OCT. It is important to note that this color mapping scheme does not preserve absolute reflectivities. Rather, the color table is chosen to exactly span the range of reflectivities in the image. One must be careful in interpreting specific colors as indicative of the same feature across different images with varying SNRs. Currently, an 8-bit color table is used which leads to a 0.15 dB quantization between each color value in a typical image with a SNR of 45 dB.

4.2.2 Bit-Shift Logarithmic Transformation

An approximate logarithmic transformation was developed to enable both the rapid display of multiple thumbnail images and the real-time display of images during data acquisition without the use of floating-point operations. This approximate transformation relies exclusively on addition, bit-shift, bit-test, and logical operators and is performed on an integer representation of the reflectivity.

Reflectivity values are represented internally in a two-byte signed integer format directly after 16-bit analog-to-digital conversion. Bits are tested successively starting from most to least significant to determine one of 7 ranges in the color table (Figure 4-1). Once a

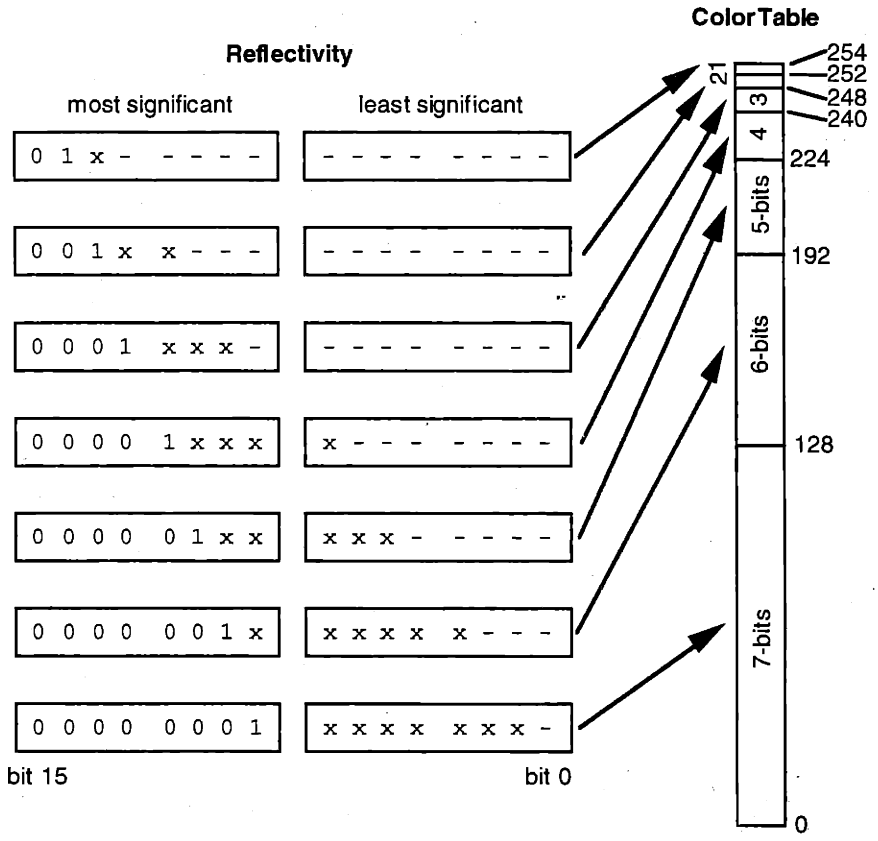

FIGURE 4-1. Schematic of bit-shift logarithmic transformation.

given range is selected, then the next most significant bits (denoted by an "x") are linearly mapped into that range as shown. Note that bit 15 is a sign bit which is always zero for positive integers. Listing 4-1 shows an implementation of this algorithm in C.

```
if (data & 0x4000)
   log_data = (data >> 13 & 0x01) + 128+64+32+16+8+4;
else if (data & 0x2000)
   log_data = (data >> 11 & 0x03) + 128+64+32+16+8;
else if (data & 0x1000)
   log_data = (data >>  9 & 0x07) + 128+64+32+16;
else if (data & 0x0800)
   log_data = (data >>  7 & 0x0F) + 128+64+32;
else if (data & 0x0400)
   log_data = (data >>  5 & 0x1F) + 128+64;
else if (data & 0x0200)
   log_data = (data >>  3 & 0x3F) + 128;
else if (data & 0x0100)
   log_data = (data >>  1 & 0x7F;
else
   log_data = 0;
```

LISTING 4-1. C code example of bit-shift logarithmic transformation.

Figure 4-2 plots the approximate logarithm function on a log scale. A true logarithm would appear as a straight line on the graph. The approximate function, however, is essentially a connected series of seven segments corresponding to the seven ranges in Figure 4-1. The x-axis position of the curve (*i.e.* the DC offset of the approximation) can be varied in powers of two by shifting the locations of the 1's in Figure 4-1 either left (to increase the offset) or right (to decrease the offset).

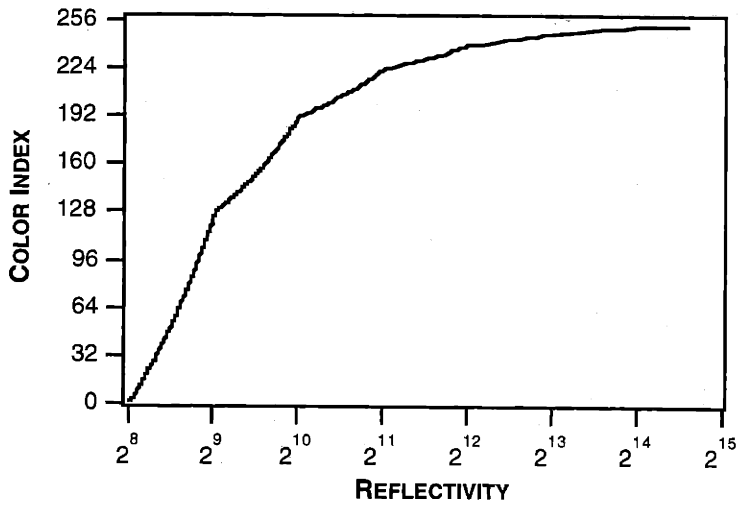

FIGURE 4-2. Approximate logarithmic transform.

The true and not the approximate logarithm was used for the post-processing and display of all images after data acquisition.

4.3 Cross-Correlation Scan Registration

Since the nominal axial resolution of OCT is 10 μm, images are highly sensitive to artifacts caused by eye motion in the axial direction during the data acquisition period, which is 2.5 seconds for a typical image consisting of 100 A-scans (one-dimensional axial profiles of reflectivity versus distance). Involuntary axial eye motions may be due to respiration, heart beat, tremor, and vibration of the headrest. An imaging processing algorithm was developed to mitigate the effects of axial motion. This algorithm assumes that structural variations in the transverse direction are small compared to those in the longitudinal direction and that no significant motion occurs on the time scale of a single A-scan (25 ms).

4.3.1 Cross-Correlation Algorithm

Since motion is assumed to occur on the time scale of image acquisition rather than on the time scale of a single A-scan, the effect of axial motion is to cause longitudinal shifts in the position of each A-scan. The motion may be compensated for by estimating the artifactual shift in each A-scan and then using this estimate to re-register the axial position of each scan in the image. Let R_{ij} be the acquired OCT image matrix of reflectivity (expressed on a logarithmic scale), where the row index i denotes the longitudinal pixel in each A-scan and the column index j corresponds to each A-scan (Figure 4-3). The cross-correlation between a pair of

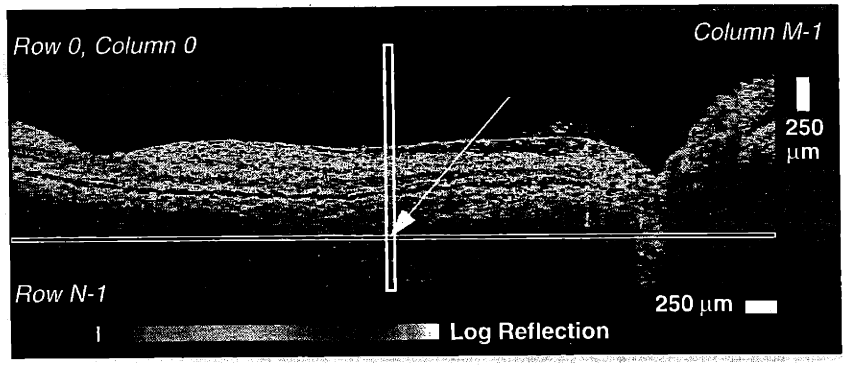

FIGURE 4-3. Reflectivity matrix corresponding to an OCT image of the fovea and optic disc.

adjacent A-scans $j-1$ and j is defined as

$$\text{xcorr}_{j-1,\,j}(k) = \sum_{i\,=\,\text{all rows}} R_{i,\,j-1} R_{i+k,\,j}. \tag{4.3}$$

The cross-correlation involves sliding (up and down in row-space) the j^{th} A-scan relative to the $j-1^{\text{th}}$ A-scan and summing up, for each row that overlaps, the products of the reflectivities of the two A-scans for that row. The cross-correlation is a function of the variable k which measures the offset in rows (during the "sliding") between the two A-scans. Figure 4-4 visually depicts the cross-correlation for a pair of A-scans, which for the purposes of illustration,

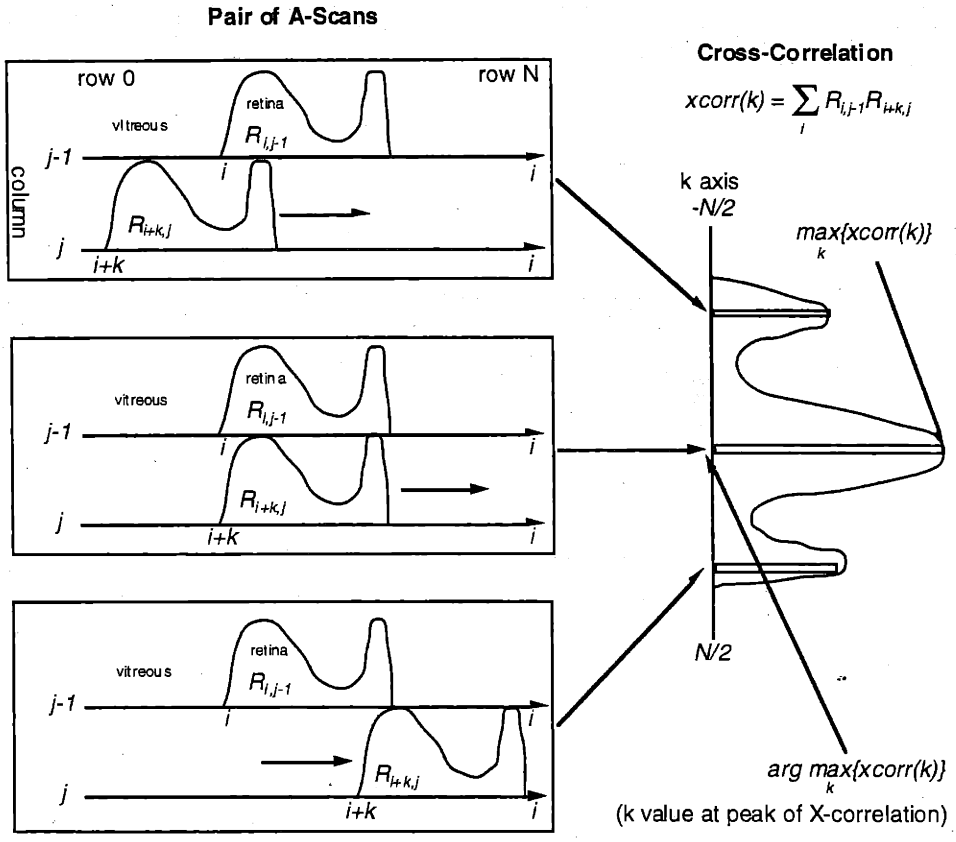

FIGURE 4-4. Cross-correlation of a single pair of adjacent A-scans.

are now displayed horizontally (with the row index 0 on the left and row N on the right). In Figure 4-4, the reflectivity (*i.e.* the false color value shown in Figure 4-3) is plotted as a function of the row number which is displayed horizontally (corresponding to increasing depth in Figure 4-3) for a pair of A-scans. In Figure 4-4, the lower (j^{th}) A-scan is slid left-to-right (in row-space) across the upper ($j-1^{th}$) A-scan which is depicted for three different offsets k (as one moves down in the figure). A plot of the cross-correlation function (which is a function of the different offsets k) appears on the right in the Figure 4-4. The variable k increases as one moves down in the figure. The peak of the cross-correlation function indicates where the two A-scans overlap the most. The logarithm of the reflectivity rather than the true reflectivity is correlated in order to increase the weighting from minimally reflective tissue layers.

Let C_j be a vector which describes the retinal contour (*i.e.* the actual retinal surface height as a function of the A-scan position j). An estimate of the motion corrupted retinal surface contour vector $\tilde{C}_j$ may be recursively constructed from the cross-correlation for each successive pair of A-scans in the image as follows:

$$\tilde{C}_j = \tilde{C}_{j-1} + \arg\max_k \{\mathrm{xcorr}_{j-1,j}(k)\}$$
$$\tilde{C}_0 = 0 \qquad (4.4)$$

where the argument maximum (*arg max*) function returns the offset k which corresponds to the peak value of the cross-correlation, as shown in Figure 4-4. Thus, each pair of adjacent A-scans in the image is cross-correlated to find the offset k of maximum overlap or similarity between the scans. These optimal offsets for each pair of A-scans are recursively added together to produce the motion corrupted contour estimate.

An estimate of the true retinal surface contour C_j may be obtained from $\tilde{C}_j$ by low-pass filtering of $\tilde{C}_j$ if the transverse variation in image features is small compared to contour variations created by movement. The difference between $\tilde{C}_j$ and its filtered counterpart C_j indicates the number of pixels in the longitudinal direction that each A-scan must be shifted to (presumably) remove the effects of axial motion. An example of the cross-correlation procedure on actual image data is given in Section 4.3.3.

The cross-correlation concept is an adaptation of the familiar matched-filter concept in communications theory, which is used to estimate the arrival time of a known deterministic signal embedded in random noise. The matched-filter, which essentially cross-correlates the incoming corrupted signal with its ideal counterpart, is the optimal maximum likelihood estimator in the case of additive white gaussian noise [60].

4.3.2 Cross-Correlation Implementation

The complexity of the cross-correlation re-registration algorithm goes as $O(N^2M)$ where N is the number of rows or longitudinal pixels in the image, and M is the number of columns or A-scans. Two strategies may be employed to reduce computation time. First, and most importantly, the cross-correlation step may be performed over a limited, fixed range Δk of offsets if the amplitude of the eye motion is also limited. This significantly reduces the complexity of the algorithm to $O(NM)$ which is linear in image area NM. For a given image area, the computation time is approximately reduced to $2\Delta k/N$ of the time required without limiting the offset. In practice, this results in about a 96% time reduction for the typical values $N = 500$ and $\Delta k = 10$.

Since much of the image area remains unused, an additional computational savings may be realized trimming the unused edges of each A-scan before cross-correlation. One might expect to achieve a substantial reduction in computation time because in most cases of retinal imaging less than 1 mm of the 2.6 mm axial scan length is occupied by the actual image. Therefore, a greater than 60% savings should be obtained because N is effectively smaller. In practice, however, determining the useful boundaries of each A-scan can be difficult. A simple thresholding method can either lead to underestimation of the usable length if the threshold is set too high (or the SNR of A-scan is too weak), or to overestimation of the usable length if the threshold is set too low (and large noise spikes are considered as parts of the image). Since underestimation of the usable length might potentially lead to inaccurate cross-correlations, a threshold which overestimated the length was chosen. This reduced the expected computational savings.

Digital low-pass filtering of the contour estimate was accomplished by convolution with a 21 element Blackman windowed finite-impulse-response (FIR) filter [78]. Several cut-off frequencies were provided which could be selected by the user, including 0, $\pi/25$, $\pi/10$, and $\pi/5$ radians (Figure 4-5). As usual 2π radians corresponded to the sampling frequency ω_s which was normally 40 Hz (the reference mirror repetition rate).

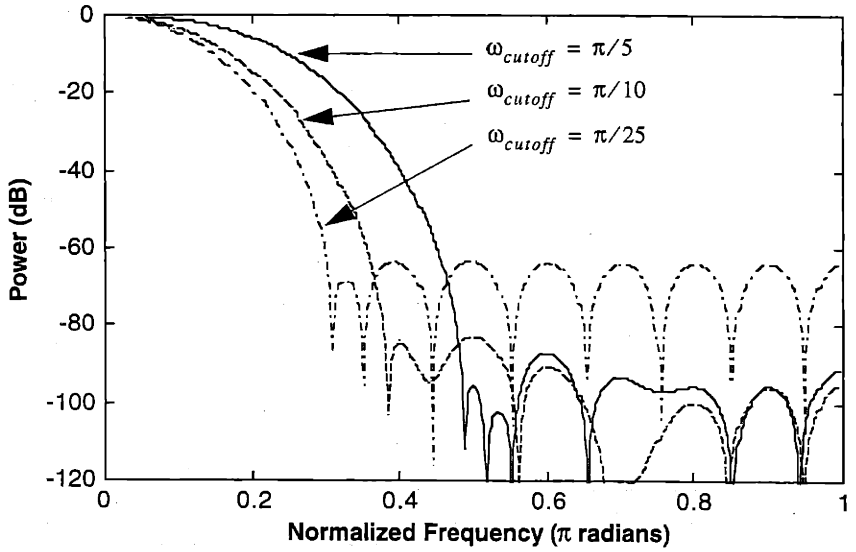

FIGURE 4-5. FIR filters used for low-pass filtering.

4.3.3 Experimental Eye Motion Spectra

Figure 4-6 shows an OCT acquired through a healthy fovea which has not been corrected for axial motion. The OCT contains 512 A-scans, or pixel columns, and was acquired in

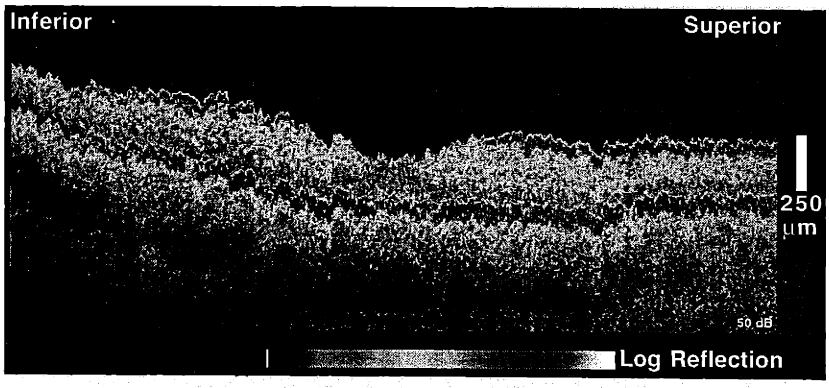

FIGURE 4-6. OCT uncorrected for axial motion.

12.8 seconds. The scan is significantly longer than OCTs normally obtained from patients, which normally consist of 100 A-scans acquired in 2.5 seconds. The longitudinal eye motion, which is significant over the time period of the extended scan, causes high spatial frequency variations in the axial position of each A-scan. A large amplitude low-frequency displacement is also evident, especially inferior to the fovea. Figure 4-7 shows the same OCT after cross-correlation scan registration, with a cut-off frequency of 0 Hz. The layered structure of the retina

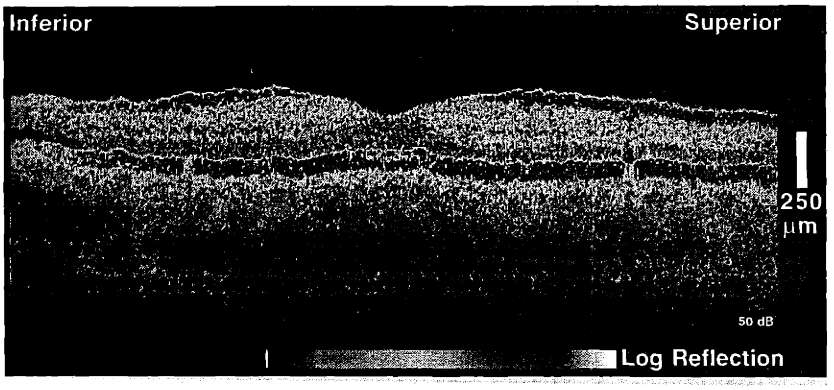

FIGURE 4-7. OCT in Figure 4-6 after cross-correlation scan registration.

is more apparent, including the separation between the retinal pigment epithelium and choriocapillaris directly beneath the fovea. Retinal blood vessels are clearly visible both inferior and superior to the fovea which were not as clearly demarcated in the unfiltered image.

Figure 4-8 displays the contour estimate, as determined by successive cross-correlation of adjacent A-scans according to Equation (4.4), before and after low-pass filtering for the OCT in Figure 4-6.

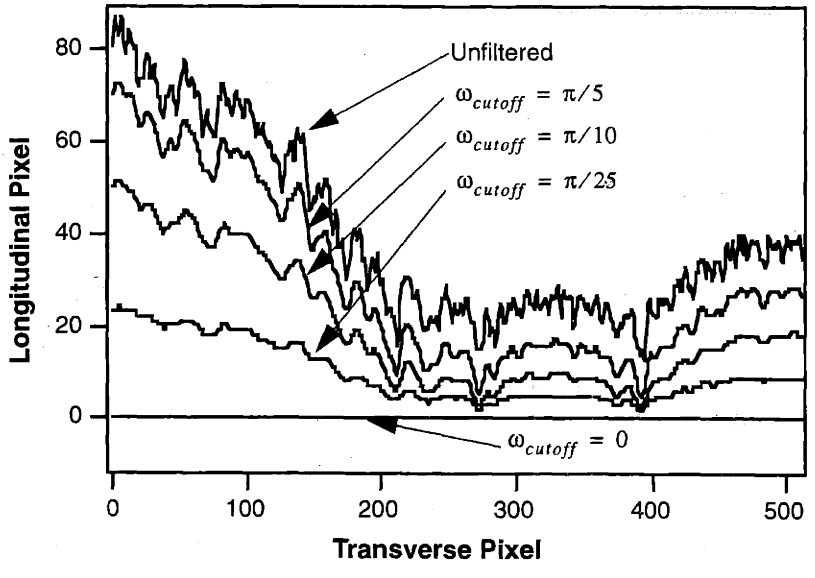

FIGURE 4-8. Unfiltered and filtered contour estimate from Figure 4-6.

The cross-correlation contour estimate enabled the power spectra of the axial eye movement to be investigated. Three OCTs were acquired from each of three healthy volunteers. The cross-correlation method was used to provide an estimate of the axial motion, resulting in nine 512 point contours. The frequency spectrum for each contour was computed applying a 512 point Hamming window followed by a 2048 point FFT. The corresponding fre-

quency resolution was 0.08 Hz. Figure 4-9 shows the average of these nine spectra plotted on a logarithmic scale after normalization of the y-axis to units of microns of axial displacement.

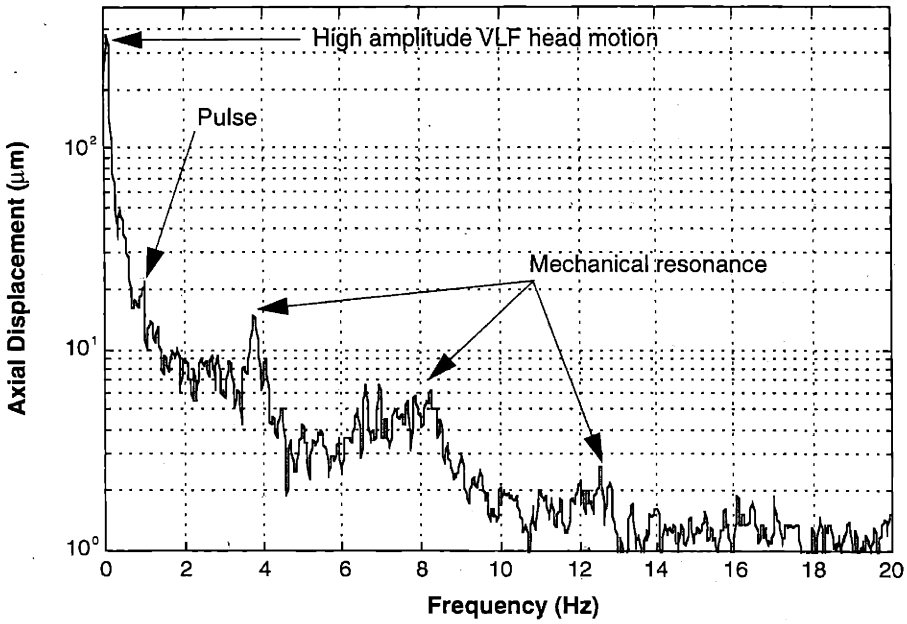

FIGURE 4-9. Spectrum of axial eye motion.

Note that the axial displacement displays an approximate $1/f$ character which is dominated by very low-frequency motion. The low-frequency component most likely corresponds to high amplitude head motion due to involuntary muscle movements over long time periods. Figure 4-9 shows that this motion is on the scale of a millimeter. The axial displacement spectrum descends below 2 μm at approximately 10 Hz. Thus, an OCT image would have to be acquired in about 100 ms to completely freeze ocular motion. A narrow peak at approximately 1 Hz most likely corresponds to axial motion caused by intraocular blood flow and associated pulsations. The amplitude of this motion is about 20 μm. Finally, three peaks are noted at 4, 8, and 12 Hz. A possible source for these harmonically related peaks is the resonance frequency of the slit-lamp headrest.

4.3.4 A-Scan Interleaving

The cross-correlation algorithm assumes that the frequency components of axial eye motion can be separated from normal variations in retinal contour by low-pass filtering. This assumption will become invalid as faster OCT systems are developed. With a faster scanning rate, the effective temporal frequency of spatial retinal contour variations is increased; however, the frequency of axial eye movements remains the same. If the spectrum of axial motion overlaps the spectrum of retinal contour variations, then removal of axial motion by filtering becomes impossible.

Interleaving the scanning pattern on the retina provides a means of addressing this problem. With interleaving, A-scans are acquired in non-sequential transverse positions on the retina. For example, every third transverse pixel on the retina might be sampled starting from the first pixel (*i.e.* #1, 4, 7, ...), followed by every third pixel starting at the second pixel (*i.e.* #2, 5, 8, ...), followed by every third pixel starting at the third pixel (*i.e.* #3, 6, 9, ...). If the pixels are finally displayed in their correct order (*i.e.* #1, 2, 3, ...), then the frequency of spatial features remains unchanged. However, the spectrum of axial eye movements is aliased to higher frequencies since this spectrum has been effectively downsampled by the interleaving.

The effects of interleaving on the temporal spectrum of eye motion may be best understood visually with reference to Figures 4-10 and 4-11. Figure 4-10 depicts the process of interleaving in the time domain while Figure 4-11 provides the equivalent frequency domain description. Assume that the axial eye motion is a continuous function of which we have acquired N sequential samples at rate $\omega_s = 2\pi/T$ rad/s. (Figure 4-10A). Let the continuous function have a bandwidth of ω_c rad/s. Then, the frequency domain representation of the sampled function, shown in Figure 4-11A, is given by the discrete-time Fourier transform (DTFT). Without loss of generality, let us represent the DTFT by a rectangular function with amplitude A, bandlimited to $\Omega_c = \omega_c T$ radians. (Recall that the sampling frequency ω_s corresponds to a frequency of 2π in the discrete-time Fourier domain).

The first transformation step is to periodically replicate the sampled signal in the time-domain (Figure 4-10B). Periodic replication in time corresponds to sampling in frequency (Figure 4-11B). The frequency samples are each spaced by $2\pi/N$ radians. The second transformation step is to downsample the periodically replicated signal in time (Figure 4-10C) by factor i, which we shall call the *interleaving factor.* After downsampling, the samples in time are spaced by $T' = iT$. In frequency, the downsampling corresponds to a stretching of the frequency axis and a scaling of the amplitude axis (Figure 4-11C). The stretched bandwidth is $i\Omega_c$ radians. To preserve signal energy, the amplitude is correspondingly scaled down to A/i. Note that the separation between frequency samples also increases to $i2\pi/N$ radians.

Aliasing of the signal in frequency occurs if $i\Omega_c > \pi$, which provides an upper limit on the interleaving factor i. The aliasing may be tolerable, however, as discussed later. The final transformation involves windowing in time to recover a sequence of length N followed by normalization of the time axis so that the sampling period is again T (Figure 4-10D). In frequency, this corresponds to periodic convolution with a sinc function (Figure 4-11D). The width of the main lobe of the sinc function is $2\pi/N$, which is a factor of i less than the separation between the samples in frequency.

The effect of interleaving then is to approximately stretch the frequency bandwidth (plus or minus a few sinc functions) of the axial motion noise while leaving the spectrum of the actual retinal contour unaffected. If the axial motion spectrum is assumed to be rectangular, then interleaving by a factor of i should reduce the noise in the passband by the same factor due to scaling of the amplitude axis. Aliasing is prevented if

$$2i\frac{\omega_c}{\omega_s} < 1 \tag{4.5}$$

where ω_c is the bandlimit of the axial motion noise and ω_s is the reference mirror repetition rate. In Section 4.3.3, the axial motion noise was found to be approximately bandlimited to 10 Hz. Therefore, with a sampling frequency of 40 Hz, the optimal interleaving factor (assuming a rectangular noise spectrum) is $i = 2$. Faster OCT instruments will of course be able to use more interleaving and can potentially achieve more noise reduction.

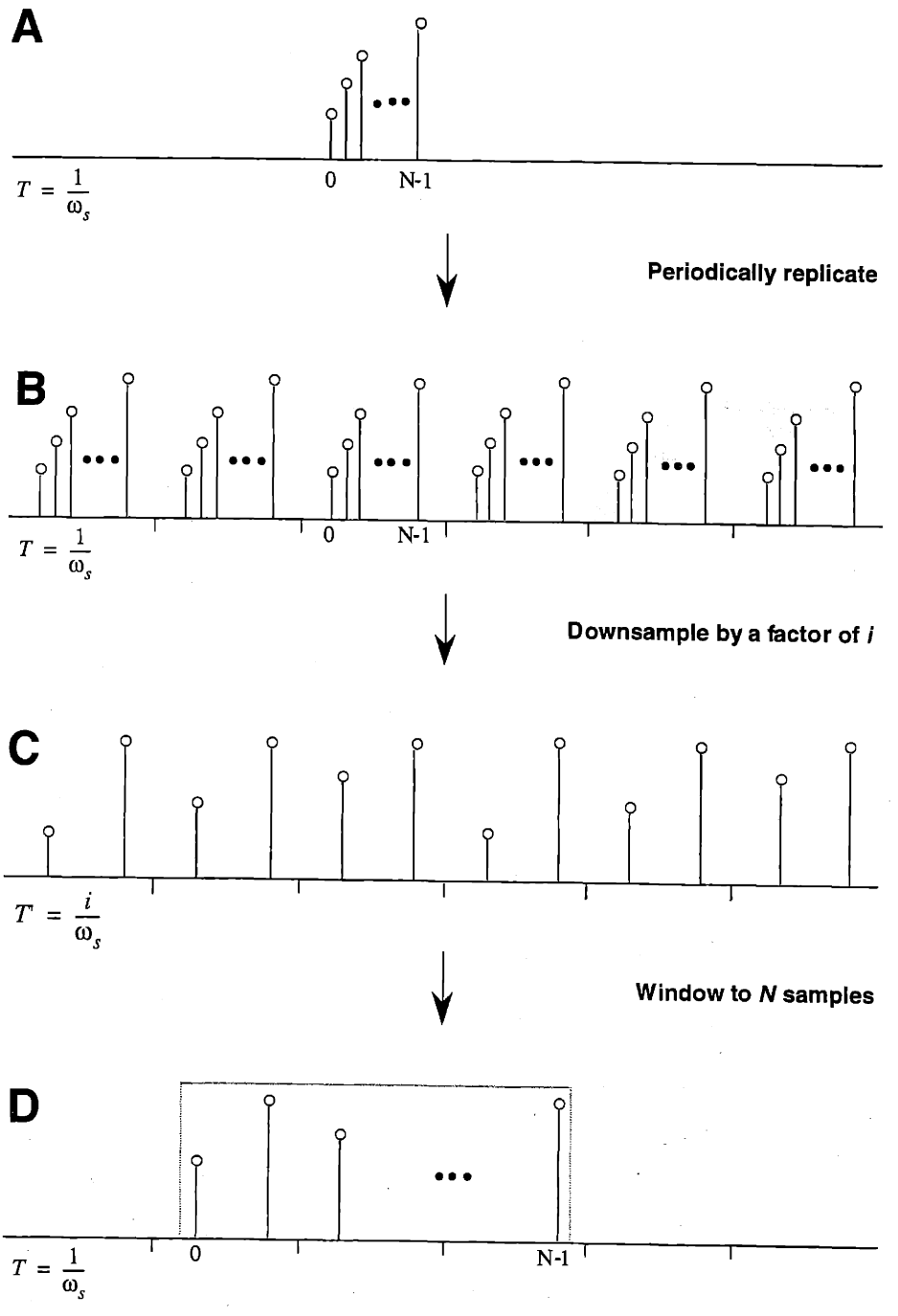

FIGURE 4-10. Time-domain description of A-scan interleaving.

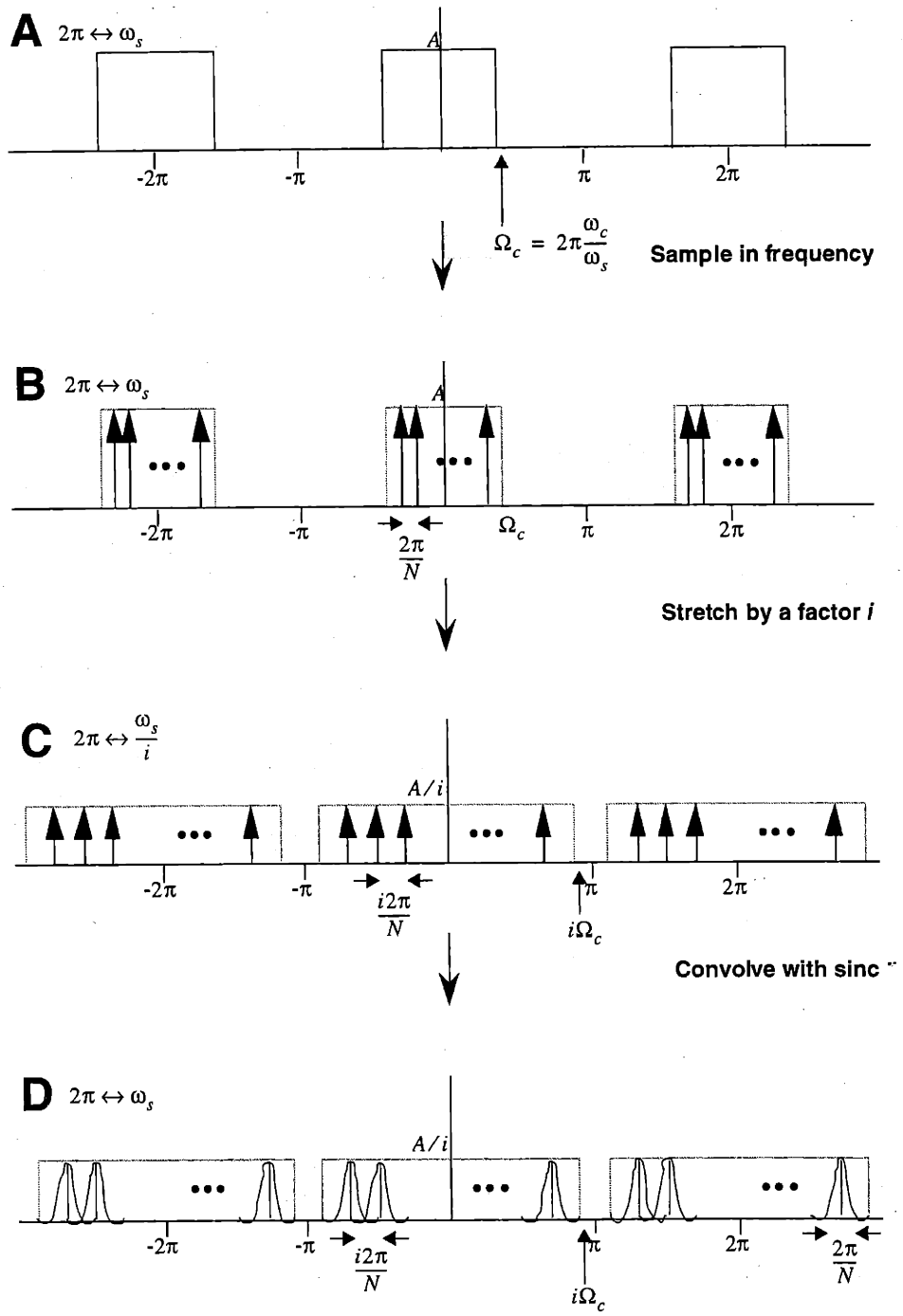

FIGURE 4-11. Frequency-domain description of A-scan interleaving.

For an arbitrary noise spectra function $N(\omega)$, aliasing can be advantageous if the noise power decays rapidly with increasing frequency. This is the case if stretching $N(\omega)$ removes more noise from the pass-band of the filter used to smooth the contour estimate than would enter by aliasing. In general, the optimal interleaving factor i is chosen to minimize the noise in the passband, *i.e.*, to minimize

$$\sum_{k=-\infty}^{\infty} \int_0^{\omega_{lp}} \frac{1}{i} N\left(\frac{\omega - k\omega_s}{i}\right) d\omega \tag{4.6}$$

where ω_{lp} is low-pass cutoff of an ideal, rectangular filter used to separate axial motion noise from the actual retinal contour.

4.4 Cropping

A long axial scanning length was chosen to facilitate the alignment of the reference arm, which must be matched in absolute distance to the position of the retina. For a normal retina, the actual image occupies less than 1 mm of the 2.6 mm axial scan length. The OCTs were automatically cropped in the axial direction for display purposes. First, the image (usually 100 A-scans by 500 longitudinal pixels) was divided into blocks of 10 A-scans by 20 longitudinal pixels. A block was considered to be full (*i.e.* contain actual reflectivity data as opposed to being composed of background noise) if its mean signal level was at least 3 dB greater than the thresholded image noise floor of 6 dB. The image was then cropped to the smallest one of four preset lengths which contained all the full blocks.

4.5 Bilinear Interpolation

Bilinear interpolation was used to map pixels of reflectivity occurring on an $M \times N$ data grid (usually 100×250) to a $P \times Q$ grid (usually 600×117) on the screen. Thus, data expansion usually occurred in the horizontal (A-scan) direction, while data compression usually occurred vertical (axial) direction. In bilinear interpolation, the reflectivity of each point i in the screen grid is computed from a linear combination of the reflectivities from the surrounding four points in the data grid (Figure 4-12) as

$$R_i = \left(1 - \frac{\delta x}{\Delta x}\right)\left(1 - \frac{\delta y}{\Delta y}\right)R_1 + \left(\frac{\delta x}{\Delta x}\right)\left(1 - \frac{\delta y}{\Delta y}\right)R_2 + \left(1 - \frac{\delta x}{\Delta x}\right)\left(\frac{\delta y}{\Delta y}\right)R_3 + \left(\frac{\delta x}{\Delta x}\right)\left(\frac{\delta y}{\Delta y}\right)R_4 . \tag{4.7}$$

Bilinear interpolation preserves actual data values if the location of R_i coincides with a point on the data grid. It is also important to note that data compression does not result in pure decimation unless the data grid size is an integer multiple of the screen grid size. If duplicate computations are avoided, the $4PQ$ number of coefficients (4 coefficients for each screen grid point) in Equation (4.7) can be reduced to $2P + 2Q$ coefficients by precalculation.

The difference between pixel duplication/decimation (Figure 4-13) and bilinear interpolation (Figure 4-14) is illustrated below for a typical OCT containing 100 A-scans by 250 rows of a patient with a macular hole.

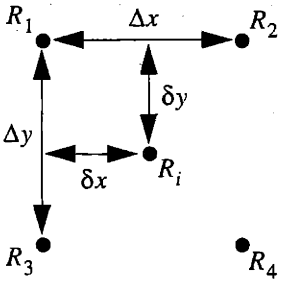

FIGURE 4-12. Geometry of bilinear interpolation in cartesian coordinates.

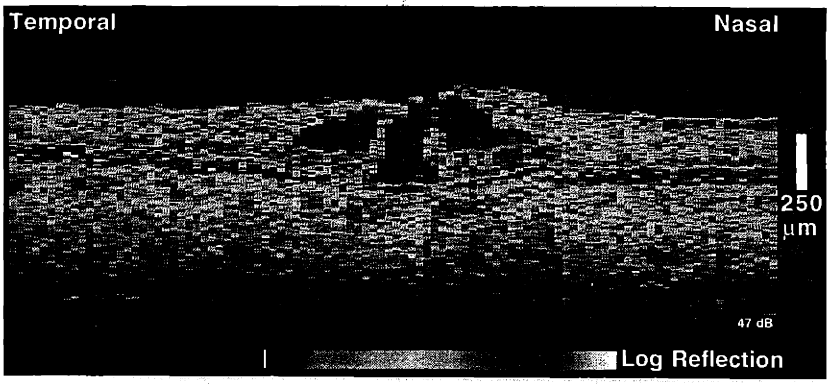

FIGURE 4-13. OCT without bilinear interpolation.

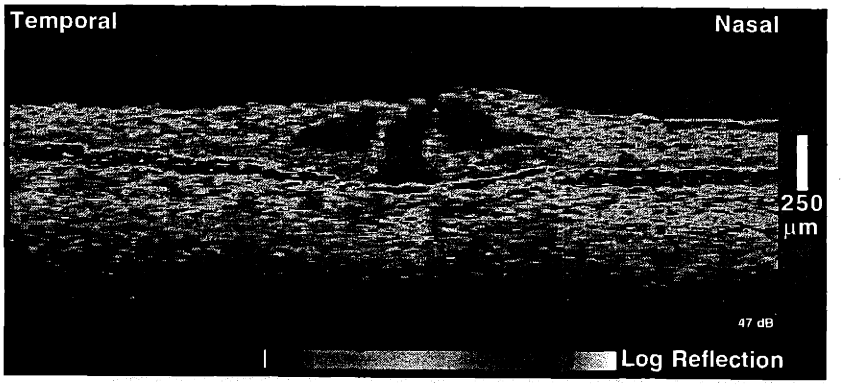

FIGURE 4-14. OCT with bilinear interpolation.

4.6 Retinal Thickness

Algorithms were developed to automatically identify the superficial and deep neurosensory retinal boundaries to permit calculation of retinal thickness. Measurement of retinal thickness is important in quantifying macular edema, or abnormal fluid accumulation within

the neurosensory retina, which often leads to retinal thickening. Macular edema is a potential consequence of many ocular conditions such as diabetic retinopathy, epiretinal membrane formation, ocular inflammation, retinal vascular occlusion, and cataract extraction. It is important to measure macular thickness in order to track the progress of laser photocoagulation treatment for macular edema. Macular thickness measurement might also be a potentially useful screening method for the development of edema, especially in patients with diabetes.

The challenge is to identify the retinal boundaries in the face of varying intraretinal morphology and signal-to-noise conditions. Retinal morphology may be disrupted in many disease states. Diabetic retinopathy in particular often leads to the presence of hard exudate and cyst formation which can lead to abnormally high or low intraretinal reflectivity respectively. Signal-to-noise can vary with optical alignment, cataracts, and other media opacity. In high signal-to-noise conditions and in ocular inflammation, intravitreal reflections might be confused with retinal reflections. In low signal-to-noise conditions, retinal reflections are minimally visible, particularly in the fovea. The signal-to-noise can vary within a given OCT image, for example, if the pupil obstructs part of the scanning beam.

A robust boundary detection algorithm was developed which consists of the following steps: smoothing, edge-detection, and error correction. Special consideration was given to low signal-to-noise conditions.

4.6.1 Smoothing

Speckle noise is associated with any coherent imaging technique involving random media. Image speckles occur in OCT because reflectors spaced closer than a coherence length can either constructively or destructively interfere depending on their exact separation. Speckle noise can be considered to be a random, multiplicative noise. This noise becomes additive after logarithmic transformation. Low-pass filtering or smoothing techniques may then be applied.

The following two-dimensional, center-weighted kernel was chosen for image smoothing:

$$\frac{1}{16}\begin{bmatrix} 1 & 2 & 1 \\ 2 & 4 & 2 \\ 1 & 2 & 1 \end{bmatrix}. \tag{4.8}$$

The kernel was normalized to a volume of unity to preserve signal energy. Five cycles of repeated, two-dimensional convolution with this 3×3 kernel were empirically found to produce a useful level of smoothing. This repeated convolution was equivalent to convolution with a single 11×11 kernel which is plotted in Figure 4-15. The equivalent kernel had the frequency characteristics shown in Figure 4-16 and was approximately a two-dimensional low-pass filter with a cut-off of about 0.1π radians. Note the quite significant ripples in the stop-band which extends to about 0.4π radians in both dimensions. The amplitude of the largest ripple approached 60% of the passband amplitude.

While a filter with a sharper transition and fewer ripples could have been designed, the simple kernel expressed in Equation (4.8) had computational advantages. First, the cut-off frequency or amount of smoothing could easily be adjusted by changing the number of repeated convolutions rather than by redesign of the filter. Second, since every element in the

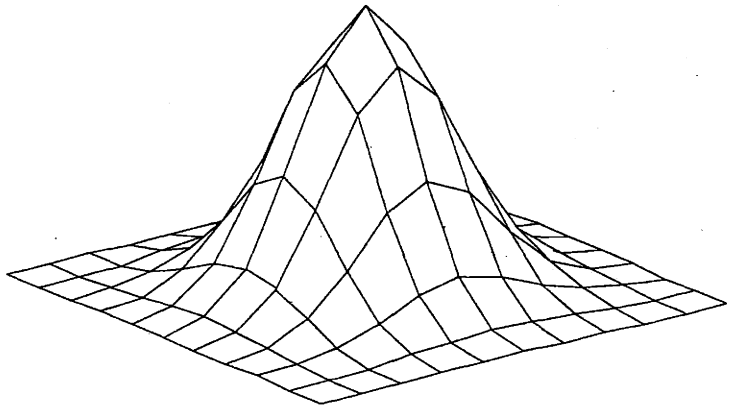

FIGURE 4-15. 11×11 center weighted kernel used for smoothing.

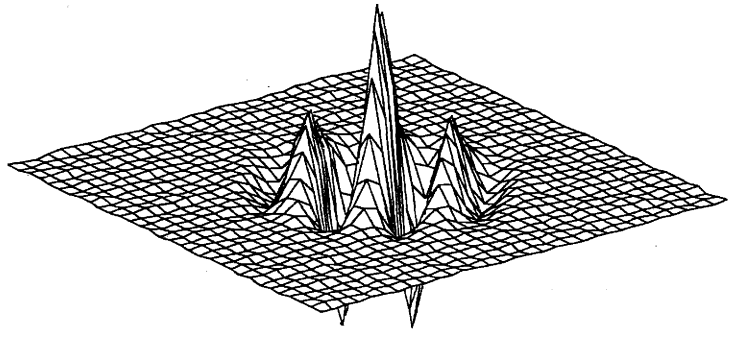

FIGURE 4-16. Frequency domain amplitude of the kernel in Figure 4-15.

kernel could be expressed as a power of two, division operations could be replaced in actual implementation with much faster bit shifting operations. Figures 4-17 and 4-18 show an example of a circular OCT acquired around the optic disc before and after smoothing.

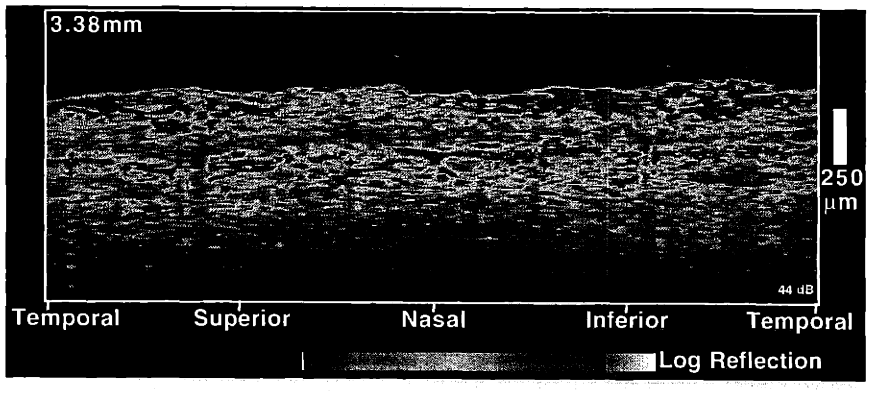

FIGURE 4-17. OCT before smoothing.

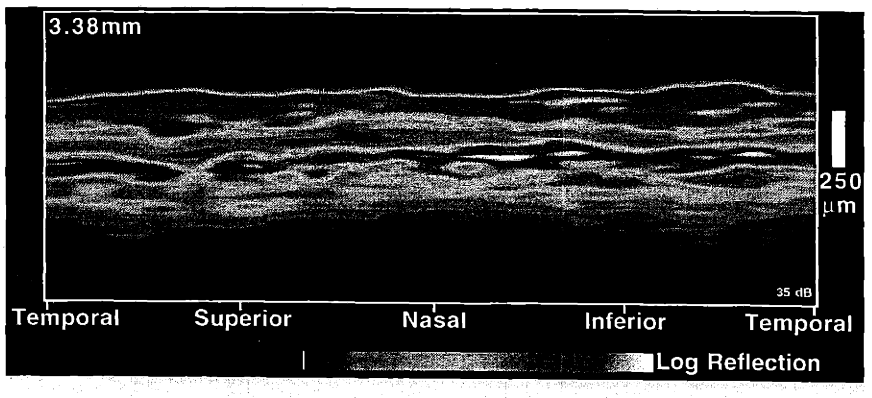

FIGURE 4-18. OCT after smoothing with the kernel in Figure 4-15.

4.6.2 Edge-Detection

A one-dimensional edge-detection kernel was employed after smoothing to compute, approximately, the derivative of reflectivity versus axial distance for each A-scan in the OCT image. The 11 element column vector

$$\begin{bmatrix} -1 & -1 & -1 & -1 & -1 & 0 & 1 & 1 & 1 & 1 & 1 \end{bmatrix}^T \tag{4.9}$$

was convolved with each column vector (A-scan) in the image to identify sharp transitions which might indicate horizontal edges. An 11 instead of a typical 3 element vector was used to reduce the effects of noise (which is generally amplified after this approximate differentiation). An *edge* matrix was produced in which large positive numbers indicated sharp low-to-high transitions in reflectivity and negative numbers indicated high-to-low transitions. An example of such a matrix displayed in false-color is shown in Figure 4-19. Note that the color

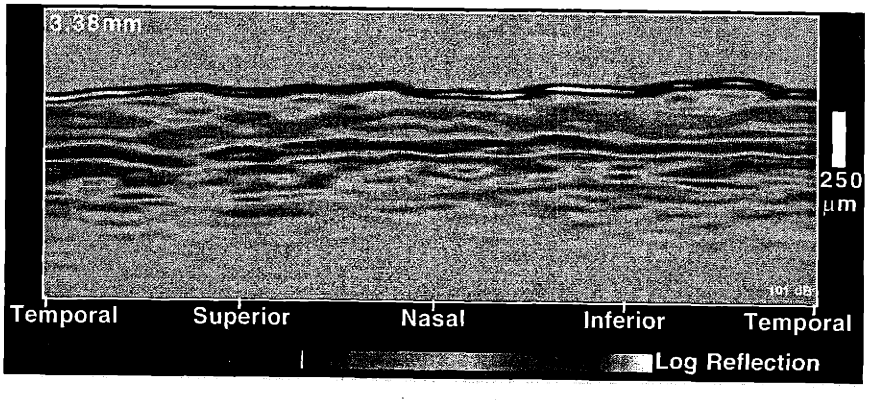

FIGURE 4-19. Edge image corresponding to Figure 4-18.

scale spans the entire range of values. Yellow in the image indicates zero value (no edges). Brighter colors such as red and white indicate positive values (low-to-high edges), and darker colors such as green and blue indicate negative values (high-to-low edges).

The location of the vitreoretinal interface and the retinal pigment epithelium (RPE) define the inner and outer boundaries respectively of the neurosensory retina. These two boundaries are nominally associated with the strongest two edges in each A-scan identified with the kernel (4.9) because of the high contrast in optical reflectivity between (1) the non-reflective vitreous and reflective neurosensory retina, and (2) the minimally reflective photoreceptors and the highly reflective RPE/choriocapillaris.

The strongest edges in each A-scan were identified from each column vector in the edge matrix using peak-detection. A *peak* was defined to be a local maximum in each column which was at least 15 pixels wide (*i.e.* separated from the next closest local maximum by at least 7 pixels). The highest two peaks in each A-scan were identified. The vitreoretinal interface was assumed to occur at the location of the anterior highest peak and the RPE was placed at the location of the posterior peak. The absolute highest peak was equally likely to correspond with either the vitreoretinal interface or the RPE.

In most cases, this procedure identified the retinal boundaries correctly in more than 90% of the A-scans. The error correcting step described in Section 4.6.3 was used to reconstruct the boundaries in the remaining 10% of A-scans. Edge-detection was more effective than threshold identification of the retinal boundaries because edge-detection was independent of the absolute signal level in the image.

4.6.3 Error correction

Errors in the edge-detection procedure described in Section 4.6.2 usually resulted in radical discontinuities in the estimates of both the anterior and posterior boundaries of the neurosensory retina. This might occur, for example, with an abnormal region of high intraretinal reflectivity creating a strong intraretinal boundary. Any abnormal edge which was stronger than either of the two retinal boundaries could have a similar effect. Since the actual retinal boundaries were continuous, errors in the boundaries appeared as discontinuous line segments (Figure 4-20). These errors were identified and corrected using an interpolation and

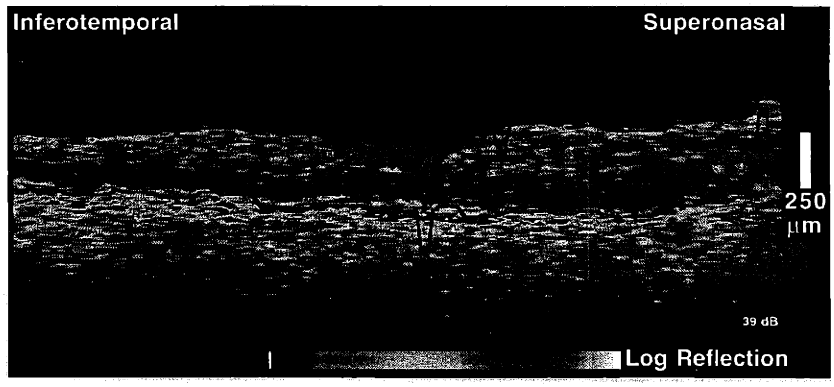

FIGURE 4-20. Retinal profiles before error correction.

local edge-detection algorithm (Figure 4-21). In contrast to the initial phase of edge-detection, this correction procedure used information which was available in both the axial and transverse directions.

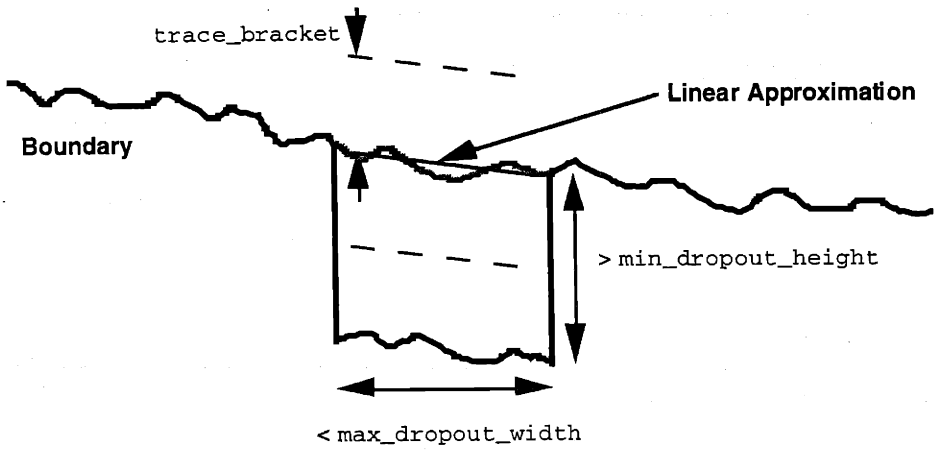

FIGURE 4-21. Dropout identification and error correction.

Discontinuous segments in a retinal boundary, or *dropouts*, were identified by first locating the position of all discontinuities. A discontinuity was indicated when two transversely adjacent pixels in the boundary were separated in longitudinal distance by more than `min_dropout_height` pixels. If two discontinuities were closer in transverse distance than `max_dropout_width` pixels, then a dropout was identified between the discontinuities.

Dropouts were corrected by first approximating the boundary in the region of the dropout using linear interpolation (*i.e.* a straight line was drawn between the discontinuities in the dropout). The position of the actual boundary in the dropout region was then determined by searching each A-scan for the local maximum edge in a strip centered on the straight line approximation. The width of the searchable strip was limited to within `trace_bracket` pixels of the linear approximation to the boundary.

Typical values for a 100 A-scan by 500 row image were `min_dropout_height = 20` pixels, `max_dropout_width = 10` pixels, and `trace_bracket = 15` pixels. Figure 4-22 shows the error corrected retinal profiles for the OCT in Figure 4-20.

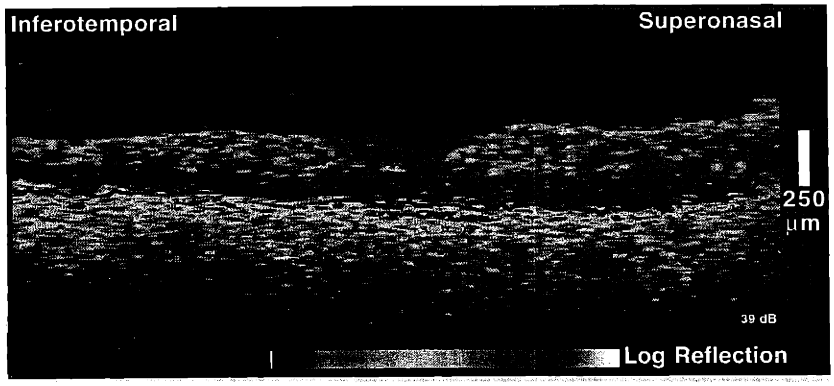

FIGURE 4-22. Retinal profiles in Figure 4-20 after error correction.

4.6.4 Low Signal-to-Noise Conditions

In exceptionally low signal-to-noise conditions, the vitreoretinal interface occasionally did not produce an edge which could be identified using the procedure given in Sections 4.6.2 and 4.6.3. To account for this situation, the location of the vitreoretinal interface was also estimated using a conventional thresholding algorithm. After smoothing according to Section 4.6.1, each A-scan was searched, from anterior to posterior, for the first pixel which was greater than 3 dB above the noise floor. This sensitive criteria usually identified the true vitreoretinal interface in low SNR conditions, but could often be disrupted by non-zero intravitreal reflectivity and noise. The boundary created using this sensitive procedure was then compared to the boundary determined by edge-detection (Figure 4-23).

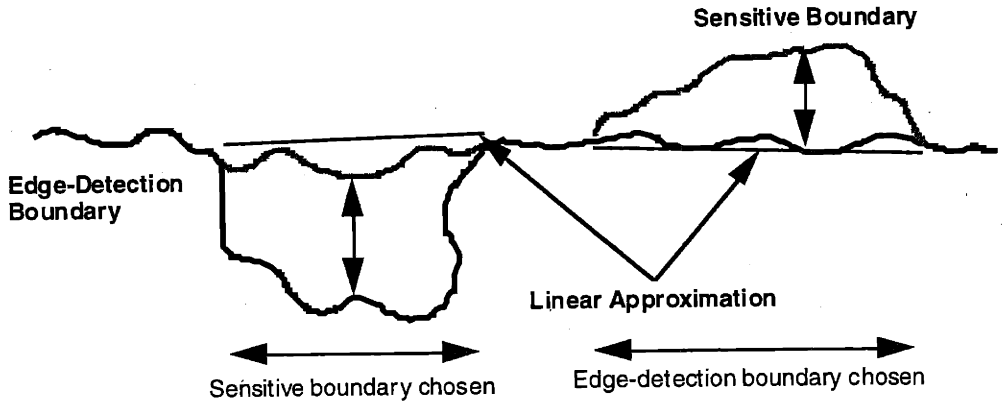

FIGURE 4-23. Boundary selection procedure.

Regions in which the difference between the two boundaries was greater than one pixel were identified. Linear approximation was used to estimate the true boundary in these regions. The boundary which was closer to the linear approximation was then chosen as representative of the true boundary.

In some cases, there was a complete absence of a retinal boundary in some portion of the image. This condition would usually occur with (1) patient blinks which caused a complete loss of signal during the blink, or (2) blood vessels or hard exudate which caused shadowing and loss of the reflections from the RPE and choroid. In these cases, the retinal boundary was estimated in the region of signal loss using linear interpolation Figure 4-24 shows an example of shadowing of the RPE reflection by intraretinal exudate.

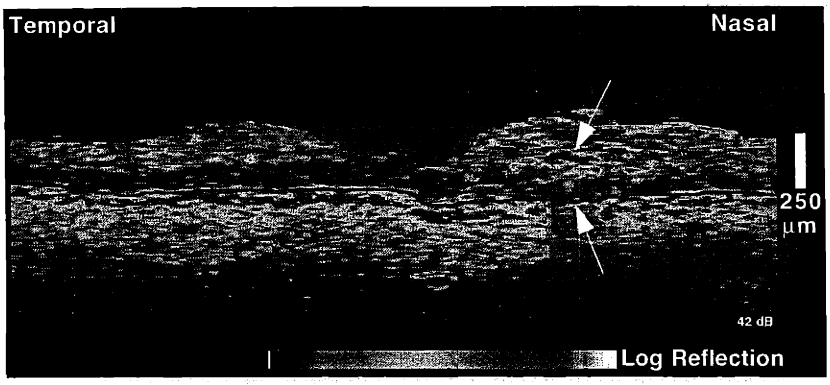

FIGURE 4-24. Shadowing of the RPE by intraretinal exudate.

4.6.5 Assumption of Refractive Index

Retinal thickness was calculated from the number of pixels between the inner and outer retinal boundaries. A constant retinal refractive index of 1.36 was assumed to convert time-of-flight delay to intraretinal distance. This assumption was expected to induce a negligible error in the thickness measurements because the refractive index was expected to deviate no more than 5% from the estimated value (consider that the difference in refractive index between the retina and water is only 2%). A 5% difference in index over the entire retinal thickness of approximately 250 µm would result in a 13 µm error in measurement. This figure is commensurate with the longitudinal resolution of the instrument.

4.7 Retinal Nerve Fiber Layer Thickness

Precise measurement of retinal nerve fiber layer (NFL) thickness may be useful in evaluating patients with glaucoma, in distinguishing between patients with papilledema and crowded optic nerves, and in evaluating other neurodegenerative diseases. A computer algorithm was developed to estimate NFL thickness from circular OCT images acquired in a cylindrical section surrounding the optic disc. The NFL was assumed to correlate with the extent of the highly reflective (and usually "red") layer at the vitreoretinal interface. Again, the challenge was to develop a procedure which was relatively insensitive to changes optical alignment which would affect the signal-to-noise ratio in each image.

Unfortunately, the determination of the NFL boundary was not as straightforward as the determination of retinal thickness. Three threshold based algorithms were developed. Three methods were also developed for determining the threshold, which could vary across each image to account for local variations in signal-to-noise.

4.7.1 Identification of the Photoreceptor Layer

The anterior boundary of the NFL was assumed to lie at the vitreoretinal interface. The comparatively thin (< 10 µm) inner limiting membrane was neglected. The posterior boundary of the NFL was known to occur somewhere between the vitreoretinal interface and the location of the photoreceptor layer. After the inner and outer boundaries of the neurosensory retina were determined according to the algorithm outlined in Section 4.6, the photoreceptor layer was identified using one of two methods.

In the first method, the location of the photoreceptor layer was established for each A-scan as the position of minimum reflectivity (after smoothing according to Section 4.6.1) within the posterior 1/3 of the area between the vitreoretinal interface and the RPE. In the second method, the center of the photoreceptor layer was assumed to lie 50 μm anterior to the RPE. While the first method was computationally more complex, it was not as sensitive to potential errors in the RPE location and therefore slightly more robust.

4.7.2 Methods for Determining NFL Thickness

Three threshold based algorithms, hereafter denoted *edge*, *count*, or *sum*, were investigated to estimate NFL thickness. Thresholds were computed (described in more detail in Section 4.7.3) individually for each image to provide consistency over different signal-to-noise conditions. All algorithms operated on individual A-scans separately. The edge algorithm was, loosely, a derivative based algorithm and operated on the smoothed (see Section 4.6.1) reflectivity matrix. In contrast, the count and sum algorithms were integration based methods and operated on the unsmoothed reflectivity matrix. Examples of each of the three algorithms run on the same OCT are depicted in Figures 4-26, 4-27, and 4-28.

Edge Algorithm

In the *edge* algorithm, pixels in each smoothed A-scan were evaluated in an upwards fashion starting at the photoreceptor layer until a super-threshold reflectivity was encountered. The location of this first super-threshold pixel established the initial location of the posterior NFL boundary. Then, starting at the vitreoretinal interface, pixels were evaluated in a downwards fashion until the first sub-threshold pixel after a super-threshold pixel was located. If the pixels located by the two searches were adjacent to each other, then the posterior NFL boundary was confirmed. If the two pixels were separated, then one of these pixels was chosen as the location of the NFL boundary based on the average reflectivity of the intervening pixels. If the average reflectivity exceeded the threshold, then the deeper pixel was selected; otherwise, the shallower pixel was selected. Figure 4-25 provides a flowchart of this procedure.

Both a downward and an upward search were performed to reduce potential variability due to spurious intraretinal reflections. Since the *edge* algorithm determined the NFL thickness by locating a boundary, this method nominally considered the area occupied by blood vessels located within the NFL as contributing to the NFL thickness. Figure 4-26 shows an example of the NFL boundary determined by the *edge* algorithm. The threshold was selected to be 15 dB below the filtered maximum reflectivity in the both the neurosensory retina and choroid (see Section 4.7.3 for more information on threshold calculation). In the image, the vitreoretinal interface is demarcated with a white line, while the posterior boundary of the NFL and the RPE are demarcated with blue lines.

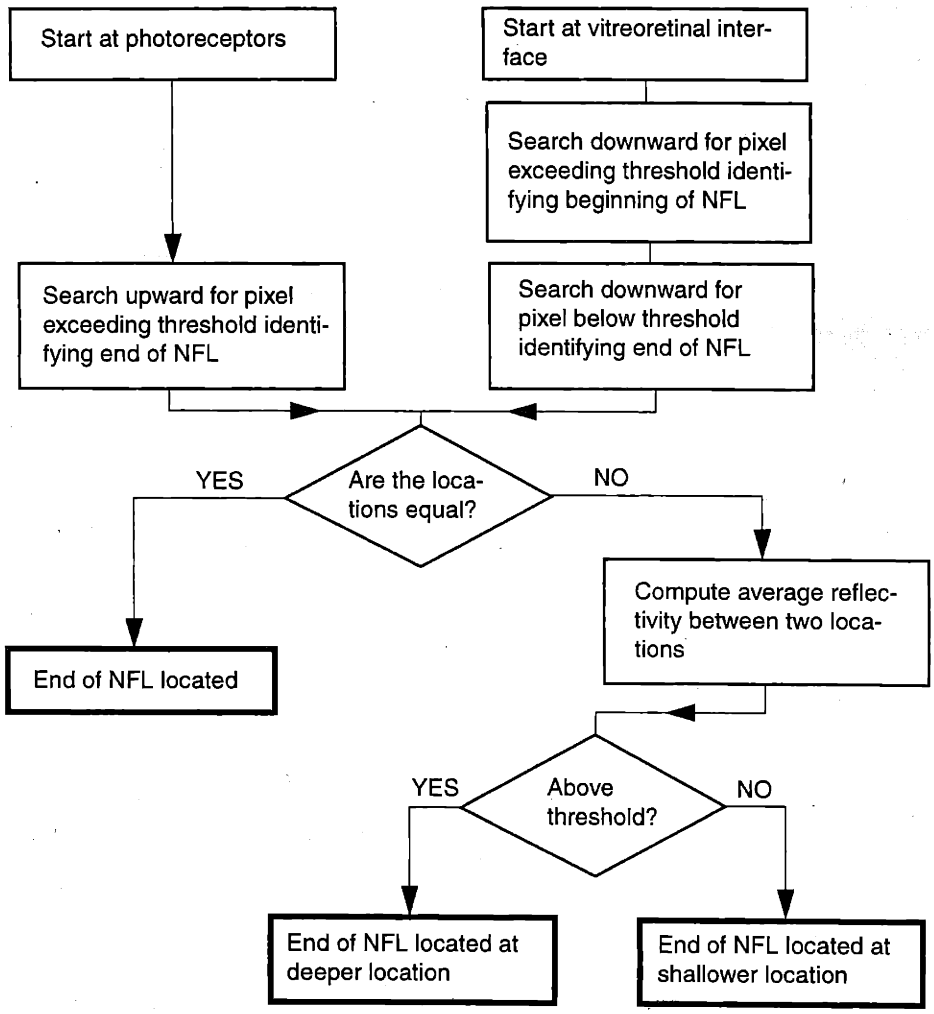

FIGURE 4-25. Edge algorithm flowchart.

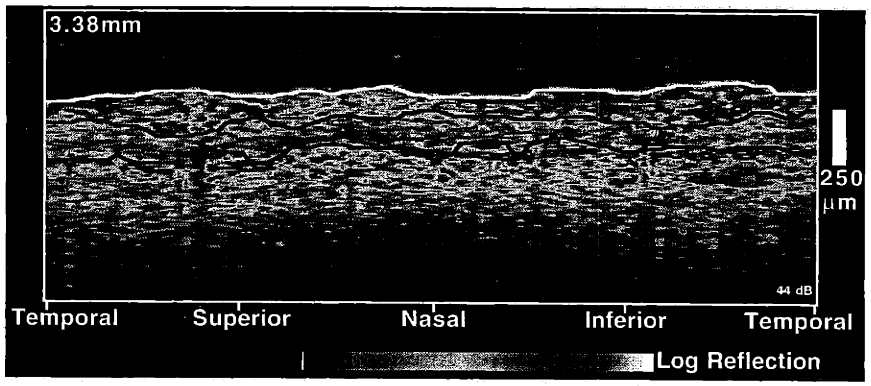

FIGURE 4-26. NFL thickness determined by the *edge* algorithm

Count Algorithm

For each A-scan, the *count* algorithm considered the total number of super-threshold pixels between the vitreoretinal interface and photoreceptor layer as indicative of the NFL thickness (in units of pixels). Counting was performed on the original, unsmoothed data. The count algorithm nominally did not include the area of intraretinal blood vessels in its estimation of NFL area. Figure 4-27 shows an example of the NFL boundary determined by the count algorithm. The threshold for each A-scan was chosen to be 15 dB less than the filtered maximum reflectivity in both the neurosensory retina and choroid (see Section 4.7.3 for more details on threshold calculation).

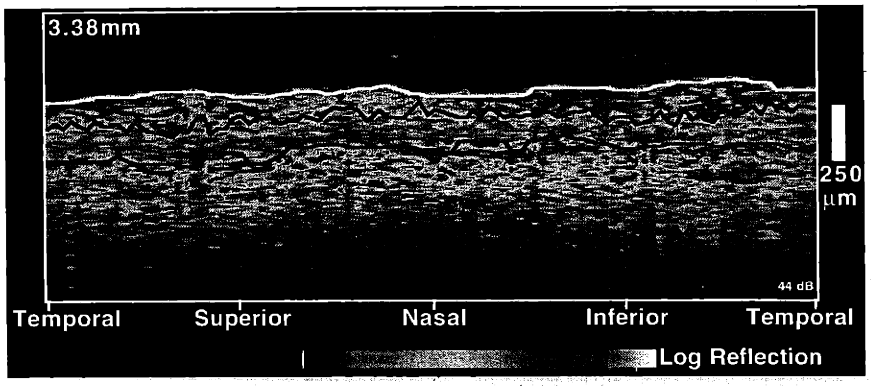

FIGURE 4-27. NFL thickness determined by *count* algorithm.

Sum Algorithm

The *sum* algorithm evaluated the reflectivity R_{ij} of all pixels between the vitreoretinal interface and 50 µm anterior to the photoreceptor layer. Given a particular threshold T_j for each A-scan, the NFL thickness (in units of pixels) for that A-scan was given as

$$\frac{1}{T_j}\sum_i R_{ij}. \tag{4.10}$$

Thus, the *sum* algorithm assumed that the integral of reflectivity above the photoreceptor layer was indicative of NFL thickness. This method was expected to give a result similar to the conventional clinical technique of nerve fiber layer photography, in which NFL thickness is based on a photographic estimate of total reflected, red-free illumination.

Summation according to Equation (4.10) was attempted both in the linear and logarithmic domains of reflectivity. While linear summation was more physically plausible, NFL thickness values were often offset in practice by extremely large values of reflectivity in this method. Logarithmic summation provided more clinically relevant information although the concept of multiplying reflectivities in the linear domain was physically less plausible. Figure 4-28 provides an example of the NFL boundary determined with the sum algorithm. The threshold value for each A-scan was chosen to equal the filtered maximum reflectivity in both the neurosensory retina and choroid (see Section 4.7.3).

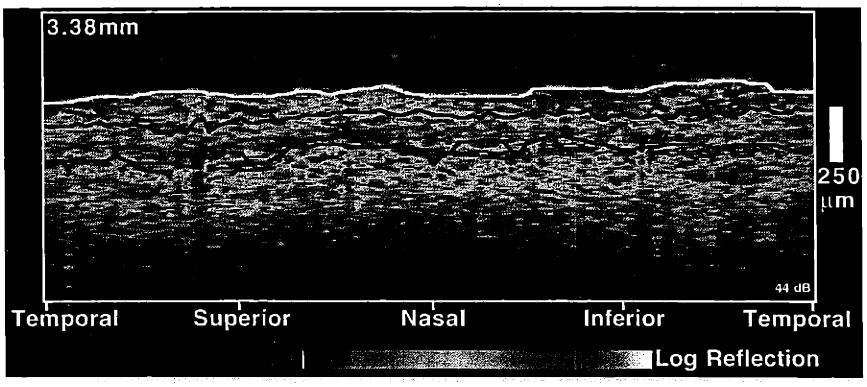

FIGURE 4-28. NFL thickness determined by the *sum* algorithm.

4.7.3 Methods for Determining the Threshold

Threshold determination for each of the three NFL thickness algorithms described in Section 4.7.2 was important to maintain reproducibility and reliability between different patient visits, optical alignment, and variation in optical power. To ensure that the algorithms were not sensitive to variations in signal-to-noise, even within the same OCT image, thresholds were determined for each A-scan individually based on a constant fraction of the local maximum value of reflectivity.

One of three different maximums could be used as a reference value of reflectivity for threshold computation, including (1) the maximum reflection in the entire A-scan (both the neurosensory retina and choroid), (2) the maximum reflection in the neurosensory retina (NSR) only, or (3) the maximum reflection in the RPE, choriocapillaris, and choroid. These methods were found to have different advantages and disadvantages (see Section 7.4). Thresholding based on the NSR maximum alone produced the most reproducible measurements of NFL thickness between patient visits. However, it was also observed that average NFL reflectivity appeared to decline in patients with glaucoma relative to choroidal reflectivity. Thus, thresholding based on the NSR reflection was less sensitive to glaucomatous NFL loss than the other two methods because the difference between NSR and choroidal reflectivity was not considered. Thresholding based on the choroidal reflectivity accounted for this difference, but led to measurements which were more variable between visits since the NSR reflectivity was not perfectly correlated with the choroidal reflectivity. Choosing the threshold based on the absolute maximum reflection in each A-scan provided an intermediate trade-off between reproducibility and sensitivity to glaucomatous change.

After the maximum values for each A-scan were compiled into a row vector, a constant was subtracted (in the logarithmic domain) from each vector element to provide an initial value for the thresholds. The thresholds were then smoothed to remove extreme values by convolution with a 21 element Blackman windowed FIR low-pass filter with a cut-off frequency of $\pi/10$ (Figure 4-5). Since the signal was periodic due to the circular geometry of the OCT (acquired around the optic disc), circular convolution was used.

4.7.4 Report of NFL Thickness

NFL thickness was reported by overall mean, average over quadrants (superior, inferior, temporal, nasal), average over hemifield (superior/inferior hemifield versus temporal/nasal hemifield), average over clock hour, or by each individual A-scan. The boundaries chosen by the computer were also plotted on the OCT image for clinical review.

Multiple OCT images could also be averaged so that an NFL thickness based on more than a single measurement could be reported. Averaging could be performed in one of two manners, either (1) by averaging each image before extraction of NFL thickness, or (2) by calculation of NFL thickness from each image individually before averaging. Method (1) was found to be unreliable due to differences in longitudinal eye position between images. Although the images were registered with each other before averaging using a cross-correlation method, inaccuracies in registration led to abnormally thick measurements of NFL thickness which increased with the total number of images. Therefore, only method (2) was useful in practice. Figure 4-29 displays three consecutive OCTs profiling NFL thickness around the optic disc in a single subject. Figure 4-30 displays an example report of average NFL thickness computed from the scans in Figure 4-29 using method (2). The average NFL boundaries are

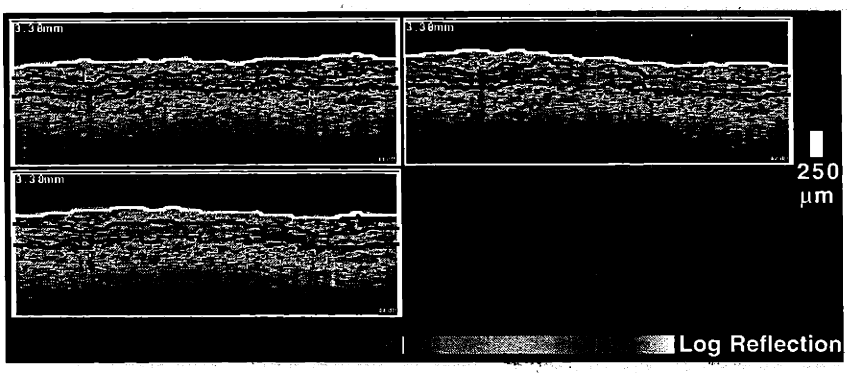

FIGURE 4-29. Three circular OCTs profiling NFL thickness around the optic disc.

overlayed on a single representative OCT by adding the average NFL thickness to the vitreoretinal interface boundary for that particular OCT. Mean values of NFL thickness are annotated below the image. The ratio 148/109 in the report is the average superior/inferior hemifield NFL thickness divided by the average temporal/nasal hemifield thickness. Note that the average NFL boundary in Figure 4-30 differs slightly from the NFL boundary in Figure 4-26, in which a single OCT was used without averaging.

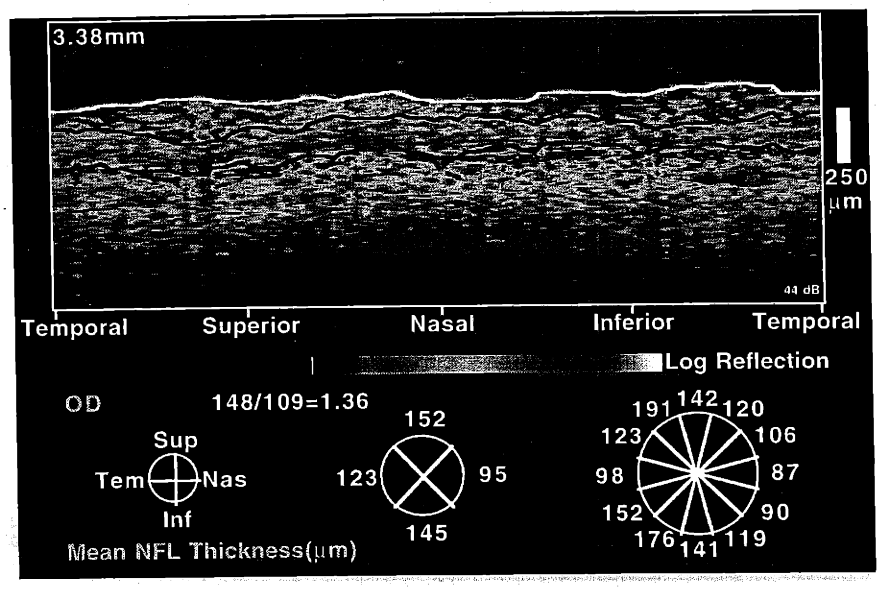

FIGURE 4-30. Average NFL thickness from the three OCTs in Figure 4-29.

4.8 Topographic Mapping

The utility of OCT in clinical practice depends on the ability of the physician to accurately and quickly interpret the OCT results in the context of conventional clinical examination. In the standard technique of slit-lamp biomicroscopy, retinal features are assessed topographically. Therefore, topographic methods of displaying retinal and NFL thickness were developed for OCT which could be directly and intuitively compared with slit-lamp examination. In these methods, multiple OCT cross-sections were acquired in a variety of patterns on the retina to create a 3-dimensional dataset of information. Then, retinal or NFL thickness was extracted from each cross-section to form a 2-dimensional dataset which could be displayed in false color.

4.8.1 Topographic Mapping of Macular Thickness

Measurement of retinal thickness in the macula is particularly important in patients with diabetic macular edema where it is necessary for treatment evaluation to determine whether macular thickening involves the fovea. Thus, a scanning pattern was chosen which (1) concentrated measurements in the central fovea where accurate information was most important, and (2) enabled the distance to the central fovea of any macular thickening to be measured accurately.

Six consecutive OCT scans were obtained at equally spaced angular orientations in a radial spoke pattern centered on the fovea (Figure 4-31). The retinal thickness data was displayed in two complementary manners. For quantitative interpretation, the macula was divided into nine regions including of a central disc of 500 µm diameter (hereafter known as the foveal region), and an inner and outer ring, each divided into four quadrants, with outer diameters of one and two disc diameters respectively (Figure 4-32). An average retinal thickness was reported for each of the nine regions. The mean±standard deviation (SD) central foveal thickness was also recorded for the six A-scans at the intersection of all the tomograms in the central macula. The SD provided a simple estimate of the measurement reproducibility.

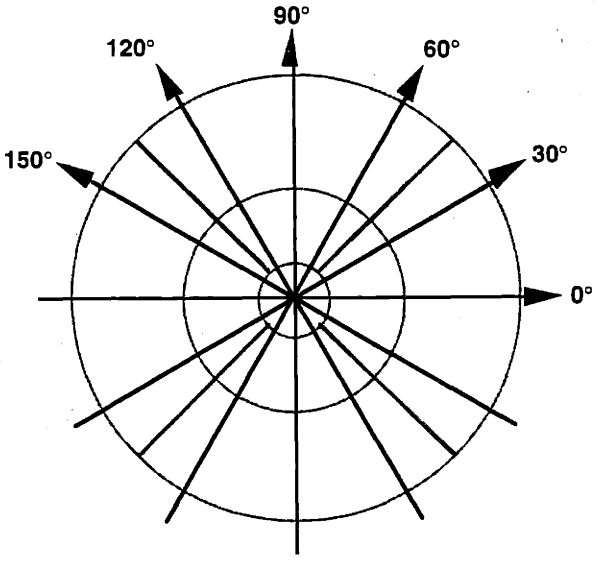

FIGURE 4-31. Radial topographic map scanning protocol.

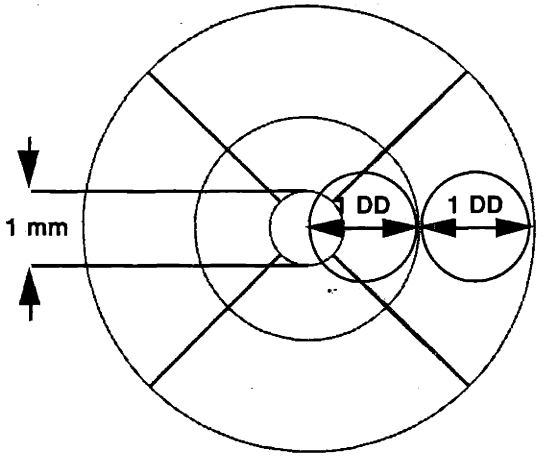

FIGURE 4-32. Radial topographic map regions.

A false-color topographic display was also developed. Macular thickness was converted to a false-color value for every point within two disc diameters from the center, with brighter colors indicating areas of increased retinal thickness. Bilinear interpolation in polar coordinates was performed to estimate thicknesses in the wedges between each OCT scan (Figure 4-33) In exact analogy to the cartesian coordinate case (Equation (4.7)), the reflectivity R_i of an arbitrary pixel is computed from a linear combination of the surrounding four pixels as

$$R_i = \left(1-\frac{\delta\theta}{\Delta\theta}\right)\left(1-\frac{\delta r}{\Delta r}\right)R_1 + \left(\frac{\delta\theta}{\Delta\theta}\right)\left(1-\frac{\delta r}{\Delta r}\right)R_2 + \left(1-\frac{\delta\theta}{\Delta\theta}\right)\left(\frac{\delta r}{\Delta r}\right)R_3 + \left(\frac{\delta\theta}{\Delta\theta}\right)\left(\frac{\delta r}{\Delta r}\right)R_4 . \qquad (4.11)$$

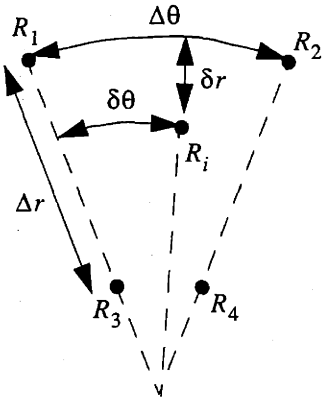

FIGURE 4-33. Geometry of bilinear interpolation in polar coordinates.

Each OCT was centered on the patient's fixation, which was assumed to correspond to the central fovea. In patients with eccentric or imperfect fixation, the examiner could choose to offset each OCT after data acquisition so that the fovea would be positioned centrally. The location of the fovea was estimated from each OCT using a computer algorithm which searched for a local minimum in total intraretinal reflectivity which usually coincided with the relative absence of plexiform layers in the foveal region. For each OCT, the examiner was given a choice of accepting either the center of the OCT (fixation) or the computer estimate of minimum intraretinal reflectivity as the position of the central fovea. This procedure minimized examiner bias while permitting limited user intervention.

For each A-scan comprising the image, the computer calculated the average intraretinal reflectivity in a 20 pixel length (105 μm) strip starting from 4 pixels (20 μm) below the vitreoretinal interface and extending toward the photoreceptor layer. The average intraretinal reflectivities were compiled into a row vector which was then low-passed filtered using a 21 element Blackman windowed FIR filter with a cut-off frequency of $\pi/25$ (Figure 4-5). The position of the central fovea was assigned to the location of the minimum value in the filtered vector.

Figure 4-34 displays an example of the six radial OCTs obtained from a healthy volunteer. The computer generated boundaries at the vitreoretinal interface and RPE are indicated by purple lines. The arrows on each image indicate the position of fixation (the center of each image) and computer estimate of the actual foveal position. An "R" indicates that the examiner chose the computer estimate of the foveal position, while an "F" indicates that fixation was chosen. Figure 4-35 displays the topographic map corresponding the OCT scans illustrated in Figure 4-34.

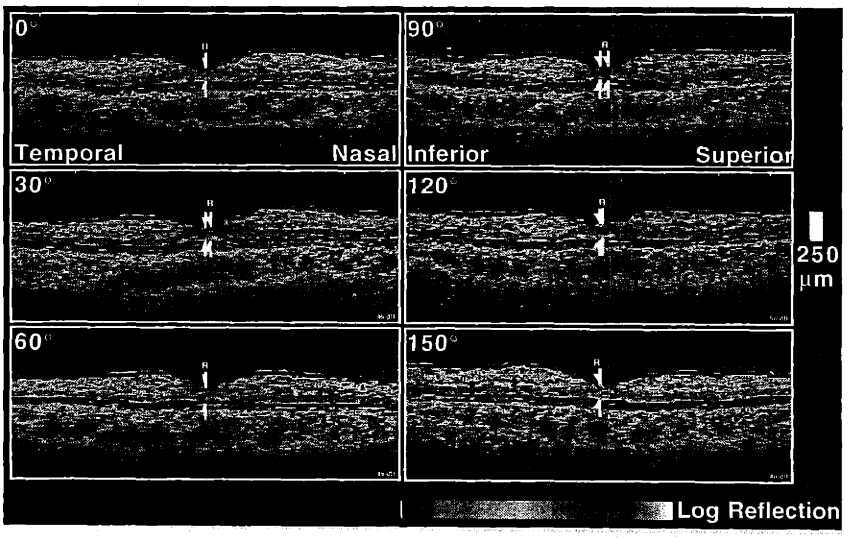

FIGURE 4-34. Radial OCTs from a healthy macula.

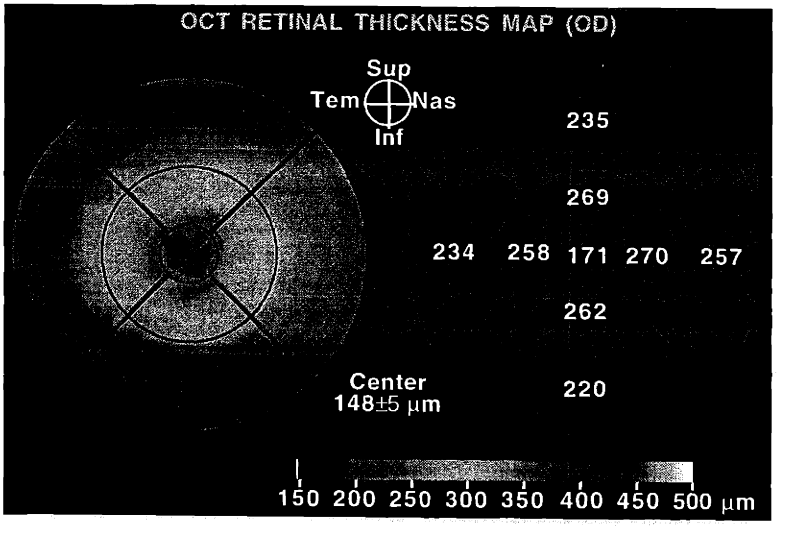

FIGURE 4-35. Radial topographic map corresponding to Figure 4-34.

4.8.2 Topographic Mapping of Retinal Nerve Fiber Layer Thickness

Measurement of NFL thickness around the optic nerve head is potentially important in the early detection and management in glaucoma. Glaucomatous NFL loss can manifest both as diffuse thinning of the NFL or as focal NFL dropouts. NFL dropouts appear as wedge-shaped regions emanating from the disc. A radially oriented scanning pattern similar to that used for macular thickness would risk missing these focal dropouts.

Instead, six concentric, cylindrical OCT scans were obtained at varying diameters around the optic disc (Figure 4-36). The OCTs were concentrated closer to the disc where information on NFL thickness was determined to be more predictive of glaucomatous nerve

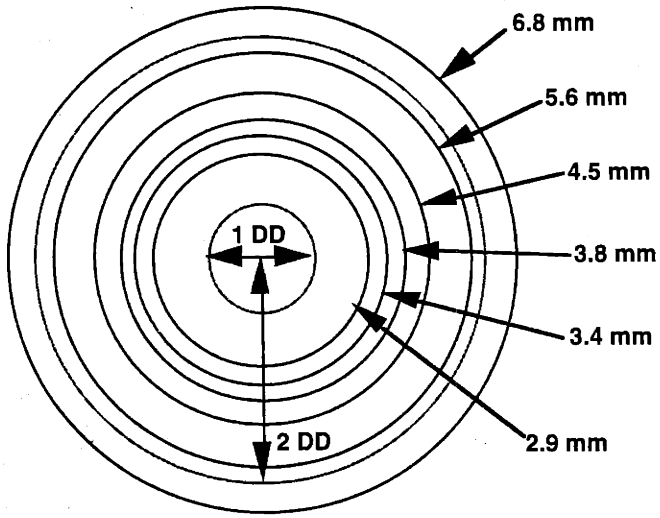

FIGURE 4-36. Scan diameters for topographic mapping with concentric circular scans around the optic disc.

fiber loss. The innermost cylindrical scan was offset by approximately half a disc diameter from the edge of the ideal disc to allow for variations in actual optic disc size and to avoid scanning over regions of peripapillary atrophy if present.

NFL thickness was displayed in false color where bilinear interpolation in polar coordinates (see Figure 4-33 and Equation (4.11)) was used to estimate the thickness in the ring-shaped regions between each OCT scan. Figures 4-37 and 4-38 display an example of a topographic map of NFL thickness obtained around the optic nerve head of a healthy volunteer.

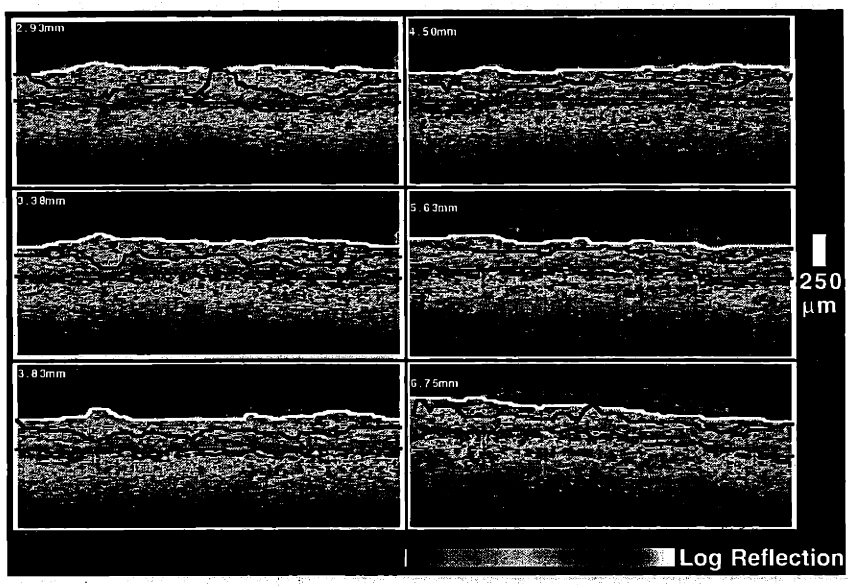

FIGURE 4-37. Concentric circular OCTs around the optic nerve head.

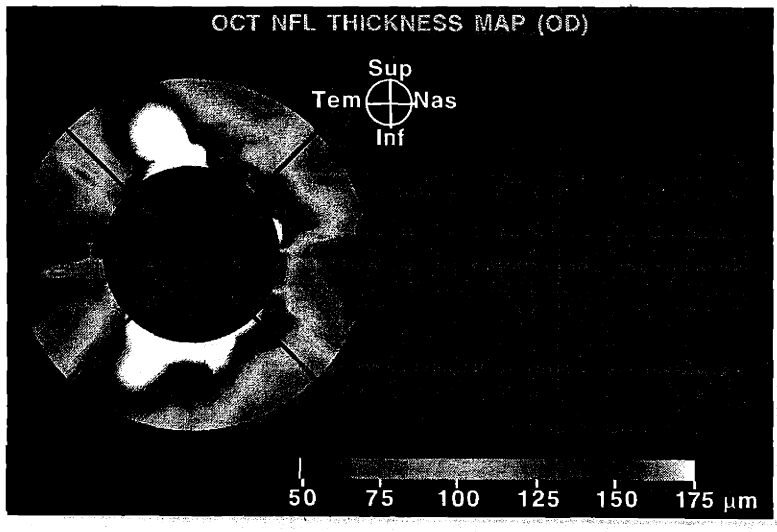

FIGURE 4-38. Topographic map of NFL thickness corresponding to OCTs in Figure 4-37.

Chapter 5

IMAGE INTERPRETATION

5.1 Introduction

The physical basis of OCT imaging depends on the contrast in optical reflectivity between different tissue microstructures. In ophthalmology, OCT is a powerful diagnostic tool for a variety of ocular diseases when combined with the conventional clinical techniques of direct and indirect ophthalmoscopy, fluorescein angiography, and visual field testing. In many cases, a definitive diagnosis may be established directly from the OCT images. As described in Chapter 4, quantitative measurements may be extracted from the OCTs using image processing techniques. The availability of quantitative information makes OCT useful for longitudinally tracking small changes in tissue structure and the development or resolution of disease processes.

This Chapter will provide a brief explanation of light propagation through tissue, describe the anatomical features visible on OCT tomograms of the normal macula and optic disc, and provide a framework for interpreting OCT images of retinal pathology.

5.2 Optical Properties of Tissue

Since light incident on and reflected from deeper tissue layers must pass through more superficial layers before detection, the reflections from internal tissue structures depend critically on the effects of overlying tissue. An understanding of the general concepts of light propagation through tissue is essential to develop a basis for interpretation of OCT images. Modeling light propagation and scattering through turbid media is a complex problem. Several formalisms based on different approximations have been developed, including Mie theory, radiative transport theory, diffusion theory, and Monte Carlo simulation.

5.2.1 Mie Scattering Theory

Mie scattering theory is an exact solution for the scattering of a plane electromagnetic wave by a single, homogenous, isotropic sphere [79-81]. Since the theory is based on a rigorous solution of Maxwell's equations, it includes the effects of polarization, interference, and diffraction. Since OCT is a coherent imaging technique, these effects are important considerations in image formation. However, the general field solution is impossible to calculate using Mie theory for a large random distribution of particles. The benefit of Mie theory lies in the ability to calculate *a priori* general parameters, such as the scattering and absorption coefficients, and the anisotropy factor, which can be used in some of the other models described

below. These parameters are only applicable to media composed of uniform refractive spheres; however, several generalizations based on particle size can be made based on the results from Mie theory.

Rayleigh scattering is a special case of Mie theory, giving an analytical solution for the scattered field valid for particles with dimensions much smaller than a wavelength. In the Rayleigh limit, the incident electric field is assumed to have no variation across the dielectric sphere. The incident field induces a time-harmonic dipole moment in the particle, which consequently radiates a scattered field analogous to a classical Hertzian dipole. Thus, for a Rayleigh particle, the total scattered power is proportional to the incident intensity and inversely proportional to the fourth power of the wavelength. The phase of the scattered field is always matched to the phase of the excitation, since the induced dipole responds instantaneously to the exciting field. The scattered power also has a $\cos\theta$ dependence, where θ is the angle between the incident and the scattered fields. A scattering anisotropy parameter

$$g = \langle \cos\theta \rangle \tag{5.1}$$

may be defined as the average cosine of the scattering angle which is a convenient indication of the directionality of scattering. For isotropic, or symmetric scattering, $g \to 0$; for highly forward directed scattering, $g \to 1$; and for highly backscattering particles $g \to -1$. Since the Rayleigh scattered power is symmetric with respect to the scattering angle θ, $g = 0$ and the scattering is isotropic.

The general Mie solution of scattering from a spherical particle of arbitrary size is difficult and requires an infinite series solution. Numerical evaluation, however, provides several insights into the scattering behavior of spherical particles [59]. For example, the scattering cross-section increases with increasing particle size indicating that the total scattered power also increases. The scattering also becomes increasingly forward directed and $g \to 1$ quickly. Finally, the phase of the scattered field exhibits increasing variation with the scattering angle. These effects may be understood intuitively if one considers a large scattering sphere to be composed of an infinite number of radiating dipoles. These dipoles exhibit interference and diffraction effects analogous to a radiating aperture. It is well known, for example, that the angular width of the radiation pattern from an aperture antenna decreases with increasing aperture size which, by analogy, explains the highly forward scattering nature of large particles.

5.2.2 Radiative Transport Theory

Radiative transport theory is a heuristic approximation to the scattering problem and deals with the transport of energy through turbid media rather than the propagation of electromagnetic fields [81]. Thus, interference, diffraction, and polarization effects are ignored. The transport equation describes the propagation of the specific intensity $I(r, \hat{s})$ through tissue, where $I(r, \hat{s})$ is the intensity per unit steradian (solid angle) at the position r in the direction of the unit vector $\hat{s}$. $I(r, \hat{s})$ is decreased by absorption and scattering in the media, but increased by light that is scattered from other directions $\hat{s}'$ into $\hat{s}$. The transport equation is the continuity relation which describes these interactions and is given by

$$\hat{s} \cdot \nabla I(r, \hat{s}) = -(\mu_a + \mu_s) I(r, \hat{s}) + \mu_s \int_{4\pi} \rho(\hat{s}, \hat{s}') I(r, \hat{s}') d\Omega + S(r, \hat{s}) \tag{5.2}$$

where μ_a is the absorption coefficient, μ_s is the scattering coefficient, $d\Omega$ is the differential solid angle in the direction of $\hat{s}'$, $\rho(\hat{s}, \hat{s}')$ is the normalized scattering phase function, and $S(r, \hat{s})$ is the distributed source function. Equation (5.2) may be intuitively understood as follows. The term $\hat{s} \cdot \nabla I(r, \hat{s})$ is the differential increase in the specific intensity in the direction $\hat{s}$. The specific intensity is decreased by losses $\mu_a I(r, \hat{s})$ and $\mu_s I(r, \hat{s})$ due to absorption and scattering out of $\hat{s}$, respectively. The integral in Equation (5.2) represents the increase in intensity due to scattering from directions $\hat{s}'$ back into $\hat{s}$, and $S(r, \hat{s})$ describes any sources at r also emitting light into $\hat{s}$.

The absorption and scattering coefficients μ_a and μ_s have units of inverse length and describe the attenuation of light due to absorption and scattering. One may view μ_a or μ_s as the probability of an absorption or scattering event occurring per infinitesimal distance of propagation. Thus the intensity of light which has not been either scattered or absorbed after propagating a distance z through a random medium is reduced by a factor of

$$e^{-(\mu_a + \mu_s)z} \tag{5.3}$$

from the incident intensity. The mean free-path (MFP) length between two absorption or scattering events is given by either $1/\mu_a$ or $1/\mu_s$ respectively.

The phase function $\rho(\hat{s}, \hat{s}')$ is the probability density function for scattering from $\hat{s}$ into $\hat{s}'$. If the scattering is symmetric about the direction $\hat{s}$ of the specific intensity, then the phase function is only a function of the scattering angle θ between $\hat{s}$ and $\hat{s}'$. Then effects of the phase function can be summarized using the anisotropy factor g defined in Equation (5.1). In this case, a description of the scattering medium is reduced to three parameters, μ_a, μ_s, and g, known as the transport coefficients.

5.2.3 Diffusion Theory

In the multiple scattering limit, the transport equation (5.2) may be simplified into the more tractable diffusion equation [81-89]. The diffusion approximation is valid away from tissue boundaries or sources when scattering dominates absorption. In this limit, it can be shown that the multiply scattered component of the specific intensity $I(r, \hat{s})$ obeys the steady state diffusion equation

$$-D\nabla^2\phi(r) + \mu_a\phi(r) = s(r) \tag{5.4}$$

where $s(r)$ is a source term, $\phi(r)$ is the total diffuse fluence rate given by

$$\phi(r) = \int_{4\pi} I(r, \hat{s}) d\Omega \tag{5.5}$$

and D is the diffusion coefficient:

$$D = \frac{1}{3[\mu_a + \mu_s(1-g)]}. \tag{5.6}$$

Note only the combined factor $\mu_s(1-g)$ appears in the diffusion equation. Therefore, it is customary to define a reduced scattering coefficient $\mu'_s = \mu_s(1-g)$. In the diffusion limit, anisotropic scattering ($g \neq 0$) described by a scattering coefficient μ_s is indistinguishable from

isotropic scattering ($g = 0$) described by a reduced scattering coefficient μ'_s. Thus, the diffuse intensity for an anisotropic scattering system may be analyzed as an equivalent isotropic system. A transport, or forward scattering mean free-path may be defined such that

$$mfp_{forward} = \frac{1}{\mu_a + \mu_s(1-g)} \tag{5.7}$$

representing the mean free-path between absorption and scattering events in the equivalent isotropic system.

The diffusion equation (5.4) is a steady-state equation and valid only after equilibrium has been established. To analyze the transient dynamics of the fluence $\phi(r, t)$, a time-dependent term may be phenomenologically added, giving

$$-D\nabla^2\phi(r, t) + \frac{1}{c}\frac{\partial}{\partial t}\phi(r, t) + \mu_a\phi(r, t) = s(r, t). \tag{5.8}$$

Equation (5.8) only applies for times much greater than the mean free time between scattering events after all the sources have been turned on.

In general the diffusion approximation is not valid for imaging with OCT. The dominant contribution to the OCT signal is derived from light which propagates to a particular layer in the tissue without scattering or absorption, experiences a single scattering event in the backwards direction, and returns to the detector without further scattering or absorption. In contrast to this singly backscattered light, light that has undergone multiple scattering events, but no absorption, may also be detected if it happens to take a path which returns to the detector. The optics of the OCT system make it improbable that multiple scattered light will travel on such a path, because the confocal and interferometric nature of the detection process places additional requirements on the temporal and spatial coherence of the detected light. Thus, for all practical purposes, the OCT signal may be considered to be exclusively comprised of light that has undergone just a single backscattering event at the tissue layer of interest.

5.2.4 Monte Carlo Simulation

Monte Carlo simulation is based on radiative transport theory and improves on the approximations in diffusion theory [90-93]. Light distribution in tissue is calculated by probabalistically propagating individual photons during discrete units of time. For each time interval, a given photon has a probability of absorption or scatter defined by the transport coefficients μ_a and μ_s respectively. The direction of each scattering event, if one occurs, is determined by a random number weighted by an assumed phase function.

Unlike diffusion theory, Monte Carlo methods are applicable near tissue boundaries and sources, for all times, and for few scattering events. A complete phase function is assumed and not compressed into a single anisotropy parameter. However, the computational resources required by a Monte Carlo program can be considerable. For example, to simulate an optical detection system with a dynamic range of 100 dB would require computationally propagating at least 10^{10} photons, each through multiple scattering events, for each photon detected.

5.2.5 Transport Coefficients for Biological Tissue

The diffusion approximation of radiative transport theory reduces the properties of the scattering medium to three parameters: the absorption and scattering coefficients μ_a and μ_s, and the anisotropy parameter g. While these parameters clearly cannot describe many of the characteristics of a turbid media, they are standard, intuitive, and permit a quick comparison of the optical properties of various biological tissues. The transport parameters may be measured by many techniques, including steady-state and time-resolved optical reflectance and transmittance [94-97].

In general, μ_a, μ_s and g depend on the wavelength. For biological tissue, the wavelengths between 600 and 1300 nm are known as the "therapeutic window" because these wavelengths fall outside the absorption bands of hemoglobin, melanin, and water so that light has the deepest penetration into tissue. For light in the therapeutic window, typical values of the transport parameters are $\mu_a = 1\ cm^{-1}$, $\mu_s = 100\ cm^{-1}$, and $g = 0.9$. Thus, a typical tissue has a MFP between absorption events of 1 cm, and a MFP between scattering events of 100 μm, and a forward scattering MFP of 1 mm. For most tissue, scattering dominates absorption and each scattering event is highly forward directed [97].

The strength of the OCT signal at a particular tissue layer is defined by the amount of incident light which is transmitted without absorption or scattering to that layer, by the proportion of this light which is directly backscattered, and by the fraction of the directly backscattered light which returns to the detector without further attenuation. The proportion of the incident light which is directly backscattered by a tissue structure defines the reflectivity of that structure. Thus, the OCT signal from a particular tissue layer is a combination of its reflectivity and the absorption and scattering properties of the overlying layers. The internal reflectivity of a homogenous tissue layer depends on both the layer's scattering coefficient and its scattering anisotropy. A highly reflective tissue will have both a high scattering coefficient and a strong disposition to scatter light in the perfectly backwards direction. A strong return signal will occur on OCT if the spatial frequency of the local index variations falls within a bandwidth determined by the coherence structure of the light source [98]. Strong reflections therefore occur at the boundaries between two medias, for example, between two materials of different refractive indices.

Thus, although the diffusion approximation is not, in general, valid for OCT imaging, the concepts of scattering and absorption mean-free paths, and scattering anisotropy may be used to make comparative predictions regarding different tissues and optical properties. A tissue with a relatively short scattering MFP, for example, attenuates the OCT signal more quickly with propagation distance than a tissue with a longer scattering MFP. Similarly, it is evident that longer wavelengths in the therapeutic window may be used to provide increased penetration through highly scattering tissue due to the dependence of the scattering MFP on wavelength [99].

5.3 Normal Retina [26, 45]

OCT provides a image of optical reflectivity in a thin, cross-sectional tissue slice. In the retina, this cross-sectional view provides information that is complementary to the *en face* view of ophthalmoscopy and is useful in the diagnosis and management of several diseases of the macula and optic nerve. An understanding of the morphology of the healthy retina on OCT is essential to appreciating the changes that occur in retinal pathology.

5.3.1 Retinal Histology

A histological slice of the retina is shown Figure 5-1. The outermost retinal layer (1) consists of the retinal pigment epithelium (RPE) which is a single pigmented cell layer resting on basement membrane known as Bruch's membrane. Bruch's membrane separates the RPE from the outer retinal blood supply known as the choroid. The innermost layer of the choroid is comprised of an interconnected network of vessels known as the choriocapillaris. The rod and cone processes (2) of the photoreceptors lie between the RPE and the outer limiting membrane (3), which separates the rods and cones from the photoreceptor cell bodies. The photoreceptor cell bodies comprise the outer nuclear layer (4). The outer plexiform layer (5) contains synaptic connections between the photoreceptors and the bipolar cell bodies, which form the inner nuclear layer (6). The inner plexiform layer (7) contains the connections between the bipolar cells and the ganglion cell bodies (8) of the retinal nerve fibers. The retinal nerve fiber layer (9) carries the retinal signals through to the optic disc and eventually forms the optic nerve. The inner limiting membrane (10) separates the neurosensory retina from the vitreous body (VB), a clear gel which lies between retina and the lens.

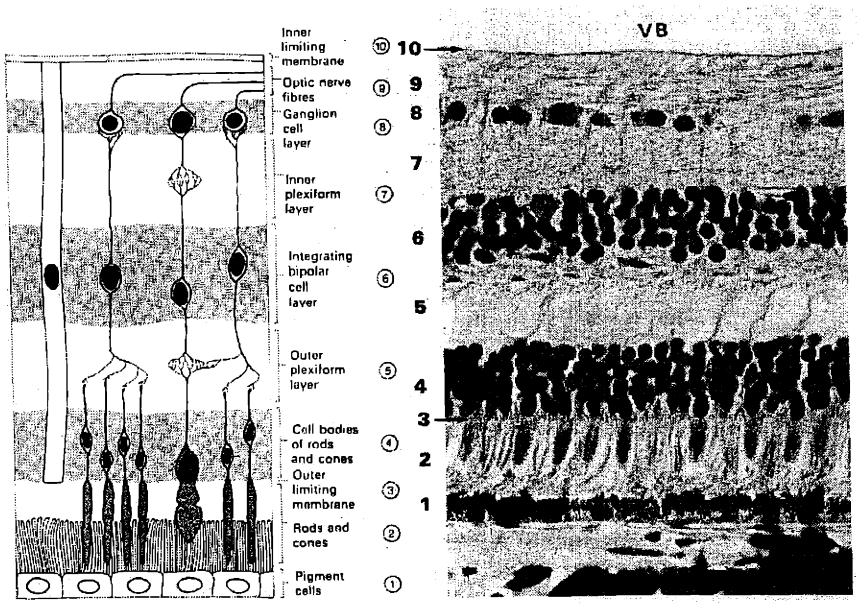

FIGURE 5-1. Histological section of the retina (H & E) [100].

A histological section taken through the fovea is shown in Figure 5-2. The fovea lies at the point where the visual axis of the cornea and lens intersects with the retina and is consequently the retinal region of least refractory distortion. The foveal architecture is also adapted

for maximum visual acuity. The inner retinal layers are displaced laterally in order to minimally distort incident light, retinal blood vessels are absent, and the photoreceptors are almost exclusively cones. In the fovea, as opposed to the peripheral retina, a one-to-one mapping exists between the photoreceptors and bipolar cells, which means that each photoreceptor in the fovea is individually represented in the visual cortex.

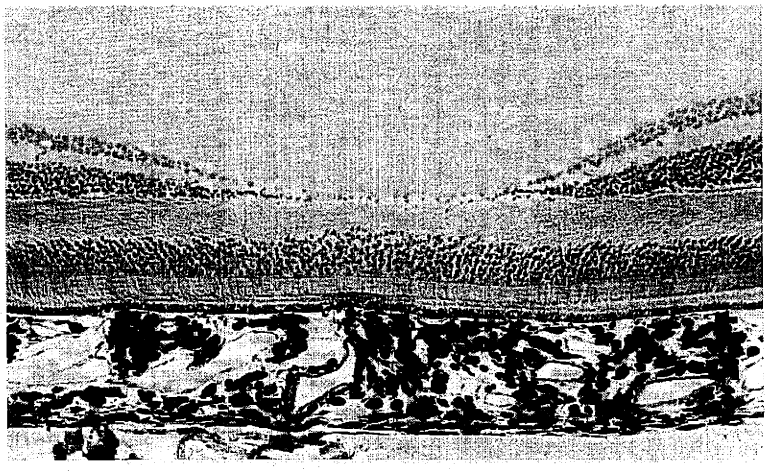

FIGURE 5-2. Histological section of the fovea (Masson's trichrome) [100].

5.3.2 Papillomacular Axis

Figure 5-3 shows a large field-of-view OCT of a healthy retina including both the macula and peripapillary region. Large scale anatomic features, such as the fovea, optic disc, and retinal profile are evident in the tomogram and are identifiable by their characteristic morphology. The vitreoretinal interface is demarcated by the contrast between the non-reflective vitreous and the backscattering surface of the retina. The fovea appears to the left in the tomogram as a characteristic thinning of the retina and shows the lateral displacement of the retina anterior to the photoreceptors. The optic disc appears to the right in the tomogram, showing the optic nerve head contour and evidence of normal cupping.

A highly reflective red layer delineates the posterior boundary of the retina in the tomogram, and corresponds to the retinal pigment epithelium (RPE) and choriocapillaris. This posterior layer terminates at the margin of the optic disc consistent with the termination of choroidal circulation at the lamina cribosa. Below the choriocapillaris, relatively weak scattering returns from the deep choroid and sclera, due to attenuation of the signal after passing through the neurosensory retina, RPE, and choriocapillaris. A dark layer indicative of minimal reflectivity appears just anterior to the choriocapillaris layer, and represents the outer segments of the retinal photoreceptors. The intermediate layers of the retina anterior to these segments exhibit moderate backscattering. The inner margin of the retina shows another area of bright backscattering, a red layer that corresponds in location and in anatomical variation to the retinal nerve fiber layer (NFL). According to the tomogram, the NFL increases in thickness from the macula to the optic disc as expected from normal anatomy.

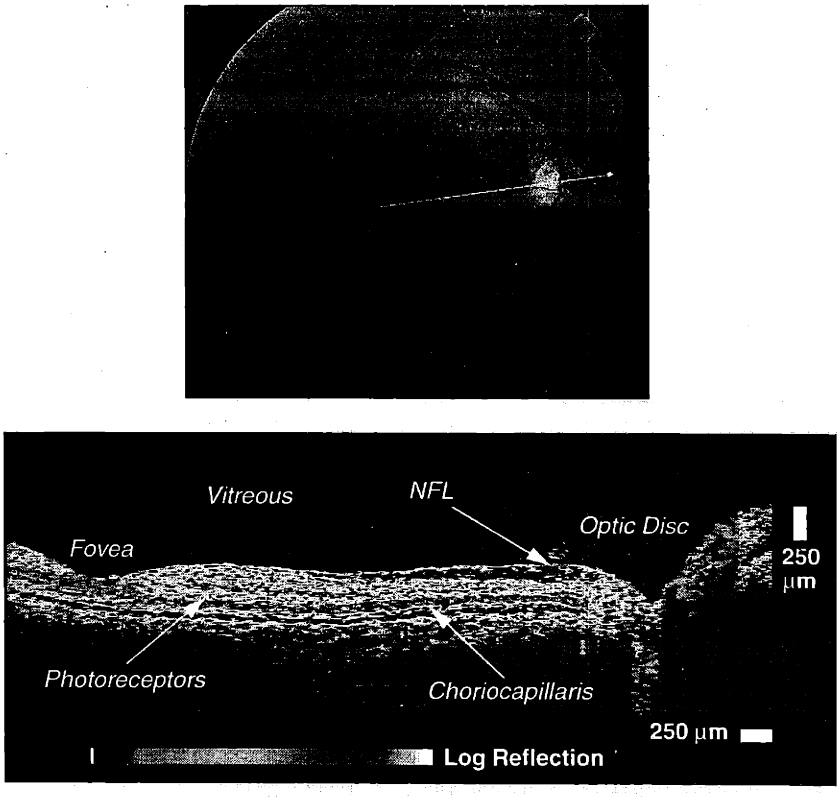

FIGURE 5-3. Normal fovea and optic disc along the papillomacular axis.

5.3.3 Fovea

A narrow field-of-view image (Figure 5-4) of a normal fovea further delineates the contrast between different retinal layers. The image is displayed twice expanded in the vertical direction. The anterior and posterior margins of the retina are again defined by highly reflective layers corresponding to the NFL and RPE/choriocapillaris. The RPE appears distinct from the choriocapillaris directly beneath the fovea, where the pigmentation is the heaviest. Above the minimally reflective photoreceptors, alternating layers of moderate and low reflectivity reveal the stratified structure of the retina. Moderate backscattering is observed from the inner and outer plexiform layers (IPL, OPL), which like the NFL, consist of a fibrous structures running perpendicular to the incident beam. In contrast, minimal backscattering is noted from the nuclear layers, in which, like the photoreceptors, the cell bodies are oriented parallel to the incident light. Retinal blood vessels are identified by their increased backscatter and by their shadowing of the reflections from the RPE and choriocapillaris. The larger choroidal vessels also appear in the image and have minimally reflective, dark lumens.

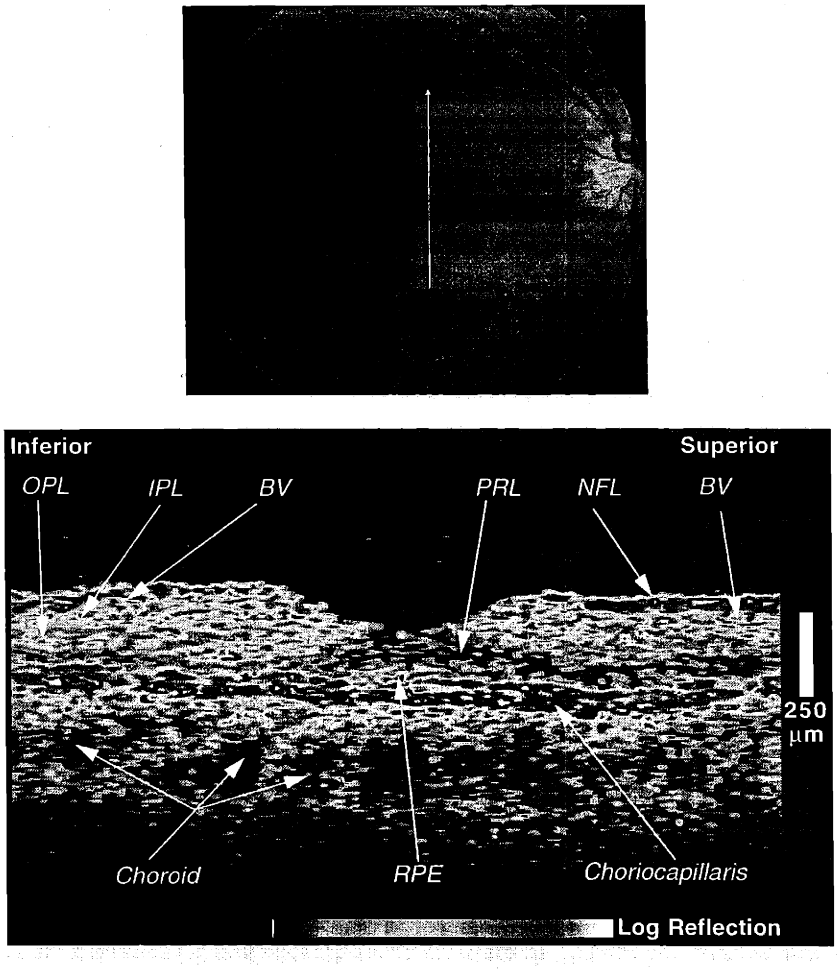

FIGURE 5-4. Narrow field-of-view OCT of a normal fovea.

5.3.4 Serial Sagittal OCTs Through the Macula

In analogy to X-ray computed tomography (CT) or magnetic resonance imaging (MRI), information on three-dimensional structure may be obtained by using the optical sectioning capability of OCT to acquire serial images of consecutive slices through the retina. As an example, six sagittal tomograms were obtained consecutively from a healthy macula with a lateral displacement of 225 µm between each image (Figure 5-5).

Characteristic features of the retina appear consistently in the serial sections. The anterior and posterior surfaces of the neural retina are demarcated by backscattering at the NFL and vitreoretinal interface, and the highly backscattering red layer representing the RPE and choriocapillaris. The sequence of tomograms shows the development and resolution of the foveal depression, which reaches its maximum depth at the fovea centralis. Retinal blood vessels derived from the superior and inferior branches of the central retinal artery are evident in the tomograms from the partial shadowing of the deep retinal structure beneath the vessels.

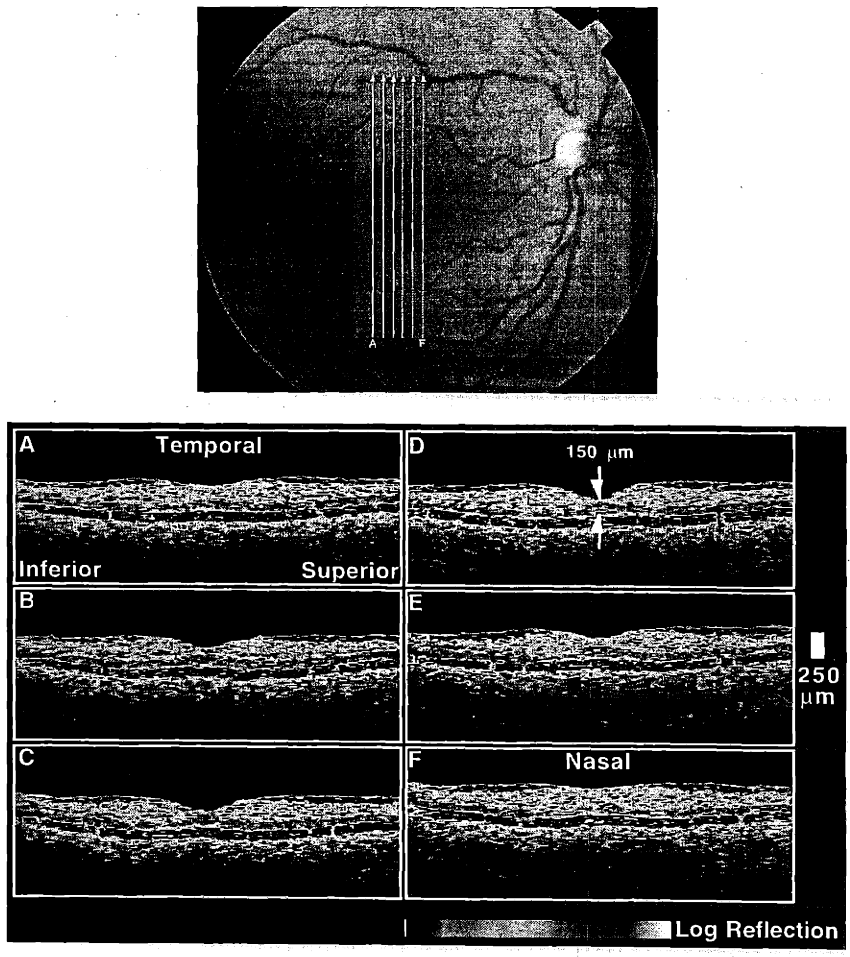

FIGURE 5-5. Serial sagittal OCTs through a normal macula.

5.3.5 Serial Radial OCTs Through the Optic Disc

Figure 5-6 displays OCT sections taken through different radial planes, each passing through the center of the optic nerve head, which are useful in comparing nerve fiber thickness through different planes and in assessing the profile of the optic disc. In the 90° tomogram (taken perpendicular to the papillomacular axis), high backscatter (red) is visible from the NFL and from a band defining the posterior boundary of the sensory retina, corresponding to the RPE and choriocapillaris. The tomogram shows the NFL expanding towards the optic disc to occupy nearly the entire retinal thickness, commensurate with the presence of the inferior and superior arcuate nerve fiber bundles. In comparison, the 0° tomogram (taken parallel to the papillomacular axis) exhibits a thinner NFL consistent with fewer nerve fibers in this area. The surface contour and normal cupping of the disc are visualized in all of the tomograms. The termination of the choroid at the lamina cribosa is also delineated.

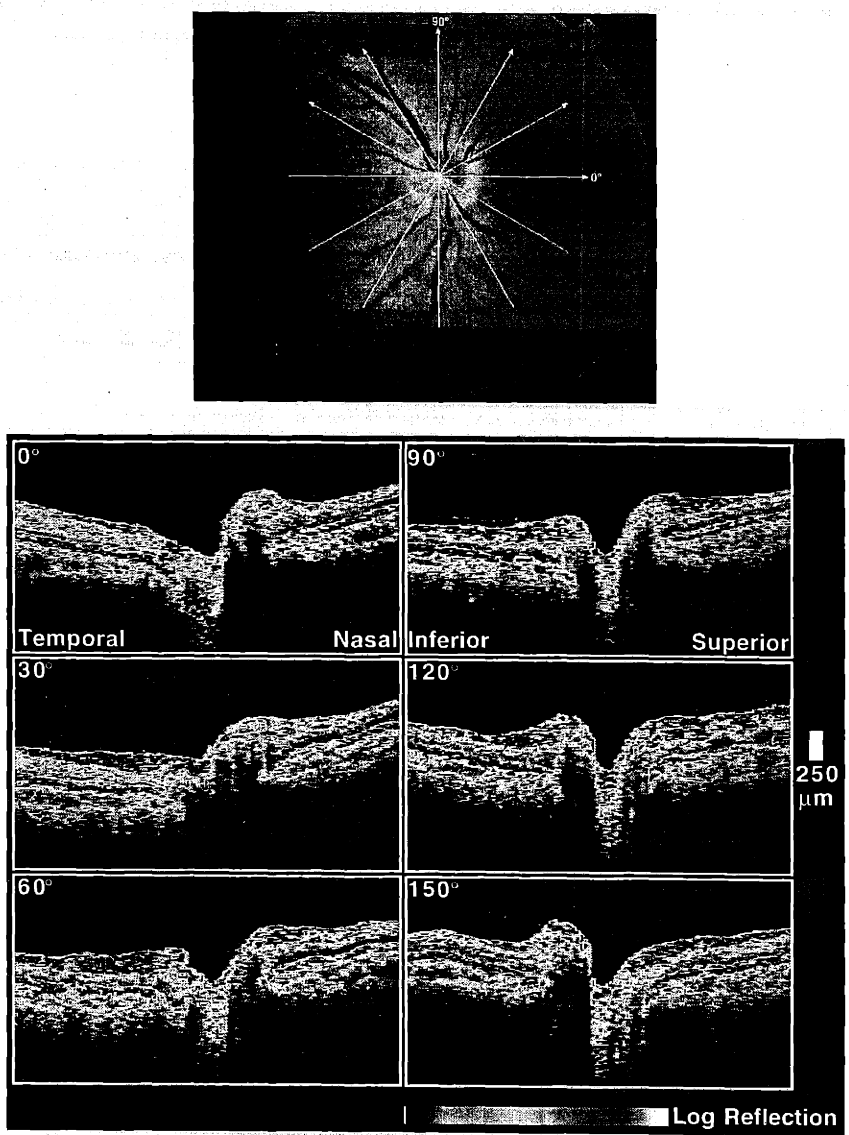

FIGURE 5-6. Radial OCTs through a normal optic disc.

5.3.6 Circular OCTs in the Peripapillary Region

Documentation of nerve fiber layer thickness and degeneration in the peripapillary region may be important in the diagnosis and treatment of glaucoma and other neurodegenerative diseases. A useful way of assessing the NFL in this area is to image cylindrical tissue sections centered around the optic disc. Figure 5-7 shows two circular OCTs with different diameters, each centered on the nerve head. Each tomogram is displayed unwrapped and corresponds to a clockwise scan around the optic disc.

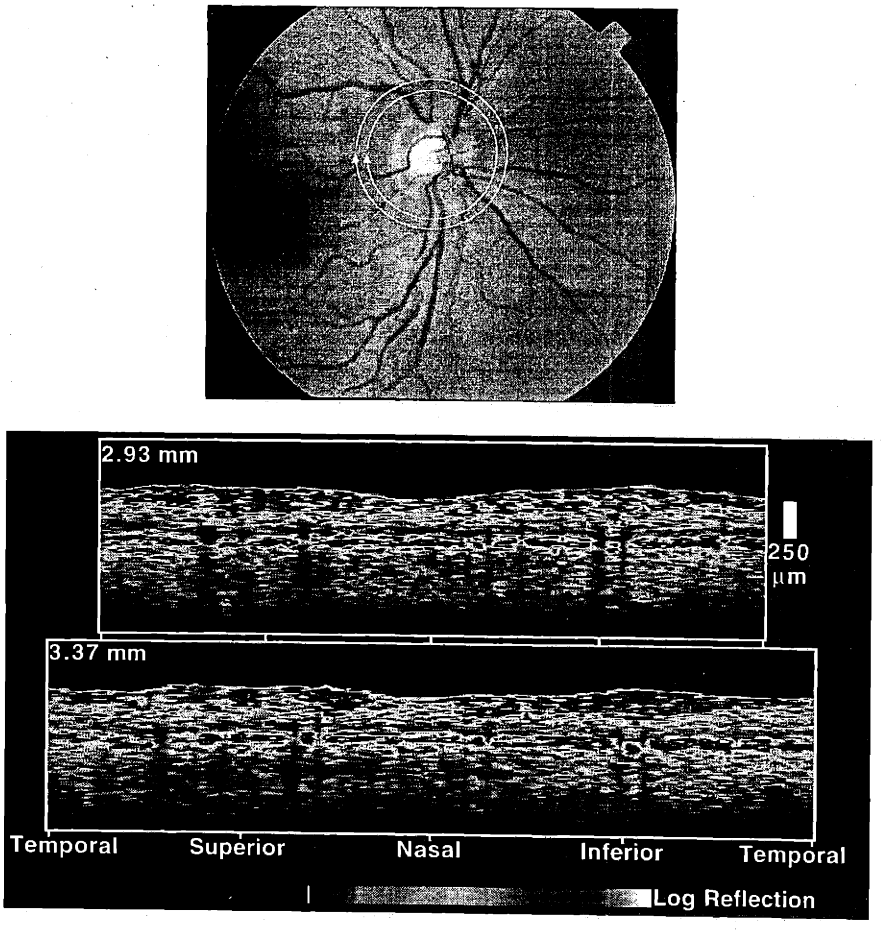

FIGURE 5-7. Circular OCTs obtained around a normal optic disc.

The anterior and posterior highly backscattering layers represent the NFL and choriocapillaris/RPE, respectively. The inferotemporal and superotemporal nerve fiber bundles are evident in both tomograms as localized thickenings in both the NFL and retina. The bundling becomes more diffuse in the images as the distance from the optic nerve head increases with a larger scan diameter, as expected from normal anatomy.

5.4 Interpretation of OCT Images [26]

The evaluation of OCT images depends on the ability of the observer to identify both differences in the relative reflectivity of different tissue layers and morphological changes in tissue structures. In some cases, because of the high axial resolution of the OCT images, small changes in morphology may be difficult to assess by direct observation of the images. In these cases, automated computer image processing tools may be used to extract precise quantitative measurements from the images.

5.4.1 Retinal Thickness

Retinal thickness is an important consideration in the assessment of many macular diseases. The high axial resolution of OCT combined with the well-defined contrasts in reflectivity at the anterior and posterior boundaries of the retina make OCT uniquely suited for measurement of this parameter.

Retinal thickness may be increased with edema. The accumulation of intraretinal fluid will lead to both an increased retinal thickness, and also a change in the scattering properties of the tissue. An important location to measure retinal thickening is directly in the fovea, where edema can have a profound effect on visual acuity. This type of measurement can be particularly useful in tracking patients with macular edema due to diabetic retinopathy (Figure 5-8), or for screening and following patients with cystoid macular edema following cataract surgery.

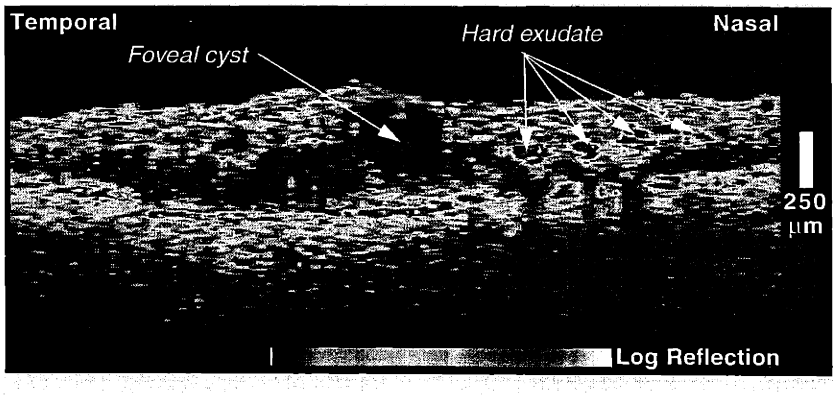

FIGURE 5-8. Diabetic retinopathy.

Retinal edema may be differentiated from retinal traction by the identification of cystic spaces within the retina, indicative cystoid macular edema, or by visualization of the posterior hyaloid or an epiretinal membrane, which may be causing retinal traction.

Decreased retinal thickness often occurs with atrophy or scarring and may be either focal or diffuse.

5.4.2 Reflectivity

Changes in retinal architecture or cellular morphology result in changes in optical properties which may be observed on the OCT tomograms. The apparent reflectivity measured by OCT is a combination of the actual reflectivity and the scattering and absorption characteristics of the overlying media. Thus, the apparent reflectivity for retinal imaging may be affected by abnormalities in the cornea, aqueous, lens, vitreous, and anterior retinal layers.

Causes of increased or hyper-reflectivity include inflammatory infiltrate into any layer of the retina or choroid, fibrosis, such as in a disciform or other scar, hard exudate, and hemorrhage. Hard exudate is highly reflective, but completely blocks the reflections from the deeper retinal layers (Figure 5-8). Blood also has a high scattering coefficient, which has two effects. The high proportion of backscattered light leads to a bright reflection from hemor-

rhage; however, the scattering is also significant, which results in a rapid attenuation of the incident light as it propagates through the blood. Thus, blood vessels are most readily identified by their shadowing effect on the reflection from the RPE and choriocapillaris. The attenuation of the incident light depends on the thickness of the scattering medium. Thin hemorrhages appear as thin, highly reflective bands that have little effect on the underlying tissue. Thick hemorrhages, however, completely attenuate the probe light after more than approximately 200 μm.

Decreased, or hypo-reflectivity may be caused by retinal edema, in which fluid accumulation leads to a decreased density of microscopic scatterers and a corresponding reduction in the scattering coefficient (Figure 5-8). Alterations in cellular structure such as hypopigmentation of the RPE may also result in reduced reflectivity.

These morphological causes of reduced backscattering must be distinguished from alterations in the incident light caused by dense cataracts, cloudy media, astigmatism, poorly centered intraocular lens implants, or poor alignment of the OCT instrument while imaging. Abnormalities in the intervening structures typically cause a diffuse hypo-reflectivity throughout the OCT image, in all retinal layers. Focal decreases in reflectivity may be caused by shadowing from hyper-reflective tissues, such as hemorrhage, hard exudate, or a detached RPE. Local reductions in backscattering may also occasionally occur through silhouetting of the scanning probe beam by a narrow pupil. In this case, the reflectivity from all retinal layers is proportionately reduced, and the region of reduced reflectivity dynamically changes with alterations in the alignment of the delivery system.

The distinction between blood, serous fluid, and exudate is also made on the basis of reflectivity. The scattering coefficient, which along with anisotropy determines reflectivity, is essentially proportional to the concentration of particles in the fluid. Serous fluid, containing few cells, is optically transparent, so its accumulation is immediately recognized on OCT as a region devoid of backscattering. Blood, in contrast, has a large number of cells and a very high scattering coefficient, leading to both enhanced reflectivity and increased attenuation of the incident light. Cloudy exudate typically has an intermediate appearance between blood and serous fluid on OCT images.

5.4.3 Detachments of the Sensory Retina and Retinal Pigment Epithelium

OCT is extremely useful for evaluating detachments of the neurosensory retina and RPE. Neurosensory detachments appear as a shallow elevation of the retina, with an optically clear space between the retina and RPE (Figure 5-9). The backscattering from the normally minimally reflective photoreceptors is increased, resulting in a well-defined fluid-retina boundary.

Serous detachments of the pigment epithelium have a distinctly different appearance (Figure 5-10). The reflective band corresponding to the RPE is focally elevated over an optically clear space. Like the photoreceptors in the neurosensory detachment, the detached RPE is more highly reflective than normal, perhaps due to a refractive index difference between serous fluid and the choriocapillaris, or due to decompensation and morphological changes in the RPE cells themselves. The increased reflectivity from the RPE strongly shadows the backscattering signal from the choroid below the detachment, often even obscuring the reflective boundary between the serous fluid and the basement membrane. The angle of the detachment is also more acute in a pigment epithelial as compared to a neurosensory detachment because of the tight adherence of RPE cells to the basement membrane at the edge of the detachment, which supports an increased fluid pressure.

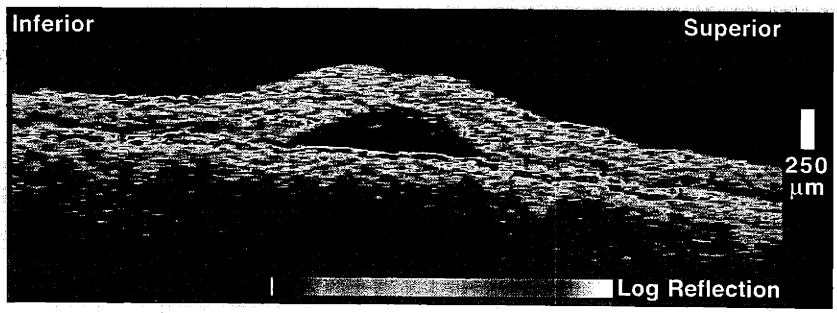

FIGURE 5-9. Neurosensory retinal detachment.

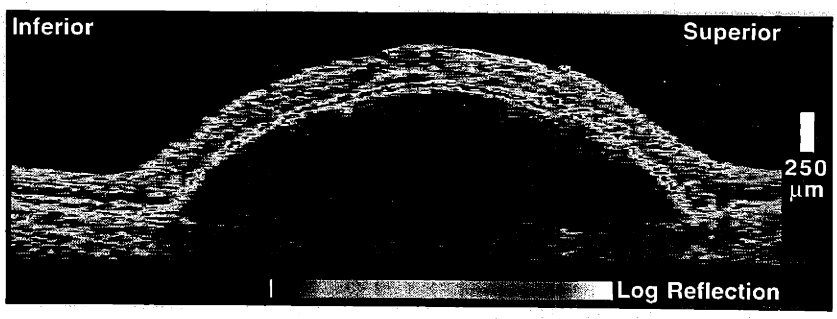

FIGURE 5-10. Serous detachment of the RPE.

The increased reflectivity from the photoreceptors in a neurosensory detachment may mimic the high reflectivity from the pigment epithelium, but rarely does it significantly shadow the reflections from the RPE and choroid. Thus, the distinction between a neurosensory and a pigment epithelial detachment relies on assessing the strength of the reflection below the serous fluid collection, and evaluating the angle of the detachment.

Neurosensory detachments may occasionally be confused with severe retinal edema and schisis-like cavities on OCT, since in many cases the fluid accumulation and reduced backscattering which occurs with edema is preferentially seen in the outer retinal layers (Figure 5-11). It is important in these cases to identify a smooth and continuous fluid-retina boundary to establish the diagnosis of a sensory retinal detachment.

Hemorrhagic detachments of the RPE have all of the characteristics of a serous RPE detachment, except that an optical backscatter signal corresponding to blood is observed directly beneath the detached RPE (Figure 5-12). The blood usually appears moderately, rather than highly, backscattering because of the attenuation of the incident light through the detached RPE. The optical penetration through both the detached RPE and hemorrhage is usually less than 100 µm.

Fibrovascular pigment epithelial detachments also show some optical backscatter within the sub-RPE space (Figure 5-13). However, a lower scattering coefficient compared to blood results in reduced apparent reflectivity from the fibrovascular proliferation and increased penetration of the probe light, which often reaches the choroid. Other lesions, such as a vitelliform lesion, may have a similar appearance of constant mild to moderate reflectivity extending between an elevated RPE and the choroid.

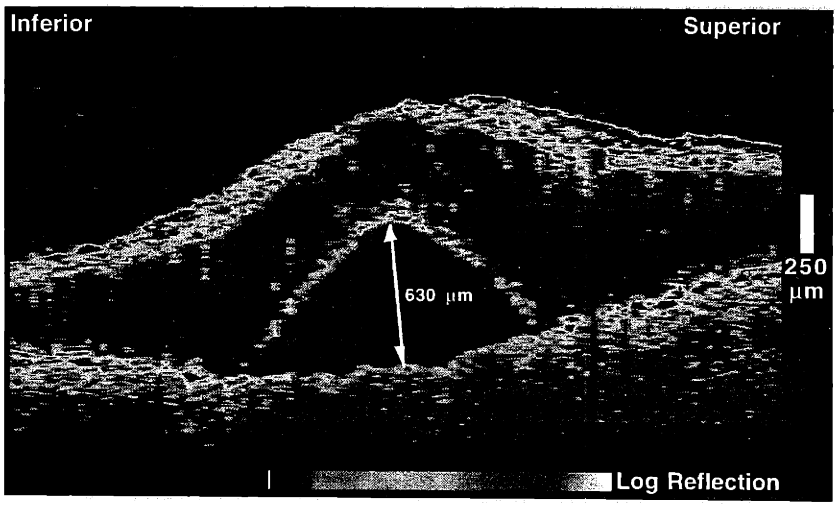

FIGURE 5-11. True retinal detachment *(arrow)* below a schisis-like cavity caused by severe retinal edema.

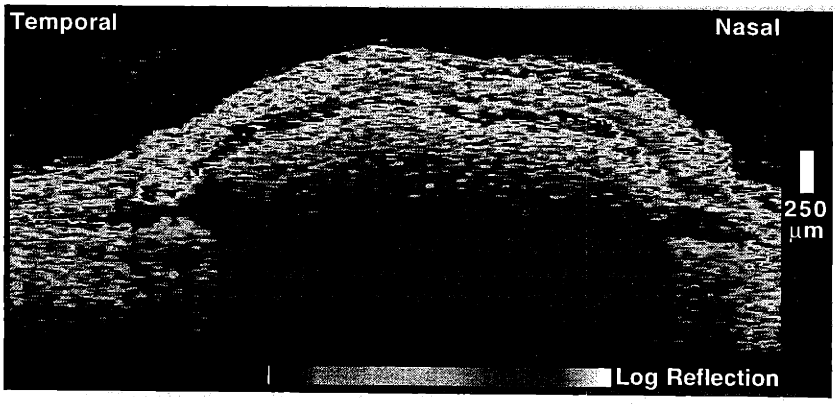

FIGURE 5-12. Hemorrhagic detachment of the RPE.

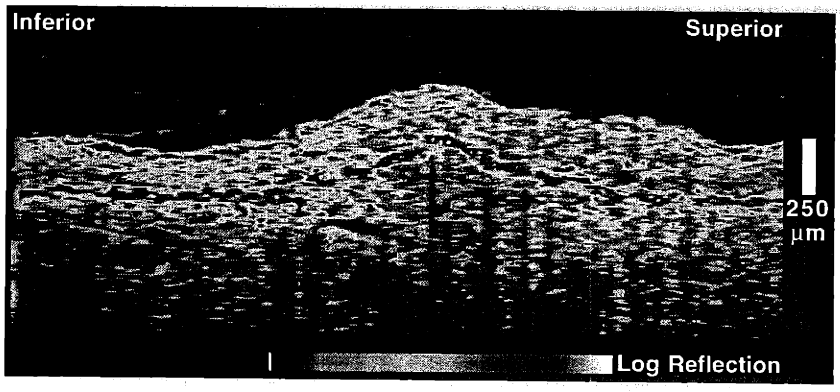

FIGURE 5-13. Fibrovascular pigment epithelial detachment.

Confluent soft drusen may be mistaken for small pigment epithelial detachments. However, no shadowing occurs with soft drusen and mild reflectivity, often indistinguishable from the choroidal reflectivity, extends from the elevated RPE down to the choroid (Figure 5-14).

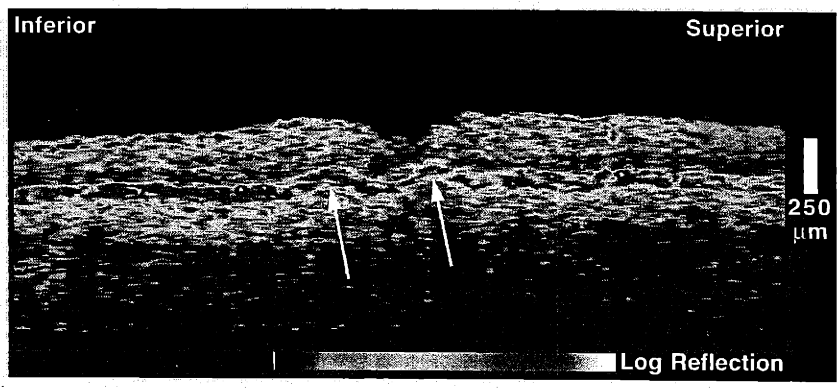

FIGURE 5-14. Soft drusen.

5.4.4 Fovea

Changes in the morphology of the fovea indicative of disease are often observed on the OCT image. Loss of foveal photoreceptors can be assessed with OCT, and occurs with full-thickness macular holes (Figure 5-15), central scarring or fibrosis, and other macular lesions. Steepening of the foveal contour is commonly associated with epiretinal membranes and macular pseudoholes (Figure 5-16) or lamellar holes (Figure 5-17). Loss or flattening of the foveal contour may occur with impending macular holes, foveal edema, or foveal neurosensory detachments. Vitreomacular traction may result in flattening or protrusion of the fovea (Figure 5-18).

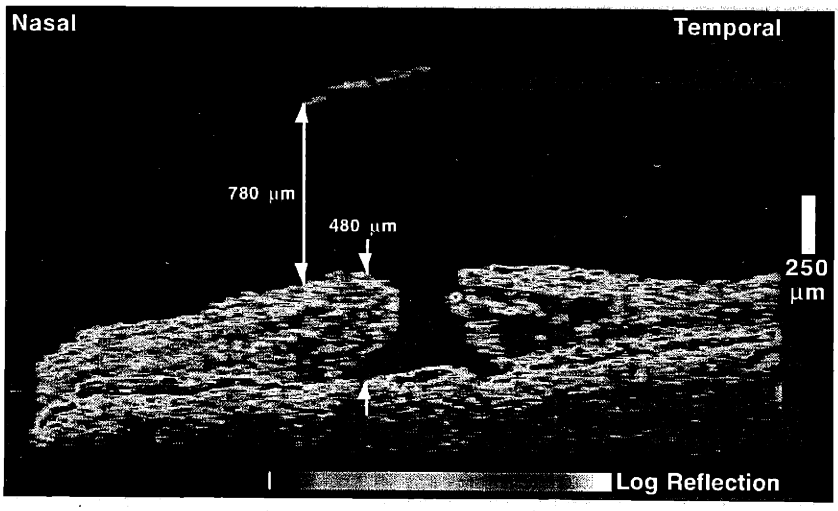

FIGURE 5-15. Full-thickness macular hole with operculum.

FIGURE 5-16. Macular pseudohole and epiretinal membrane *(arrow)*.

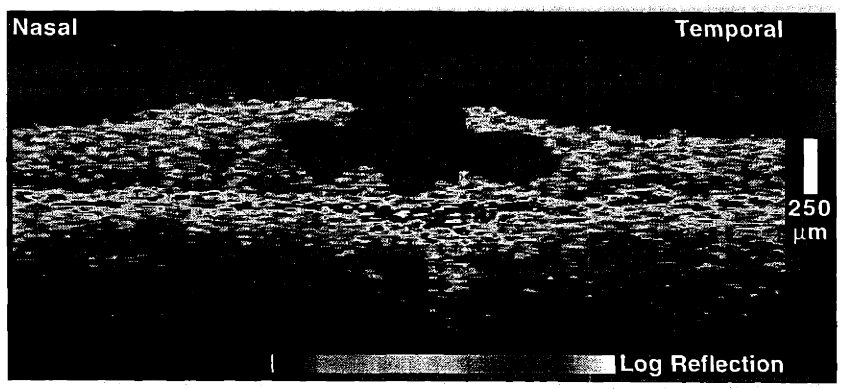

FIGURE 5-17. Partial thickness or lamellar hole.

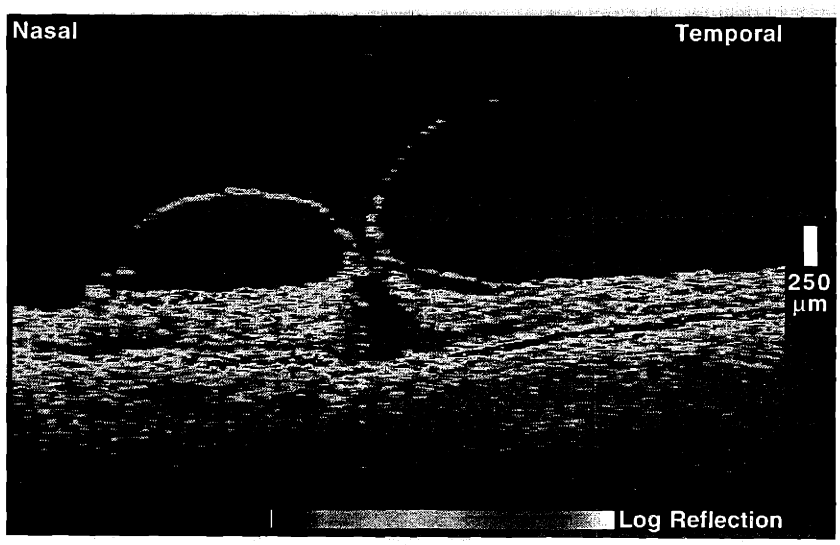

FIGURE 5-18. Vitreomacular traction directly in the fovea.

5.4.5 Retinal Pigment Epithelium and Choriocapillaris

While the RPE and choriocapillaris are difficult to distinguish on the OCT tomogram, their combined reflection, which defines the posterior boundary of the neurosensory retina on the OCT image, provides useful information on chorioretinal pathologies such as age-related macular degeneration and choroidal neovascularization.

Hyperpigmentation of the RPE leads to increased reflectivity, mild thickening of the posterior reflective boundary, and concomitant shadowing of the backscattering from the choroid. Detachments of the RPE also lead to choroidal shadowing, as discussed above. Disciform scars and other fibrosis appear as a severely thickened posterior reflection due to the high reflectivity and extension of fibrotic structures into the retina (Figure 5-19).

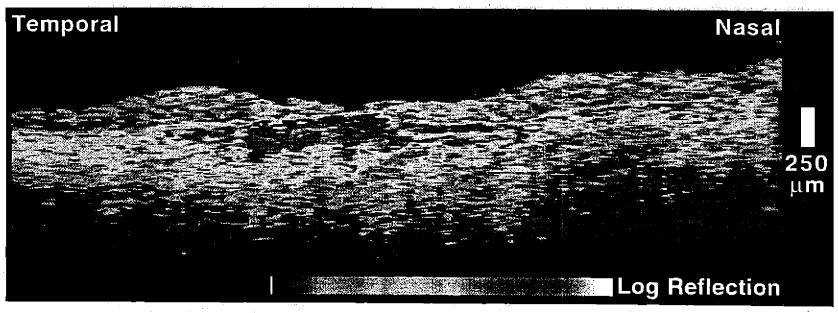

FIGURE 5-19. Disciform scar.

Hypopigmentation or pigment epithelial atrophy results in decreased reflection and an associated window defect, enabling increased penetration of the probe beam to the choroid, and higher reflectivity from the deeper layers (Figure 5-20). Retinal thinning in the fovea is also noted.

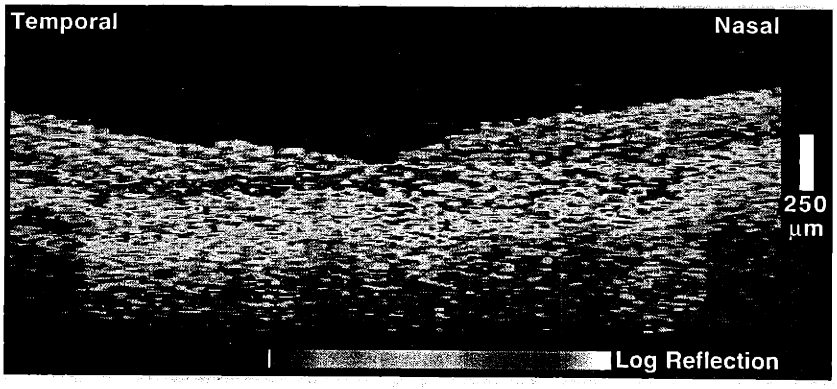

FIGURE 5-20. Geographic atrophy.

Disruption of the reflection corresponding to the RPE and choriocapillaris is a good indicator of choroidal neovascularization (Figure 5-21). The ingrowth of new blood vessels through breaks in Bruch's membrane results in fragmentation and thickening of the posterior reflection due to the architecture of the neovascular membrane. This fragmentation and thickening may sometimes be difficult to discern, but may be associated with a thickening of the overlying neurosensory retina due to intraretinal or subretinal fluid leakage from the new vessels.

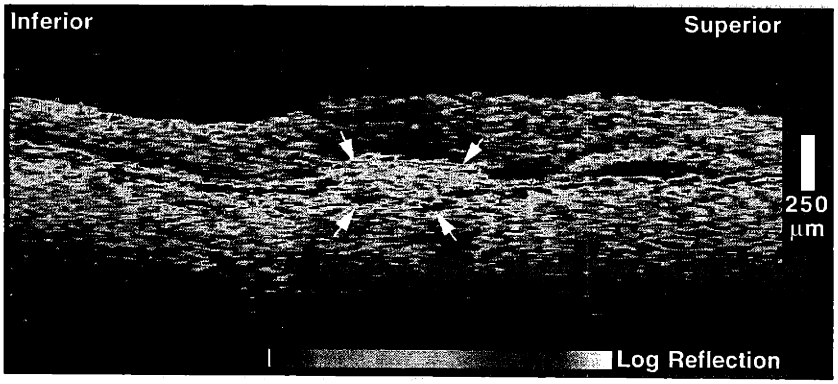

FIGURE 5-21. Choroidal neovascular membrane.

5.4.6 Vitreous and Vitreoretinal Interface

Many diseases of the vitreous and retina affect the vitreoretinal interface. The normal vitreous gel is optically transparent, providing a high contrast boundary between the vitreous and retina. Significant backscatter signal may be observed from the vitreous with inflammatory infiltrate (Figure 5-22), vitreous condensations, or hemorrhage (Figure 5-23). An operculum or pseudo-operculum may also present as a focal, thin area of backscatter anterior to the retinal surface. The posterior hyaloid membrane is nominally indistinguishable from the superficial retina on the OCT image, but becomes apparent when the posterior vitreous is detached (Figure 5-18). The reflection from the posterior hyaloid is typically weak and often appears patchy because the vitreous gel and the intervening fluid have similar indices of refraction.

An epiretinal membrane may be observed easily if it is separated from the neurosensory retina (Figure 5-24). Often, however, the membrane will be tightly adherent to the retinal surface, in which case the distinction between it and the retina depends on differences in optical reflectivity, and on the presence of secondary features, such as a macular pseudohole, or traction detachment of the retina. The reflection from an epiretinal membrane is usually stronger than that observed from the underlying retinal tissue.

An epiretinal membrane which is separated from the retina is distinguished from the posterior hyaloid based on the membrane's higher reflectivity, greater thickness, and differences in contour. A contracted epiretinal membrane usually has a flatter contour than a detached posterior hyaloid, indicating greater tension.

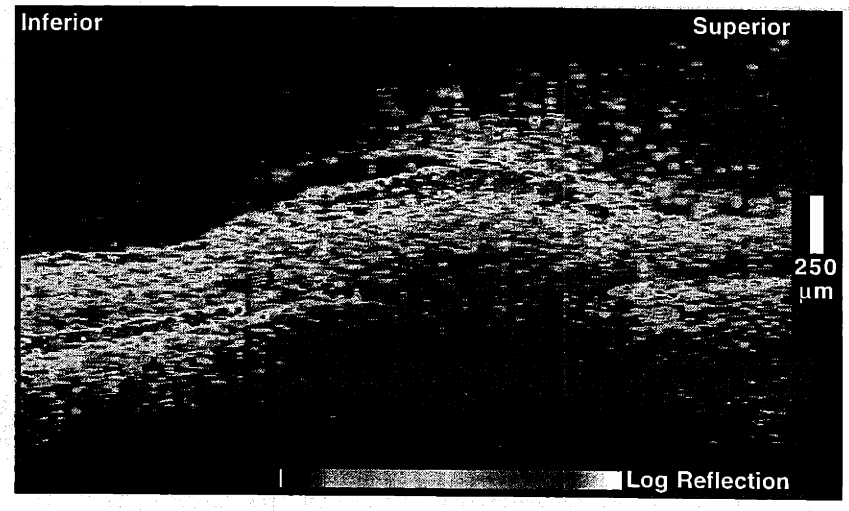

FIGURE 5-22. Vitritis.

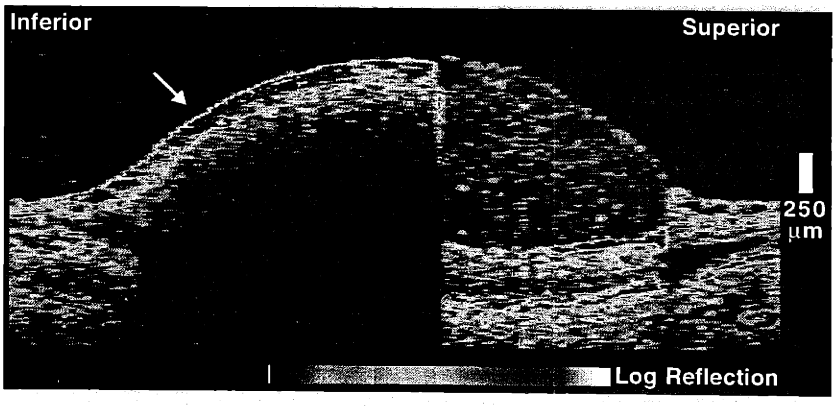

FIGURE 5-23. Subhyaloid hemorrhage *(arrow)*.

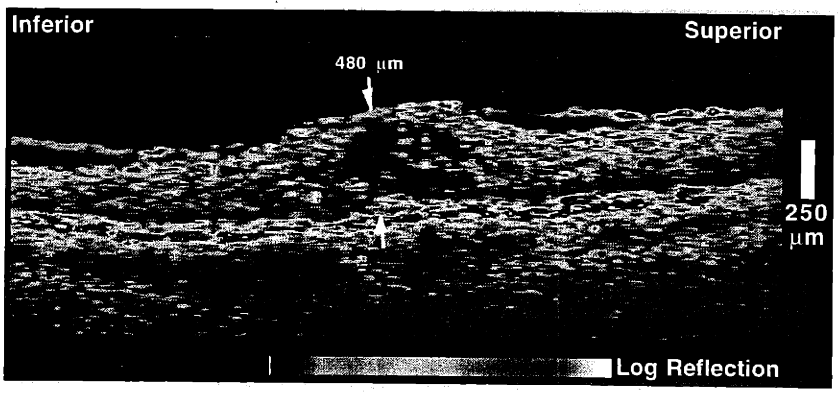

FIGURE 5-24. Epiretinal membrane.

5.4.7 Nerve Fiber Layer

Alterations in the thickness of the retinal nerve fiber layer may be a powerful indicator of the onset of neurodegenerative diseases such as glaucoma or fluid accumulation in papilledema and papillitis. The NFL appears in the OCT images as a highly backscattering layer in the superficial retina and exhibits increased reflectivity compared to the deeper retinal layers. NFL thickness may be assessed at individual points on a cylindrical or linear OCT in the peripapillary region. Alternatively a computer algorithm can be used to evaluate both retinal and NFL thickness. Figure 5-25 shows a clockwise circular OCT around a normal optic disc. Computer generated profiles of the NFL and retinal boundaries are displayed, and the NFL thicknesses are reported as either averages over each quadrant or clock hour (see Chapter 4 for more details).

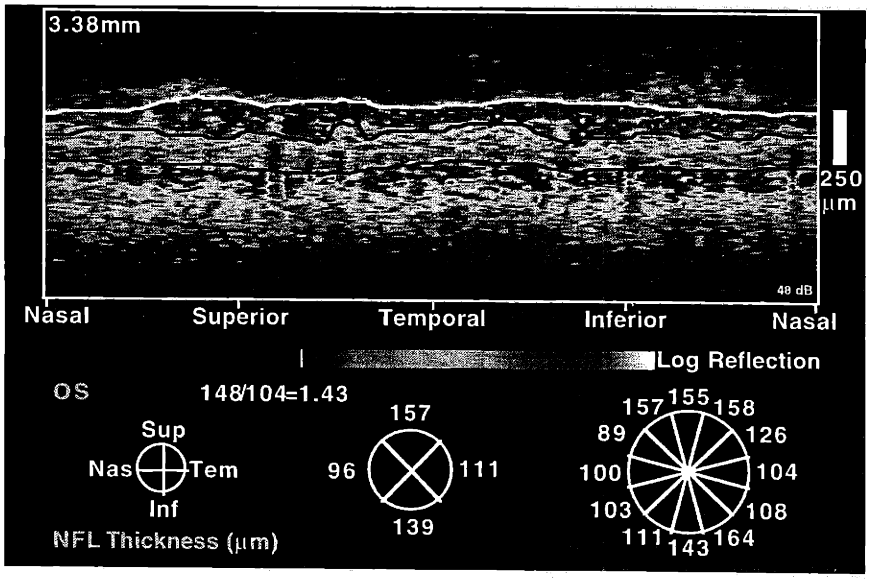

FIGURE 5-25. Circular OCT around a normal optic disc.

Careful inspection of the circular tomograms is required to identify focal NFL defects, which must be distinguished from normal variations in reflectivity and NFL thickness. The observation of depressions from both the anterior and posterior margins of the NFL is a helpful indicator of actual thinning.

5.4.8 Optic Disc

Linear OCTs through the optic disc are useful for assessing disc and cup parameters (Figure 5-26). The points at which the choriocapillaris terminates at the lamina cribosa may be used to determine the boundaries of the disc. Extrapolation of these points to the retinal surface defines a line segment which measures the disc diameter. Total retinal and retinal nerve fiber layer thickness can also be assessed at these points. The cup diameter may be estimated by choosing a line segment parallel to the line segment defining the disc diameter, but taken at a certain depth into the cup. The disc and cup diameters can provide an estimate of disc, cup,

and neuroretinal rim areas. The cross-sectional appearance of the disc can indicate papilledema when swollen (Figure 5-27), or glaucomatous atrophy when hollowed into a "U" shape (Figure 5-28).

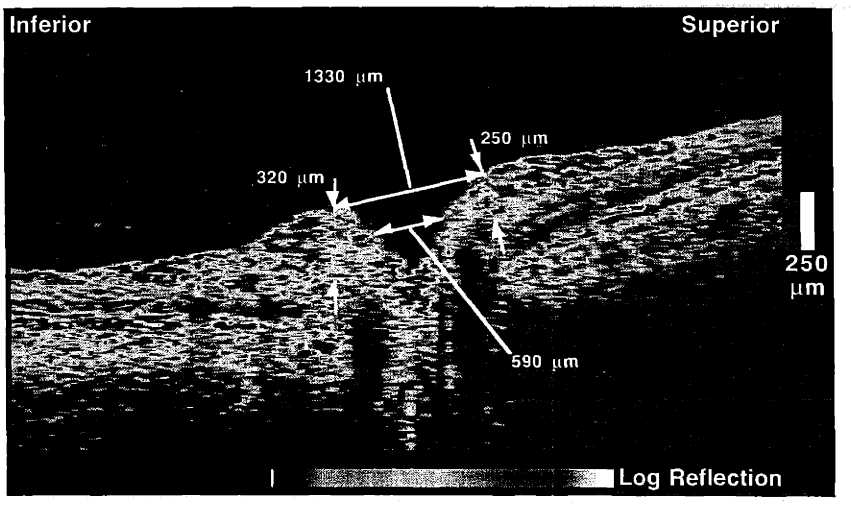

FIGURE 5-26. Normal optic disc with measurements of cup and disc diameter.

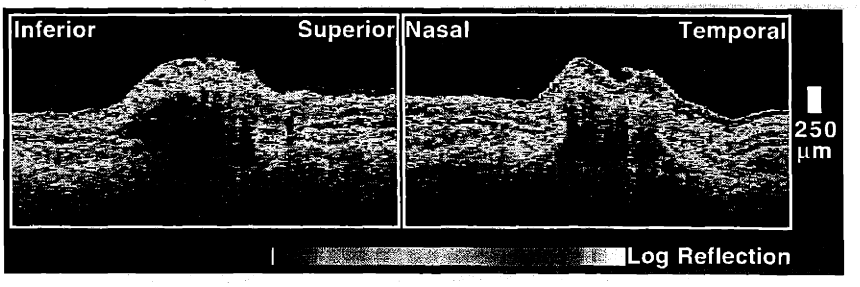

FIGURE 5-27. Swollen optic disc in papilledema.

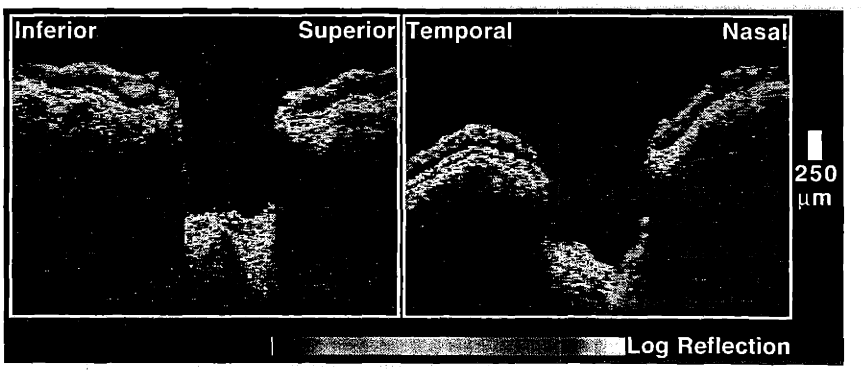

FIGURE 5-28. "U" shaped optic disc in end-stage glaucoma.

Chapter 6

MACULAR DISEASE

6.1 Introduction

OCT has found clinical application in the diagnosis and management of many macular diseases [26, 45, 101]. In particular, in preliminary clinical trials, OCT has proven to be the method of choice for the diagnosis and treatment follow-up of idiopathic macular hole [102]. The high axial resolution of OCT is also extremely useful for evaluating retinal detachments occurring in central serous chorioretinopathy [103], and retinal thickening due to macular edema [104]. In these conditions, OCT is capable of detecting small longitudinal changes in an objective and quantitative manner, in contrast to the traditional technique of slit-lamp biomicroscopy which is subjective. The topographic methods of mapping retinal thickness with multiple OCTs described in Chapter 4 are particularly effective in assessing retinal thickening in diabetic retinopathy, a leading cause of vision loss. OCT may have potential in providing a cross-sectional evaluation of age-related macular degeneration and choroidal neovascularization [105].

6.2 Macular Hole [102]

A macular hole in the fovea can cause a devastating loss of central vision. Recent advances in the surgical treatment of idiopathic full-thickness macular holes have increased the chances of recovering or preventing vision loss in patients with this disease [106-111]. Lesions that ophthalmoscopically resemble various stages of macular hole development, however, can be relatively common [112, 113]. Consequently, several techniques are currently under study which may provide additional diagnostic information in cases of macular hole. Laser biomicroscopy can improve the visualization of fine retinal structures when evaluating macular holes, but it is still limited by the comparatively coarse depth resolution of slit-lamp biomicroscopy [114]. Ultrasound B-scan has been useful in assessing the vitreoretinal interface and separation of the posterior hyaloid membrane which may be an important risk factor in hole development [115]. Echography can also provide information concerning macular thickening and the possible presence of an operculum [116]. The resolution of ultrasound, however, is fundamentally limited to approximately 150 μm axially and 500 μm transversely because of its acoustic wavelength in the retina. Thus, ultrasound cannot effectively cross-sectionally image macular holes, and cannot quantitatively evaluate hole diameter or small changes in subretinal fluid accumulation surrounding a full-thickness hole. Microperimetry with the scanning laser ophthalmoscope can assess small functional changes in visual field or fixation behavior in patients with macular holes, and is helpful in differentiating macular holes from macular cysts [117, 118].

6.2.1 Diagnosis of Macular Holes

The ability to differentiate a full-thickness macular hole from a macular pseudohole, partial-thickness hole, or a macular cyst is important in defining appropriate treatment. The high-resolution tomographic images provided by OCT can directly identify full-thickness holes by their complete loss of retinal tissue in the fovea. In contrast, macular pseudoholes and partial-thickness holes show an altered foveal pit contour with an intact outer neurosensory retina.

CASE 6-1. Macular hole and macular pseudohole (Figure 6-1). An 82-year-old woman had epiretinal membrane in both eyes *(top)*. In OCT of her right eye *(middle)*, the epiretinal membrane was associated with a full-thickness macular hole and a visual acuity of 20/100. Her left eye *(bottom)* had a visual acuity of 20/30 with a macular pseudohole. Retinal tissue was evident at the base of the pseudohole but not the macular hole. The epiretinal membrane was visible in the OCTs both eyes. In the right eye it was separated from the inner retinal surface while in the left eye it was tightly adherent to the inner limiting membrane *(arrow)*.

Lamellar or partial thickness macular holes, most often due to rupture of macular cysts, may also ophthalmoscopically resemble full-thickness holes. The visual acuity, which is often worse in eyes with a true macular hole due to the complete loss of photoreceptors, may not accurately indicate the diagnosis.

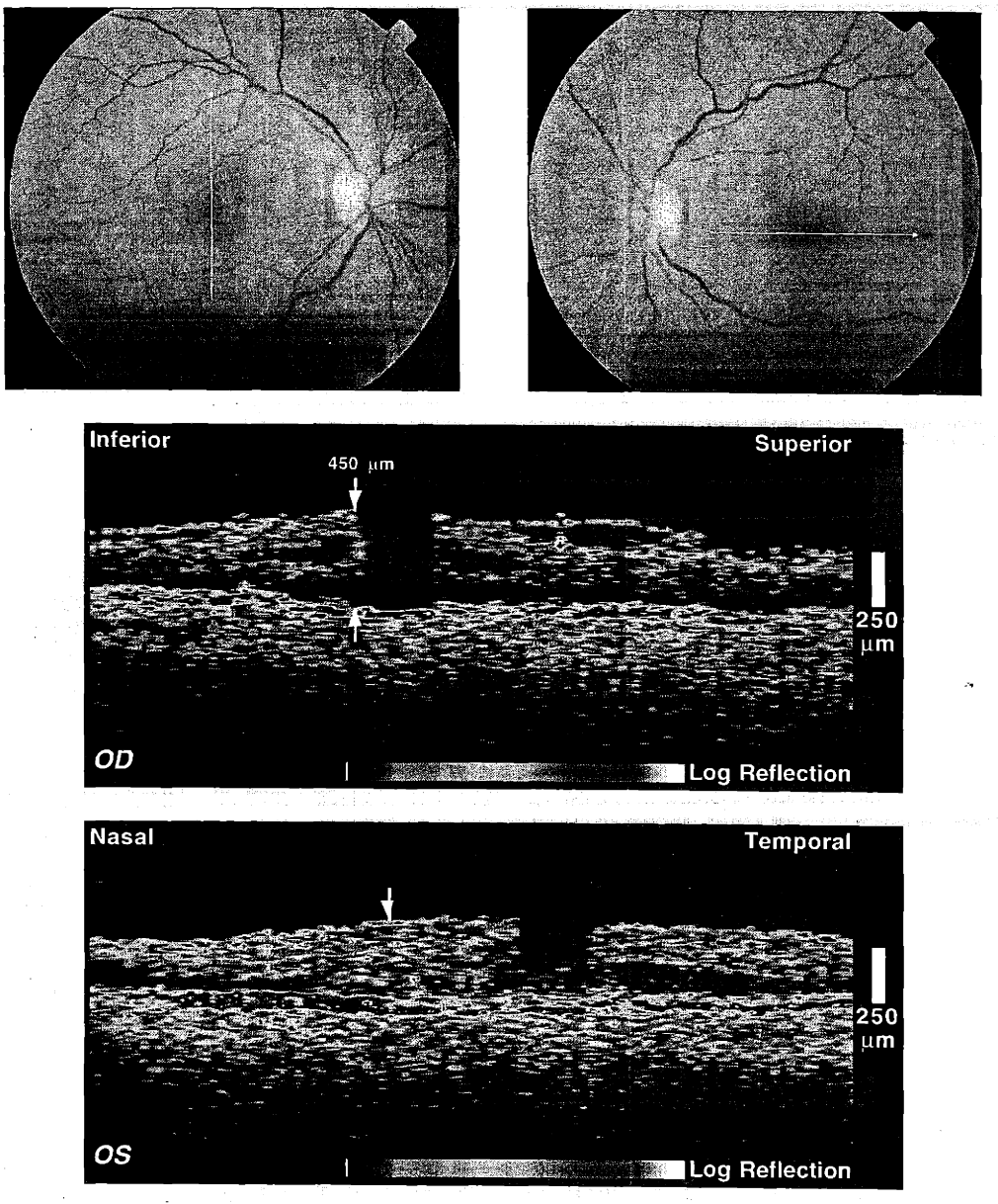

FIGURE 6-1. Case 6-1. Middle: macular hole OD. Bottom: macular pseudohole OS.

CASE 6-2. Macular hole and lamellar macular hole (Figure 6-2). A 69-year-old woman had a full-thickness macular hole in her right eye and a lamellar macular hole in the left. The visual acuity (20/100 OD and 20/200 OS) was worse in the eye with the partial thickness hole compared to the eye with a full-thickness hole.

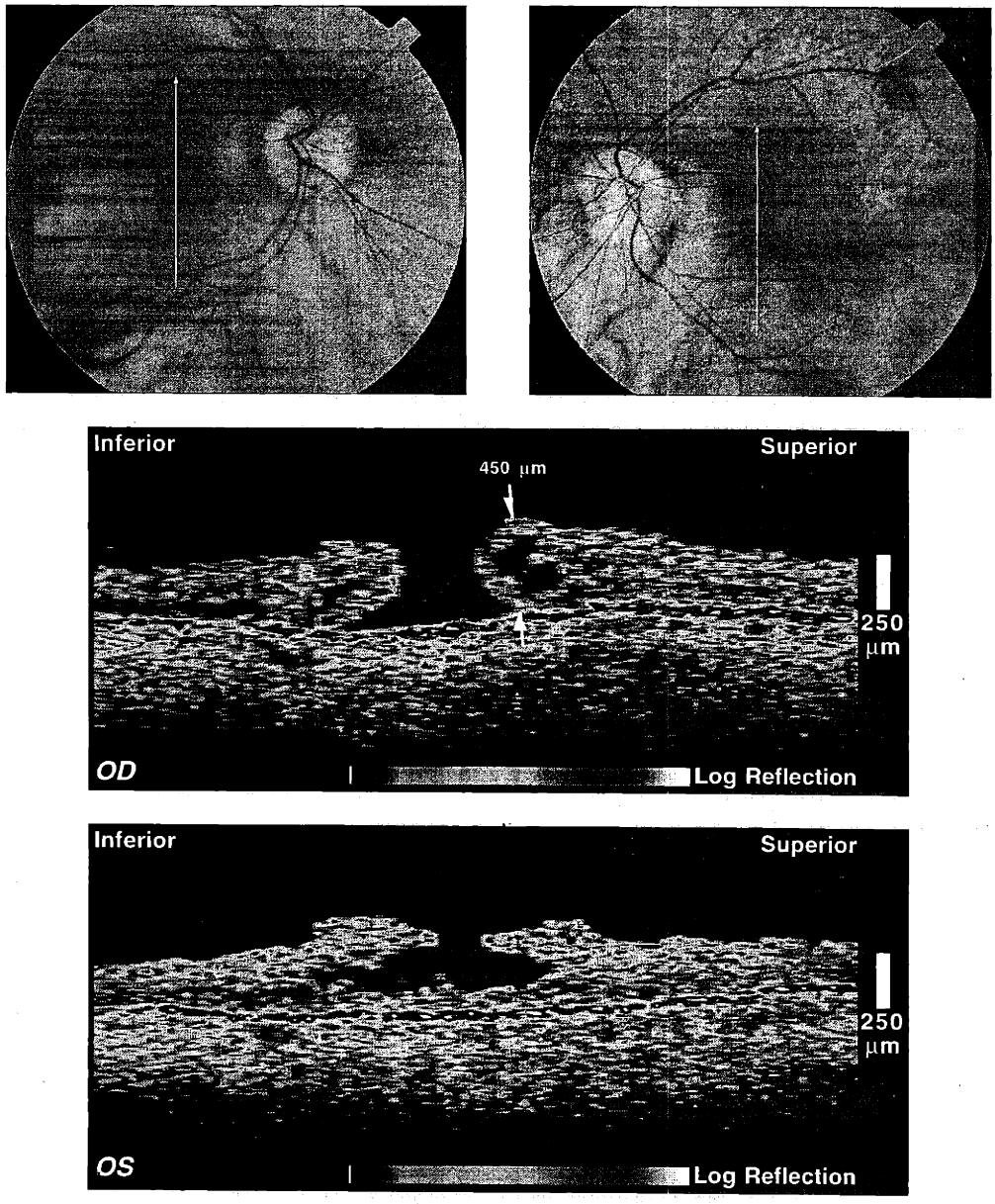

FIGURE 6-2. Case 6-2. Middle: full-thickness macular hole OD. Bottom: lamellar hole OS.

6.2.2 Staging of Macular Holes

Gass has described a system for staging the development of macular holes based on detailed biomicroscopic examination [119-121]. OCT confirms Gass' interpretation. A Stage 1, or impending hole, appears biomicroscopically as a yellow spot (Stage 1A) or ring (Stage 1B) corresponding to either a foveolar or foveal detachment respectively. On OCT, Stage 1 impending holes appear as a foveal cyst (Stage 1A) or foveolar detachment (Stage 1B) as shown in Figure 6-3. A Stage 2 macular hole consists of a partial break in the surface of the retina with a

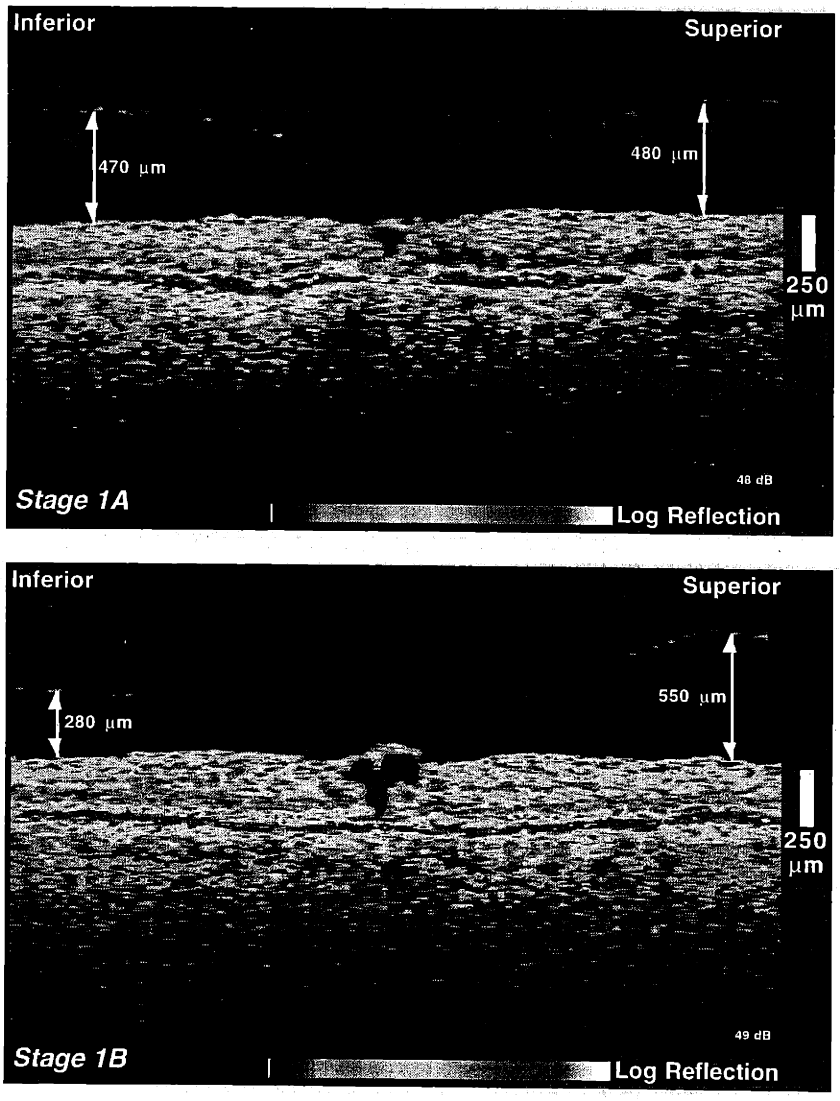

FIGURE 6-3. Impending macular holes. Top: Stage 1A. Bottom: Stage 1B.

small full-thickness loss of retinal tissue (Figure 6-4). Often the posterior hyaloid membrane can be observed inserting into an attached operculum. A Stage 3 hole is a fully developed hole. An operculum is sometimes visible and is completely separated from the edges of the hole. The degree of vitreofoveal separation may be assessed by the distance of the operculum from the surface of the retina, or in some cases by direct observation of the posterior hyaloid

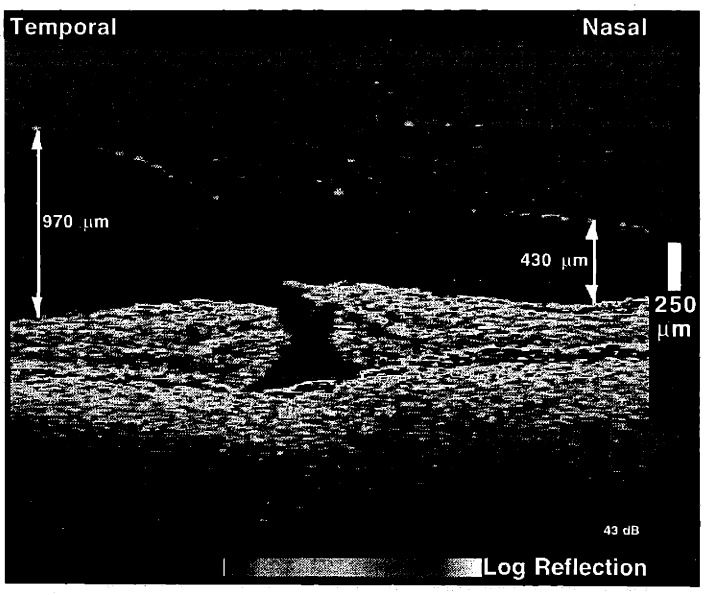

FIGURE 6-4. Stage 2 macular hole.

membrane (Figure 6-5). OCT also shows a variable range of surrounding retinal detachment and subretinal fluid accumulation. A complete separation of the posterior vitreous from the optic disc and macula is seen with a Stage 4 hole (Figure 6-6).

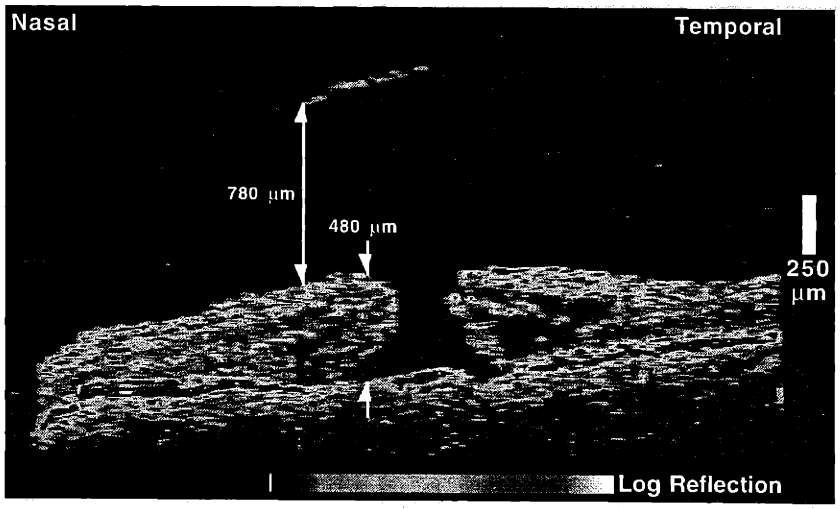

FIGURE 6-5. Stage 3 macular hole with operculum.

Accurate staging of macular holes may also be important for evaluating possible surgical interventions. According to one study, while most Stage 2 macular holes will progress to Stage 3 full-thickness holes with possible significant visual loss (acuity 20/70 to 20/200), approximately half of Stage 1 impending holes will abort with spontaneous vitreofoveal separation and an improvement in visual acuity to between 20/20 and 20/40 [112]. The aborted

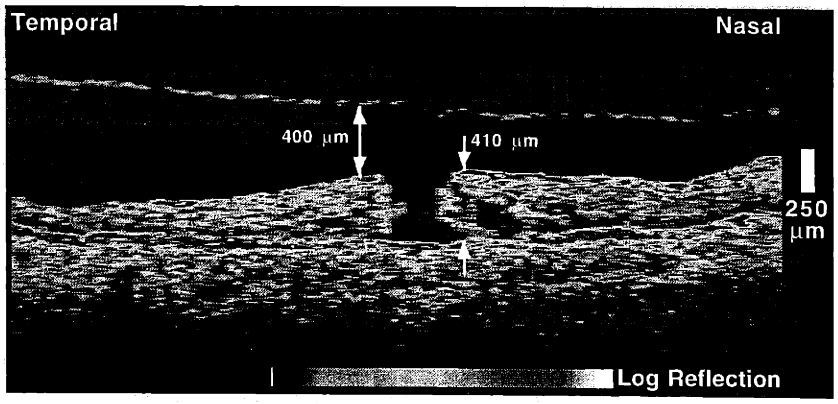

FIGURE 6-6. Stage 4 macular hole.

stage of hole formation is characterized by a pseudo-operculum in front of the fovea (Figure 6-7). Stage 1 holes, however, are difficult to diagnose and may simulate either Stage 2 or Stage 3 holes biomicroscopically [112].

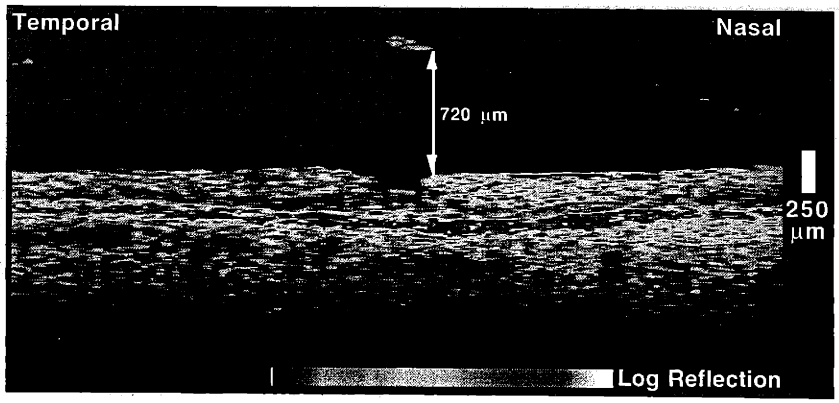

FIGURE 6-7. Aborted macular hole with pseudo-operculum.

6.2.3 Pathogenesis of Macular Hole Formation

Vitreomacular traction has long been implicated in the pathogenesis of hole formation. Several studies have shown that vitreous detachment or removal appears to protect against further hole development [122]. According to Gass, the traction by the posterior hyaloid is tangential, due to a shrinkage of the precortical vitreous [119, 121]. Studies with OCT have demonstrated that this traction is actually oblique, as depicted in Figures 6-3 and 6-4, and is temporally preceded by a perifoveal posterior vitreous separation with foveal adhesion.

CASE 6-3. Development of a macular hole. Figure 6-8 shows the development of a full-thickness Stage 2 macular hole as observed in the left eye (the fellow eye of a full-thickness macular hole) of a 63-year-old woman over a period of seven months. The initial OCT shows a perifoveal posterior vitreous detachment exerting oblique traction on a normal appearing fovea. No abnormalities on slit-lamp examination were observed at this time. The patient's visual acuity OS declined from 20/20 to 20/80 during this time period.

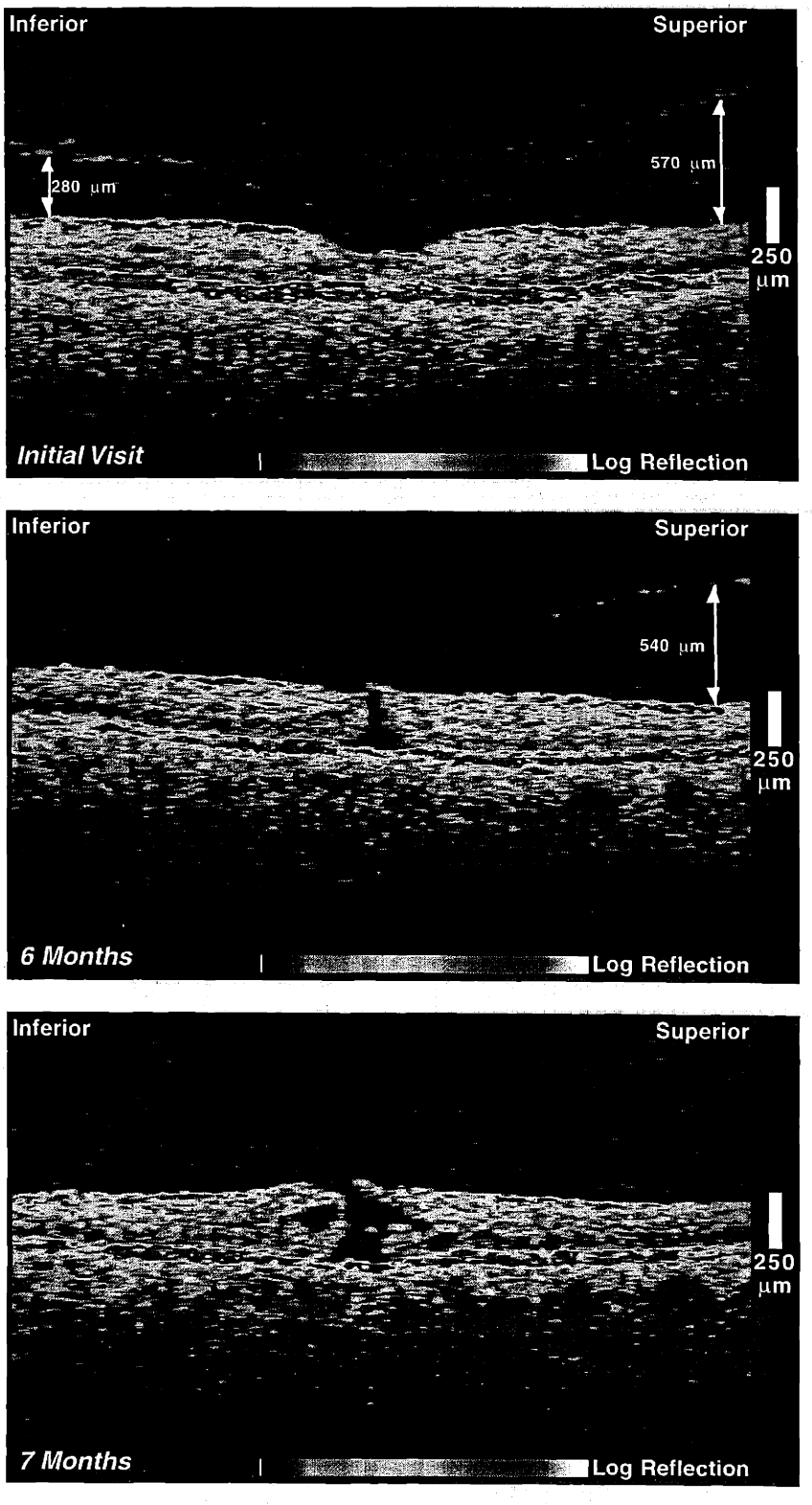

FIGURE 6-8. Macular hole pathogenesis (Case 6-3). Top: normal fovea with partial detachment of posterior vitreous exerting oblique traction. Middle: Stage 1B hole 6 months later. Bottom: Stage 2 hole after 7 months.

6.2.4 Fellow Eyes and Risk of Macular Hole Formation

The evaluation of the vitreomacular interface with OCT can help assess the risk of macular hole formation in the fellow eyes of macular holes. The a priori risk of hole development in a fellow eye is approximately 2% [123-125]. Hole formation can be effectively prevented with vitrectomy surgery, which has its associated risks of hemorrhage, retinal detachment, and epiretinal membrane formation [126]. Thus, OCT of the fellow eye may be important in evaluating potential vitrectomy to prevent full-thickness hole formation. Based on the pathogenesis of hole formation defined by OCT, either a Stage 1 hole or a partial posterior vitreous detachment with foveal adhesion might predict a high relative risk of hole formation in the fellow eye (Figure 6-9). A lower relative risk would be predicted with a complete posterior

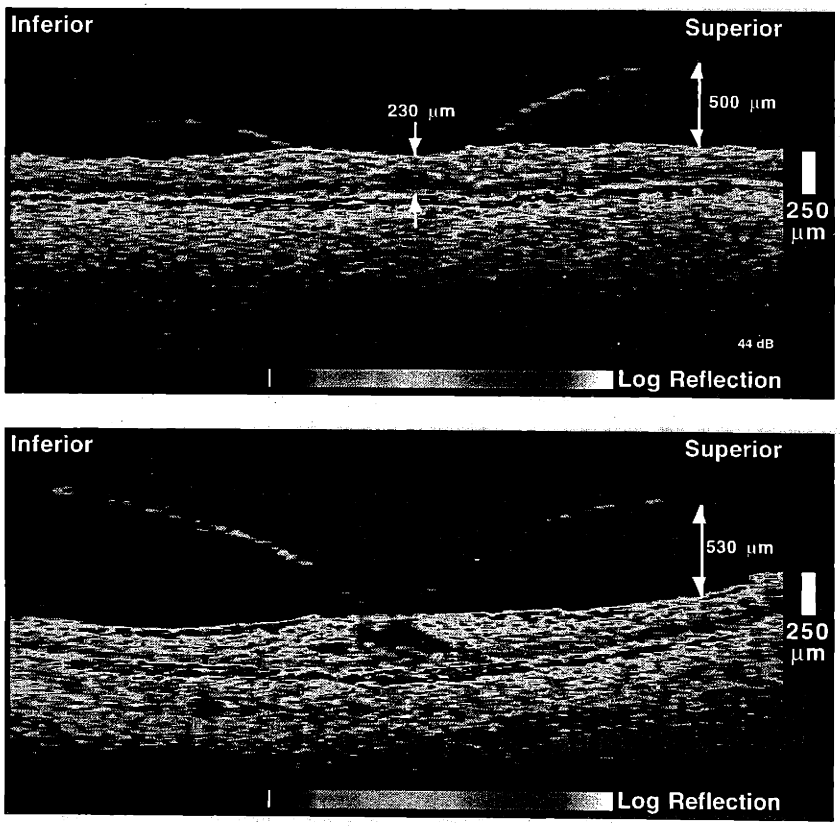

FIGURE 6-9. Fellow eyes with a predicted high relative risk of hole formation. Top: partial vitreous detachment with foveal adhesion. Bottom: impending macular hole.

vitreous detachment or a pseudo-operculum indicating an aborted stage of hole formation (Figure 6-10). A series of 49 fellow eyes of patients who had a full-thickness macular hole in contralateral eye were analyzed with OCT (Table 6-1). Table 6-1 shows that five (10%) of these eyes would be at a high or very high predicted relative risk of macular hole formation, while 14 (29%) would be regarded as having a low predicted relative risk of hole development.

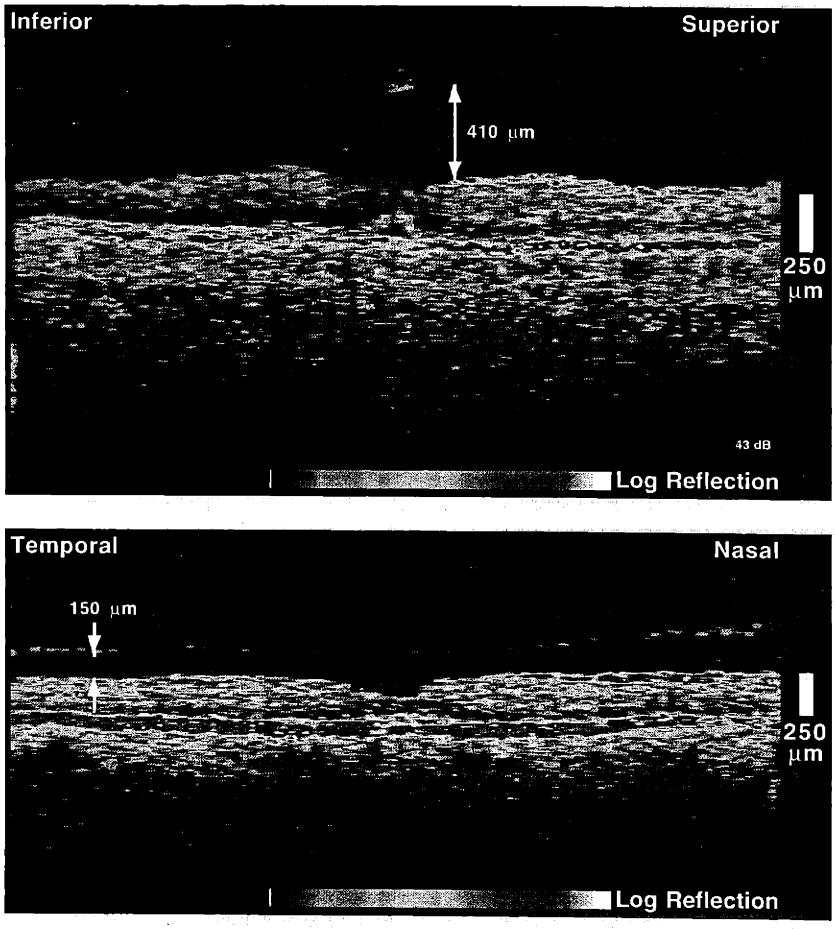

FIGURE 6-10. Fellow eyes with a predicted minimal relative risk of hole formation. Top: aborted Stage 1B hole with pseudo-operculum. Bottom: complete posterior vitreous detachment.

Foveal Morphology	Vitreous Status	Predicted Relative Risk	Eyes (N=49)
Normal	Attached	Moderate	18 (37%)
	Complete detachment	Low	13 (27%)
	Partial detachment with foveal adhesion	High	4 (8%)
	Pseudo-operculum	Low	1 (2%)
Impending (Stage 1) hole	Partial detachment with foveal adhesion	Very high	1 (2%)
Full-thickness hole	Variable	n/a	3 (6%)
Lamellar hole, epiretinal membrane, or cyst			6 (12%)
Other			3 (6%)

TABLE 6-1. Predicted relative risk of hole formation in the fellow eyes of macular holes based on the OCT description of foveal morphology and vitreous status.

6.2.5 Pre-Operative Surgical Evaluation of Macular Holes

Since the initial description by Kelly and Wendel [107] in 1991, vitrectomy and intraocular gas tamponade has been an accepted therapy for idiopathic macular hole. Wendel *et al.* [108] have shown that visual success, defined as two or more Snellen lines of improvement, can be achieved in 55% of eyes after macular hole surgery. A greater proportion (73%) of eyes may exhibit anatomic success, or flattening of the cuff of retinal detachment surrounding the hole as viewed by contact lens examination. However, the initial post-operative evaluation of patients who have received macular hole surgery may be difficult. The latency to visual improvement after surgery can range from a few weeks to many months [107] preventing a meaningful early assessment of visual success. The evaluation of anatomic success with indirect biomicroscopy can be difficult with small holes and may be complicated in the initial stages of recovery by a hazy post-operative view or the reflex from remaining intraocular gas.

The surgical prognosis of eyes undergoing macular hole surgery depends on many factors. Wendel *et al.* reported that visual success correlated inversely with the duration of symptoms. Other factors which may be important include the stage or size of the hole and surrounding cuff of subretinal fluid [109], the presence of an epiretinal membrane, patient compliance with strict face-down positioning, and the use of intraoperative adjuncts such as transforming growth factor β_2 (TGF-β_2) [110, 111] or autologous serum.

The ability of OCT to predict the anatomical outcome of macular hole surgery was assessed by retrospective examination of pre-operative OCTs in 27 patients. Seven of the 27 eyes had a Stage 2 hole, 13 eyes had a Stage 3 hole, and two eyes were Stage 4. Five eyes were examined before repeat surgery after previous vitrectomy surgery failed.

Measurements of macular hole various dimensions were extracted from the OCTs. Each measurement was tested with logistic regression analysis for a statistically significant correlation. The dependent variable was anatomic success or failure as evaluated by OCT. Measurements were extracted directly from the single best OCT obtained through the center of each macular hole. Several dimensions were measured, including the minimum hole diameter, the diameter at the base (retinal pigment epithelium) of the hole, and the distance between the base and the top of the hole (a measure of the surrounding retinal detachment and intraretinal edema). The minimum hole diameter was measured parallel to the contour of the base diameter at the point of minimum separation between the left and right hole edges. An operculum, if present, was disregarded in the measurement.

A composite, dimensionless *hole form factor* was also investigated. For each image of a macular hole, a trapezoid was formed using the two parallel line segments defining the base and minimum hole diameters. The lengths of the left and right arms of the trapezoid were measured and the following parameter was constructed:

$$\text{form factor} = \frac{\text{left arm length} + \text{right arm length}}{\text{base diameter}}. \tag{6.1}$$

Examples of these measurements are provided in Figures 6-11 and 6-12 below. The form factor was expected to yield quantities close to 1.0 for holes which (approximately) had sufficient tissue in the surrounding cuff of retinal detachment to span the entire base diameter of the hole. This parameter considered the ratio between the overlying tissue dimensions and the hole base diameter to be more important than the hole base diameter alone. Holes with an anvil or hourglass configuration (Figure 6-11) were weighted as more amenable to surgery than holes with a punched-out or rectangular configuration (Figure 6-12). Tall and narrow holes were deemed more likely to close than short and wide holes.

Measurements of hole base diameter and hole height were not correlated by logistic regression to the anatomic outcome ($p = 0.4$ and $p = 0.5$ respectively). The minimum hole diameter approached significance ($p = 0.06$) with larger diameters predicting a reduced probability of anatomic success. The composite hole form factor was significantly associated with the probability of anatomic success ($p = 0.02$). The logistic relationship between the hole form factor and the probability of anatomic success is plotted in Figure 6-13 using the maximum likelihood parameters estimated from the data. Form factors close to 1.0 suggest an increased probability of hole closure. Figure 6-13 demonstrates that eyes with form factors greater than 0.9 have a greater than 80% chance of anatomic success, while form factors less than 0.5 predict a success rate smaller than 25%. A histogram showing the frequency and range of form factors is shown on the same scale as the regression plot. In the current series of eyes, clinically useful pre-operative predictions of prognosis (*i.e.* a predicted success rate greater than 80% or less than 25% which might have influenced the decision to proceed with surgery) would have been obtained in approximately six of 28 (21%) surgeries.

Although the logistic model was statistically significant, the study has several limitations. A limited population was used which was not controlled for other factors which could influence anatomic and visual success. These factors included the duration of symptoms, the use of intraoperative adjuncts such as autologous serum, first versus repeat operations, and concurrent cataract surgery.

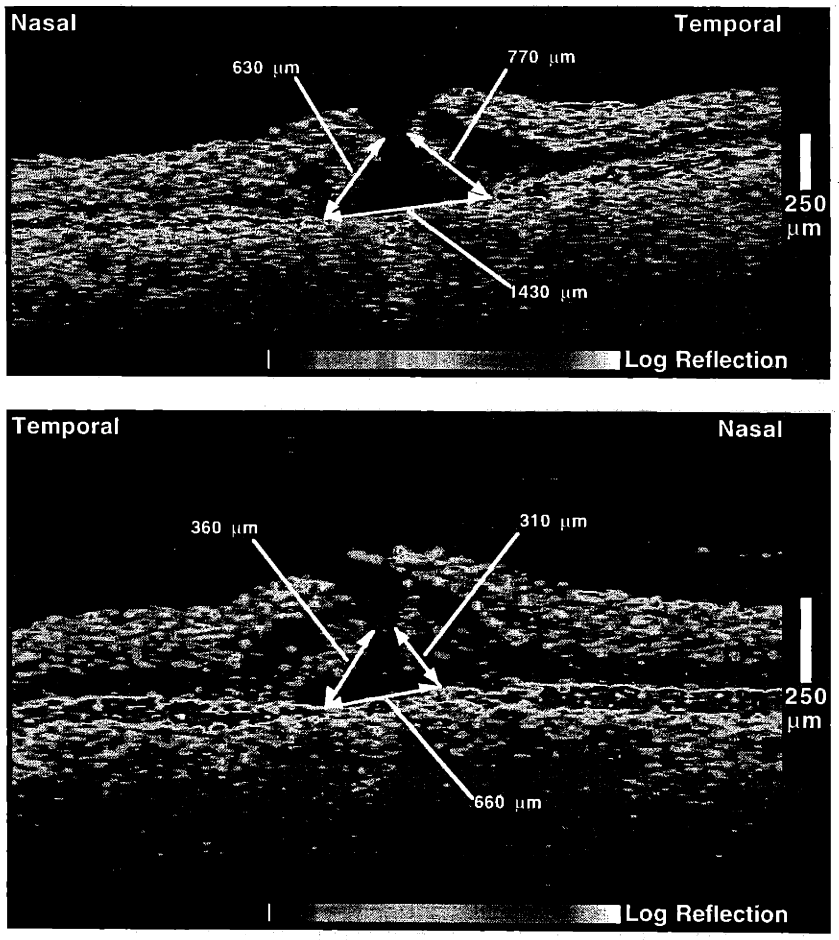

FIGURE 6-11. Macular holes with a form factor close to one suggesting an increased probability of anatomical surgical success.

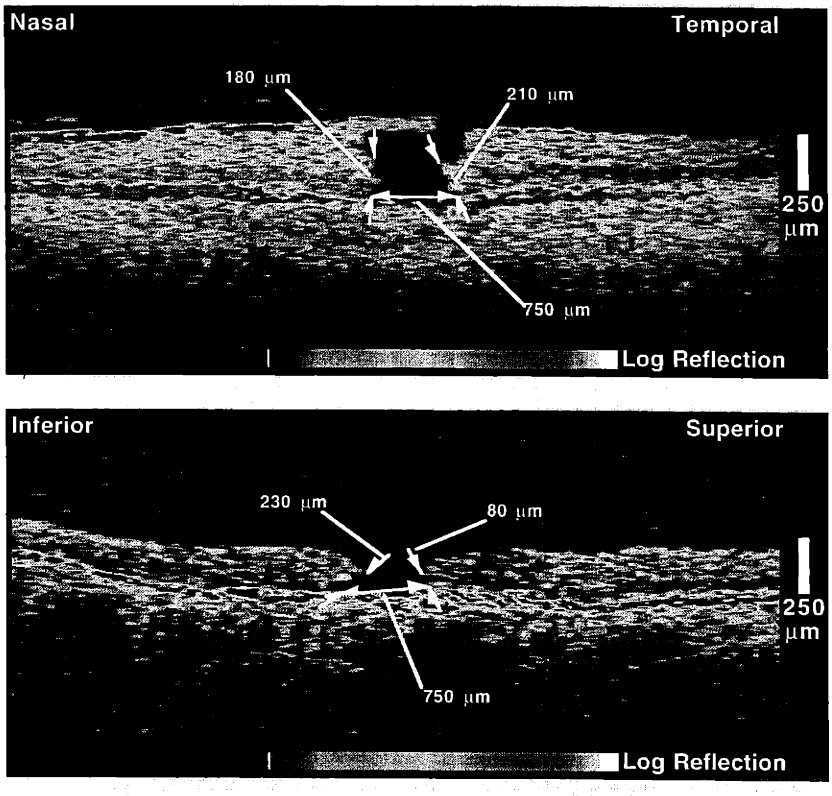

FIGURE 6-12. Macular holes with a small form factor suggesting a reduced probability of anatomical surgical success.

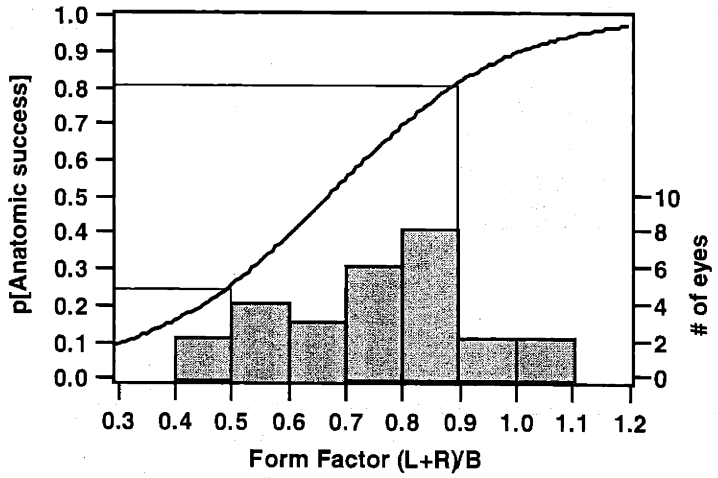

FIGURE 6-13. Prognosis of macular hole surgery with histogram.

6.2.6 Post-Operative Surgical Evaluation of Macular Holes

Post-operative OCTs could be classified into one of the four following categories each defining a distinct anatomic appearance of the fovea:

- *Open*: A full-thickness hole remains in the macula.
- *Closed*: Reapproximation of the edges of the hole is achieved and the foveal structure appears normal. The central foveal thickness is greater than 100 μm. (Figure 6-14)
- *Thin*: The retina is reattached surrounding the hole with an absence of intraretinal or subretinal fluid. However, the central foveal thickness measures less than 100 μm (Figure 6-15).
- *Foveolar detachment*: Reapproximation of the edges of the hole is achieved. However, a pocket of subretinal fluid remains directly beneath the fused edges (Figure 6-16).

Anatomic success as determined by OCT was defined by the subtypes of *closed, thin,* or *foveolar detachment*. Anatomic failure corresponded with a classification of *open*.

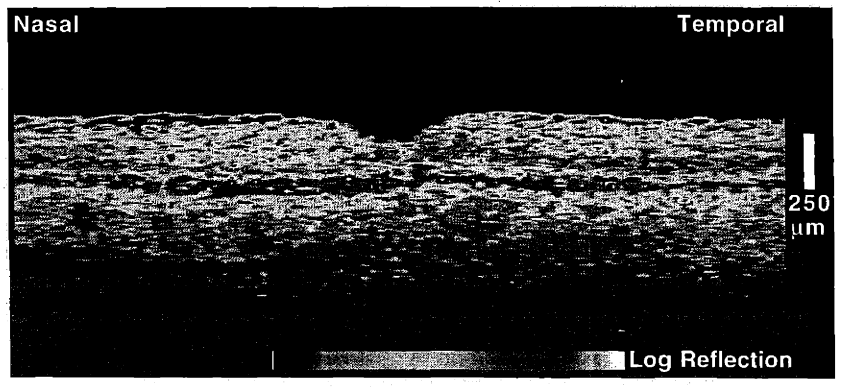

FIGURE 6-14. *Closed* hole and normal fovea after macular hole surgery.

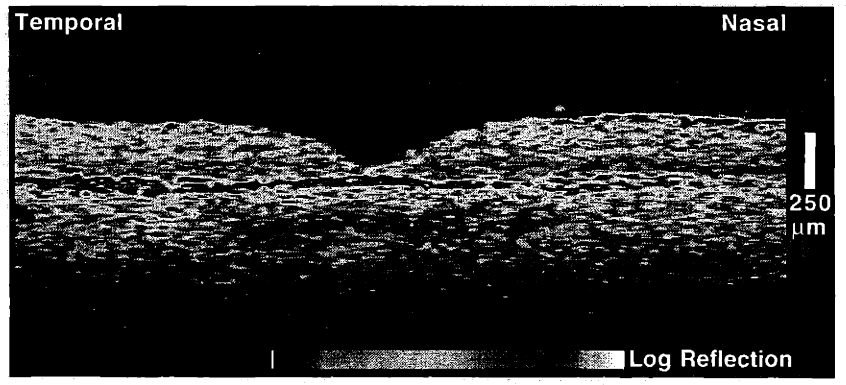

FIGURE 6-15. *Thin* fovea after macular hole surgery.

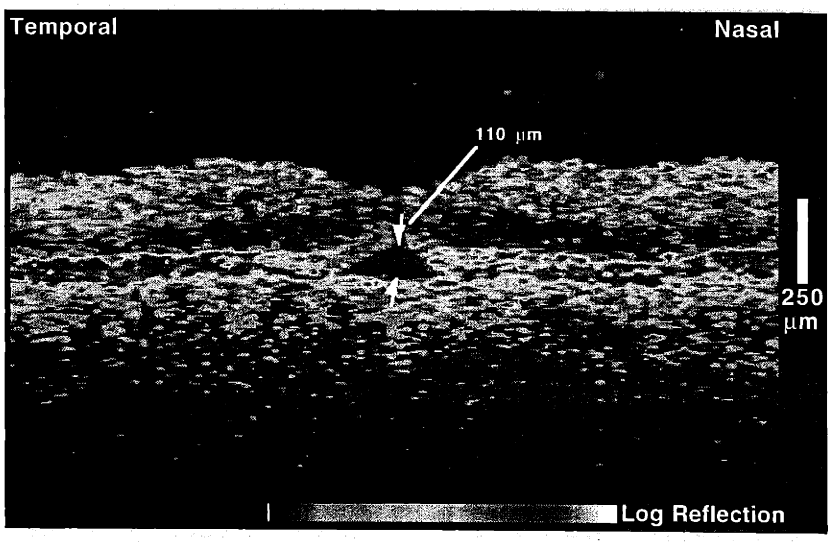

FIGURE 6-16. *Foveolar detachment* after macular hole surgery.

Table 6-2 compares the OCT classification of post-operative foveal anatomy with both biomicroscopic observation and resulting visual success or failure in 39 eyes which had received surgery for a full-thickness macular hole. In general, the OCT assessment of ana-

# of Eyes		Slit-lamp Biomicroscopy		Visual Acuity	
		Anatomic Success	Anatomic Failure	> 2 Lines Improvement	≤ 2 Lines Improvement
OCT	Anatomic Success	21	2	18	5
	Anatomic Failure	2	14	2	14
OCT Success Subtypes	Closed	10	0	8	2
	Foveolar Detachment	3	2	4	1
	Thin	8	0	6	2

TABLE 6-2. OCT compared to biomicroscopy and visual acuity after macular hole surgery.

tomic success or failure corresponded with both biomicroscopic examination (χ^2 test, $p = 2 \times 10^{-7}$) and visual success or failure (χ^2 test, $p = 2 \times 10^{-5}$). There were exceptions, however. In two eyes OCT demonstrated reapproximation of hole edges and a *foveolar detach-*

ment while clinical examination observed no hole closure. There were also two eyes in which biomicroscopy showed no evidence of a remaining hole, but OCT demonstrated a full-thickness defect. A significant improvement in visual acuity was noted post-operatively in these same two eyes. Finally, five eyes with anatomic success as evaluated with OCT did not show an improvement in visual acuity after surgery. At least three of these five eyes had been symptomatic for longer than six months.

Macular holes that were completely *closed* after surgery demonstrated a normal appearing fovea on OCT with a complete reapproximation of the hole edges. In studies where histopathological correlation has been obtained in surgically treated macular holes, reapproximation of hole edges was also observed [127, 128]. A small (< 20 μm) break in the external limiting membrane was typically evident with apparently normal photoreceptors adjacent to the break. Glial cell proliferation was sometimes present. The resolution and contrast of the OCT images was not sufficient to identify either of these features. However, the optical reflectivity from the photoreceptor layer in these treated holes appeared normal on OCT examination. Three holes which were initially closed post-operatively exhibited late reopening. Tangential traction by a developing epiretinal membrane has been hypothesized to play a role in reopening [129]; however, no evidence of such a process was observed in the OCT images.

Post-operative foveas classified as *thin* were also considered to be successful anatomic outcomes based on the reattachment of the rim of retina and reduction in macular edema surrounding the hole. Minimal retinal tissue was evident in the central fovea in these eyes on OCT. This tissue may correspond to fibroglial proliferation which sealed the hole, but still left a gap between the hole edges. A similar finding was noted in a previous histopathological study of a spontaneously sealed hole [130].

Eyes with a post-operative *foveolar detachment* exhibited reapproximation of hole edges above a small collection of subretinal fluid. The eyes in this category were most likely to be the source of disagreement between biomicroscopic and OCT examination. This disagreement was perhaps due to a misinterpretation of the detachment as indicating a free hole edge on biomicroscopy. Multiple follow-up OCTs were obtained in two of five eyes with a foveolar detachment. In both of these eyes, continuing resolution of subretinal fluid was accompanied by improvements in visual acuity over a period of several months. In one eye, the foveolar detachment completely resolved after five months leaving a completely closed hole with a normal appearing fovea. It is possible that most holes which will eventually close after surgery pass through a foveolar detachment phase during the recovery process. The difference between the two OCT classifications may reflect a difference in latency between the initial and final post-operative anatomic result. More detailed studies are needed to determine whether this latency period may be related to factors such as intraocular pressure or patient compliance with strict prone positioning. This hypothesis suggests that eyes with a foveolar detachment which show no progressive anatomic or visual improvement may benefit from simple outpatient gas injection alone followed by face-down positioning, rather than a repeat pars plana vitrectomy with complete air-fluid exchange.

Figure 6-17 shows post-operative visual acuity organized by OCT anatomic classification. Visual acuities were converted the logarithm of the minimum angle of resolution (MAR) as follows: if the visual acuity is represented as

$$\text{visual acuity} = \frac{\text{testing distance}}{\text{distance for normal eyes}} \tag{6.2}$$

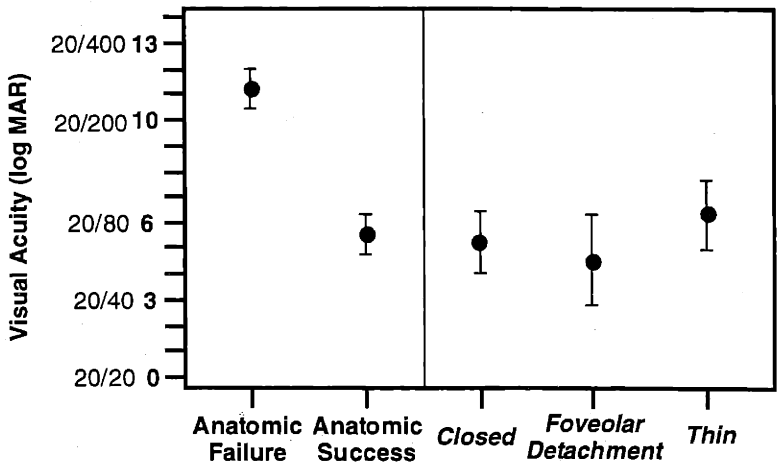

FIGURE 6-17. Visual acuity after macular hole surgery.

then the log MAR score is defined as

$$\log MAR = 10\log\left(\frac{\text{distance for normal eyes}}{\text{testing distance}}\right). \tag{6.3}$$

Therefore a log MAR score of 0 corresponds to 20/20 vision and each doubling of the visual angle increases the score by 3 units (*e.g.* 20/40 = 3, 20/80 = 6, 20/100 = 10). Figure 6-17 shows that the mean log MAR score of 5.5 (about 20/70) for eyes with anatomic success by OCT was significantly lower than the mean score of 11.2 (about 20/300) for unsuccessful eyes (Student's T-test, $p = 4 \times 10^{-5}$). Each of the different subtypes of anatomic success (*closed, thin, foveolar detachment*) had a significantly lower mean log MAR score than the mean score for anatomic failure. However, the differences between the three subtypes of anatomic success were not significant at the 0.05 level. Mean visual improvement in log MAR units was also tested (Figure 6-18). Anatomically successful surgeries resulted in a mean improvement of 3.1 units (halving of the minimum visual angle) while unsuccessful surgeries showed a decrement of 0.47 units. This difference was statistically significant (Student's T-test, $p = 0.007$). No significant differences in visual improvement were noted between the four OCT classifications individually due to the small sample sizes (ANOVA, $p = 0.08$). Also, five eyes had a follow-up period of less than six weeks which could have influenced post-operative measurements of visual acuity.

Anatomic outcome was correlated with the pre-operative hole form factor (defined in Section 6.2.5). Eyes classified as *open* or *thin* had a mean form factor 0.67 whereas eyes categorized as *closed* or *foveolar detachment* had a mean form factor of 0.84. This difference was statistically significant (Student's T-test, $p = 0.008$).

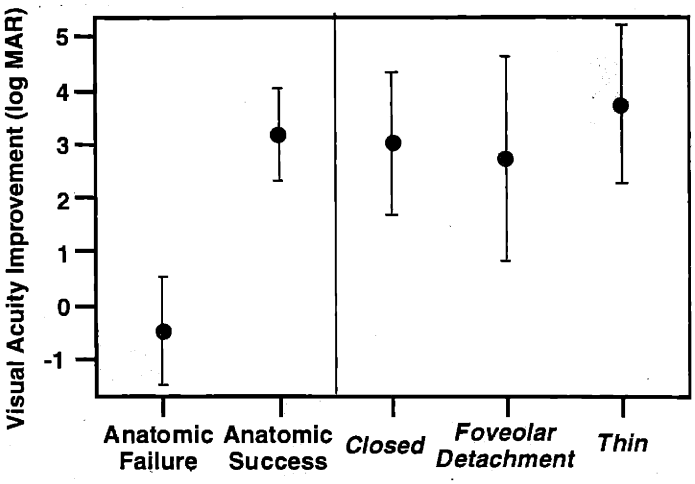

FIGURE 6-18. Visual acuity improvement after macular hole surgery.

6.2.7 Limitations of Macular Hole Imaging.

Further study is needed to determine the sensitivity of OCT in picking up the weak reflection from the posterior hyaloid. When the posterior vitreous boundary was visible on the OCTs it was very close to the detectivity limit of the system. It is possible that eyes which were evaluated as having no posterior vitreous detachment actually did have a detachment which was undetectable, giving a false-negative result.

The accuracy of pre-operative OCTs depended on the examiner's ability to place the probe beam on the center of the hole, since OCTs obtained through peripheral portions of the hole would lead to incorrect measurements of hole diameter. In practice, since the hole was often difficult to identify on the infrared video camera monitor of the fundus, multiple OCTs were acquired at slightly varying positions through the fovea. The OCT with the largest reproducible hole base diameter was then selected as representing the center of the hole. Artificially large hole diameters could appear in the images, however, if the patient visually tracked the scanning probe beam during image acquisition. Thus, the examiner was required to carefully monitor the infrared view of the fundus to ensure that such tracking did not occur. It should be noted that the use of the hole form factor, which is approximately a dimensionless ratio of transverse lengths, minimizes the adverse effects of visual tracking and eccentrically placed scans compared to measurements of hole diameter alone.

6.3 Central Serous Chorioretinopathy [103]

Central serous chorioretinopathy is a frequently encountered retinal disorder, which in its most prevalent form involves a detachment of the neurosensory retina secondary to one or more focal fluorescein angiographic leaks at the level of the retinal pigment epithelium [131-135]. The duration of the sensory retinal detachment varies, but usually it resolves within 4 to 6 months [133-136]. Typically the young to middle-age male is affected during a period of unusual emotional stress. Currently, the techniques for monitoring resolution of the detachment are limited to slit-lamp biomicroscopy and fluorescein angiography. OCT provides a means for quantitatively monitoring the extent and height of the retinal detachment which is more sensitive to small changes than biomicroscopy. Longitudinal examinations with OCT are able to track the natural resolution of the sensory retinal detachment and reductions in subretinal fluid accumulation are often noticed before subsequent improvements in visual acuity.

CASE 6-4. Resolution of central serous chorioretinopathy (Figure 6-19). A 57-year-old man noticed an abrupt onset of visual blurring in his left eye over the period of a day. He described the area as gray with sharply defined borders. Slit-lamp biomicroscopy showed a shallow serous elevation of the neurosensory retina in the macula including the fovea *(top, left)*. His visual acuity in this eye was 20/25. Fluorescein angiography displayed multiple, focal areas of hyperfluorescence *(top, right)*. An area superotemporal to the fovea showed increasing hyperfluorescence with intense late leakage. Two hyperfluorescent spots were also noted superior to the optic disc and nasal to the fovea, consistent with either pigment epithelial detachments or window defects. A horizontal OCT *(top)* directly through the fovea illustrated a 230 μm elevation of the neurosensory retina above an optically clear space corresponding to a fluid-filled cavity. The patient returned for a follow-up visit six weeks later with no improvement in visual acuity. Slit-lamp examination revealed that the serous elevation had decreased since the previous visit. A repeat OCT *(middle)* taken at this time confirmed the decrease in subretinal fluid accumulation to 120 μm directly beneath the fovea. On follow-up examination another two months later, the patient noted a decrease in the size of the scotoma in his left eye, and his visual acuity had returned to 20/20. There was no remaining subretinal fluid observed on indirect ophthalmoscopy. A third OCT *(bottom)* showed that the detachment had completely resolved directly beneath the fovea. However, a residual region of fluid accumulation remained temporal to the fovea.

Before the onset of symptoms, patients usually develop areas of serous RPE detachment which eventually lead to detachment of the overlying and surrounding retina. The size of the RPE detachment is variable and often difficult to detect.

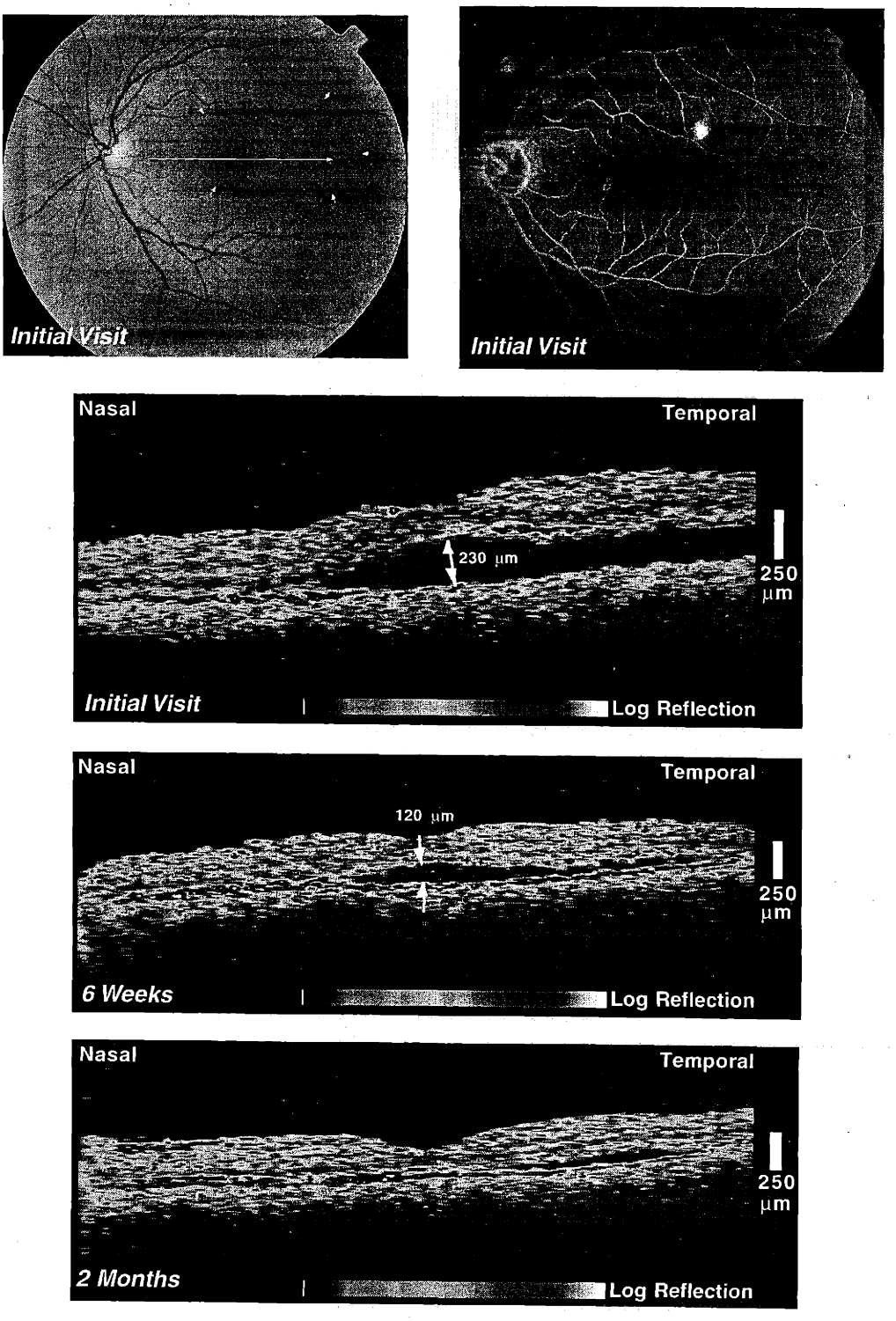

FIGURE 6-19. Natural resolution of central serous chorioretinopathy (Case 6-4).

CASE 6-5. RPE break in central serous chorioretinopathy (Figure 6-20). The left eye of 35-year-old man with a history of central serous chorioretinopathy in his right eye was examined. Indirect ophthalmoscopy revealed a small RPE detachment at the temporal edge of the macula. Fluorescein angiography *(top)* showed pooling of dye within the detachment surrounded by a large area of hyperfluorescence *(arrows)*. OCT *(middle and bottom)* demonstrated a subfoveal pigment epithelial detachment surrounded by a neurosensory detachment consistent with central serous chorioretinopathy. The vertical OCT *(bottom)* identified an RPE break allowing communication of fluid between the RPE detachment and the neurosensory elevation *(arrow)*.

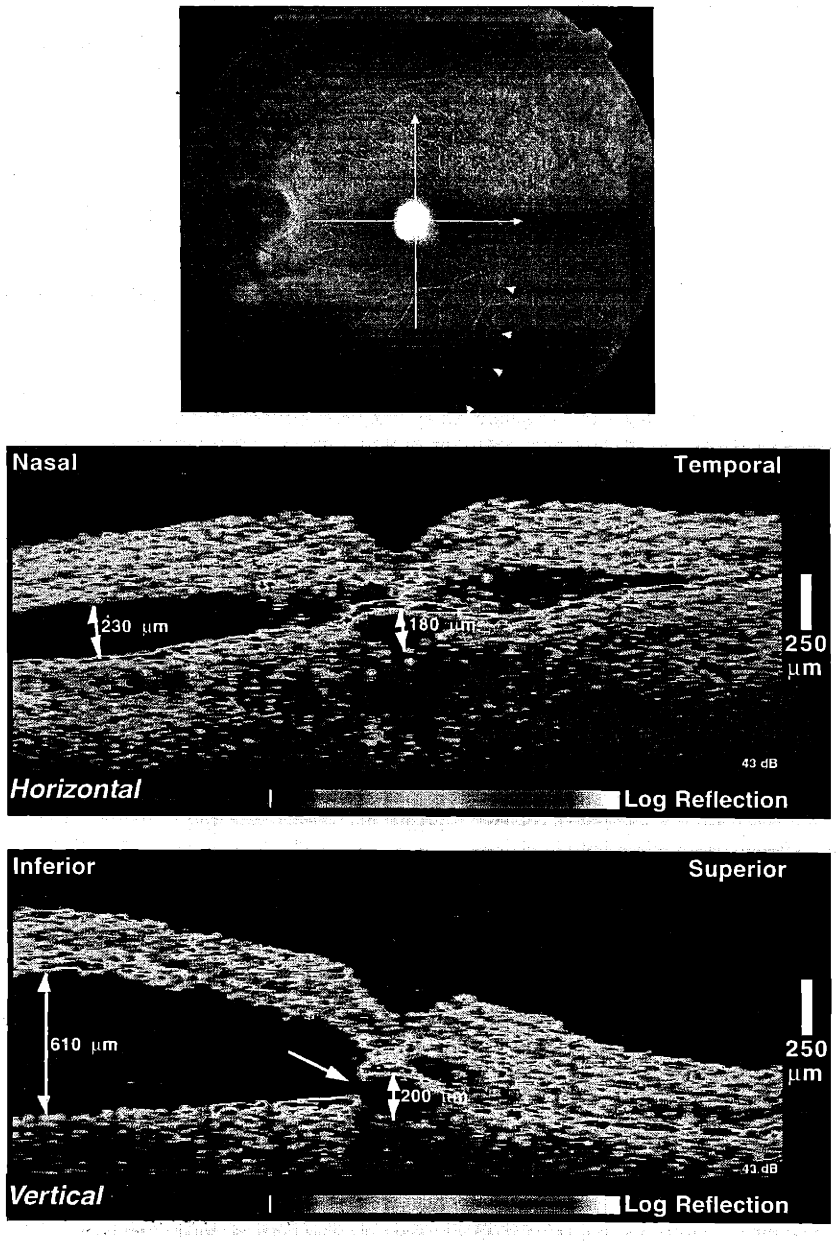

FIGURE 6-20. RPE break in central serous chorioretinopathy (Case 6-5).

If visual symptoms persist for an abnormally long period, or if the patient's occupation requires that visual improvement occur more rapidly, laser photocoagulation treatment may be applied to leakage points observed on fluorescein angiography.

CASE 6-6. Laser treatment of central serous chorioretinopathy (Figure 6-21). A 65-year-old man noted decreasing vision in his right eye over the period of 1 month. On examination, his visual acuity in this eye was 20/50. Indirect ophthalmoscopy showed a serous elevation of the neurosensory retina directly in the macula. A small hyperfluorescent spot with late leakage superior to the fovea was seen on fluorescein angiography *(top, left)*. A vertical OCT *(middle)* was obtained slightly nasal to the fovea through both the neurosensory detachment and the hot spot located superior to the fovea displayed on angiography. The OCT showed a small serous retinal detachment, with a height of 110 μm. The neurosensory retina above the detachment was thickened consistent with edema. A focal elevation of the RPE was noted just superior to the neurosensory detachment, consistent with a small serous detachment of the RPE *(arrow)*. The patient elected to receive argon laser photocoagulation treatment in this eye, applied to the hot spot observed on fluorescein angiography. On follow-up examination one month later, he described greatly improved vision and his acuity had returned to 20/25. Slit-lamp examination showed that the retinal detachment had flattened. A repeat OCT *(bottom)* confirmed resolution of the serous detachment disappearance of the intraretinal edema. A slight disturbance in the RPE was seen consistent with a laser scar *(arrow)*. The reflectivity from the photoreceptors in this area also appeared to be increased.

The diagnosis of central serous chorioretinopathy may be difficult in cases where the serous detachment is small. OCT appears to be highly sensitive to small elevations of the neurosensory retina because of the clear difference in optical reflectivity between retinal tissue and serous fluid. Although central serous chorioretinopathy typically affects adults between 20 and 50 years of age, the disease may be mistaken for age-related macular degeneration and subretinal neovascularization in older patients [137]. The occult form of choroidal neovascularization may show a similar angiographic appearance to central serous chorioretinopathy when a focal leakage point is present. OCT can provide additional diagnostic information in these cases by confirming the existence of a neurosensory detachment versus abnormalities in the choriocapillaris or RPE caused by a neovascular membrane (see Section 6.5).

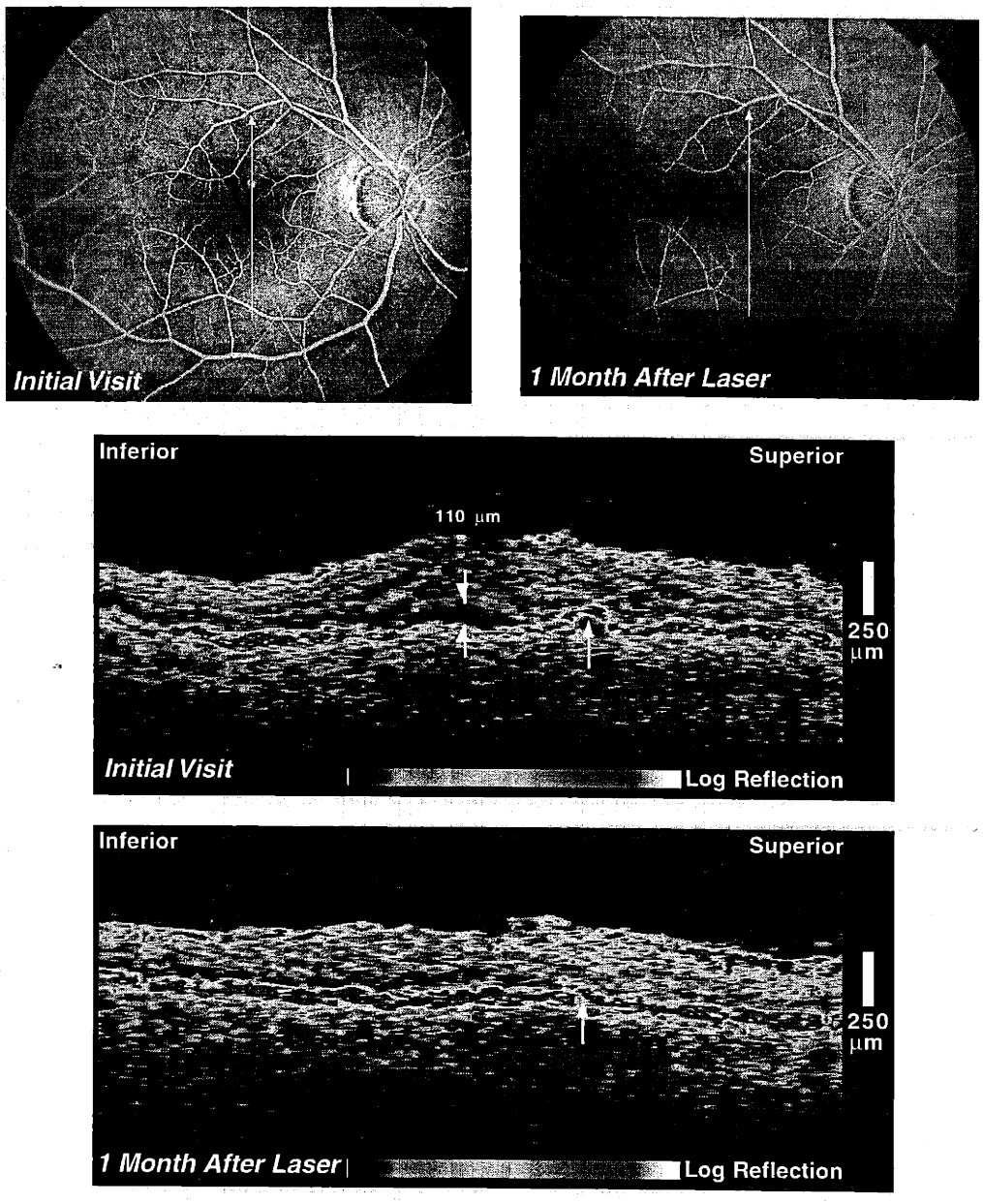

FIGURE 6-21. Laser treatment of central serous chorioretinopathy (Case 6-6).

6.4 Diabetic Retinopathy and Macular Edema [104]

Macular edema is a common cause of vision loss in patients with diabetic retinopathy, retinal vein occlusion, and uveitis, and is not an infrequent complication of cataract surgery. While fluorescein angiography is typically used to qualitatively assess vascular leakage in patients with macular edema, actual macular thickening is better correlated with loss of visual acuity [138]. In patients with diabetic retinopathy, macular edema is clinically significant, as defined by the Early Treatment Diabetic Retinopathy Study (ETDRS) protocol, if hard exudate or retinal thickening is observed within 500 μm of the center of the foveal avascular zone [139]. Traditional methods of evaluating macular thickening, including slit-lamp biomicroscopy and stereo fundus photography, are relatively insensitive to small changes in retinal thickness [139]. Thus, several new techniques for quantitatively measuring retinal thickness have been explored [8].

Studies in patients with diabetic retinopathy are presented here as a prototype for macular edema of any etiology. The topographic mapping protocol described in Chapter 4 was used to assess macular thickness in 182 eyes of 107 patients with diabetic retinopathy, in 55 eyes from 31 patients with diabetes but no ophthalmoscopic evidence of retinopathy, and in 73 eyes from 41 healthy volunteers. For each eye, six consecutive OCTs were obtained at equally spaced angular orientations in a radial spoke pattern centered on the fovea (Figure 4-31). This pattern had the advantage of concentrating measurements in the central fovea where accurate information was most important. A computer algorithm was used to profile the inner and outer retinal boundaries for each OCT and retinal thickness was automatically computed from these boundaries (Section 4.6). Macular thickness was displayed as a false-color topographic map, and as averages over nine ETDRS-like regions covering the macula (Figure 4-35). The mean±standard deviation (SD) central foveal thickness was also recorded for the six A-scans at the intersection of all the OCTs in the central macula. This standard deviation provided a simple internal estimate of the reproducibility the OCTs.

Although many methods could have been used to sample retinal thickness throughout the macula, the radial scanning pattern concentrated measurements in the central macula where information was most important. Additionally, the individual OCTs permitted visualization of intraretinal features such as cysts and hard exudate which would not have been available from other scanning patterns that did not have the A-scans closely spaced in one dimension.

The radial pattern of six tomograms sampled macular thickness at all clock hours. Bilinear interpolation in polar coordinates was used to estimate thickness in the wedges between each tomogram for the false-color display. No interpolation was used to compute average thickness by ETDRS region. This protocol would be expected to miss very focal edema situated in a wedge which spanned less than a clock hour. In our experience, the likelihood of this occurring was minimal, especially near the fovea where the tomograms were more closely spaced. With six OCTs used to radially map macular thickness, the arc length of a clock hour 500 μm from the center was approximately 250 μm. More detailed mapping could be obtained, if desired, by increasing the number of tomograms in the radial pattern. Since each image was acquired in 2.5 seconds, the total time required to perform all six scans in a given eye was usually less than a minute. The radial scanning pattern kept the patient's fixation constant for all OCTs which enabled the six scans to be performed in succession after the initial alignment.

6.4.1 Normal Macular Thickness

The topographic mapping protocol was performed on 73 eyes from 41 healthy volunteers (mean age 38 years, range 23 to 79 years), including 40 eyes from 23 women and 32 eyes from 18 men. The mean±SD retinal thickness by region is displayed in Figure 6-22 and Table 6-3. The mean±SD foveal thickness was 174±18 μm and never exceeded 216 μm in any of the

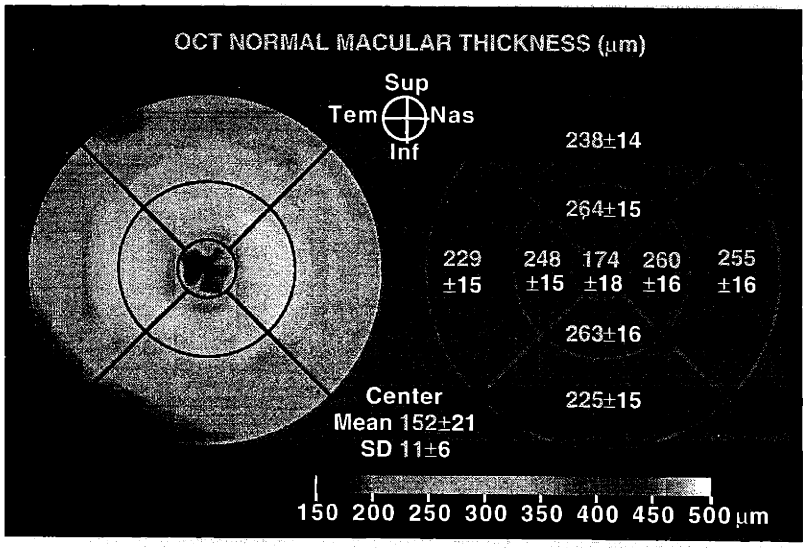

FIGURE 6-22. Normal macular thickness.

normal eyes. As expected, retinal thickness reached a minimum in the fovea, was largest within one disc diameter of the center, and decreased towards the periphery. The temporal quadrant was thinnest. Within one disc diameter of the center, the superior and inferior quadrants were thickest due to the superior and inferior arcuate bundling of nerve fibers. The nasal retina was thickest two disc diameters from the center due to the convergence of nerve fibers approaching the optic disc. Figure 6-22 also illustrates a false-color topographic map from a typical healthy eye which provides an example of these normal variations.

The SD of the average thickness for each region outside the central 500 μm radius was uniformly about 15 μm showing that there was relatively little variability in average retinal thickness outside the fovea. The SDs of 18 μm and 21 μm for the average foveal and central foveal thickness respectively were slightly larger. The SD of the six central macular measurements provides a simple estimate of the measurement reproducibility for a given patient. The average value of this reproducibility estimate over healthy eyes was 11 μm. Age was not significantly correlated with average foveal thickness within 500 μm of the center. However, the mean±standard error average foveal thickness was significantly different among men (181±4 μm) and women (169±4 μm) (Student's T-test, $p = 0.04$).

Region		Retinal Thickness (Mean±SD μm)			
		Normal (N=73)	Diabetes (N=55)	NPDR (N=148)	PDR (N=34)
	Center	152±21	158±20	244±125	236±140
	Reproducibility	11±6	14±9	20±12	19±11
< 500 μm disc	Fovea	174±18	179±17	256±114	254±133
Inner Ring (500 μm to 1 DD radius)	Superior	264±15	261±18	296±72	308±108
	Inferior	263±16	263±16	298±71	299±113
	Temporal	248±15	246±16	285±74	281±96
	Nasal	260±16	255±18	292±70	311±121
Outer Ring (1 DD to 2 DD radius)	Superior	311±121	237±16	264±55	284±89
	Inferior	225±15	223±14	255±56	253±92
	Temporal	229±15	229±15	257±50	259±55
	Nasal	255±16	255±16	273±46	304±97

DD = disc diameter (1.5 mm)
Diabetes = diabetes with no slit-lamp evidence of retinopathy
NPDR = non-proliferative diabetic retinopathy
PDR = proliferative diabetic retinopathy

TABLE 6-3. Macular thickness in healthy and in diabetic eyes by region.

6.4.2 Diabetic Macular Edema

OCT was used to examine 182 eyes from 107 patients with diabetic retinopathy (mean age 60 years, range 25 to 81 years), including 98 eyes from 55 males and 84 eyes from 52 females. On slit-lamp examination, 148 eyes were diagnosed with non-proliferative or background diabetic retinopathy (NPDR) and 34 eyes had proliferative diabetic retinopathy (PDR). The mean±SD retinal thickness by region for these eyes is reported in Table 6-3. As expected the mean macular thickness was larger in all regions for eyes with NPDR or PDR compared to normals. This difference was most significant in the average and central foveal thicknesses indicating the predominance of central versus more peripheral edema. The SD in thickness for each region was greater among eyes with NPDR or PDR compared to normals which was a direct consequence of the variable extent and location of macular edema in the diabetic eyes. There were no significant differences in average thickness in any region between eyes with NPDR and eyes with PDR. Comparison of the average SD of the six measurements obtained through the central macula revealed that measurements in eyes with diabetic retinopathy appeared to be less reproducible than those from normal eyes.

Slit-lamp biomicroscopy was used to grade clinically significant macular edema based on the presence or absence of macular thickening or hard exudate within 500 μm of the central macula. Figure 6-23 displays a histogram of average foveal thickness within 500 μm of the center as measured by OCT. Mean foveal thickness was considered to be abnormal or clini-

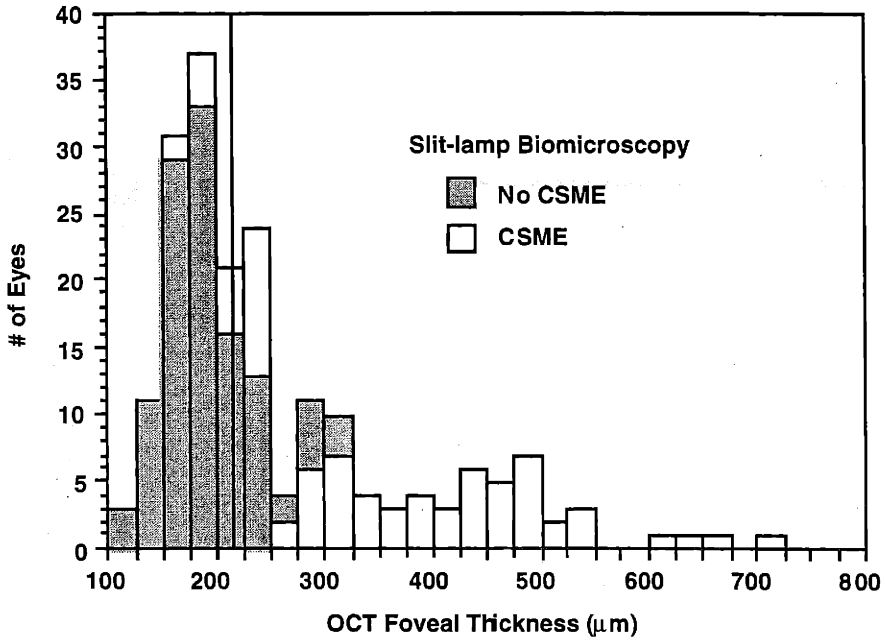

CSME = clinically significant macular edema

FIGURE 6-23. Histogram of OCT measured foveal thickness.

cally significant on OCT when it was greater than the maximum value observed for normal eyes (*i.e.* greater than 216 μm), indicated by a vertical line on the histogram. According to Figure 6-23, OCT evaluation agreed with slit-lamp examination for normal and extreme values of foveal thickness, but disagreed often when foveal thickness was between 200 and 325 μm. Similar results were obtained for OCT measurements of central macular thickness. Central macular thickness was highly correlated by linear regression with average foveal thickness (R^2 = 0.97) and these two measurements were essentially equivalent in evaluating clinically significant macular thickening. Thus, both measurements of central macular thickness and measurements of foveal thickness averaged over a central disk of 500 μm radius appeared to be more sensitive than slit-lamp examination for evaluating CSME.

The OCT topographic map of retinal thickness generally correlated with conventional clinical examination. Retinal thickening or hard exudate observed on slit-lamp biomicroscopy almost always correlated with increased thickness on OCT, but there were some occasions in which OCT detected thickening in the absence of any abnormality on slit-lamp examination. Edema was difficult to detect clinically when there was no hard exudate in the central macula and diffuse rather than focal macular thickening was present reducing the variation in retinal surface contour. OCT retinal thickness also generally correlated with regions of fluorescein leakage; however, increased macular thickness was occasionally evident on OCT in the absence of leakage.

CASE 6-7. Diabetic macular edema and exudate (Figure 6-24). This 55-year-old woman with a 14 year history of diabetes had moderate NPDR in her right eye associated with a visual acuity of 20/25. Severe exudate and extrafoveal macular edema which was not clinically significant was noted on slit-lamp examination *(top, left)*. Fluorescein angiography *(top, right)* revealed late leakage surrounding the fovea consistent with macular edema. The OCT topographic map *(bottom)* showed retinal thickening not involving the fovea which generally corresponded with regions of hard exudate and fluorescein leakage. Hard exudate was visible in the cross-sectional OCTs *(middle)* as focal intraretinal areas of high reflectivity.

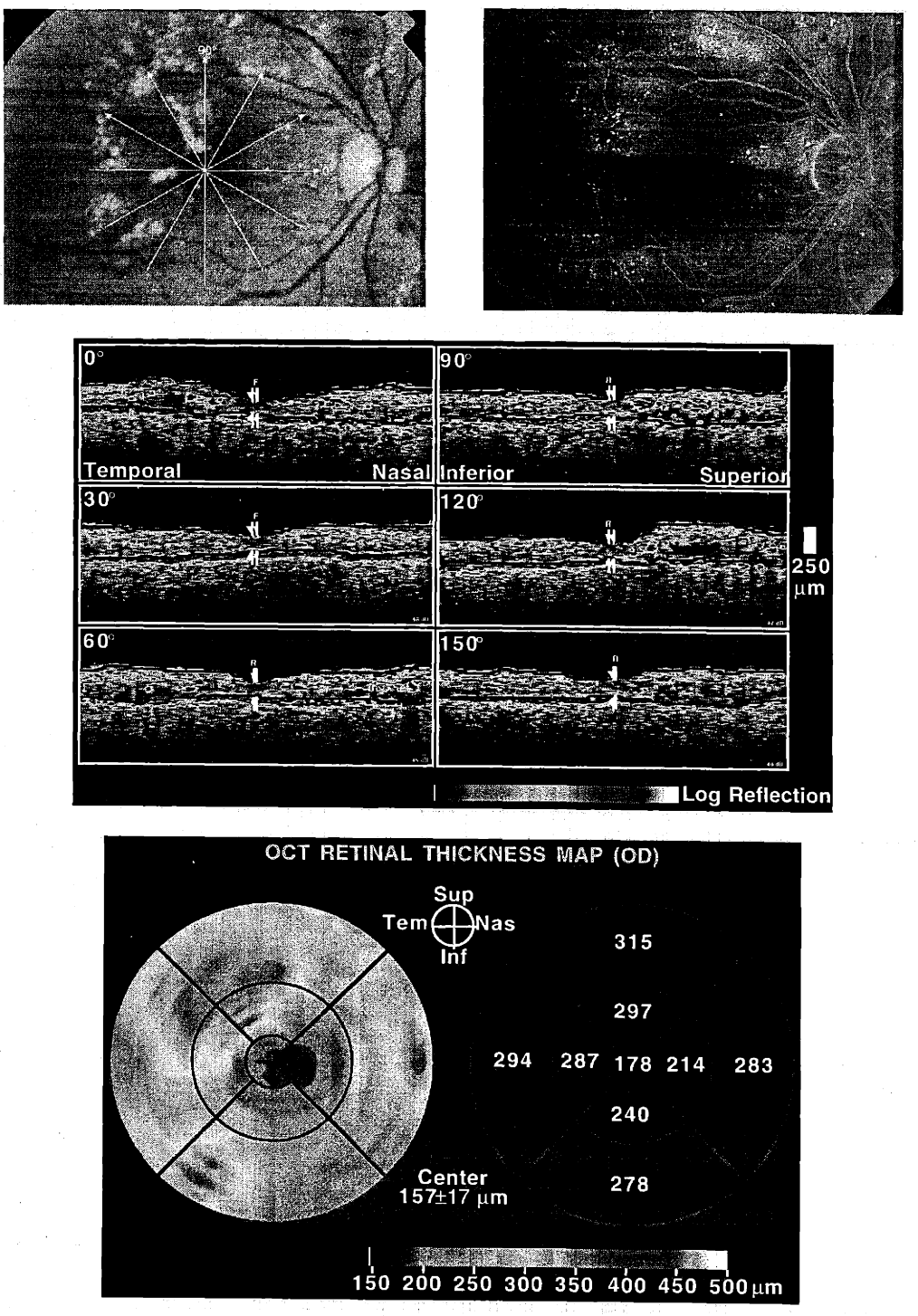

FIGURE 6-24. Diabetic macular edema and exudate (Case 6-7).

CASE 6-8. Minimal clinically significant macular thickening (Figure 6-25). A 66-year-old man with NPDR had a visual acuity of 20/25 in his right eye. Slit-lamp biomicroscopy showed multiple dot and blot hemorrhages but no evidence of clinically significant macular edema *(top)*. Fluorescein angiography was not performed. OCT revealed two focal regions of macular thickening superotemporal and nasal to the fovea which corresponded to areas of hemorrhage on ophthalmoscopy *(bottom)*. OCT showed that the foveal thickness was increased at 220 μm which was consistent with clinically significant macular thickening.

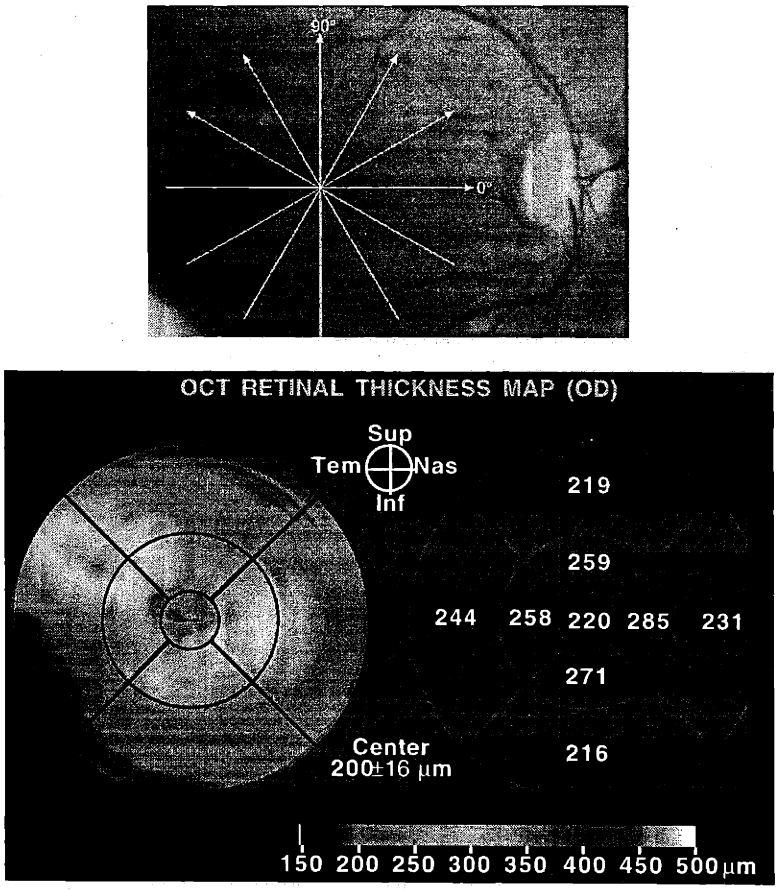

FIGURE 6-25. Minimal clinically significant macular thickening (Case 6-8).

6.4.3 Laser Treatment of Diabetic Macular Edema

The topographic mapping protocol is useful for longitudinally monitoring patients for the development of macular edema and for following the resolution of edema after laser treatment. Geographic information was helpful since edema often presented or began to resolve outside of the fovea before affecting central macular thickness. The false-color map of retinal thickness provides an intuitive and efficient method of comparing retinal thickness over several visits which could be directly compared with slit-lamp observation.

CASE 6-9. Development and resolution of diabetic macular edema (Figure 6-26). A 50-year-old man with NPDR and CSME in the right eye was examined *(top)*. His visual acuity OD was 20/25. OCT at the initial visit *(top)* showed foveal and juxtafoveal macular thickening which was most significant temporally and corresponded with areas of hard exudate. Eight months later, the patient's visual acuity OD had decreased to 20/40. OCT *(middle)* displayed a substantial increase macular thickness centrally. Focal laser photocoagulation was performed and the patient returned five months later. On follow-up examination, the visual acuity OD had returned to 20/20. OCT *(bottom)* showed resolution of the edema with a normal foveal and central macular thickness. A remaining area of minimal retinal thickening was evident nasal to the fovea.

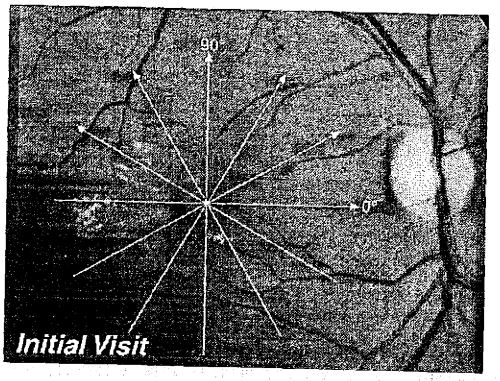

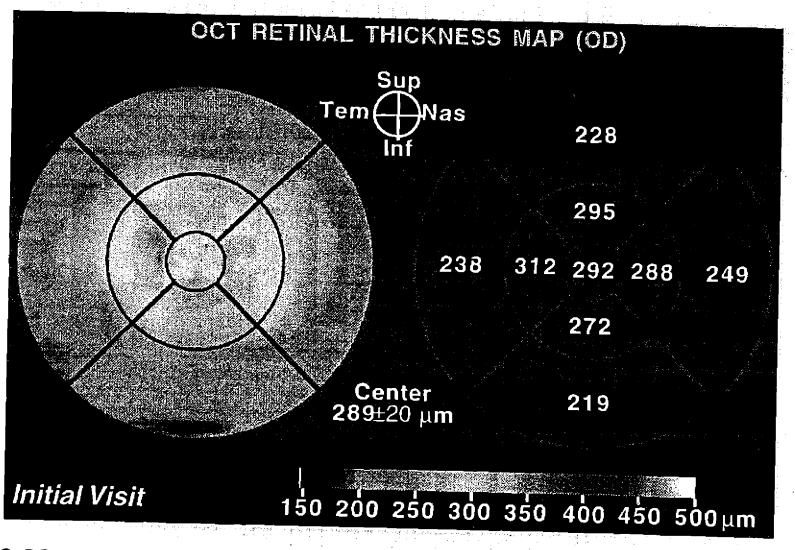

FIGURE 6-26. Development and resolution of diabetic macular edema (Case 6-9).

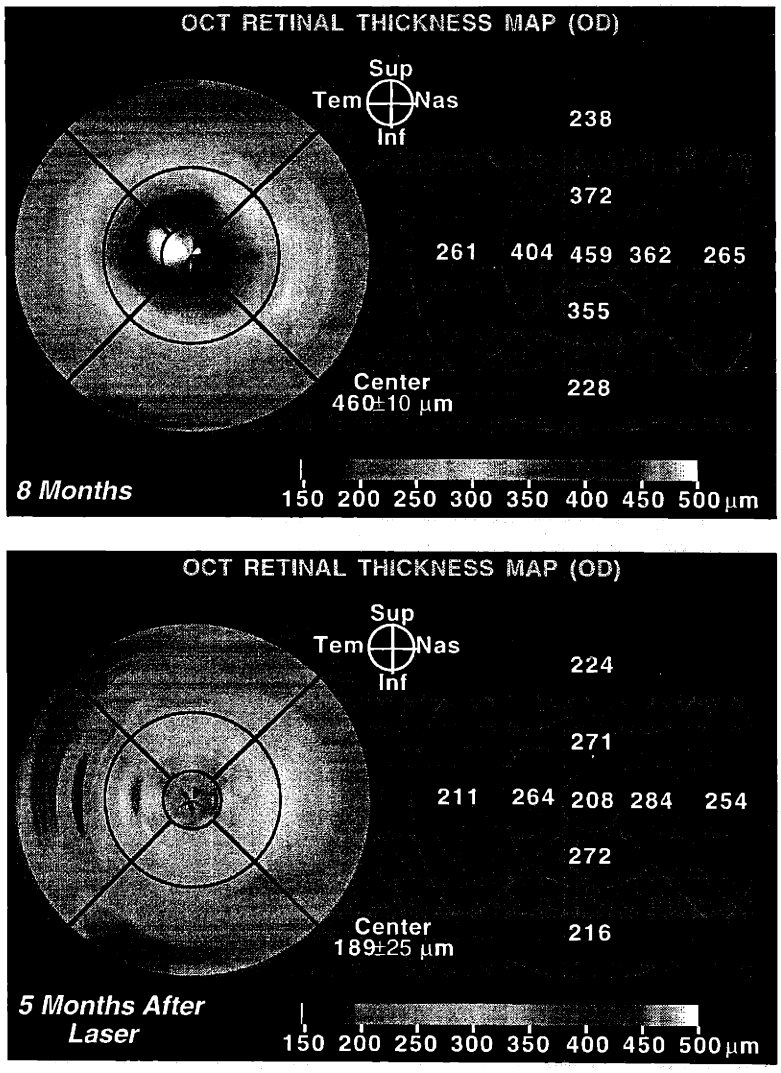

FIGURE 6-26. Development and resolution of diabetic macular edema (Case 6-9). *(Continued)*

CASE 6-10. Extrafoveal resolution of diabetic macular edema (Figure 6-27). A 69-year-old man with NPDR had a visual acuity of 20/40 in his left eye. Slit-lamp biomicroscopy *(top)* revealed significant retinal thickening inferotemporally within one disc diameter of the center and minimal CSME. OCT *(top)* confirmed both regions of increased retinal thickness. Grid yellow dye laser was applied to the inferotemporal region of increased retinal thickness according to leakage observed on fluorescein angiography. The patient returned two months later for follow-up with no improvement in his visual acuity OS. OCT *(middle)* demonstrated a regional decrease in the inferotemporal retinal thickness; however, the average foveal thickness and central foveal thickness had not significantly changed from the initial examination. A significant decrease in foveal thickness was not noted until ten months after laser treatment at which time the foveal thickness was within the normal range *(bottom)*. The patient's visual acuity remained at 20/40.

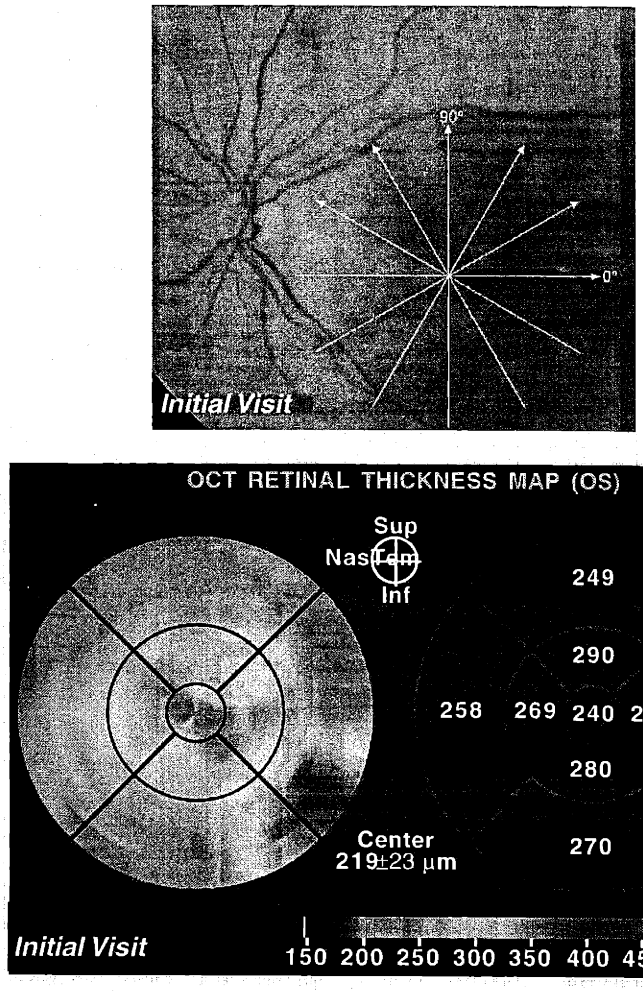

FIGURE 6-27. Extrafoveal resolution of diabetic macular edema (Case 6-10).

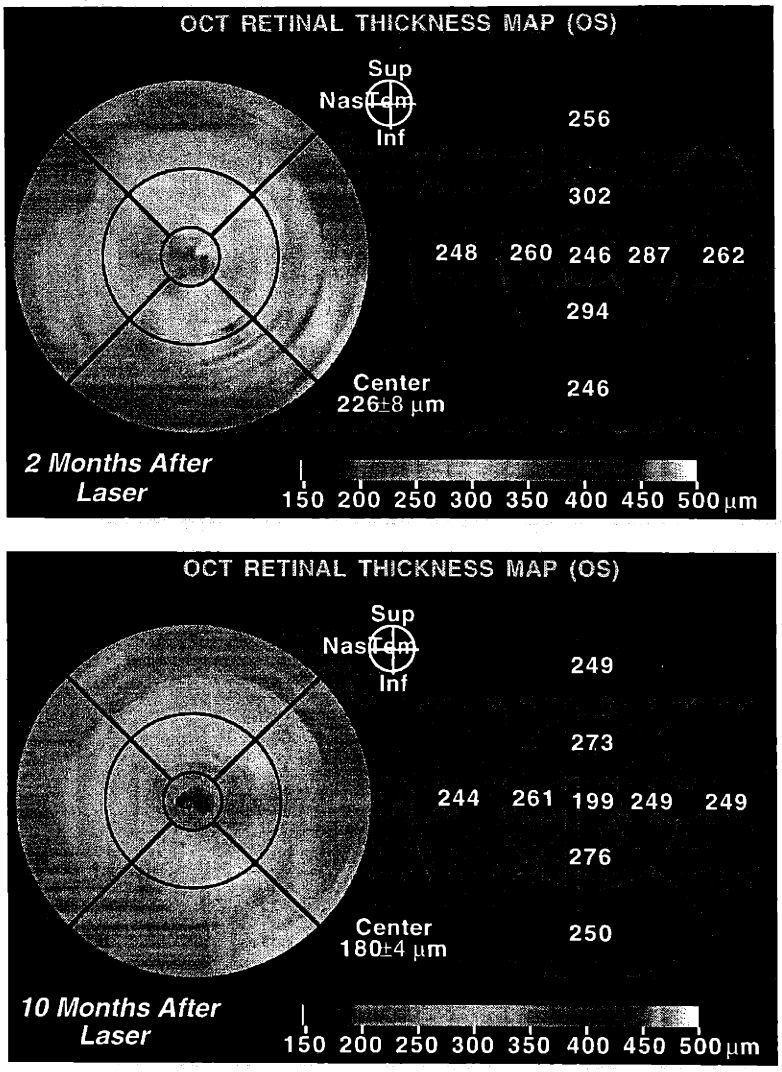

FIGURE 6-27. Extrafoveal resolution of diabetic macular edema (Case 6-10). *(Continued)*

6.4.4 Screening for Early Diabetic Macular Edema

OCT has the potential to screen patients with early non-proliferative retinopathy for the development of macular thickening. We also attempted to investigate whether some patients with diabetes might develop early macular edema before the onset of ophthalmoscopically visible retinopathy. Fifty-five eyes from 31 patients with diabetes but with no evidence of retinopathy on slit-lamp examination were evaluated with OCT to determine whether macular thickening was present in this population (mean age 55 years, range 32 to 84 years). These patients included 41 eyes from 23 men and 14 eyes from 8 women. As a population, the average macular thickness in these eyes showed no significant difference from normals in any of the nine regions (Table 6-3). Two of the diabetic eyes had foveal thicknesses of 221 µm and 230 µm which were both greater than the maximum foveal thickness observed for any of the normal eyes (216 µm). (Alternatively, a two SD figure of 210 µm could have been used to screen absolute macular thickness). The reproducibility figures for these eyes were 24 µm and 53 µm respectively.

Comparison of macular thickness between right and left eyes in the same patient provides an additional means of identifying early macular edema. Left and right average foveal thickness were highly correlated among the 30 normal subjects in which both eyes were imaged (Figure 6-28). The mean±SD absolute difference in foveal thickness between these left

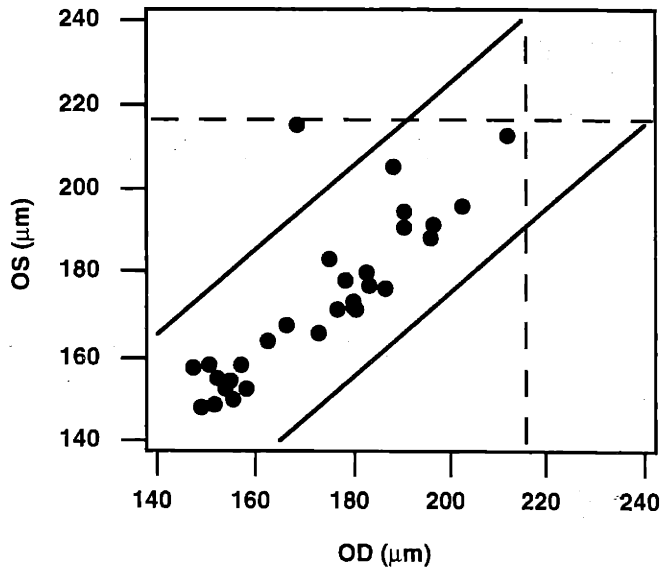

FIGURE 6-28. Left versus right foveal thickness in normal eyes.

and right eyes was 6±9 μm. Dashed lines on the graph indicate the maximum foveal thickness observed for normal eyes (216 μm). The solid lines demarcate a strip within which the difference between left and right foveal thickness was less than 2 standard deviations away from the mean difference in normal subjects (±24 μm). Left and right foveal thickness was also correlated in the 23 patients in which both eyes were imaged who had diabetes without retinopathy (plotted in Figure 6-29 with the same dashed and solid lines defined in Figure 6-24). In these eyes, the mean±SD absolute difference in foveal thickness was 9±8 μm.

Three of the diabetic patients (*A*, *B*, *C* on Figure 6-29) exhibited a difference between eyes (51 μm, 28 μm, and 26 μm respectively) which was greater than two SDs larger than the mean for normals. Two of these patients (*A*, *B*) also had abnormally thick foveas as described above. One of these two suspicious patients (*A*) had an unacceptable reproducibility estimate of 53 μm. Patient *B*, however, exhibited acceptable reproducibility and a left foveal thickness which was both greater than all normals and significantly increased compared to the patient's contralateral eye. Based on these findings, it appears that patient B would be a candidate for more frequent and detailed follow-up in his left eye, perhaps including fluorescein angiography.

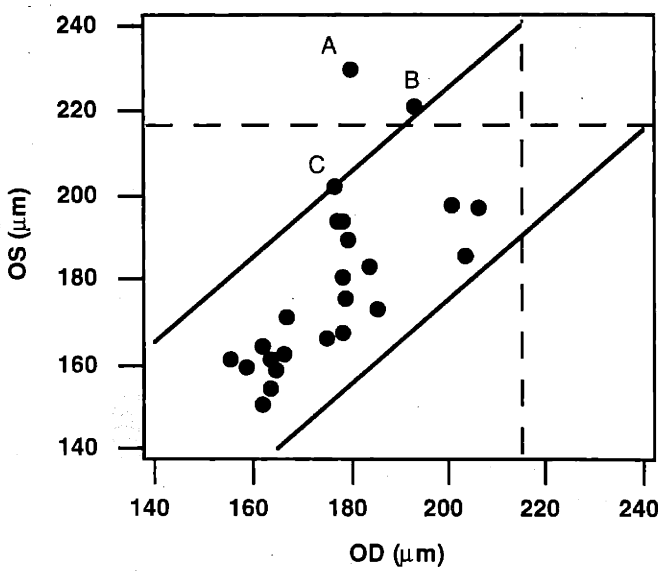

FIGURE 6-29. Left versus right foveal thickness in diabetic eyes without retinopathy.

6.4.5 Macular Thickening and Visual Acuity

Optical coherence tomography measurements of foveal thickness (averaged within a radius of 500 μm from the center) were compared with visual acuity using linear regression in 237 diabetic eyes with either no retinopathy, non-proliferative retinopathy, or proliferative retinopathy (Figure 6-30). The foveal thickness, averaged over eyes with the same visual acuity, correlated with visual acuity expressed on a logarithmic scale ($R^2 = 0.79$).

6.4.6 Limitations of OCT Imaging of Diabetic Macular Edema

Since all OCTs in the radial pattern intersected in the center, the standard deviation of the six central thickness measurements provided an estimate of the test reproducibility and reliability. This reproducibility figure typically varied between 5 and 20 μm for normal subjects. Eyes with retinopathy tended to exhibit poorer reproducibility. Larger deviations suggested imperfect fixation and could be used to quantify the reliability of the OCTs. In patients with eccentric or varying fixation, the central fovea was often laterally displaced slightly from the center of the OCT image. In these cases, the computer provided an estimate of the lateral displacement by identifying the position of minimum total intraretinal reflectivity which was usually characteristic of the relative absence of plexiform layers in central fovea (see Section 4.8.1). The examiner was then given a choice to offset the center of the OCT to this position. Human intervention was necessary because the computer would occasionally confuse the reduced intraretinal reflectivity characterizing a cyst for the reduced reflectivity within fovea. The examiner was usually able to identify the fovea based on its characteristic cross-sectional morphology in most eyes without severe edema. Thus, while complete manual identification of the fovea would have been feasible, the computer algorithm permitted a binary decision which minimized examiner bias. Future developments in the feature recognition algorithm should lead to a completely automated identification technique. In any case, imperfect fixa-

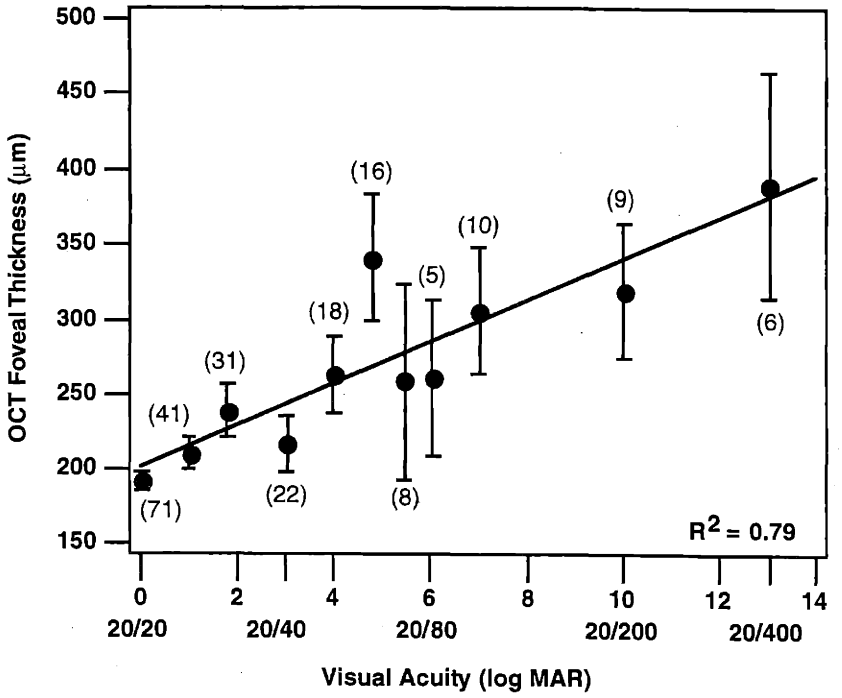

FIGURE 6-30. Macular thickness versus visual acuity.

tion was a concern mostly for patients with advanced disease and generally was not a factor with more mild edema. Furthermore, the reproducibility figure provided an objective context within which one could interpret the OCT results from the patients with more problematic fixation.

Other potential sources of artifacts included refractive error and saccadic eye motion. As described in Section 3.6.5, differences in refractive power or magnification could therefore lead to inaccurate measurements of transverse dimensions which would affect the actual size of the nine ETDRS-like regions on the macula. Measurements of central macular thickness were not affected by refractive error and these measurements could also have been used to assess clinically significant macular thickening. Saccadic eye motions which occurred during the 2.5 seconds required for each of the six OCTs could result in inaccurate measurements of retinal thickness if there was significant local variation in thickness. Transverse eye motion was more problematic in patients with advanced disease and poor fixation. However, the influence of eye motion could be assessed in the central fovea with the reproducibility figure in a manner similar to fixation losses.

6.5 Age-Related Macular Degeneration [105]

Age-related macular degeneration (AMD) is the leading cause of blindness in the United States. The clinical presentation of AMD is varied, but may be classified into exudative and non-exudative findings. Non-exudative lesions include drusen (Figure 5-14) and geographic atrophy (Figure 5-20). Choroidal neovascularization and its associated exudative maculopathy, including both serous and hemorrhagic detachments of the neurosensory retina and RPE, are responsible for the majority of vision loss in AMD. Laser photocoagulation treatment effectively reduces or delays severe vision loss in eyes with AMD and choroidal neovascularization (CNV) [140-143]. Many eyes with exudative AMD, however, lack the fluorescein angiographic features required for treatment eligibility according to the Macular Photocoagulation Study (MPS) guidelines [144-146]. Therefore, new imaging techniques have been studied in an attempt to better visualize such occult neovascularization [1-3].

OCT was used to morphologically study eyes with exudative AMD and to evaluate the potential for better defining angiographically classic and occult choroidal neovascularization. OCTs were correlated with the results from conventional clinical examination including slit-lamp biomicroscopy and fluorescein angiography. Based on these studies, a preliminary classification scheme for CNV on OCT imaging was developed. In patients with exudative changes associated with AMD and/or CNV, the OCT classification was compared and correlated with the fluorescein angiographic description to better understand the capabilities and limitations of the imaging technique.

6.5.1 OCT Classification of Exudative AMD

OCT permitted direct visualization of CNV in cross-section, providing a structural rather than functional assessment of neovascularization. After review of all the OCTs of AMD, exudative changes were empirically found to be distributed among the five following categories:

- *Well-defined CNV*: A fusiform thickening and disruption of the reflective band corresponding to the RPE and choriocapillaris with well-defined boundaries (*e.g.* Case 6-11 below). The thickening extends upwards in the OCT creating a "bump" in the normal contour of the RPE which defines the boundaries of the CNV.

- *Poorly-defined CNV*: Diffusely enhanced choroidal backscatter and disrupted reflections from the RPE and choriocapillaris with poorly defined boundaries and associated with subretinal or intraretinal fluid (*e.g.* Case 6-13 below). The enhanced reflectivity is confined below and blends into the normal contour of the RPE, which is unaffected. Subretinal or intraretinal fluid must be observed to distinguish this enhanced choroidal reflectivity from increased choroidal reflections due to pigmentary atrophy.

- *Serous PED*: A sharp elevation of the reflection corresponding to the RPE over an optically clear space shadowing the reflections from the choroid below (*e.g.* Figure 5-10).

- *Fibrovascular PED*: An elevation of the reflection corresponding to the RPE over a mild to moderately backscattering region between the detached pigment epithelium and choroid (*e.g.* Case 6-12 below). A clear distinction is noted between the bright (red) reflection from the RPE, and the moderate (green/yellow) sub-RPE reflections. No optical shadowing of the choroid is visible.

- *Hemorrhagic PED*: An elevation of the reflection corresponding to the RPE over a highly backscattering region which attenuates rapidly towards the outer retina and completely shadows the choroidal reflection (*e.g.* Figure 5-12).

Thus, CNV visible on OCT could be categorized as *well-defined*, *poorly-defined*, or as a *fibrovascular PED*. These classifications did not necessarily correspond to similar fluorescein angiographic descriptions.

Angiographically classic CNV usually presented as *well-defined CNV* on OCT suggesting the penetration of new vessels through breaks in the RPE. The ingrowth of fibrous tissue leading to disciform scar formation caused additional thickening and an increasingly enhanced and more uniform reflection from this layer (*e.g.* Figure 5-19). Disciform scars and *well-defined CNV* were difficult to distinguish based on their size or uniformity of reflection alone on OCT. However, disciform scars were most often associated with retinal atrophy or thinning, while true CNV usually presented with intraretinal or subretinal fluid accumulation. Subretinal hemorrhage also was visualized as an abnormal region of enhanced backscatter below the neurosensory retina on OCT. Subretinal hemorrhage could be distinguished from CNV by the enhanced attenuation of the probe beam and optical shadowing of the choroid in the case of hemorrhage, but not CNV.

CASE 6-11. Classic CNV (Figure 6-31). A 67-year-old man noticed a central gray spot in his left visual field for six weeks prior to examination. He reported enlargement of this spot over the most recent month. Slit-lamp biomicroscopy revealed a gray, mildly elevated subretinal lesion with a surrounding hypopigmented halo and minimal subretinal fluid. The patient's visual acuity OS was 20/60. Fluorescein angiography (FA) *(top, left)* exhibited a well-defined hyperfluorescent lesion centrally consistent with classic, subfoveal CNV. OCT *(middle)* showed increased thickening and disruption of the RPE and choriocapillaris. Reduced intraretinal optical reflectivity and loss of the normal foveal contour was noted centrally consistent with intraretinal fluid accumulation. One month later, the patient's visual acuity OS had declined to 20/160. Dilated fundus examination and FA *(top, right)* demonstrated enlargement of the neovascularization. A follow-up OCT *(bottom)* also showed enlargement of the focal thickening and disruption of the RPE and choriocapillaris. A slight increase in the central macular edema was noted, and a new region of subretinal fluid accumulation was identified superior to the fovea.

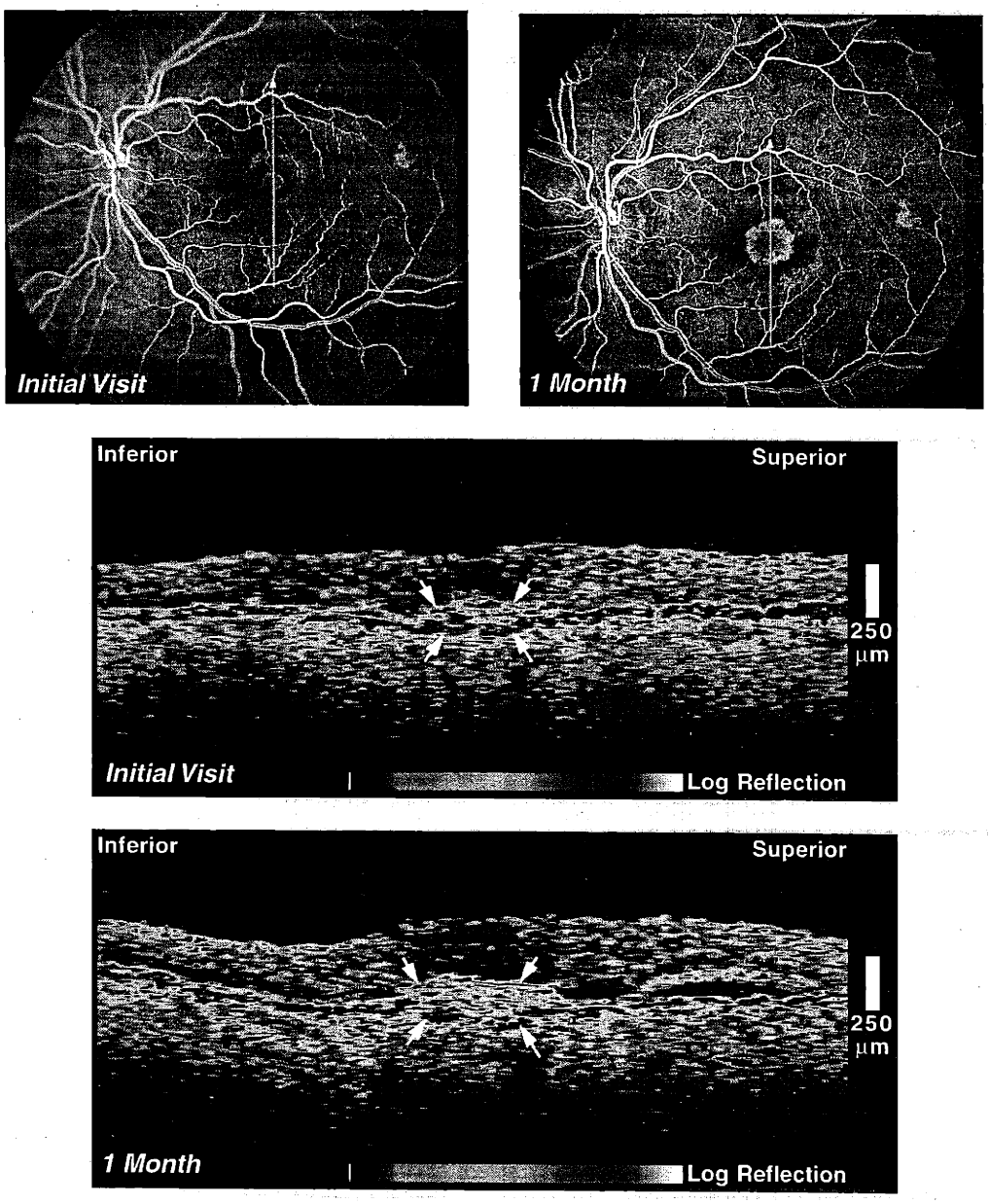

FIGURE 6-31. Classic CNV (Case 6-11).

Both angiographically classic and occult CNV presented as *fibrovascular PED* on OCT. In these lesions, the reflection from the RPE appeared elevated as in a serous RPE detachment. The region below the RPE, however, was moderately reflective consistent with fibrovascular or neovascular proliferation and in contrast to an optically clear region of subretinal fluid.

CASE 6-12. Fibrovascular pigment epithelial detachment (Figure 6-32). An 84-year-old woman with a visual acuity of 20/200 in her right eye had a fibrovascular pigment epithelial detachment in the central macula with mild subretinal fluid and hemorrhage. FA *(top)* exhibited a well-defined area of hyperfluorescence centrally which showed progressive dye leakage as the angiogram progressed. Irregular hyperfluorescence with mild late leakage was noted surrounding the central lesion. OCT *(bottom)* demonstrated an elevation of the retina and RPE *(arrowheads)* over a moderately backscattering region *(arrows)* consistent with fibrovascular proliferation. A small amount of subretinal fluid was identified superior to the lesion. The optical penetration through this lesion was significantly greater than that observed through sub-pigment epithelial hemorrhage.

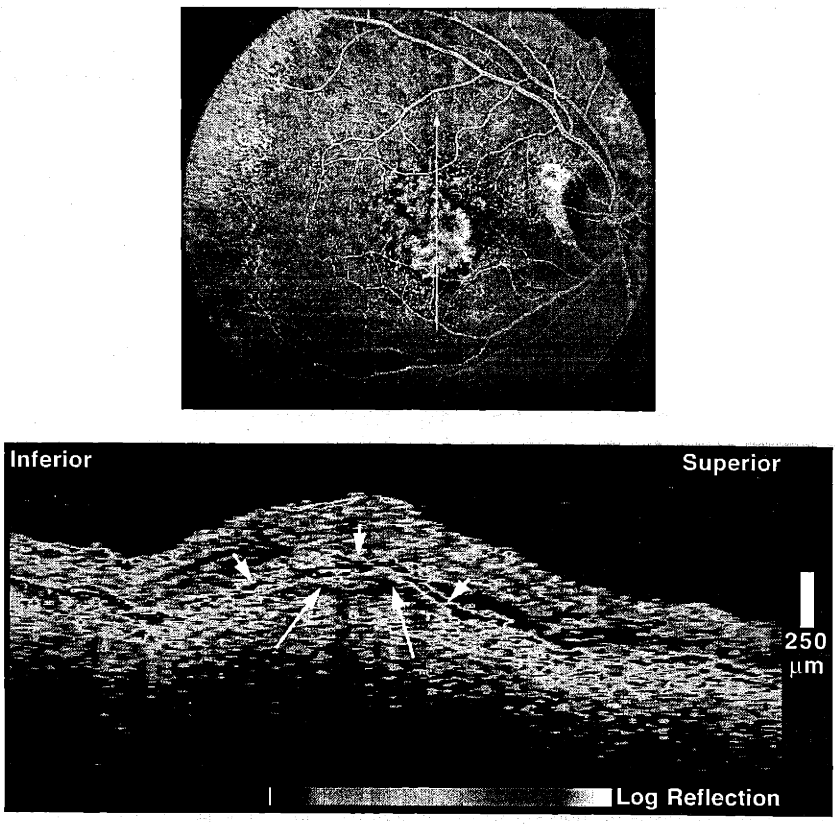

FIGURE 6-32. Fibrovascular pigment epithelial detachment (Case 6-12).

Finally, *poorly-defined CNV* was characterized on OCT by diffuse, enhanced reflectivity from the choroid. These lesions were difficult to demarcate clearly on the tomograms; however, the increased choroidal backscatter was usually associated with intraretinal or subretinal fluid, or cyst formation. The presence of intra- or sub-retinal fluid on OCT was necessary to establish a classification of *poorly-defined CNV* since diffuse changes in choroidal reflectivity alone could often be mimicked by RPE changes influencing the penetration of the probe beam into the choroid. On FA, most of these lesions were characterized as late leakage of an undetermined source.

CASE 6-13. Occult CNV poorly-defined on OCT (Figure 6-33). A 38-year-old woman noted blurred vision in her left eye approximately seven months prior to examination. Her visual acuity OS was 20/300 on examination. Dilated ophthalmoscopy was notable for pigment epithelial atrophy and mottling in the central macula, and subretinal fluid with a small amount of hemorrhage inferior to the fovea. FA *(top)* displayed mottled hyperfluorescence superior to the fovea. A focal spot of hypofluorescence surrounded by hyperfluorescence was observed inferiorly consistent with hemorrhage and fluid accumulation. Leakage of undefined origin was observed in the late phase. OCT *(bottom)* displayed a large intraretinal, optically clear space corresponding to a cyst. The retina was mildly thickened surrounding the cyst. The reflection from the RPE and choriocapillaris was disrupted and the choroidal reflectivity *(arrowheads)* was diffusely enhanced with poorly defined boundaries.

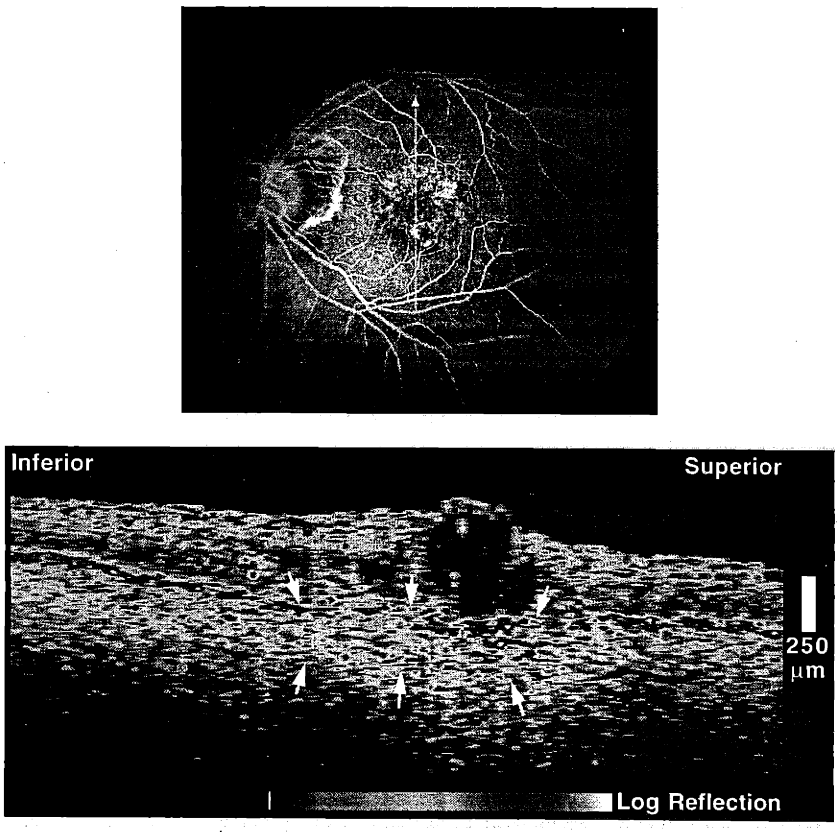

FIGURE 6-33. Occult CNV poorly-defined on OCT (Case 6-13).

6.5.2 Correlation of OCT and Fluorescein Angiography

Correlation of OCT and FA was performed in 90 eyes from 86 patients which had exudative changes associated with AMD, but no previous laser treatment, isolated drusen, geographical atrophy, or disciform scarring. The population comprised the right eye in 40 patients, the left eye in 42 patients and both eyes in 4 patients. The lack of bilateral involvement was secondary to the large number of referred patients who already had involvement of one eye with a disciform scar. The results are summarized in Table 6-4.

# of Eyes		Fluorescein Angiography				
		Classic CNV	Occult CNV	Classic & Occult CNV	Serous PED	Hemorrhagic PED
OCT	Well-defined CNV	7	5	1		
	Fibrovascular PED	1		2		
	Poorly-defined CNV		30	1		
	Serous PED		5		24	
	Hemorrhagic PED					2
	Incorrect Orientation	1	3	1		

CNV = choroidal neovascularization
PED = pigment epithelial detachment

TABLE 6-4. OCT versus fluorescein angiographic classification of exudative age-related macular degeneration.

CNV classified as *well-defined* or *fibrovascular PED* on OCT (23 of 80 eyes) had well demarcated boundaries (potentially amenable to treatment). These membranes included both angiographically classic CNV (8 of 9 eyes) and a subset of angiographically occult CNV (12 of 50 eyes). Classic CNV on FA presented both as *well-defined CNV* (7 of 9 eyes) and as *fibrovascular PED* (1 of 9 eyes) on OCT. Angiographically occult CNV which appeared *well-defined* on OCT was sometimes due to the presence of hemorrhage blocking the FA but not OCT (3 of 5 eyes).

Both serous and hemorrhagic detachments of the RPE were reliably diagnosed with OCT (31 eyes). However, OCT was not able to detect CNV beneath serous PEDs because of optical shadowing and the absence of a detectable reflection from the RPE/choriocapillaris in

5 eyes. In 5 eyes, the OCT probe beam was incorrectly positioned on the fundus and did not scan through a membrane, usually extrafoveal, which was identified on FA. Therefore, no comparison could be obtained in these eyes.

In general, angiographically classic CNV appeared as *well-defined CNV* on OCT, while angiographically occult neovascularization was characterized as either as *fibrovascular PED* or *poorly-defined CNV*. However, there were some important exceptions. Classic CNV sometimes presented as a *fibrovascular PED* on OCT. In these cases OCT may have been sensitive to the difference between predominantly subretinal versus predominantly sub-RPE neovascularization. Thus, well-defined CNV on OCT may represent new vessels which are penetrating through single or multiple focal breaks in Bruch's membrane. In contrast, the reflection from the RPE in a fibrovascular PED on OCT appears intact and suggests that neovascularization is confined below the RPE. While more investigation is required, these results suggest that OCT may provide useful structural information which may have utility, for example, in evaluating patients for possible surgical removal of subfoveal CNV [147]. Although only a minority of CNV due to AMD is amenable to surgical removal, OCT may be useful for defining surgically approachable membranes in other diseases, such as ocular histoplasmosis.

It is likely that angiographically occult CNV classified as *fibrovascular PED* on OCT corresponded to fibrovascular PEDs on FA; however, stereoscopic angiograms were not available to accurately identify these lesions according to MPS guidelines. A subset (12 of 50 eyes) of angiographically occult CNV presented as *well-defined CNV* on OCT. Some of these cases were characterized by hemorrhage which obscured the fluorescein angiogram, but not the OCT. The near infrared wavelength and high detection sensitivity of OCT allowed enhanced penetration and imaging capability through blood compared to FA. In other cases of occult CNV, a well-defined thickening and disruption of the RPE/choriocapillaris was noted on OCT in the absence of large hemorrhage. Further study is required to define the structural characteristics of these membranes.

6.5.3 Clinical Applications of OCT Imaging in AMD

Vision loss in AMD is most often due to the development of CNV and related manifestations such as detachments of the RPE or neurosensory retina. OCT examination of patients with exudative AMD were able to quantify many of the biomicroscopic signs of AMD. Minimal subretinal fluid could be detected with OCT and appeared as a non-reflective space between the RPE and neurosensory retina. In contrast, retinal edema manifested as increased retinal thickness and a diffuse decrease in retinal reflectivity due to a reduced density of optical backscatter sites within the retina. In both cases, the amount of fluid accumulation could be quantified with high precision because of the high optical contrast at the vitreoretinal interface and RPE. Serous detachment of the RPE was distinguished from serous detachment of the neurosensory retina by elevation of the reflective layer corresponding to the RPE (compare Figures 5-9 and 5-10). When detached, this layer shadowed the reflections from the choriocapillaris and deeper choroid.

OCT was useful in assessing intraretinal and subretinal fluid and in distinguishing small neurosensory or pigment epithelial detachments. In these cases, OCT appeared to be more sensitive than biomicroscopic examination, and changes in retinal thickness or subretinal fluid accumulation could be objectively assessed with a single, permanently recorded number. OCT was sometimes effective in evaluating potential subfoveal involvement of fluid or CNV in tomograms where the foveal depression was immediately visible. OCT was also useful in structurally monitoring exudative AMD before and after laser treatment. The non-contact and non-invasive OCT examination was better tolerated by patients than either FA or slit-lamp biomicroscopy.

CASE 6-14. Occult CNV well-defined on OCT (Figure 6-34). An 80-year-old woman complained of intermittent blurry vision OS over the past several weeks. On examination, her visual acuity OS was 20/25 and slit-lamp biomicroscopy revealed a shallow pigment epithelial detachment above fixation without hemorrhage or exudate. Fluorescein angiography *(top)* showed early speckled hyperfluorescence superior and temporal to the fovea, and late leakage consistent with occult CNV. OCT *(bottom)* demonstrated a *well-defined* subfoveal membrane with subretinal fluid inferior to the fovea.

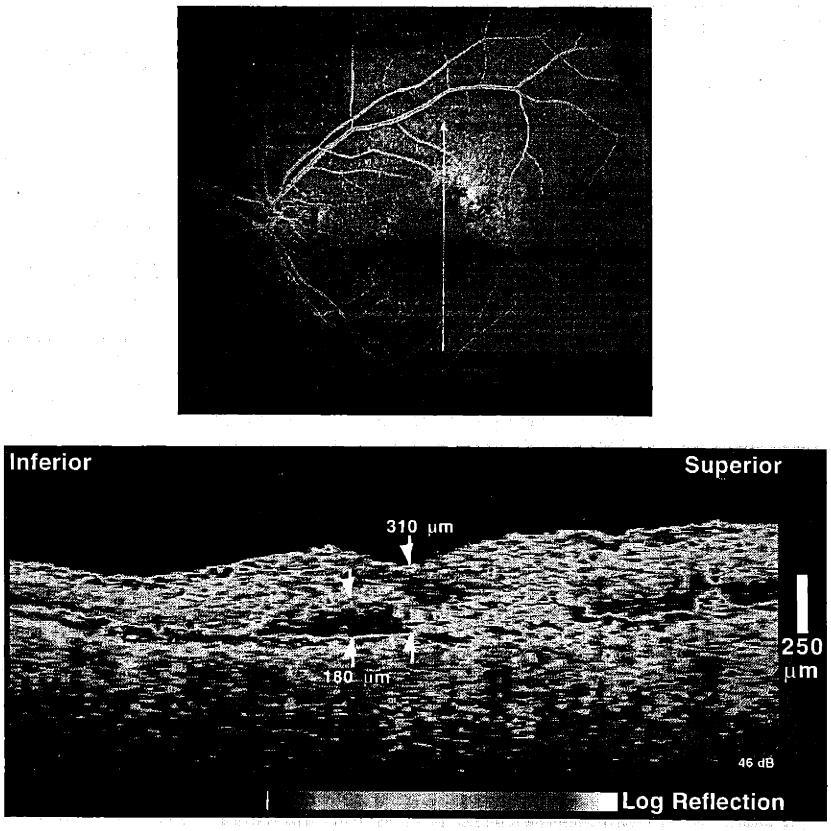

FIGURE 6-34. Subfoveal involvement of CNV not evident on angiography (Case 6-14).

CASE 6-15. CNV before and after laser treatment (Figure 6-35). An 83-year-old woman was referred for evaluation of recurrent CNV in her left eye. She had received laser photocoagulation in this eye two months earlier; however, her visual acuity had not improved from 20/125. Slit-lamp biomicroscopy showed a small pigmented lesion in the central macula with surrounding subretinal fluid and macular edema. An annulus of hyperfluorescence which increased in intensity with late leakage in later frames was evident on FA *(top, left)*. A corresponding well-defined region of retinal thickening was noted on OCT *(middle)*. The reflection from the RPE and choriocapillaris was diminished in the area of the lesion, and moderate backscatter signal was observed subretinally consistent with CNV *(arrows)*. A region of minimal backscattering consistent with subretinal serous fluid accumulation was evident temporal to the lesion. The patient received indocyanine green enhanced diode laser photocoagulation in this eye and returned one month later for follow-up. Slit-lamp biomicroscopy showed an atrophic laser scar in the macula with central pigmentation. A corresponding region of hypofluorescence was noted in all phases of the fluorescein angiogram *(top, right)*. OCT *(bottom)* showed the absence of intraretinal or subretinal fluid accumulation. The RPE and choriocapillaris appeared intact throughout the image, but showed slightly increased reflectivity in the region of the laser scar.

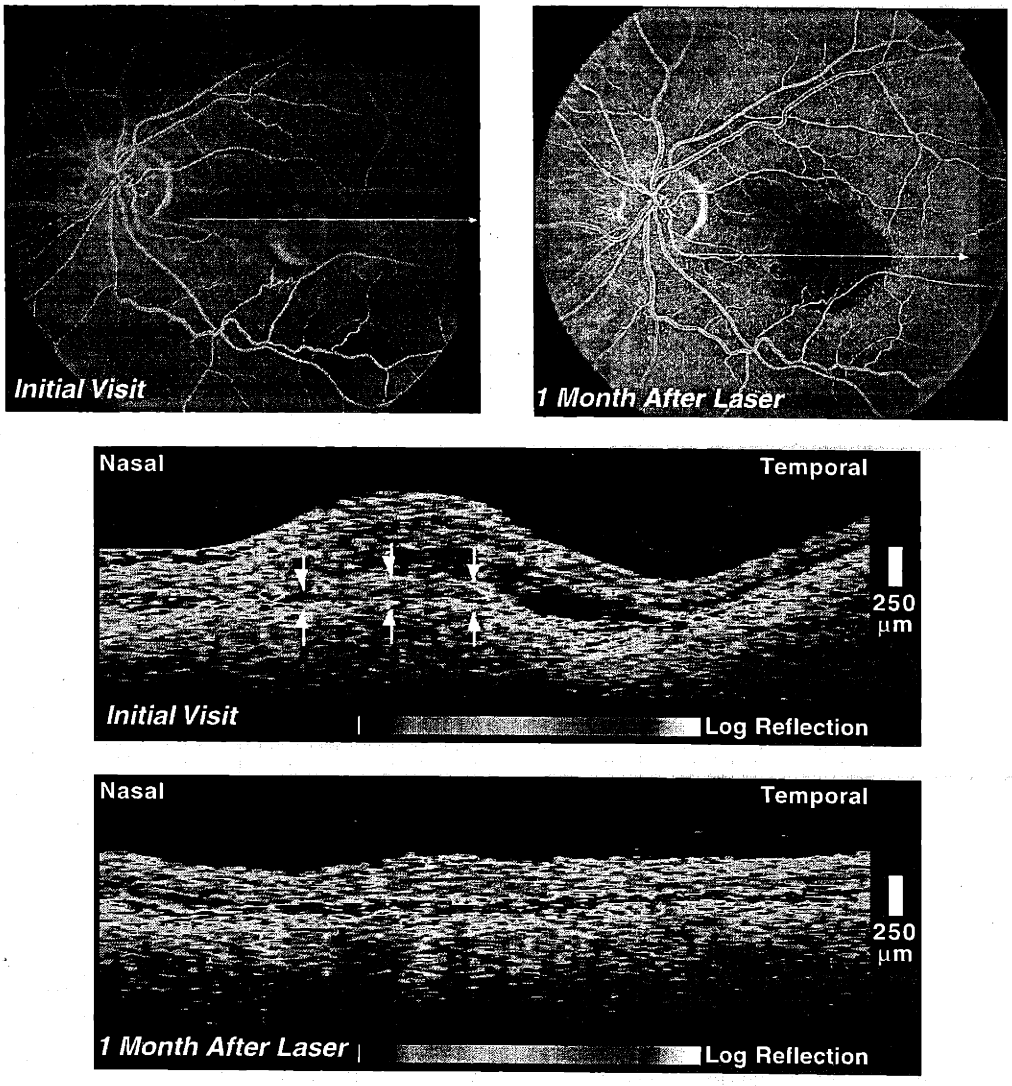

FIGURE 6-35. CNV before and after laser treatment (Case 6-15).

6.5.4 Limitations of OCT Imaging in AMD

OCT, however, is not a substitute for FA in the evaluation or treatment of CNV. Current treatment guidelines for CNV established by the Macular Photocoagulation Study (MPS) recommend laser photocoagulation over the entire area of the CNV which requires demarcation of the complete CNV boundary [140-143, 146]. Since OCT is a cross-sectional imaging modality, a single OCT only provides information on CNV boundaries within a thin tissue slice. The current acquisition time of 2.5 seconds per OCT limits the feasibility of acquiring multiple tomograms through an area of suspected CNV to adequately define the entire CNV boundary.

OCT also does not provide much additional information when there were angiographic features that obscured the boundaries of neovascular membranes. In a serous detachment of the RPE, for example, the bright hyperfluorescence from the window defect may obscure the hyperfluorescence from the CNV in the region beneath the detachment on FA. OCT also does not effectively image CNV beneath PEDs because of optical shadowing caused

by the detached RPE. Similarly, blood often obscures the boundaries of CNV on angiography. While OCT was successfully able to image CNV obscured on FA by thin hemorrhage on FA, OCT probe light was attenuated by dense subretinal or intraretinal hemorrhage which prevented adequate imaging of the choroid. Finally, it must be recognized that the reflections from particular structures within the retina on OCT are influenced by the absorption and scattering properties of intervening layers. This limitation was most apparent when attempting to distinguish true alterations in choroidal reflectivity from changes in RPE pigmentation which affected the propagation of the OCT probe beam to and from the choroid.

The use of imaging wavelengths farther in the infrared should provide increased penetration of the probe light through hemorrhage or a serous detachment of the RPE allowing better imaging of CNV beneath these lesions. Increased longitudinal resolution would provide additional information on the fine structure of the choroidal vessels and may enhance the differentiation between various retinal layers. The further development of OCT for imaging CNV is attractive for a number of reasons. Unlike FA, OCT provides purely structural information concerning abnormal vessels which may be more informative in localizing CNV than leakage of fluorescein dye, which is both a structural and functional measurement. The eligibility criteria used in the MPS clinical trials, which are based solely on angiography, apply only to a minority of cases of AMD [144]. CNV characterized as *well-defined* or *fibrovascular PED* on OCT had well demarcated boundaries which could conceivably be used to guide laser treatment. Twelve of 23 of these membranes had an occult appearance on FA and therefore would not have been eligible under MPS guidelines. Additionally, since OCT is a fiber optic technique, imaging could potentially be directly integrated with conventional laser photocoagulation treatment, providing on-line monitoring and visualization of the lesion boundaries. Finally, three-dimensional reconstructions of the retina could be obtained from multiple cross-sectional OCTs to provide complete information on the location of CNV. The tomograms forming the reconstruction could conceivably be acquired in parallel to minimize acquisition time using an OCT instrument with multiple probe beams performing simultaneous retinal scans.

Chapter 7

GLAUCOMA

7.1 Introduction

Glaucoma is a disease which affects approximately 0.5% of people 55 years and older. The incidence increases to about 2% for those 70 years and older [148, 149]. Primary open-angle glaucoma (POAG), which is the most common form, causes a progressive insidious loss of bilateral peripheral vision which is often not detected until extensive damage to the retinal nerve fiber layer (NFL) has occurred. The common perception is that elevated intraocular pressure (IOP) causes ganglion cell atrophy leading to loss of retinal nerve fibers and atrophy of the optic disc. While elevated IOP is probably the single most concomitant finding in POAG, many eyes with normal IOPs suffer from low-tension glaucoma, and many eyes with ocular hypertension do not have glaucoma. Survey studies have shown that between one third and one half of patients with POAG do not initially manifest ocular hypertension, and that as many one sixth of patients with glaucoma never have increased IOP [150, 151]. Ocular hypertension without glaucomatous damage is probably eight to ten times more common than glaucoma [151].

Thus, the diagnosis of glaucoma does not rely exclusively on IOP, but rather on the observation of glaucomatous patterns of optic nerve damage or visual field loss. Patterns of glaucomatous field loss include arcuate scotoma, paracentral scotoma, nasal step, or other advanced field loss. The accuracy of visual field testing, however, depends strongly on patient cooperation and can be affected by an inability to fixate or understand instructions. Visual field loss due to other diseases may be evident in the absence of glaucoma.

The evaluation of retinal nerve fiber layer loss and optic disc appearance relies on the traditional techniques of slit-lamp biomicroscopy, stereo fundus photography, and red-free nerve fiber layer photography. All of these techniques are subjective and variability exists even between experienced observers [152-154]. Furthermore, studies have shown that loss of up to 50% of the nerve fiber layer may precede the development of clinically detectable visual field defects and identifiable cupping of the optic disc [155-158]. Small interval changes in the appearance of the nerve head, such as notches and other local abnormalities, are often difficult to detect. Several instruments have been developed in attempt to assess the retinal nerve fiber layer and optic disc cupping in a more direct and objective manner; however none so far has gained wide acceptance in the ophthalmic community [15].

OCT has the potential for a direct, quantitative, and objective assessment of retinal nerve fiber layer (NFL) thickness [159, 160]. As described in Chapter 4, computer image processing techniques may be applied to automatically identify the reflective boundaries at the vitreoretinal interface, the retinal pigment epithelium (RPE), and the NFL. Additionally, the NFL

thickness may be displayed topographically to enable the physician to quickly compare OCT results with conventional examination. This Chapter will describe preliminary studies with OCT of the measurement of NFL thickness in normal and glaucomatous eyes.

7.2 Case Reports

CASE 7-1. Normal nerve fiber layer with asymmetric cupping (Figure 7-1). A 31-year-old white woman was a glaucoma suspect because of asymmetric cupping which was greater in the right eye than the left *(top)*. Her best corrected visual acuity was 20/25 OD and 20/40 OS. The intraocular pressure was normal in both eyes (16 mm Hg OD and 14 mm Hg OS). Red-free photography *(middle)* demonstrated a healthy nerve fiber layer in both eyes. OCT *(bottom)* also displayed normal NFL thickness in both eyes. The NFL was thickest superotemporally and inferotemporally and was thinner with increasing distance away from the optic disc, consistent with a normal distribution.

FIGURE 7-1. Normal nerve fiber layer with asymmetric cupping (Case 7-1).

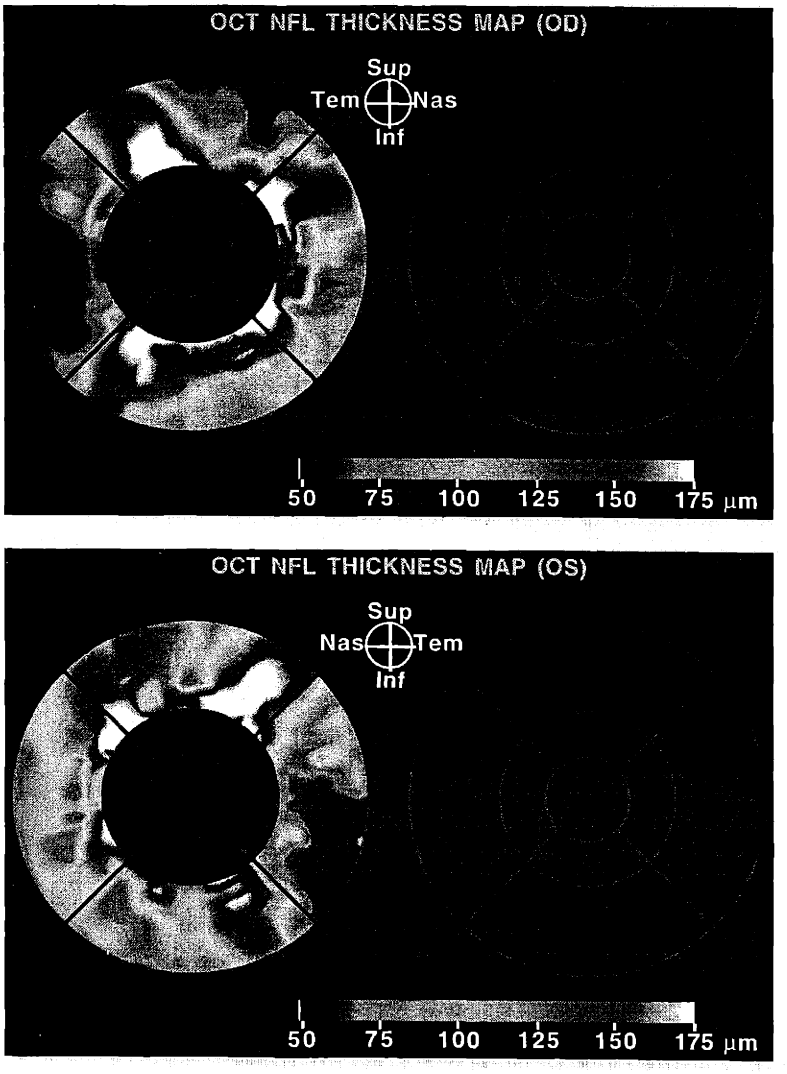

FIGURE 7-1. Normal nerve fiber layer with asymmetric cupping (Case 7-1). *(Continued)*

CASE 7-2. Advanced primary open-angle glaucoma (Figure 7-2). A 68-year-old black woman had advanced primary open angle glaucoma in her left eye. Her intraocular pressure OS was 14 mm Hg while taking timolol 0.5% twice a day and pilocarpine 4% four times a day. Her visual acuity was 20/20. Dilated fundus examination (left) showed virtually complete loss of the neuroretinal rim, attenuation of the retinal arteries and veins, and no observable red-free nerve fiber layer reflection. A Humphrey visual field (right) demonstrated a dense inferior arcuate scotoma with a possible superior arcuate defect as well, although there was low patient reliability. A circular OCT acquired around the optic disc at a diameter of 3.4 mm showed diffuse thinning of the NFL which was greater superiorly than inferiorly. The NFL thinning was especially prominent at 1:00 (compared to 5:00) which was consistent with the visual field results. The OCT topographic map of NFL thickness also indicated severe NFL loss, especially superotemporally.

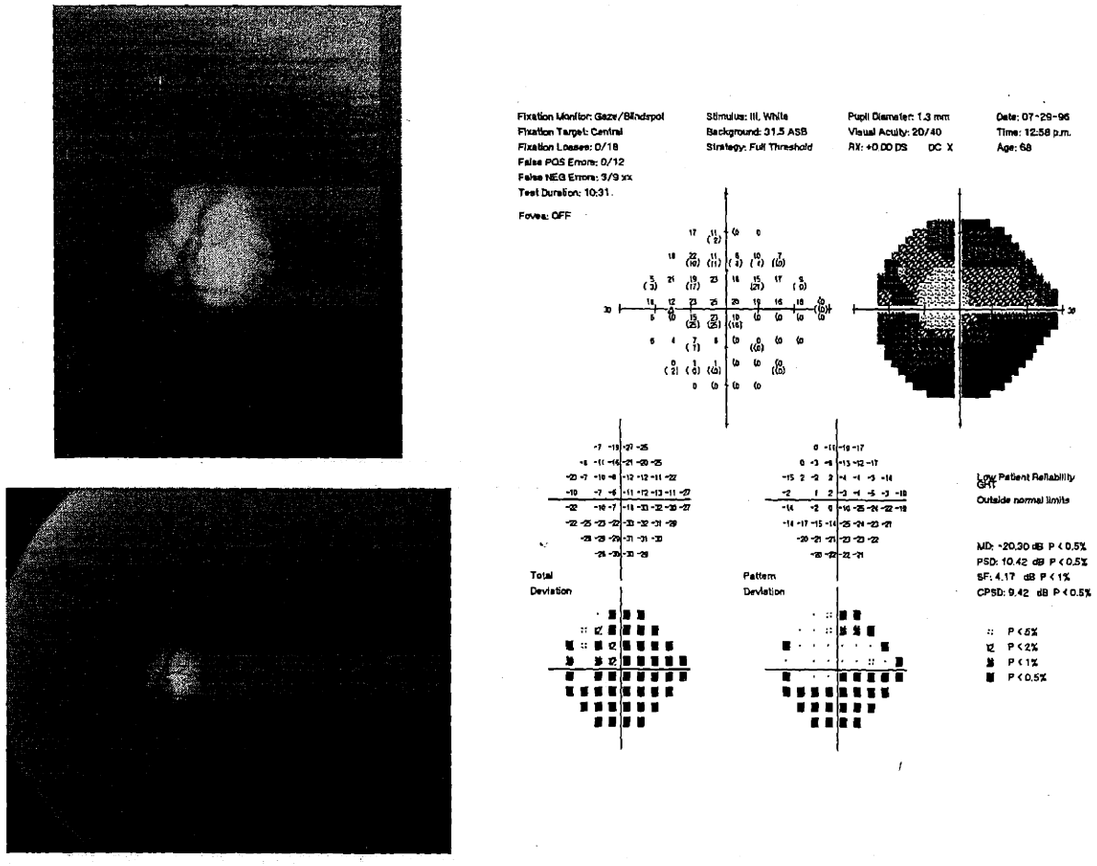

FIGURE 7-2. Advanced primary open-angle glaucoma (Case 7-2).

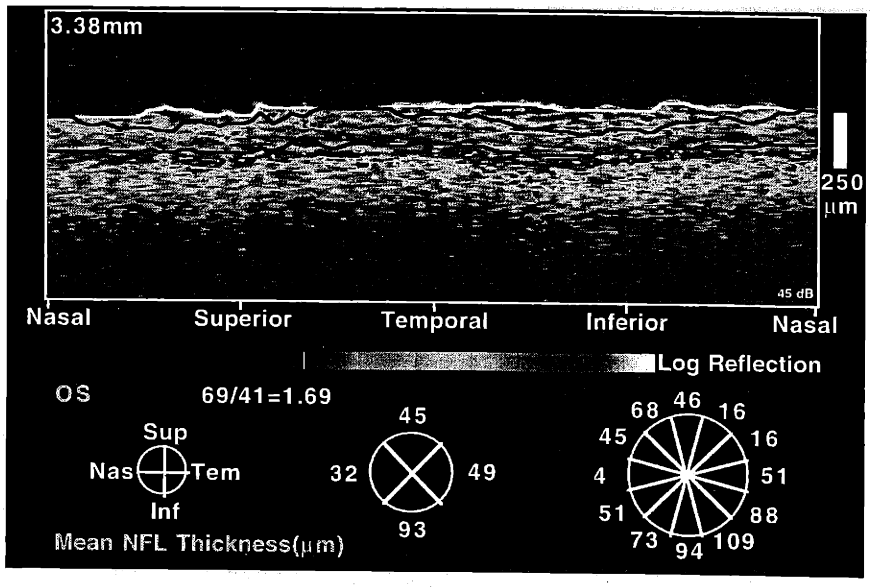

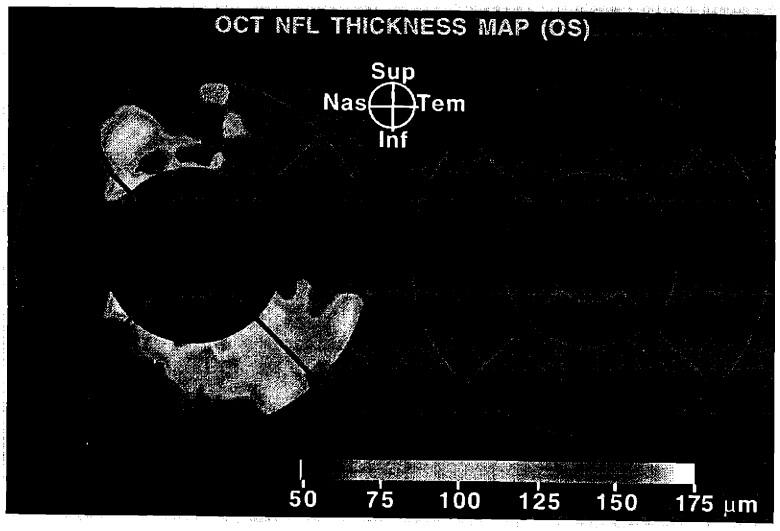

FIGURE 7-2. Advanced primary open-angle glaucoma (Case 7-2). *(Continued)*

CASE 7-3. Primary open angle glaucoma with superior arcuate visual field defect (Figure 7-3). A 68-year-old black woman was taking levobunolol 0.25% in her right eye for primary open-angle glaucoma. Her visual acuity in this eye was 20/20 with correction and the intraocular pressure was 11 mm Hg. Dilated fundus examination *(left)* revealed moderate cupping and attenuation of the neuroretinal rim from 6:00 to 8:00. There was a corresponding loss of the red-free NFL reflection inferiorly. A superior arcuate scotoma was noted on a Humphrey visual field *(right)*. Both a circular OCT around the optic disc and the OCT topographic map of NFL thickness displayed marked attenuation of the NFL inferotemporally.

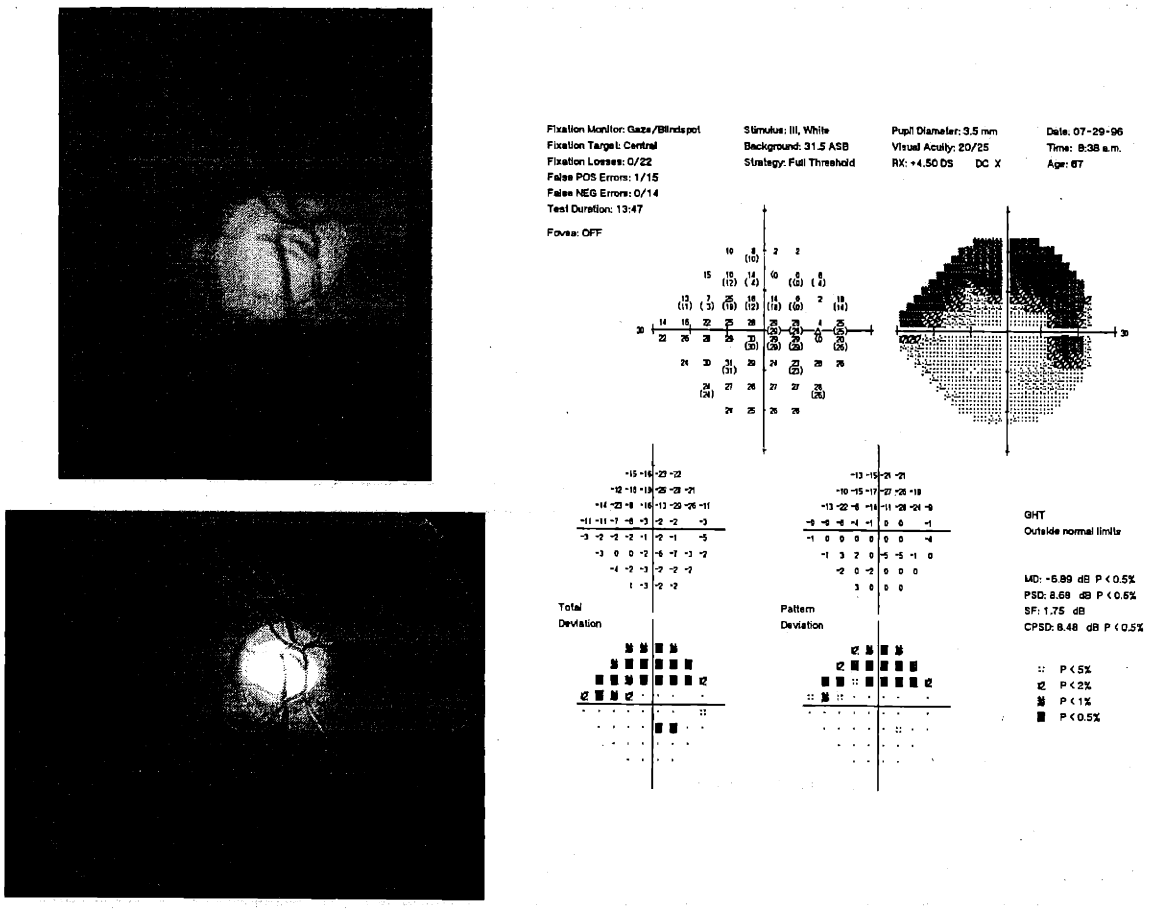

FIGURE 7-3. Open angle glaucoma with superior arcuate field defect (Case 7-3).

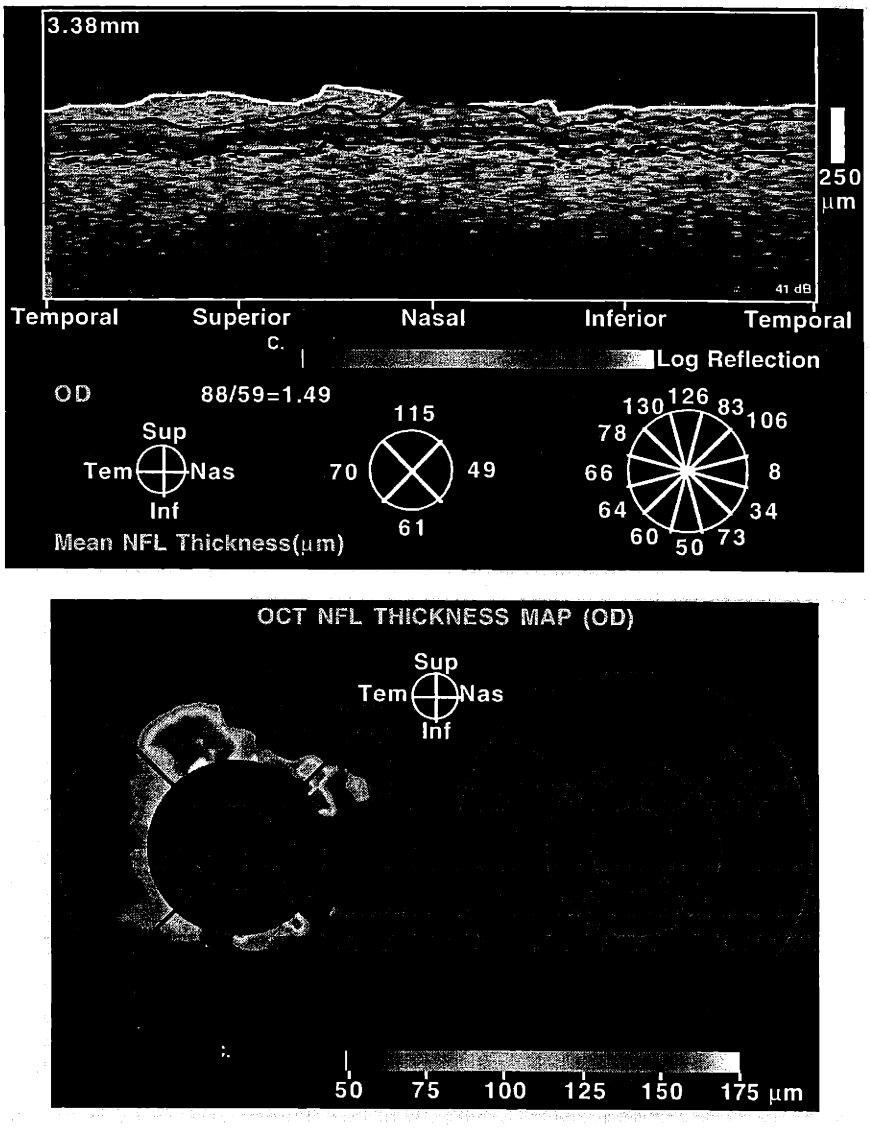

FIGURE 7-3. Open angle glaucoma with superior arcuate field defect (Case 7-3). *(Continued)*

CASE 7-4. Focal superior nerve fiber layer defect (Figure 7-4). A 58-year-old white man with primary open-angle glaucoma was taking pilocarpine Ocusert 40s weekly in both eyes. The left eye had a visual acuity of 20/15 with an intraocular pressure of 19 mm Hg. Dilated ophthalmoscopy *(left)* of this eye showed mild cupping and a subtle focal defect in the superior nerve fiber layer. A Humphrey visual field of the left eye *(right)*, however, showed no evidence of any corresponding visual field loss. A circular OCT acquired around the optic disc showed a focal region of thinning in the superior NFL measuring 70 μm *(arrow)*. The OCT topographic map of NFL thickness also showed a wedge shaped defect in the NFL superiorly.

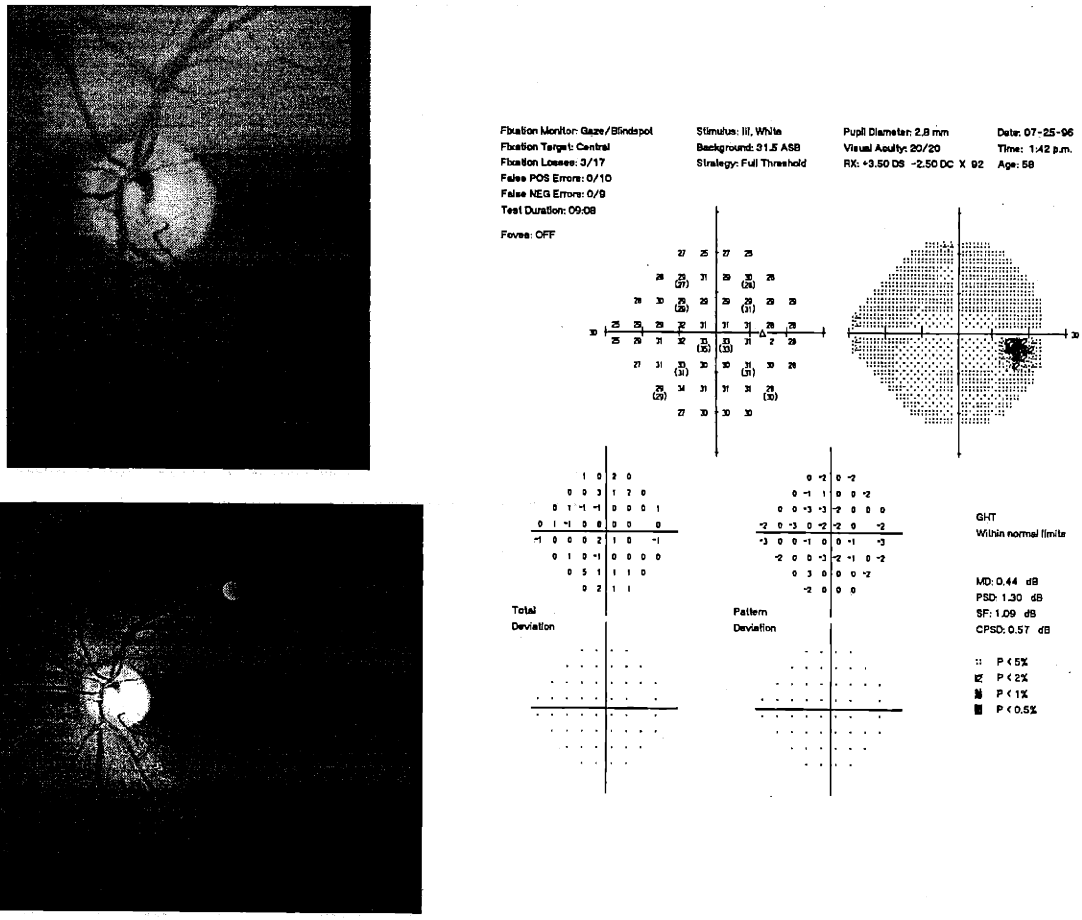

FIGURE 7-4. Focal superior nerve fiber layer defect (Case 7-4).

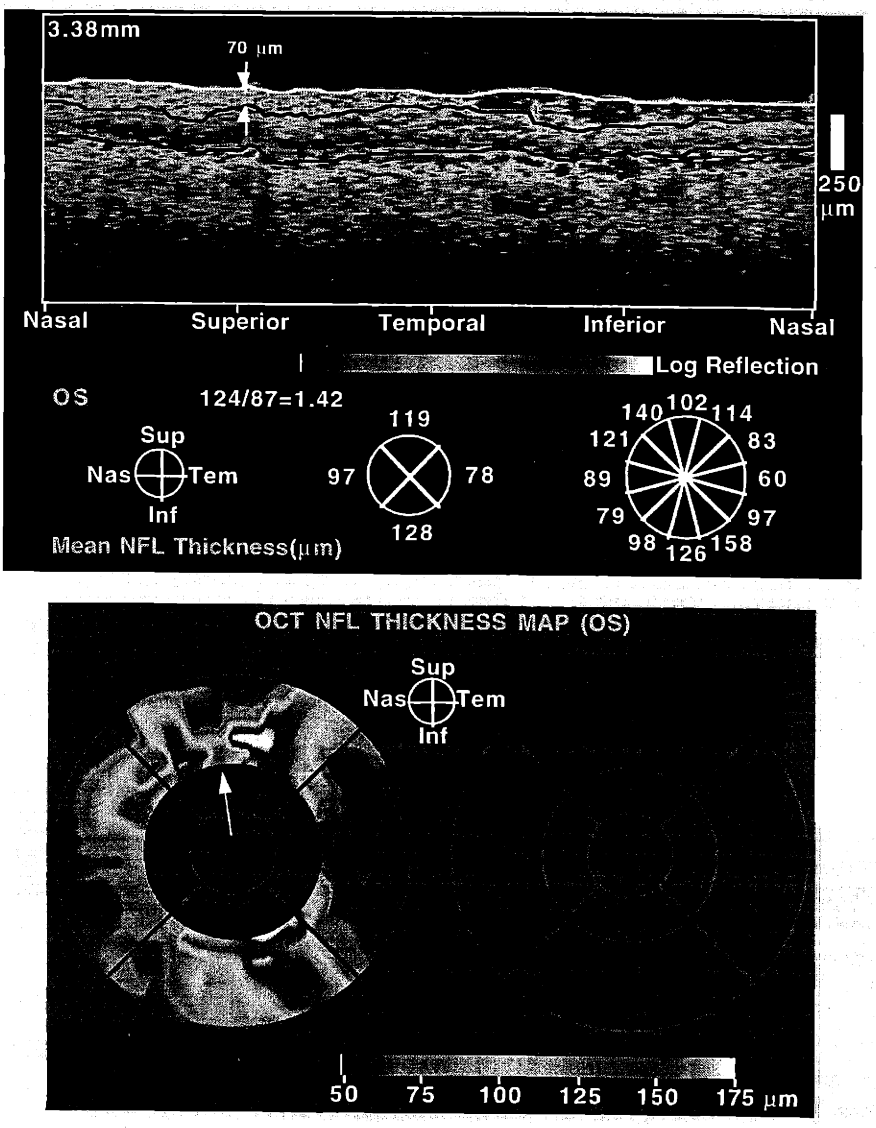

FIGURE 7-4. Focal superior nerve fiber layer defect (Case 7-4). *(Continued)*

7.3 Nerve Fiber Layer Thickness and Reproducibility

The reproducibility of the NFL thickness measurements relative to the difference in NFL thickness between healthy and glaucomatous eyes is important to assess the potential widespread applicability of OCT to the diagnosis and management of glaucoma. This Section will examine the reproducibility and population variability of NFL thickness measurements obtained from circular OCTs around the optic disc. Results are reported by individual A-scan, and for measurements averaged over clock hour, quadrant, vertical or horizontal hemifield, and overall average.

7.3.1 NFL Thickness and Reproducibility Data

A single dataset was used for NFL measurement reproducibility. Ten healthy eyes and ten eyes with glaucoma from 20 patients were examined using a 3.4 mm diameter circular OCT centered on the optic disc. Each eye was examined at five separate visits over a one month period. Fixation was accomplished by using a computer controlled flashing light in the eye being scanned.

The *edge* algorithm described in Section 4.7.2 was used to automatically compute NFL thickness from the OCTs. A threshold of 15 dB below the (filtered) maximum reflectivity in both the neurosensory retina and choroid was chosen (see Section 4.7.3). NFL thickness was reported for each individual A-scan, and as averages over clock hour, quadrant (superior, inferior, temporal and nasal), hemifield (superior/inferior, or temporal/nasal), and overall mean. An approximate two-way analysis of variance was performed. An estimate of the within patient variability was computed from the mean (averaged over patients) of the variance for each patient over the five visits. The between patient variability was estimated from the variance (over all the patients) of the mean NFL thickness for each patient (averaged over visits). The normal and glaucomatous eyes were tabled separately for this analysis.

7.3.2 NFL Thickness and Reproducibility by A-scan

The NFL thickness and reproducibility for each individual A-scan is plotted in Figure 7-5 for both normal and glaucomatous eyes. The data for normal eyes appears in the left-hand column and the data for glaucomatous eyes is to the right. The top-left graph shows the NFL thickness averaged over the 10 healthy eyes for each of the 100 A-scans. The mean NFL thickness *(solid line)* exhibits a typical double humped pattern corresponding to the superotemporal and inferotemporal bundling of nerve fibers. The nasal and temporal NFL are thinnest as expected. A prominent notch appears in the superior NFL which may correspond to the location of the inferotemporal artery and vein. A similar, but smaller notch appears in the inferonasal NFL. The dashed lines on the top-left graph provide an indication of the normal population variability and were computed for each A-scan by adding or subtracting the standard deviation (between subjects) of the mean (over each visit) NFL thickness measurement for each subject. The between subject SD is largest in the superonasal and inferonasal regions and is smallest temporally.

The bottom-left graph in Figure 7-5 compares, for healthy eyes, the between subject SD *(dotted line)* with the within subject SD *(dashed line)*. The within patient SD was computed for each A-scan by taking the average (over all subjects) of the standard deviation (between visits) of the NFL thickness measurements for each subject. Thus, the within subject SD is a measure of the measurement reproducibility. The bottom-left graph shows that the reproducibility SD is smaller than the population SD in all regions except nasally. The average within subject SD over all the A-scans is 14.6 μm which compares to an average between subject SD of 19.3 μm.

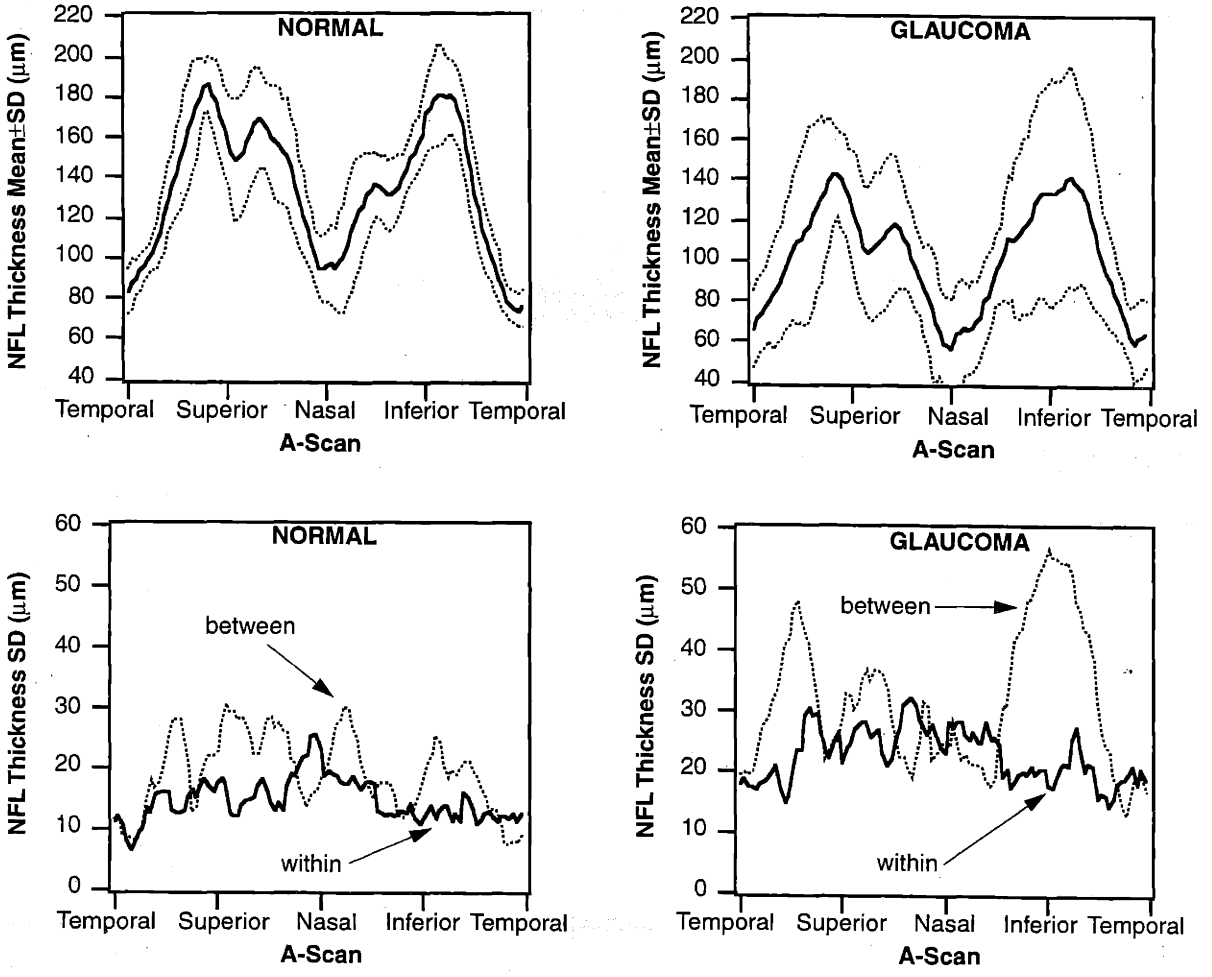

FIGURE 7-5. NFL thickness and reproducibility by A-scan. Top: population mean and SD. Bottom: population SD *(between)* compared to reproducibility SD *(within)*.

The corresponding plots for the 10 eyes with glaucoma appear on the right in Figure 7-5. The upper-right graph plots the mean and the between patient SD of the NFL thickness measurements. The double hump pattern seen in normal subjects is visible; however, the average NFL thickness is decreased. A notch possibly due to blood vessels is visible in the superior NFL, just as in the normal eyes; however, the inferonasal notch seen in normals is not evident in the glaucomatous eyes. The disappearance of the inferonasal notch may be a result of the increased between patient SD in the glaucomatous eyes which is especially prominent inferiorly.

The within *(solid line)* and between patient SD *(dotted line)* for the glaucomatous eyes are shown bottom-right graph in Figure 7-5. The between patient SD exceeds the within patient SD in all regions except nasal, just as in normals. However, both the population SD and the reproducibility SD are larger in the eyes with glaucoma compared to normals. Most of the population variability in the glaucomatous eyes occurs inferotemporally and superotemporally generally corresponding with the regions of greatest NFL thickness. The large population variance in these regions probably signifies the wide range of NFL atrophy in the

superotemporal and inferotemporal NFL bundles in eyes with glaucoma. The inferior population variability is larger than the superior quadrant variability which may signify that the inferior NFL is more often a target of glaucomatous damage. The average within patient SD over all A-scans is 22.7 μm and the average between patient SD is 31.5 μm.

7.3.3 NFL Thickness and Reproducibility by Clock Hour

Figure 7-6 repeats the data presented in Figure 7-5 except that NFL thickness is averaged over each clock hour. Averaging by clock hours decreases the variability between A-scans, but also reduces the ability to detect focal notches in the NFL thickness. Thus, in the normal eyes *(left)* the NFL means and standard deviations have the same general profile by A-scan as by clock hours; however, the superior and inferonasal notches seen in Figure 7-5 are not evident in the plots by clock hour. The between subject SD (average value over all clock hours of 17.5 μm) is greater than the within subject SD (average value of 10.3 μm) for all clock hours.

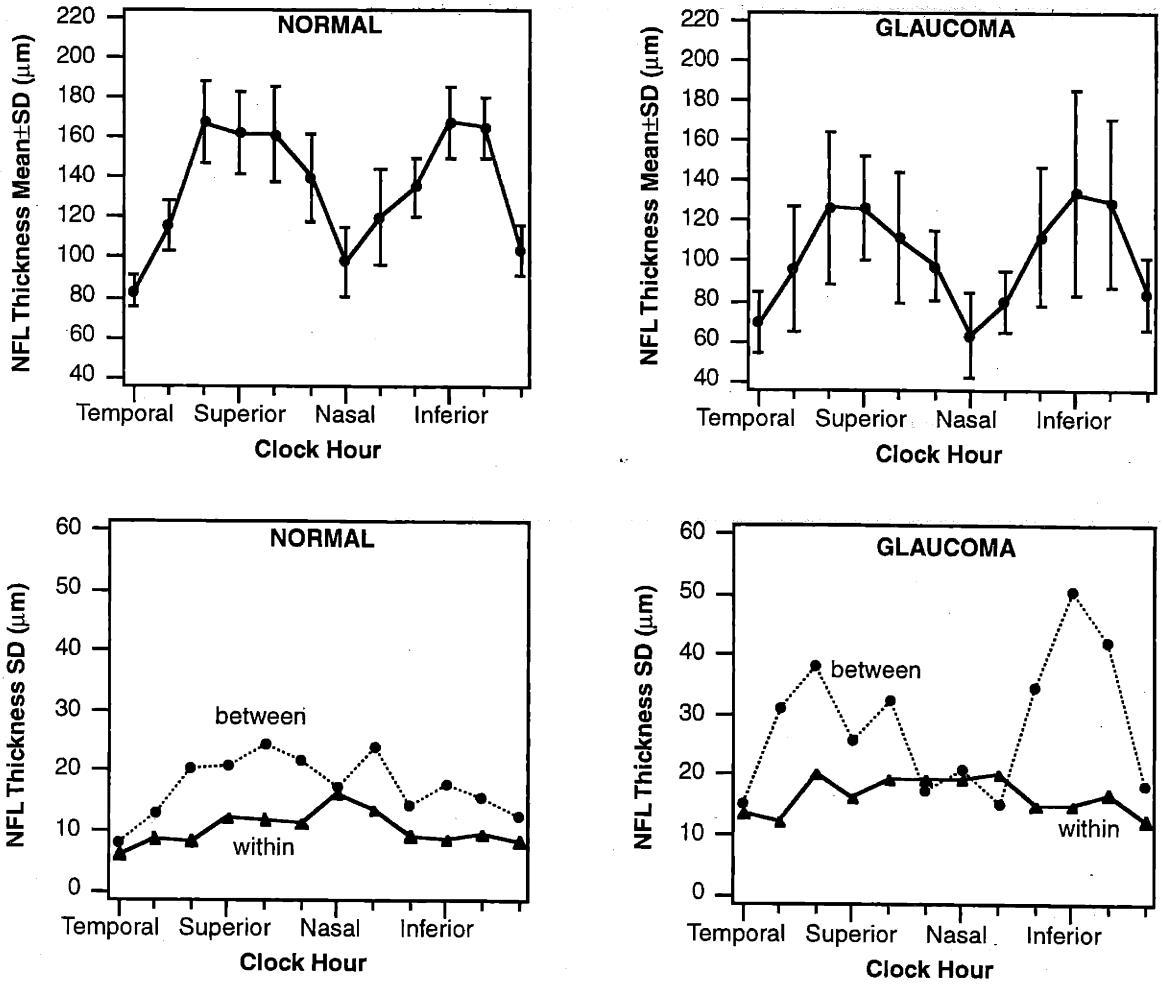

FIGURE 7-6. NFL thickness and reproducibility by clock hour. Top: population mean and SD. Bottom: population SD *(between)* compared to reproducibility SD *(within)*.

In the eyes with glaucoma *(right)*, the large population variability in the inferior region is again visible. Again, this and the relatively large superotemporal variability probably reflect the varying levels of NFL atrophy in the eyes with glaucoma. The average between patient SD over all clock hours is 28.5 μm and the average within patient SD is 16.5 μm.

7.3.4 NFL Thickness and Reproducibility by Quadrant

The NFL thickness, population variability, and reproducibility by quadrant are shown in Figure 7-7. For healthy eyes *(left)*, the between subject SD averaged over all quadrants is 13.1 μm. The average within subject SD for normal eyes is 7.4 μm. In the eyes with glaucoma *(right)*, the average between patient SD over all quadrants is 24.2 μm and the average within patient SD is 12.4 μm.

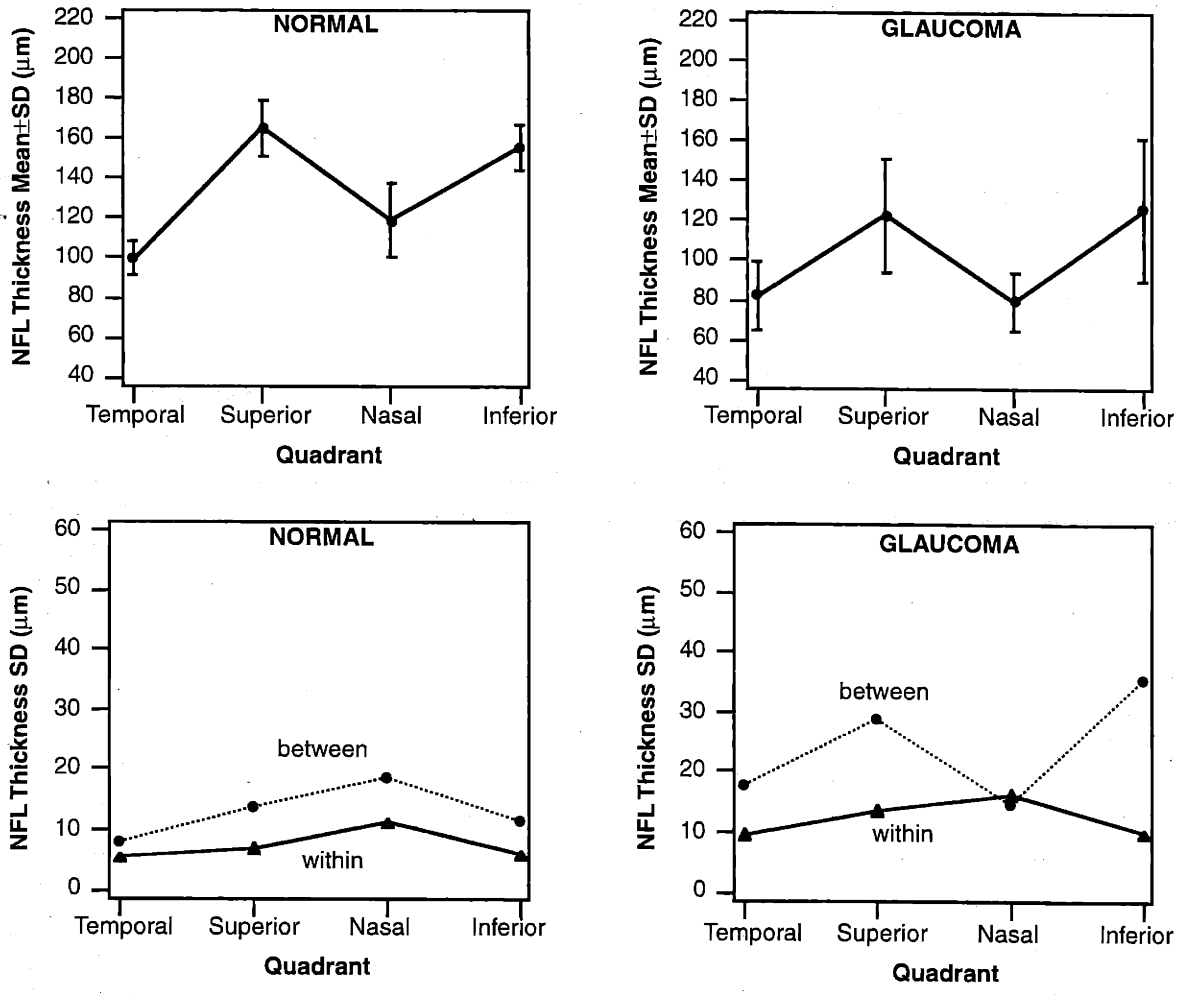

FIGURE 7-7. NFL thickness and reproducibility by quadrant. Top: population mean and SD. Bottom: population SD *(between)* compared to reproducibility SD *(within)*.

7.3.5 NFL Thickness and Reproducibility by Hemifield and Overall Mean

Figure 7-8 shows the NFL thickness and reproducibility by hemifield and overall mean. The vertical hemifield is the average NFL thickness over the superior and inferior quadrants and the horizontal hemifield is the average NFL thickness over the temporal and nasal quadrants.

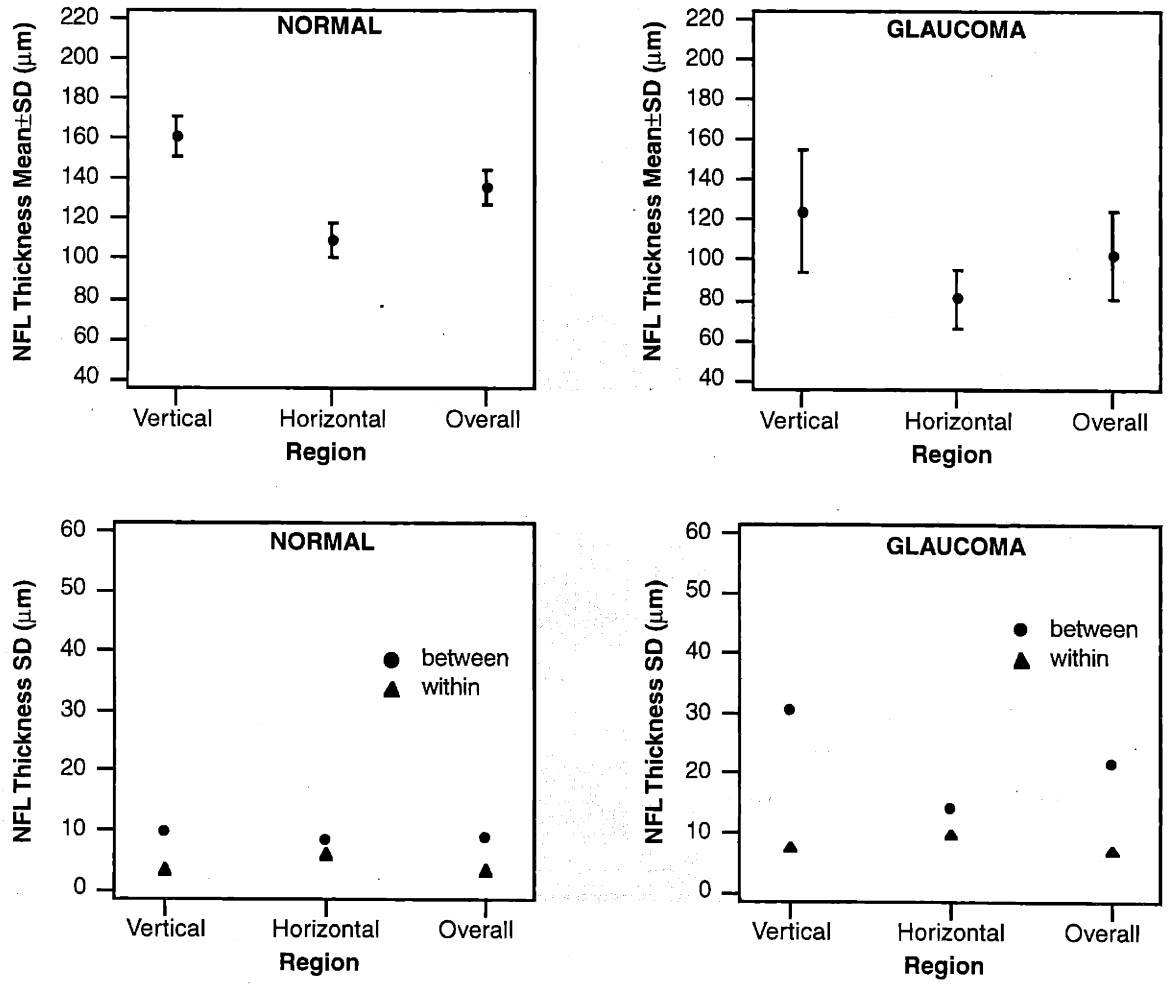

FIGURE 7-8. NFL thickness and reproducibility by hemifield (vertical or horizontal) and overall mean. Top: population mean and SD. Bottom: population SD *(between)* compared to reproducibility SD *(within)*.

7.3.6 NFL Sensitivity and Specificity

The data presented in Sections 7.3.1 through 7.3.5 provide a preliminary estimate of the reproducibility and population variance of normal and glaucomatous eyes. It is of interest to use this data to ascertain in an approximate manner whether OCT has the potential to successfully differentiate normal and glaucomatous eyes based on measurements of NFL thickness alone. As discussed in Sections 7.3.1 through 7.3.5, several measurement schemes are

possible. Intuitively, measurement of NFL thickness by individual A-scan or clock hour would provide the most sensitivity to focal NFL loss; however, averaging over quadrants or hemifields might reduce the population variances enough to increase the effective separation between the two categories. A quantitative exposition of these concepts which includes the effect of measurement reproducibility is necessary to provide an initial indication of the best methods for handling the data and an estimate of the power of the OCT test.

The standard hypothesis testing problem is formulated with reference to Figure 7-9. For a given measurement, there exists a null hypothesis H_0 (the eye is normal) characterized by a probability density with mean μ_N and variance σ_N^2, and a test hypothesis H_1 (the eye has glaucoma) characterized by a probability density with mean μ_G and variance σ_G^2. A threshold μ_0 is chosen such that if the NFL measurement is less than μ_0, then H_1 is chosen (*i.e.* the eye is considered glaucomatous). The parameter α is a measure of the Type 1 error (*i.e.* the probability of calling the eye diseased when it is in fact normal) and β measures the Type 2 error (*i.e.* the probability of calling the eye normal when it is in fact diseased). The goal of this Section will be to estimate values of μ_0, α and β for different NFL measurements based on the data presented in Sections 7.3.1 through 7.3.5.

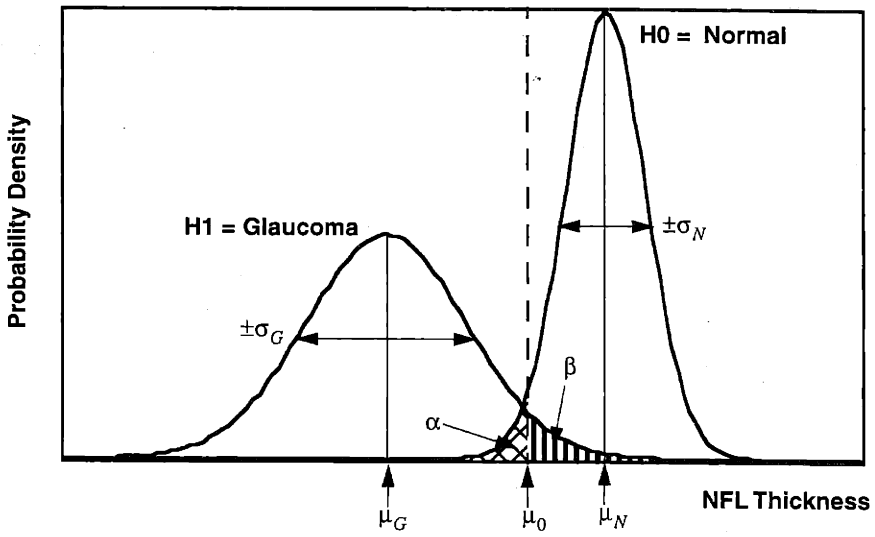

FIGURE 7-9. Glaucoma hypothesis testing problem.

Hypothesis Testing Neglecting Measurement Error

In the limit of perfectly reproducible measurements, the within patient SD is zero and the only variability derives from sampling different population members. Assume at the outset a maximum value for the Type 1 error of $\alpha = 0.1$. This is equivalent to assuming at least a specificity of 90% for identifying healthy eyes, or a 90% one-sided confidence interval about the mean for normal subjects. Since the probability density of NFL thickness for healthy eyes is mostly likely normal (*i.e.* $N(\mu_N, \sigma_N^2)$), the maximum threshold μ_0 is given by

$$\mu_0 = \mu_N - z_\alpha \sigma_N \tag{7.1}$$

where z_α is defined in terms of the cumulative distribution function $\Phi(z)$ for a unit normal probability density:

$$\frac{1}{\sqrt{2\pi}}\int_{-\infty}^{z_\alpha} e^{-\frac{x^2}{2}}dx = \Phi(z_\alpha) = 1-\alpha. \tag{7.2}$$

Note that $z_{0.1} = 1.282$. One can then calculate the Z-score Z_0 of the threshold NFL thickness μ_0 in terms of the population mean μ_G and variance σ_G^2 of eyes with glaucoma:

$$Z_0 = \frac{\mu_0-\mu_G}{\sigma_G} = \frac{\mu_N-\mu_G-\sigma_N z_\alpha}{\sigma_G}. \tag{7.3}$$

This immediately gives the Type 2 error $\beta = 1-\Phi(Z_0)$. Equation (7.3) is plotted by A-scan, clock hour, quadrant, hemifield, and overall mean in the next Section.

Hypothesis Testing Considering Measurement Error

Measurement error will in general increase both the Type 1 and Type 2 error. Let the measurement error for normal eyes be distributed as $N(0, \varepsilon_N^2)$ and the measurement error for glaucomatous eyes be distributed as $N(0, \varepsilon_G^2)$. If the average of N samples is taken to represent a single measurement, then the effective distribution in the measurement average becomes $N(0, \varepsilon_N^2/N)$ and $N(0, \varepsilon_G^2/N)$. Then, assuming that the measurement error is uncorrelated with the patient being evaluated, the measured NFL thickness is distributed as $N(\mu_N, \sigma_N^2+\varepsilon_N^2/N)$ for a healthy eye and as $N(\mu_G, \sigma_G^2+\varepsilon_G^2/N)$ for a diseased eye. In other words, the measurement error effectively acts to increase the population variability.

Following the development of Equations (7.1) and (7.3), to achieve a given Type 1 error α, the threshold μ_0 is

$$\mu_0 = \mu_N - z_\alpha\sqrt{\sigma_N^2+\frac{\varepsilon_N^2}{N}}. \tag{7.4}$$

To calculate the Type 2 error, we assume that the eye being measured is diseased. The relevant Z-score is therefore

$$Z_0 = \frac{\mu_0-\mu_G}{\sqrt{\sigma_G^2+\frac{\varepsilon_G^2}{N}}} = \frac{\mu_N-\mu_G-z_\alpha\sqrt{\sigma_N^2+\frac{\varepsilon_N^2}{N}}}{\sqrt{\sigma_G^2+\frac{\varepsilon_G^2}{N}}}. \tag{7.5}$$

The Type 2 error β is given as before. Equation (7.5) reduces to Equation (7.3) in the limit of infinite samples ($N\to\infty$) as expected. Equation (7.5) also shows that averaging more samples provides virtually no gain if the population variance σ^2 is much larger than the measurement variance ε^2.

Experimental Results for Hypothesis Testing

Equations (7.3) and (7.5) are plotted in Figure 7-10 using the estimates for the means μ_N and μ_G and the variances σ_N^2, σ_G^2, ε_N^2, and ε_N^2 given in Sections 7.3.1 through 7.3.5. A single measurement ($N = 1$) was assumed with a Type 1 error of $\alpha = 0.1$. The sensitivity

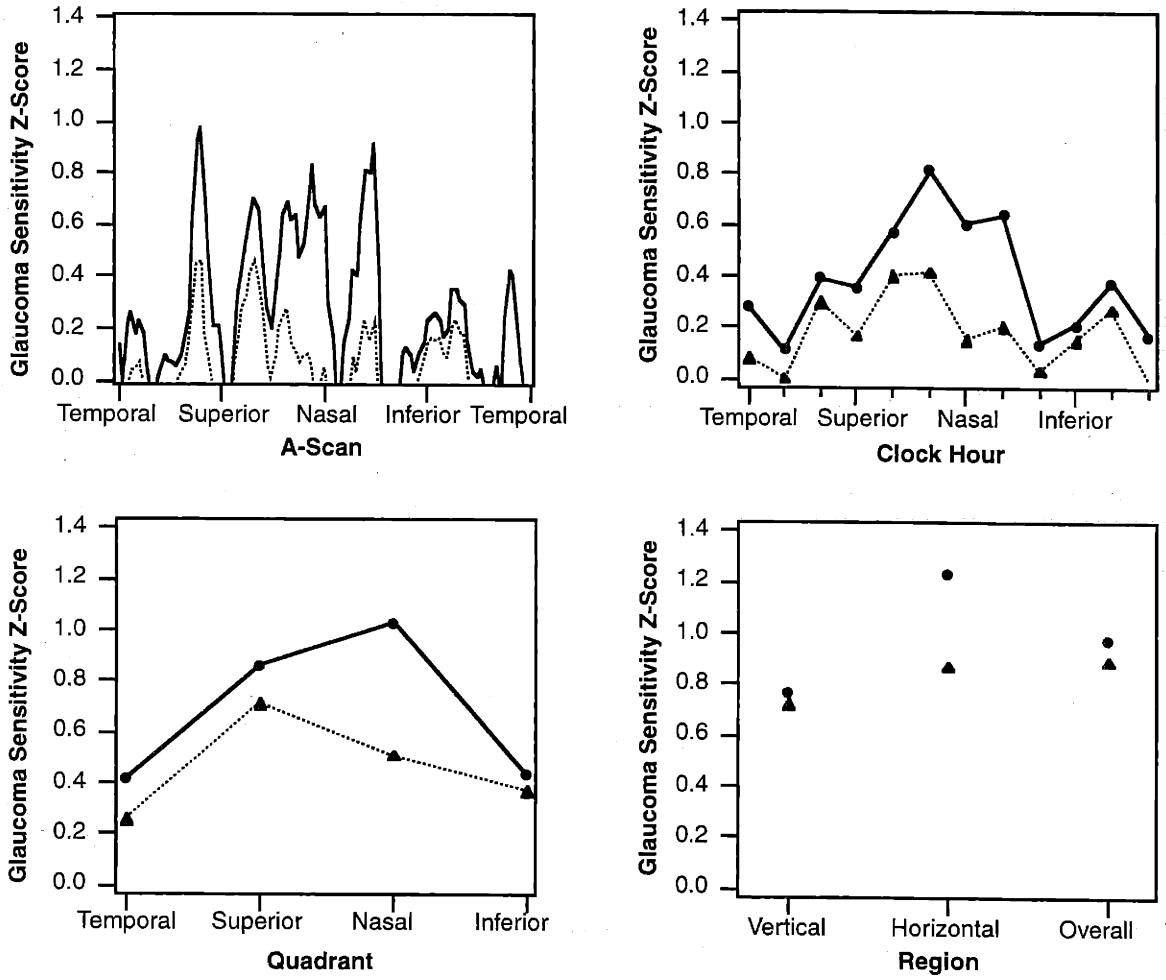

FIGURE 7-10. Hypothesis testing sensitivity assuming a Type 1 error of $\alpha = 0.1$ using the *edge* algorithm.

$(1 - \beta)$ Z-score is plotted as a solid-line or circles for the limit of infinite measurements (best case), and as a dashed-line or triangles in the limit of a single measurement (worst case). The Z-score generally increases with the size of the wedge used for a single measurement, due to decreasing population variability relative to the population mean with larger wedge sizes. This result suggests that the spatial distribution of nerve fiber layer thickness varies across different patients, but that the total amount of nerve fiber layer remains relatively constant. Thus, based on this set of data, the overall mean is the best measurement to use in separating healthy from diseased eyes. Figure 7-11 plots the relation between Z-score, sensitivity and Type 2 error for reference.

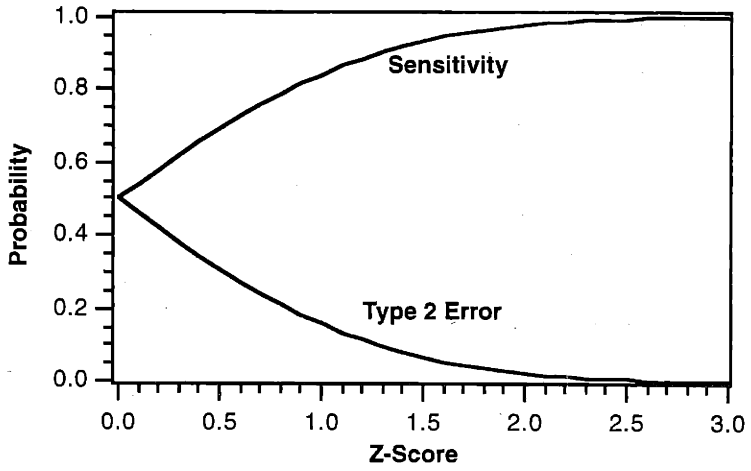

FIGURE 7-11. Sensitivity and Type 2 error versus Z-score for a one-sided test with normally distributed populations.

Physiologically, one would expect the superotemporal and inferotemporal regions to exhibit the highest sensitivity corresponding to the natural bundling of the nerve fibers in these regions. Interestingly, the nasal quadrant displays a higher than expected sensitivity which is in part due to the relatively low population variability in this area for the glaucomatous eyes. Section 7.3.7 will discuss possible reasons for this finding.

7.3.7 Limitations of the Hypothesis Testing Analysis

The analysis described in Section 7.3.6 for estimating the test sensitivity by assuming a particular specificity is limited by several factors. First, the number of subjects was small which limits the accuracy of the estimates of the population means, the population variances, and the reproducibility variances necessary to evaluate Equation (7.5). The sensitivity of Equation (7.5) to these parameters may be estimated since the population means have a t distribution and the population variances have a χ^2 distribution, both with 9 degrees of freedom. The 90% confidence intervals for these parameters for measurements of overall mean NFL thickness are displayed in Table 7-1. It is evident by inspection that these intervals can cause enormous variation in the sensitivity Z-score evaluated by Equation (7.5).

A second limitation of the analysis in Section 7.3.6 is that only a single measurement was used in the hypothesis testing process. The most reproducible and predictive parameter was the overall mean NFL thickness. Thus, the hypothesis testing algorithm was mostly likely sensitive to diffuse NFL atrophy occurring in glaucoma. However, it is also well known that focal NFL loss can occur in only a small arc around the optic disc while leaving the other nerve fibers relatively preserved. Furthermore, it is clear that visual field and nerve fiber layer defects can affect the superior and inferior NFL independently. Thus, a more sensitive and specific decision making process would be based on a combination of multiple (*e.g.* the most important clock hours or quadrants) rather than a single measurement.

These more geographically specific measurements were found to be less predictive of disease state than the overall mean. This is most likely because the overall mean was most sensitive to diffuse NFL loss. It is not surprising that an individual measurement of NFL thickness by A-scan or clock hour is less sensitive to such atrophy since these measurements

Population	Parameter	Variable	Estimate	Low	High
Normal	Population Mean	μ_N	135.4	130.4	140.4
	Population SD	σ_N	8.7	5.7	13.1
	Reproducibility SD	ε_N	3.4	2.2	5.1
Glaucoma	Population Mean	μ_G	102.8	90.2	115.4
	Population SD	σ_G	21.8	14.4	32.9
	Reproducibility SD	ε_G	7.2	4.8	10.9

TABLE 7-1. 90% confidence intervals for the overall mean NFL thickness (μm) using the *edge* algorithm.

are intrinsically more variable. However, these measurements may be more likely to detect focal or wedge-shaped loss in either the superior or inferior NFL which would cause a prominent local reduction in NFL thickness but would have less effect on the overall mean NFL thickness. Because only a small number of patients were used in the present study, it was not possible to geographically compare different OCT measurements with clinically identified regions of field or NFL loss.

The eyes with glaucoma exhibited a large population variability in the superior and inferior regions because it is likely that glaucomatous damage affects the NFL thickness in these regions first. Since the glaucoma population variability appears in the denominator of Equation (7.5), these large variations caused the superior and inferior A-scans, quadrants, and clock hours to exhibit an apparently reduced sensitivity compared to the nasal or temporal regions.

7.4 Comparison of Image Processing Algorithms

The various imaging processing algorithms discussed in Sections 4.7.2 and 4.7.3 for determining NFL thickness were compared using the sensitivity and specificity analysis described above in Section 7.3.6. Recall that the three algorithms operated on each A-scan individually, using thresholds which were also computed separately by A-scan:

- *Edge*: after smoothing the image, for each A-scan start at the photoreceptors and search upwards for the first pixel above the threshold.
- *Count*: count the number of pixels in the neurosensory retina which exceed the threshold.
- *Sum*: integrate the logarithm of the reflectivity between the photoreceptors and the inner limiting membrane.

The three possible methods for choosing the threshold for each A-scan were

- *All*: take a constant fraction of the filtered maximum reflectivity.

- *NSR*: take a constant fraction of the filtered maximum reflectivity in the neurosensory retina.

- *Choroid*: take a constant fraction of the filtered maximum reflectivity in the choroid.

Thresholding based on the maximum choroidal reflectivity was similar to thresholding on the overall maximum reflectivity; therefore only the results from the *all* and *NSR* methods are reported here. For the *edge* and the *count* algorithms, the threshold value was set to 15 dB below the filtered maximum reflectivity if the *all* method was used, and 13 dB below the maximum for the *NSR* method. For the *sum* algorithm, the threshold value equaled the filtered maximum reflectivity regardless of the thresholding method used.

7.4.1 Reproducibility of Different Algorithms

The reproducibility (within patient SD) is plotted versus the square-root of the wedge size (A-scan, clock hour, quadrant, hemifield, or overall mean) of the measurement for each of the three algorithms and two thresholds for determining NFL thickness (Figure 7-12). The reproducibility of retinal thickness measurements performed on the same data is provided for comparison (Figure 7-13). The retinal thickness reproducibility SD for A-scans in healthy eyes is approximately the full-width at half-maximum (FWHM) axial point spread function. The reproducibility SD decreases when averaging over larger regions as expected, but does not decrease linearly with the square root of the size of the wedge indicating the presence of non-random error. The retinal thickness reproducibility is slightly worse for eyes with glaucoma compared to healthy eyes.

Healthy eyes also exhibit better NFL thickness reproducibility regardless of the algorithm or threshold used for measurement. Several other trends may be identified from Figure 7-12. First, thresholding based on the neurosensory retinal reflections (*NSR*) is generally more reproducible than thresholding based on both the NSR and choroidal reflection (*all*). Thus, the choroidal reflectivity varies somewhat independently from the retinal reflectivity when there are differences in alignment. The choice of threshold is most important for the *edge* algorithm and least important for the *sum* algorithm. The *edge/NSR*, *sum/NSR*, and *sum/all* methods closely approach the reproducibility achieved for retinal thickness.

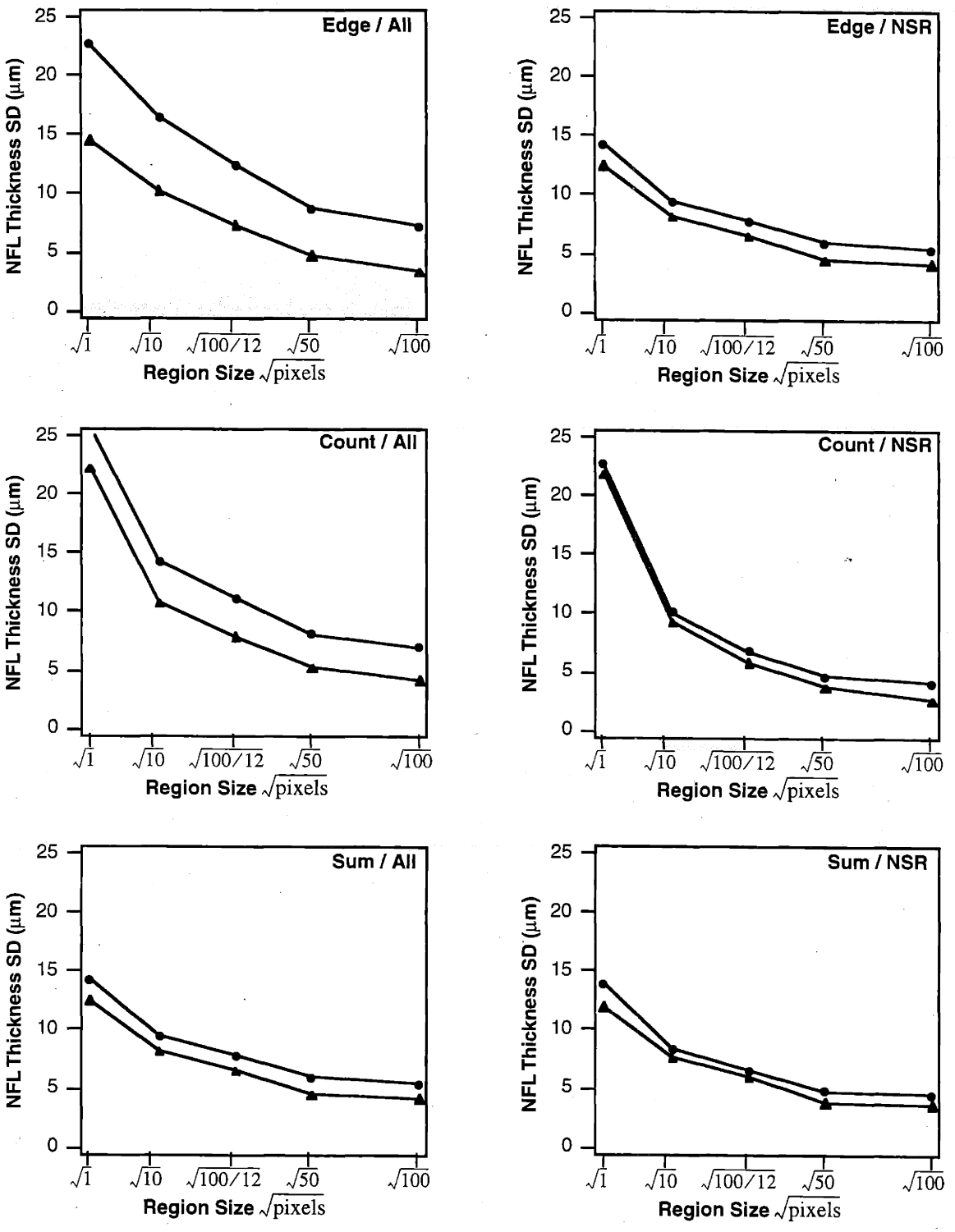

FIGURE 7-12. Reproducibility of thickness measurements for different algorithms and thresholds. Circles: average for eyes with glaucoma. Triangles: average for healthy eyes.

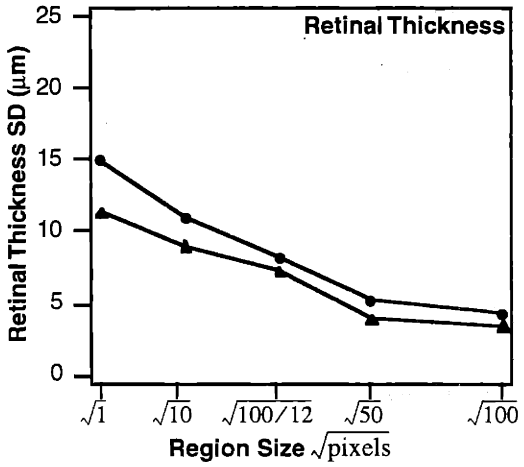

FIGURE 7-13. Reproducibility of retinal thickness measurements. Circles: eyes with glaucoma. Triangles: healthy eyes.

7.4.2 Sensitivity of Different Algorithms

The sensitivity of the different algorithms and thresholding techniques to detect diffuse glaucomatous damage was determined using the methods described in Section 7.3.6. Figure 7-14 shows that glaucoma sensitivity Z-score for the overall mean as previously defined for the various algorithms assuming a Type 1 error of $\alpha = 0.1$. The predictive value

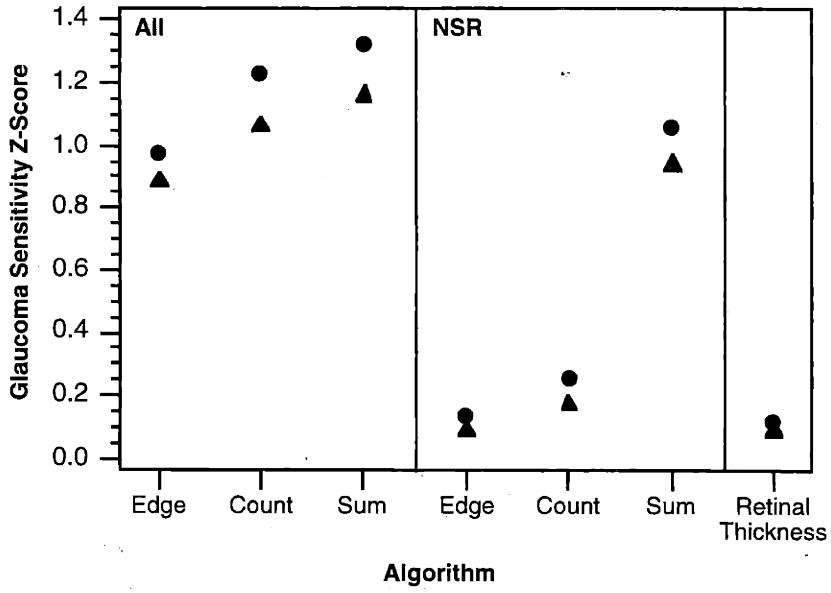

FIGURE 7-14. Sensitivity of the overall mean NFL thickness to predict glaucoma for different algorithms and threshold methods.

of the overall mean retinal thickness is also included for reference. Circles denote the best case scenario of no measurement error (infinite measurements) and triangles indicate the worst case of a single measurement. Figure 7-14 shows that NFL thickness is a better predictor of glaucoma than retinal thickness for all algorithms. The plot also shows that choosing a threshold based on the overall maximum reflectivity (*all*) is clearly better than thresholding based on the neurosensory retinal reflectivity (*NSR*) alone. This is the case despite the fact that the reproducibility is better if only the neurosensory retinal reflectivity is used. This result suggests that the NFL reflectivity itself decreases relative to the choroidal reflectivity as a consequence of glaucomatous change. The *sum* algorithm gives the best performance and is relatively insensitive to the choice of the thresholding technique. Using Figure 7-11 to convert from Z-score to sensitivity, we find that the sensitivity of a single measurement of the overall mean NFL thickness using the *sum* algorithm is 87%. The sensitivity increases to 91% in the limit of no measurement error.

Chapter 8

CONCLUSIONS

8.1 Summary

Optical coherence tomography (OCT) is a new technique for micron scale resolution cross-sectional imaging of ocular and other biological tissue. OCT is similar to ultrasound, except that image contrast relies on differences in optical rather than acoustic backscattering characteristics of tissue. In OCT, low-coherence optical interferometry is used to resolve the position of reflective or optical backscattering sites within a sample. Two-dimensional tomographic images of a thin, optical slice of tissue may be obtained with approximately 10 μm longitudinal and lateral resolution. Optical heterodyne detection and the application of optical communications principles achieve a sensitivity to reflected light as small or smaller than 10^{-10} of the incident optical power. OCT is non-contact, non-invasive, and has better resolution than ultrasound in the posterior eye. Unlike confocal imaging, the axial resolution of OCT is not limited by the pupil aperture and ocular aberrations. OCT may be implemented in a compact, low-cost, fiber-optic based interferometer that is easily coupled to existing ophthalmic instrumentation.

In collaboration with MIT Lincoln Laboratory, a clinically effective, ophthalmic imaging OCT system has been developed. A compact superluminescent diode light source is utilized and is coupled via fiber optics through a standard slit-lamp biomicroscope. The operator is able to simultaneously view a video image of the scanning OCT beam on the retina and an OCT image on a computer monitor which is updated in real-time every 2.5 seconds. The system is fully computer controlled to allow positioning of a variety of scanning patterns on the retina. Image processing algorithms have been developed to minimize the effects of eye motion during scanning, to automatically extract the thickness of various retinal layers directly from the OCT images, and to provide topographic displays of quantitative parameters such as total retinal and retinal nerve fiber layer thickness.

Over 2500 patients with a variety of macular diseases and diseases of the optic nerve head have been examined at the New England Eye Center, Tufts University School of Medicine. In patients with macular pathology, OCT images have been correlated with the conventional clinical techniques of slit-lamp biomicroscopy and fluorescein angiography. The cross-sectional view of OCT is effective in the diagnosis and monitoring of macular holes, macular edema, and retinal detachments. In patients with glaucoma, the ability of OCT to directly measure retinal nerve fiber layer thickness with micron scale resolution may lead to the first truly objective diagnostic for the presence or progression of this degenerative disease.

Macular hole is a frequently encountered retinal disease that is often difficult to diagnose accurately because there are a number of ophthalmoscopically similar appearing lesions. The disease progresses to involve a complete loss of the retina directly in the fovea leading to

a devastating reduction in visual acuity. However, surgical intervention can often prevent or correct vision loss. OCT greatly facilitates the diagnosis and staging of macular holes, ensuring appropriate treatment. OCT is diagnostically useful in separating macular holes from other ophthalmoscopically similar appearing lesions, in evaluating the stage of macular hole progression, and in evaluating the risk of hole formation in the fellow eye of patients who already have a unilateral macular hole. Pre-operative assessments of macular hole structure with OCT correlate with the probability of anatomic success after surgery. This information is useful in considering candidates for surgical treatment. OCT has been able to provide information on the pathogenesis of hole formation and the conditions which lead to the development of macular holes which may eventually lead to better treatment of this disease.

Diabetic retinopathy is the second leading cause of blindness in the United States. The development of macular edema is a major treatable cause of vision loss in patients with diabetes. Macular edema is also common manifestation of a variety of other retinal diseases including epiretinal membranes, uveitis, retinal vascular occlusions, and retinal inflammatory diseases. Intraretinal fluid accumulation may also be complication of cataract surgery. OCT is a more sensitive and objective indicator of retinal thickening due to macular edema than either slit-lamp biomicroscopy or fluorescein angiography, is useful in objectively tracking the resolution of edema following therapy, and may be effective as a screening tool for the development of retinal edema in these patients. Macular edema is traditionally evaluated by assessing retinal thickening with slit-lamp biomicroscopy, and leakage of fluorescein dye from blood vessels into the retina, which is a relatively poor indicator of vision loss. OCT is approximately ten times more sensitive to changes in retinal thickness than slit-lamp biomicroscopy and is able to provide an objective, quantitative evaluation of fluid accumulation in the macula. OCT is useful for both the early detection of macular edema, and longitudinally monitoring retinal thickness over time in patients who have received laser treatment for this disease. A topographic method of displaying macular thickness has been developed which provides both a quantitative and intuitive means of assessing retinal thickening geographically. The use of a standardized protocol means that OCT may have significant public health implications as a screening technique for the development of retinopathy in all patients with diabetes.

OCT is also more sensitive than biomicroscopy in evaluating retinal detachments, such as those occurring with central serous chorioretinopathy. The ability to objectively monitor these detachments over time is useful in evaluating the necessity or effectiveness of treatment in this disease. Furthermore, OCT shows the defects in the retinal pigment epithelium which are associated with the pathogenesis of this illness.

Glaucoma is the third leading cause blindness in the United States. The clinical evaluation of this pervasive disease is presently difficult. Current diagnostic techniques such as stereoscopic visualization of the optic nerve, nerve fiber layer photography, and evaluation of the cup-to-disc ratio are subjective with variation occurring even among experienced observers. Glaucoma is a disease of insidious onset, often leading to significant losses in peripheral vision that may not be immediately noticed by the patient. Quantitative visual field testing can provide early identification of these visual defects; however, up to 50% of the retinal nerve fiber layer may be lost before detection by standard clinical techniques. The ability of OCT to directly measure nerve fiber layer thickness may lead to an objective, early diagnostic for the onset of glaucoma, and a sensitive indicator of glaucomatous progression. OCT provides a quantitative method of directly measuring the thickness of the retina and retinal nerve fiber layer (NFL) with high resolution as a potential early glaucoma diagnostic. NFL thickness as measured by OCT correlates well with the functional status of the optic nerve as measured by traditional visual field examination, and correlates better with visual field loss than either cupping or neuroretinal rim area. Normal and glaucomatous eyes show a significant difference in

NFL thickness as measured by OCT. These studies indicate that OCT is potentially able to detect the onset of glaucoma or glaucomatous progression before significant and irreversible damage to the retina occurs.

8.2 Further Studies in Ophthalmology

These preliminary results lay the groundwork for future clinical studies in ophthalmology. The stage is set for well-controlled, randomized, prospective studies to statistically evaluate the potential benefits of OCT for managing patients with ocular disease. At the same time, preliminary explorations may be undertaken to identify other potential applications of OCT in ophthalmology. While macular degeneration, diabetic retinopathy and macular edema, and glaucoma are probably the three most important causes of vision loss in the United States, several other ocular diseases may also benefit from OCT [26]. OCT provides objective and quantitative measurements of ocular structures with high-resolution and is potentially beneficial for other conditions in both the anterior eye and retina.

8.2.1 Retina and Optic Nerve

Current diagnostic techniques for epiretinal macular membranes include slit-lamp biomicroscopy and fluorescein angiography. OCT images are useful in confirming the diagnosis of faint, diaphanous membranes, and in providing a cross-sectional assessment of factors contributing to vision loss, such as membrane opacity, retinal distortion or tractional detachment, and macular edema. The amount of foveal distortion, detachment, or edema provides an indication of the severity of the membrane. The thickness and reflectivity of the membrane on the OCT gives information on membrane opacity. Many studies have attempted to define prognostic indicators, such as membrane thickness or the presence of preoperative cystoid macular edema, to predict eventual visual outcome after epiretinal membrane surgery [161-163]. OCT provides a means to evaluate the cross-sectional characteristics of an epiretinal membrane, allowing a quantitative measurement of retinal thickness, membrane thickness, and the separation between the membrane and inner retina. Retinal thickness has been shown to be a better correlate of visual acuity than fluorescein leakage in patients with various causes of macular edema [138] and might be a predictor of surgical success in patients with an epiretinal membrane. The adhesiveness of the membrane to the retinal surface might also be a prognostic factor. OCT can image small separations of an epiretinal membrane from the retinal surface with high resolution.

Many ocular diseases cause chorioretinal inflammation [164]. Inflammation as a general rule increases the optical reflectivity from within affected tissue because the migration of inflammatory cells into the retina or vitreous increases the concentration of optical scatterers. OCT can provide dynamic images of the inflammatory process, localizing the infiltrate to specific retinal layers and providing a means to track the extent of inflammation following treatment. OCT provides a means of quantifying the reflectivity, location, and extent of inflammatory lesions in cross-section. The intensity and size of the lesion correlate with the density and extent of the infiltrate, respectively. OCT is also useful in evaluating morphological changes secondary to acute or chronic inflammation, such as retinal edema, fibrosis, and atrophy. Vision loss due to uveitis is commonly caused by macular edema which may be quantitatively assessed as retinal thickening on OCT. Serial follow-up OCT images through the fovea allow the accurate evaluation of macular fluid accumulation and provide an objective means of assessing the efficacy of pharmacological treatment. The typical "punched-out" lesion found in the presumed ocular histoplasmosis syndrome [165] appears on OCT as a focal region of elevated reflectivity in the deeper choroid. Choroidal neovascularization in this disease can also be diagnosed and localized by a disruption and fragmentation of the retinal pigment epithelium and choriocapillaris. In contrast, acute toxoplasmosis retinitis [166] or

cytomegalovirus lesions [167] exhibit enhanced backscatter due to inflammation primarily affecting the neurosensory retina. Chronic lesions progress to retinal atrophy and fibrosis, which are evident on OCT as increased retinal reflectivity, marked retinal thinning, and increased penetration of the probe light into the choroid. HIV retinopathy [167] is often manifested by cotton wool spots, probably associated with focal ischemic injury and swollen nerve fiber axons. OCT demonstrates a corresponding lesion displaying enhanced reflectivity from only the inner retinal layers.

OCT may provide an *in vivo* alternative to histopathologic techniques for the study of hereditary and acquired retinal degenerations. In eyes with adult-onset vitelliform macular dystrophy [168, 169], for example, OCT images show a moderately backscattering, subretinal lesion which is distinct from a serous detachment. The neurosensory retina is elevated overlying the lesion and exhibits an apparently compressed photoreceptor layer most likely accounting for the metamorphopsia typically occurring in these patients. Affected eyes may also demonstrate a focal loss of photoreceptors and pigmentary atrophy directly in the fovea [169] which appears on OCT as an abnormal foveal pit contour with increased light penetration into the choroid. OCT images of retinoschisis reveal a splitting of the neural retina consistent with the classically described histopathological findings [170].

Non-penetrating ocular trauma can cause chorioretinal injury. OCT is particularly useful in evaluating small retinal changes, such as a traumatic macular hole, that are difficult to observe by ophthalmoscopy. OCT also may be effective when the direct or indirect view of the retina is obscured, because only part of the pupil aperture is necessary for OCT imaging. Since OCT is non-contact and uses mostly infrared illumination, it is generally more comfortable to the traumatized patient than other examination techniques, such as contact lens biomicroscopy, fluorescein angiography, and ultrasound.

As in glaucoma, OCT is also useful for cross-sectional profiling of the optic nerve head and retinal nerve fiber layer (NFL) in neurological diseases of the optic nerve. Relative areas of NFL thinning may be quantitatively assessed and correlated with visual field performance, allowing the degeneration of retinal ganglion cell axons to be objectively measured in conditions such as ischemic optic atrophy. Measurements of NFL thickening may be useful in distinguishing true papilledema from a crowded optic nerves, or pseudopapilledema.

Both serous macular detachments and schisis-like macular separations are associated with congenital optic nerve pits [171-173]. The pathogenesis of these lesions, however, has been controversial. OCT is useful in structurally characterizing the development of these lesions [174, 175]. Neurosensory detachments appear as a complete elevation of the sensory retina overlying optically clear serous fluid. In contrast, schisis-like separations are associated with a splitting of the outer retina with vertical, bridging elements between the outer and inner retina.

8.2.2 Anterior Eye

OCT also represents a new imaging modality for clinical examination of the anterior eye [44]. Micron scale lateral and longitudinal resolution permits highly accurate biometry of large scale ocular structures, as well as the evaluation of changes in cellular morphology associated with pathologies of the cornea, iris, and lens. High sensitivity is important to detect weak backscattering from within nominally transparent structures such as the cornea and lens. Unlike ultrasonic imaging, contact with the eye or saline immersion of the eye is not required, enabling the real-time monitoring of keratorefractive therapies. In contrast to confo-

cal microscopy, the depth resolution of OCT is independent of the probe beam numerical aperture, allowing tomographic image acquisition at an arbitrary working distance from the eye.

Clinically relevant measurements available from the anterior segment in OCT include the anterior chamber depth and angle, corneal thickness and curvature, and refractive power. OCT can achieve micron scale resolution noncontact biometry, with potential applications in contact lens fitting, post-cataract surgery intraocular lens implant power calculations, real-time monitoring of keratorefractive surgery, and the accurate quantification of keratitis and corneal edema. OCT images of the crystalline lens have the potential to provide an objective grading diagnostic for cataracts. OCT may have advantages over other optical methods of cataract evaluation. Image formation can occur even through dense cataracts because of the relatively low scattering of near infrared light and the high detection sensitivity to weak reflections.

Laser thermokeratoplasty (LTK) of the cornea is a relatively new therapy currently under study for the treatment of keratoconus, refractive errors of the eye, and astigmatism [176]. In this technique, laser coagulations are placed in the corneal stroma circumferentially around the visual axis. Thermally induced collagen shrinkage at each coagulation point leads to alterations in the mechanical properties of the cornea and modification of the corneal profile. OCT can record both changes at the cellular level and differences in large scale morphology. Thus, the technique is promising as a potential adjunct to keratorefractive therapies such as LTK, where both real-time monitoring of the surgery in progress and post-operative follow-up may require evaluation of the gross corneal curvature as well as cell damage and photocoagulation penetration depth.

8.3 Future Technical Improvements

The performance parameters which characterize the OCT system include axial and longitudinal resolution, dynamic range, and image acquisition speed. Improvements in any of these specifications would result in improved image acquisition and quality. However, the overall performance is governed by the shot noise limit and improvements in one area require trade-offs in another. Ultimately, it is the maximum optical power which can be delivered to a tissue without damage which limits the performance of OCT. Within a given performance specification, sensitivity to other properties of light such as wavelength and polarization may also be used enhance the differentiation between different types of tissue.

8.3.1 Optical Power Limits

The design trade-off between axial resolution, sensitivity to weak reflections, optical power, and image acquisition speed was discussed in Section 2.7.2. In biological tissue and in the eye especially, it is the maximum optical power which usually limits the best achievable resolution, signal-to-noise ratio, and scanning velocity. Since the retina is one of the most sensitive tissues in the body to damage induced by optical radiation, optical power limits govern the ultimate achievable performance of OCT. The American National Standards Institute (ANSI) standard provides a starting point for estimating the maximum safe retinal irradiance [177].

Permanent Viewing

The most conservative retinal injury threshold may be estimated in the limit of very long exposure times. The maximum permissible exposure for permanent ($10^3 < t < 3 \times 10^4$ seconds where t is the exposure time) intrabeam viewing is given by Table 5, page 41 of the ANSI standard:

$$MPE_{permanent} = 0.320 C_A \text{ mW/cm}^2 \tag{8.1}$$

where the wavelength correction factor C_A is defined in terms of the center wavelength λ (μm) as

$$C_A = 10^{2(\lambda - 0.700)}. \tag{8.2}$$

Equations (8.1) and (8.2) are valid for the wavelength range $0.700 \le \lambda < 1.050$ μm. The maximum permissible power is determined by multiplying the MPE given in Equation (8.1) by the area of a 7 mm diameter limiting aperture at the cornea (as defined by ANSI in Table 9):

$$\text{maximum power} = 0.320 \cdot 10^{2(\lambda - 0.700)} \cdot \pi(0.35)^2 \text{ mW}. \tag{8.3}$$

Therefore, the permanent intrabeam viewing limit as defined by Equation (8.3) for a center wavelength of $\lambda = 0.84$ μm is 230 μW. Figure 8-1 plots the maximum permanent intrabeam viewing limit for all wavelengths between 0.4 μm and 1.4 μm. The reader may refer to Tables 5 and 6 of the ANSI standard for expressions for the MPE which are valid outside the wavelength range $0.700 \le \lambda < 1.050$ μm.

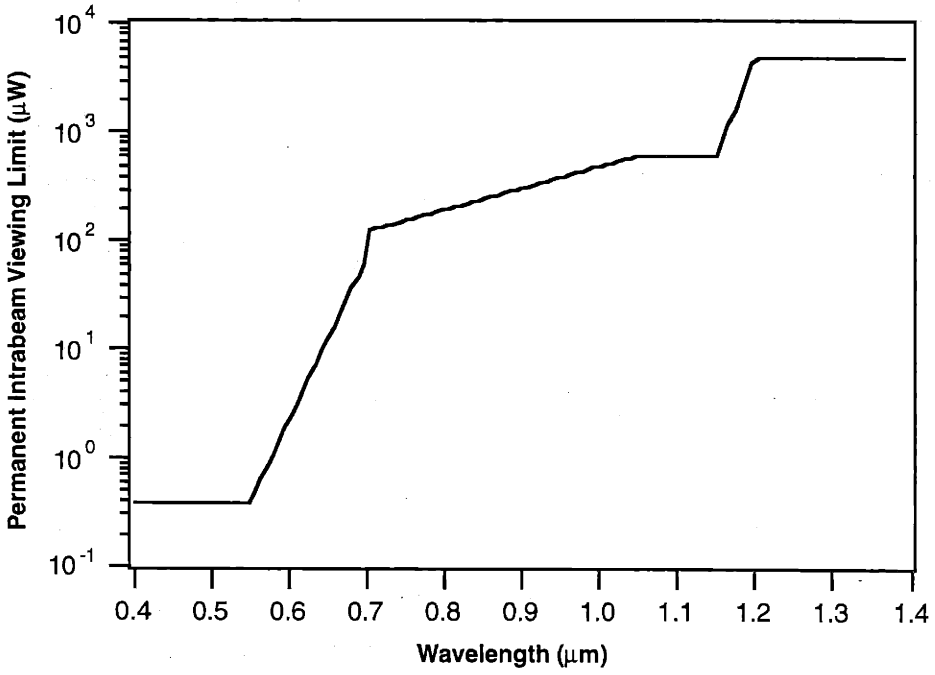

FIGURE 8-1. Maximum ocular exposure for permanent viewing.

Short Exposure Durations

In practice, exposure durations shorter than 10^3 seconds are used and the MPE is larger than shown in Figure 8-1. In the current OCT system, an image consisting of 100 A-scans is acquired in 2.5 seconds resulting in an exposure time of 25 ms for each point on the retina. In this regime, the expression for the MPE is

$$MPE = 1.8 C_A t^{3/4} \text{ mJ/cm}^2 \tag{8.4}$$

where t is the exposure duration in seconds and C_A is the correction factor defined in Equation (8.2). Equation (8.4) is valid for exposures between $18 \times 10^{-6} \leq t < 10^3$ seconds. The maximum permissible optical power may be found by dividing the MPE in Equation (8.4) by the exposure time t and then multiplying by the area of the standard 7 mm ocular limiting aperture:

$$\text{maximum power} = 1.8 \cdot 10^{2(\lambda - 0.700)} \cdot t^{-1/4} \cdot \pi(0.35)^2 \text{ mW}. \tag{8.5}$$

For $\lambda = 0.84$ μm and $t = 0.025$ seconds, the maximum optical power according to Equation (8.5) is 3.3 mW. Figure 8-2 plots the optical power limit versus the exposure duration for a variety of wavelengths. Each of the curves in Figure 8-2 has a $t^{-1/4}$ dependence similar to Equation (8.5). Again, the reader is referred to Tables 5 and 6 of the ANSI standard for expres-

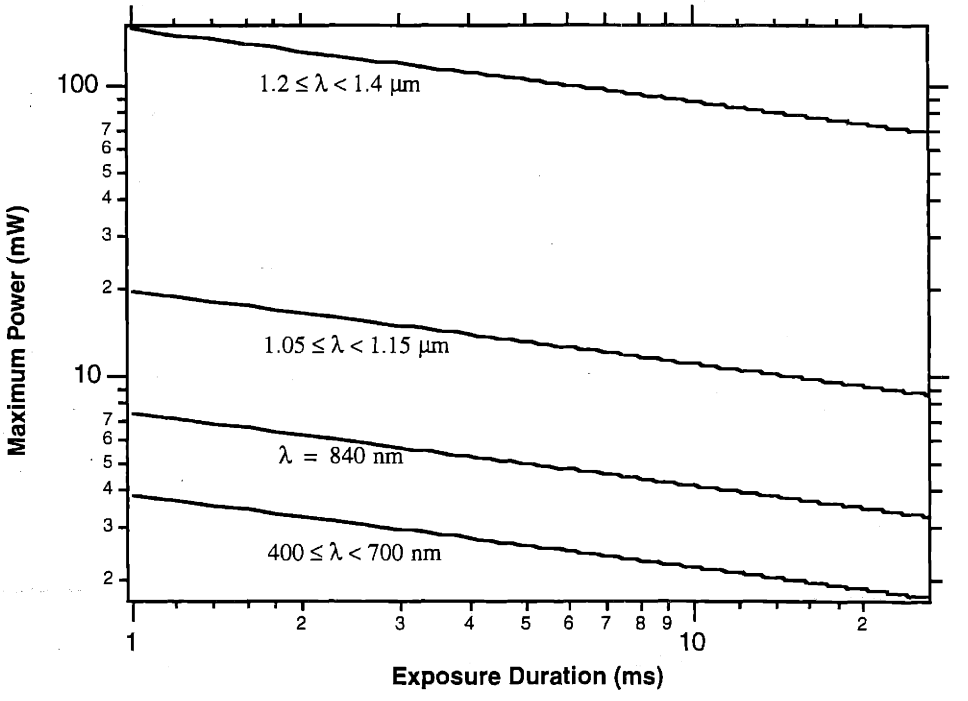

FIGURE 8-2. Maximum power for a single ocular exposure.

sions for the MPE which are valid outside the wavelength range $0.700 \leq \lambda < 1.050$ μm. Note that in both Figures 8-1 and 8-2 the permissible power increases rapidly for longer wavelengths, and especially within the wavelength range $1.15 \leq \lambda < 1.2$ μm.

Repetitive Exposures

Repetitive exposures reduce the maximum permissible power by the factor $N^{1/4}$ where N is the total number of exposures. This condition occurs during OCT imaging since the probe beam is repetitively scanned across the fundus until an image is saved. Each point on the retina is repetitively exposed at the image acquisition rate until the location of the scan on the retina is changed. For example in the current system, if 1 minute is spent acquiring a single image, then each point on the retina is sampled 24 times, and the exposure limit, reduced by a factor of $24^{1/4} = 2.2$, is 1.5 mW. If the scanning beam is also used for fixation, then this limit is further reduced. For example, in the current system, one in every ten A-scans is taken through fixation to provide flashing fixation light in the eye being scanned. If a particular eye is examined for 10 minutes, then the fovea is repetitively exposed by the internal fixation light 2400 times during the test. Thus, the MPE is reduced by $2400^{1/4} = 7$, leading to an exposure limit of 470 μW.

8.3.2 OCT Spectroscopy

The use of different optical wavelengths has the potential to create spectroscopic images of tissue. In the posterior eye, for example, it is well known that the reflection from the retinal nerve fiber layer may be enhanced through the use of red-free photography, which uses predominantly green light. The spectral reflectance of the NFL has also been quantitatively studied [178]. OCT with shorter wavelengths may increase the sensitivity of the technique to changes in retinal nerve fiber layer thickness which is important in the diagnosis of glaucoma. However, as the wavelength is shortened, the optical penetration of OCT decreases, which may be an important limiting factor. The use of wavelengths farther in the infrared has the potential to provide increased penetration through the choroid and/or hemorrhage due to the increase in scattering mean free path with increasing wavelength [99]. OCT studies in scattering media such as coronary artery have shown that wavelengths between 1.1 and 1.3 μm provide a substantially better penetration compared to wavelengths around 800 nm [54, 55]. In the eye, longer wavelengths have the potential to provide increased visualization of choroidal neovascularization through pigment epithelial detachments and hemorrhage in age-related macular degeneration.

The attenuation of light propagating to the retina through the cornea, lens, aqueous, and vitreous is also wavelength dependent. The increased safe optical power (Figure 8-1) and penetration through scattering media available with longer wavelengths must be balanced against the absorptive properties of water, since the retina is situated behind approximately 25 mm of ocular media. Figure 8-3 shows that the absorption of 5 cm of water (which is approximately the double-pass distance through the cornea, lens, aqueous and vitreous) decreases rapidly for wavelengths longer than 1.1-1.2 μm. Thus, a comparison of Figures 8-1 and 8-3 reveals that a wavelength of about 1.1 μm likely represents a reasonable upper limit on the useful OCT imaging wavelengths in the eye to maintain a high sensitivity to weak reflections.

The use of multiple wavelengths simultaneously in OCT would allow one to investigate differential absorptive and scattering properties of the eye. This type of technique, for example, could provide information on various chromophores in tissue and could potentially enhance the contrast between different retinal layers.

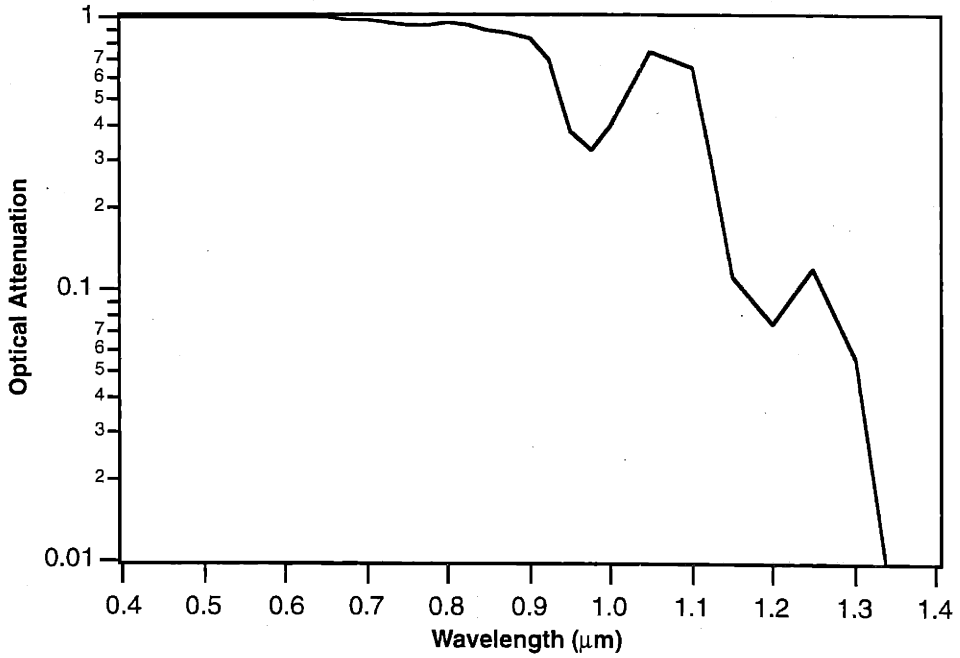

FIGURE 8-3. Optical attenuation versus wavelength through 5 cm of water.

8.3.3 Ultra-High Resolution OCT

The lateral resolution of OCT in the posterior eye is limited by the numerical aperture of the entrance pupil and ocular aberrations to approximately 10 to 20 μm (Section 3.2.8). However, the current longitudinal resolution of 15 μm only depends on the wavelength bandwidth of the light source used for imaging and may be substantially improved with the use of a broadband light source (Section 2.3). Several groups have demonstrated low-coherence interferometry or OCT systems which have achieved longitudinal resolutions better than 5 μm [179, 180]. Naturally, enhanced resolution is only obtained at the expense of either increased imaging time, reduced sensitivity to weak reflections, or increased optical power on the sample as detailed in Section 2.7.2.

In the eye, better longitudinal resolution has the potential to improve the precision of retinal thickness measurements in macular edema and retinal nerve fiber layer thickness measurements in glaucoma. Increased resolution may also lead to better delineation of choroidal neovascularization in age-related macular degeneration, increased sensitivity to epiretinal membranes which are tightly adherent to the retinal surface, and better visualization of intraretinal pathologies.

8.3.4 Polarization Sensitive OCT

Information on the birefringence of tissue structures may be obtained by controlling and sensing the polarization state of the incident and reflected probe light in OCT [181]. In the retina, the nerve fiber layer (NFL) has been shown to be the predominant source of birefringence [21, 23]. Thus, a polarization sensitive OCT system has the potential for enhanced imaging of the NFL which would be potentially useful in the diagnosis and management of glaucoma.

8.4 Conclusions

OCT is a new tomographic medical imaging modality which is sensitive to the optical properties of tissue. This thesis has demonstrated that OCT can improve the care and study of the eye. A clinically viable OCT instrument has been constructed based on engineering principles derived from optical communication theory. Computer algorithms have been developed for image management, analysis and restoration. OCT has been used to image patients with a variety of ocular diseases. OCT is effective in staging macular holes, evaluating the vitreoretinal interface in eyes at risk for a macular hole, and providing a structural assessment of macular hole surgery. In eyes with central serous chorioretinopathy, OCT can evaluate sensory retinal separations undetected at the slit-lamp. Topographic images of macular edema are able to track both the progression of macular thickening and the resolution of macular edema following laser photocoagulation, and may provide a cost-effective screening method for the development of diabetic retinopathy. OCT may provide a novel method of defining occult choroidal neovascular membranes in patients with age-related macular degeneration. OCT can also profile the thickness of the retinal nerve fiber layer with high resolution which is potentially important for the objective assessment of early glaucoma progression. These studies suggest that OCT has the potential to become an important diagnostic tool for the practicing ophthalmologist.

Chapter 9

REFERENCES

1. Guyer DR, Yanuzzi LA, Slakter JS, Sorenson JA, Hope-Ross M, Orlock DR. Digital indocyanine-green videoangiography of occult choroidal neovascularization. *Ophthalmology* 1994; **101**:1727-37.

2. Slakter JS, Yannuzzi LA, Sorenson JA, Guyer DR, Ho AC, Orlock DA. A pilot study of indocyanine green videoangiography-guided laser photocoagulation of occult choroidal neovascularization in age-related macular degeneration. *Arch Ophthalmol* 1994; **112**:465-72.

3. Sorenson JA, Yannuzzi LA, Slakter JS, Guyer DR, Ho AC, Orlock DA. A pilot study of digital indocyanine green videoangiography for recurrent occult choroidal neovascularization in age-related macular degeneration. *Ophthalmology* 1994; **112**:473-9.

4. Olsen T. The accuracy of ultrasonic determination of axial length in pseudophakic eyes. *Acta Ophthalmol (Copenh)* 1989; **67**:141-4.

5. Pavlin DJ, Sherar MD, Foster FS. Subsurface ultrasound microscopic imaging of the intact eye. *Ophthalmology* 1990; **97**:244-50.

6. Pavlin CJ, Harasiewicz K, Sherar MD, Foster FS. Clinical use of ultrasound biomicroscopy. *Ophthalmology* 1990; **98**:287-95.

7. Shahidi M, Zeimer RC, Mori M. Topography of the retinal thickness in normal subjects. *Ophthalmology* 1990; **97**:1120-4.

8. Shahidi M, Ogura Y, Blair NP, Rusin MM, Zeimer R. Retinal thickness analysis for quantitative assessment of diabetic macular edema. *Arch Ophthalmol* 1991; **109**:1115-9.

9. Zeimer RC, Shahidi M, Mori MT, Benhamou E. In vivo evaluation of a noninvasive method to measure the retinal thickness in primates. *Arch Ophthalmol* 1989; **107**:1006-9.

10. Zeimer RC, Mori MT, Khoobehi B. Feasibility test of a new method to measure retinal thickness noninvasively. *Invest Ophthalmol Vis Sci* 1989; **30**:2099-105.

11. Bille JF, Dreher GW, Zinser G. Scanning laser tomography of the living human eye. In: BR M, ed. *Noninvasive Diagnostic Techniques in Ophthalmology.* New York: Springer-Verlag; 1990:528-47.

12. Webb RH, Hughes GW. Scanning laser ophthalmoscope. *IEEE Trans Biomed Engr* 1981; **BME-28**:488-92.

13. Webb RH, Hughes GW, Delori FC. Confocal scanning laser ophthalmoscope. *Appl Opt* 1987; **26**:1492-9.

14. Bartsch DU, Intaglietta M, Bille JF, Dreher AW, Gharib M, Freeman WR. Confocal laser tomographic analysis of the retina in eyes with macular hole formation and other focal macular diseases. *Am J Ophthalmol* 1989; **108**:277-87.

15. Schuman JS, Noecker RJ. Imaging of the optic nerve head and nerve fiber layer in glaucoma. *Ophthalmol Clin No Amer* 1995; **8**:259-79.

16. Dan JA, Belyea DA, Lieberman MF, Stamper RL. Evaluation of optic disc measurements with the Glaucoma-Scope. *J Glaucoma* 1996; **5**:1-8.

17. Pendergast SD, Shields MB. Reproducibility of optic nerve head topographic measurements with the Glaucoma-Scope. *J Glaucoma* 1995; **4**:170-6.

18. Hoskins HD, Hetherington J, Glenday M, Samuels SJ, Verdooner SR. Repeatability of the Glaucoma-Scope measurements of optic nerve head topography. *J Glaucoma* 1994; **3**:17-27.

19. Azzam RMA. Photopolarimetric measurement of the Mueller matrix by Fourier analysis of a single detected signal. *Opt Lett* 1978; **2**:148-50.

20. Dreher AW, Reiter K, Weinreb R. Spatially resolved birefringence of the retinal nerve fiber layer assessed with a retinal laser ellipsometer. *Appl Opt* 1992; **31**:3730-5.

21. Weinreb RN, Dreher AW, Coleman A, Quigley H, Shaw B, Reiter K. Histopathologic validation of fourier-ellipsometry measurements of retinal nerve fiber layer thickness. *Arch Ophthalmol* 1990; **108**:557-60.

22. van Blokland GJ, Verhelst SC. Corneal polarization in the living human eye explained with a biaxial model. *J Opt Soc Am A* 1987; **4**:82-90.

23. Weinreb RN, Shakiba S, Zangwill L. Scanning laser polarimetry to measure the nerve fiber layer of normal and glaucomatous eyes. *Am J Ophthalmol* 1995; **119**:627-36.

24. Huang D, Swanson EA, Lin CP, Schuman JS, Stinson WG, Chang W, Hee MR, Flotte T, Gregory K, Puliafito CA, Fujimoto JG. Optical coherence tomography. *Science* 1991; **254**:1178-81.

25. Swanson EA, Huang D, Fujimoto JG, Puliafito CA, Lin CP, Schuman JS. Method and apparatus for optical imaging with means for controlling the longitudinal range of the sample. United States Patent #5,321,501. June 14, 1994.

26. Puliafito CA, Hee MR, Schuman JS, Fujimoto JG. *Optical Coherence Tomography of Ocular Diseases*. Thorofare, NJ: Slack Inc.; 1996.

27. Fujimoto JG, De Silvestri S, Ippen EP, Puliafito CA, Margolis R, Oseroff A. Femtosecond optical ranging in biological systems. *Opt Lett* 1986; **11**:150-2.

28. Takada K, Yokohama I, Chida K, Noda J. New measurement system for fault location in optical waveguide devices based on a n interferometric technique. *Appl Opt* 1987; **26**:1603-6.

29. Youngquist RC, Carr S, Davies DEN. Optical coherence-domain reflectometry: a new optical evaluation technique. *Opt Lett* 1987; **12**:158-60.

30. Danielson BL, Whittenberg CD. Guided wave reflectometry with micrometer resolution. *Appl Opt* 1987; **26**:2836-42.

31. Gilgen HH, Novak RP, Salathe RP, Hodel W, Beaud P. Submillimeter optical reflectometry. *IEEE J Lightwave Technol* 1989; **7**:1225-33.

32. Kobayashi M, Taylor HF, Takada K, Noda J. Optical fiber component characterization by high-intensity and high spatial resolution interferometric optical-time-domain reflectometer. *IEEE Photonics Technol Lett* 1991; **3**:564-6.

33. Wang CS, Cheng WH, Huang CJ, Burns WK, Moeller R. High-power low-divergence superradiant diode. *Appl Phys Lett* 1982; **41**:587.

34. Fercher AF, Mengedoht K, Werner W. Eye-length measurement by interferometry with partially coherent light. *Opt Lett* 1988; **13**:1867-9.

35. Huang D, Wang J, Lin CP, Puliafito CA, Fujimoto JG. Micron-resolution ranging of cornea and anterior chamber by optical reflectometry. *Las Surg Med* 1991; **11**:419-25.

36. Swanson EA, Huang D, Hee MR, Fujimoto JG, Lin CP, Puliafito CA. High-speed optical coherence domain reflectometry. *Opt Lett* 1992; **17**:151-3.

37. Hitzenberger CK. Optical measurement of the axial eye length by laser Doppler interferometry. *Invest Ophthalmol Vis Sci* 1991; **32**:616-24.

38. Hitzenberger CK, Drexler W, Fercher AF. Measurement of corneal thickness by laser doppler interferometry. *Invest Ophthalmol Vis Sci* 1992; **33**:98-103.

39. Fercher AF, Li HC, Hitzenberger CK. Slit-lamp laser Doppler interferometer. *Lasers Surg Med* 1993; **13**:447-52.

40. Hitzenberger CK, Drexler W, Dolezal C, Skorpik F, Jochem M, Fercher AF, Gnad HD. Measurement of the axial eye length of cataract eyes by laser Doppler interferometry. *Invest Ophthalmol Vis Sci* 1993; **34**:1886-93.

41. Hitzenberger CK, Baumgartner A, Crexler W, Fercher AF. Interferometric measurement of corneal thickness with micrometer precision. *Am J Ophthalmol* 1994; **118**:468-76.

42. Swanson EA, Izatt JA, Hee MR, Huang D, Lin CP, Schuman JS, Puliafito CA, Fujimoto JG. In vivo retinal imaging by optical coherence tomography. *Opt Lett* 1993; **18**:1864-6.

43. Fercher AF, Hitzenberger CK, Drexler W, Kamp G, Sattmann H. In vivo optical coherence tomography [letter]. *Am J Ophthalmol* 1993; **116**:113-4.

44. Izatt JA, Hee MR, Swanson EA, Lin CP, Huang D, Schuman JS, Puliafito CA, Fujimoto JG. Micrometer-scale resolution imaging of the anterior eye in vivo with optical coherence tomography. *Arch Ophthalmol* 1994; **112**:1584-9.

45. Hee MR, Izatt JA, Swanson EA, Huang D, Schuman JS, Lin CP, Puliafito CA, Fujimoto JG. Optical coherence tomography of the human retina. *Arch Ophthalmol* 1995; **113**:325-32.

46. Hee MR, Izatt JA, Swanson EA, Huang D, Schuman JS, Lin CP, Puliafito CA, Fujimoto JG. Optical coherence tomography for ophthalmic imaging: new technique delivers micron-scale resolution. *IEEE Eng Med Bio* 1995; **14**:67-76.

47. Clivaz S, Marquis-Weible F, Salathe RP, Novak RP, Gilgen HH. High-resolution reflectometry in biological tissues. *Opt Lett* 1992; **17**:4-6.

48. Schmitt JM, Knuttel A, Bonner RF. Measurement of optical properties of biological tissues by low-coherence reflectometry. *Appl Opt* 1993; **32**:6032-42.

49. Izatt JA, Hee MR, Owen GM, Swanson EA, Fujimoto JG. Optical coherence microscopy in scattering media. *Opt Lett* 1994; **19**:590-2.

50. Tearney GJ, Brezinski ME, Southern JF, Bouma BE, Hee MR, Fujimoto JG. Determination of the refractive index of highly scattering human tissue by optical coherence tomography. *Opt Lett* 1995; **20**:2258-60.

51. Tearney GJ, Bouma BE, Boppart SA, Golubovic B, Swanson EA, Fujimoto JG. Rapid acquisition of in vivo biological images by use of optical coherence tomography. *Opt Lett* 1996; **21**:1408-10.

52. Tearney GJ, Boppart SA, Bouma BE, Brezinski ME, Weissman NJ, Southern JF, Fujimoto JG. Scanning single-mode fiber optic catheter-endoscope for optical coherence tomography. *Opt Lett* 1996; **21**:543-5.

53. Boppart SA, Brezinski ME, Bouma BE, Tearney GJ, Fujimoto JG. Investigation of developing embryonic morphology using optical coherence tomography. *Dev Bio* 1996; **177**:54-63.

54. Brezinski ME, Tearney GJ, Bouma BE, Boppart SA, Hee MR, Swanson EA, Southern JF, Fujimoto JG. Imaging of coronary artery microstructure (in vitro) with optical coherence tomography. *Am J Cardiol* 1996; **77**:92-3.

55. Brezinski ME, Tearney GJ, Bouma BE, Izatt JA, Hee MR, Swanson EA, Southern JF, Fujimoto JG. Optical coherence tomography for optical biopsy. Properties and demonstration of vascular pathology. *Circulation* 1996; **93**:1206-13.

56. Fujimoto JG, Brezinski ME, Tearney GJ, Boppart SA, Bouma B, Hee MR, Southern JF, Swanson EA. Optical biopsy and imaging using optical coherence tomography. *Nat Med* 1995; **1**:970-2.

57. Chinn SR, Swanson EA. Blindness limitations in optical coherence domain reflectometry. *Electron Lett* 1993; :2025-7.

58. Chen WK. *Passive and Active Filters: Theory and Implementations.* New York: John Wiley & Sons; 1986.

59. Hee MR. *Biological Imaging with Low-Coherence Optical Interferometry.* SM Thesis. Massachusetts Institute of Technology; 1992.

60. Davenport WB, Jr., Root WL. *An Introduction to the Theory of Random Signals and Noise.* New York: McGraw-Hill; 1958.

61. Schwartz M. *Information, Transmission, Modulation, and Noise: A Unified Approach to Communication Systems.* Third ed. New York: McGraw-Hill; 1980.

62. Papoulis A. *Probability, Random Variables, and Stochastic Processes.* Second ed. New York: McGraw-Hill; 1984.

63. Abbas GL, Chan VWS, Yee T. A dual-detector optical heterodyne receiver for local oscillator noise supression. *J Lightwave Technol* 1985; **2**:1110-22.

64. Bennett AG, Francis JL. The eye as an optical system. In: Davson H, ed. *The Eye: Visual Optics and the Optical Space Sense.* New York: Academic Press; 1962:101-31.

65. Boff KR, Lincoln JE. *Engineering Data Compendium: Human Perception and Performance.* Wright-Patterson Air Force Base, Ohio: Harry G. Armstrong Aerospace Medical Research Laboratory; 1988.

66. Kroger RHH. Methods to estimate dispersion in vertebrate ocular media. *J Opt Soc Am A* 1992; **9**:1486-90.

67. Sivak JG, Mandelman T. Chromatic dispersion of the ocular media. *Vision Res* 1982; **22**:997-1003.

68. Santamaria J, Artal P, Bescos J. Determination of the point-spread function of human eyes using a hybrid optical-digital method. *J Opt Soc Am A* 1987; **4**:1109-14.

69. Artal P, Santamaria J, Bescos J. Retrieval of wave aberration of human eyes from actual point-spread-function data. *J Opt Soc Am A* 1988; **5**:1201-6.

70. Williams DR, Brainard DH, McMahon MJ, Navarro R. Double-pass and interferometric measures of the optical quality of the eye. *J Opt Soc Am A* 1994; **11**:3123-35.

71. Howland HC, Howland B. A subjective method for the measurement of monochromatic aberrations of the eye. *J Opt Soc Am* 1977; **67**:1508-18.

72. Walsh G, Charman WN, Howland HC. Objective technique for the determination of monochromatic aberrations of the human eye. *J Opt Soc Am A* 1984; **1**:987-92.

73. Campbell FW, Gubisch RW. Optical quality of the human eye. *J Physiol* 1966; **186**:558-78.

74. Campbell FW, Green DG. Optical and retinal factors affecting visual resolution. *J Physiol* 1965; **181**:576-93.

75. Lotmar W. Dependence of magnification upon the camera-to-eye distance in the Zeiss fundus camera. *Acta Ophthalmol (Copenh)* 1984; **62**:131-4.

76. Bengtsson B, Krakau CET. Correction of optic disc measurements on fundus photographs. *Graefe's Arch Clin Exp Ophthalmol* 1992; **230**:24-8.

77. Bengtsson B, Krakau CET. Some essential optical features of the zeiss fundus camera. *Acta Ophthalmol(Copenh)* 1977; **55**:123-31.

78. Oppenheim AV, Schafer RW. *Discrete-Time Signal Processing.* Englewood Cliffs, New Jersey: Prentice Hall; 1989.

79. Bohren CF, Huffman DR. *Absorption and Scattering of Light by Small Particles.* New York: John Wiley & Sons; 1983.

80. Kerker M. *The Scattering of Light and Other Electromagnetic Radiation.* New York: Academic Press; 1969.

81. Ishimaru A. *Wave Propagation and Scattering in Random Media.* New York: Academic Press; 1978.

82. Graaf R, Aarnoudse JG, de Mul FFM, Jentink HW. Light propagation parameters for anisotropically scattering media based on a rigorous solution of the transport equation. *Appl Opt* 1989; **28**:2273-9.

83. Karagiannes JL, Zhang Z, Grosswiener B, Grosswiener LI. Applications of the 1-D diffusion approximation to the optics of tissue and tissue phantoms. *Appl Opt* 1989; **28**:2311-7.

84. Ishimaru A. Diffusion of a pulse in densely distributed scatterers. *J Opt Soc Am* 1978; **68**:1045-50.

85. Ishimaru A. Diffusion of light in turbid material. *Appl Opt* 1989; **28**:2210-5.

86. Profio AE. Light transport in tissue. *Appl Opt* 1989; **28**:2250-5.

87. Yoon G, Prahl SA, Welch AJ. Accuracies of the diffusion approximation and its similarity relations for laser irradiated biological media. *Appl Opt* 1989; **28**:2250-5.

88. Yoo KM, Liu F, Alfano RR. When does the diffusion approximation fail to describe photon transport in random media? *Phys Rev Lett* 1990; **64**:2647-60.

89. Patterson MS, Chance B, Wilson BC. Time resolved reflectance and transmittance for the noninvasive measurement of tissue optical properties. *Appl Opt* 1989; **28**:2331-6.

90. Flock ST, Patterson MS, Wilson BC, Wyman DR. Monte carlo modeling of light propagation in highly scattering tissues I: Model predictions and comparison with diffusion theory. *IEEE Trans Biomed Eng* 1989; **36**:1162-8.

91. Flock ST, Patterson MS, Wilson BC, Wyman DR. Monte carlo modeling of light propagation in highly scattering tissues II: Comparison with measurements in phantoms. *IEEE Trans Biomed Engr* 1989; **36**:1169-73.

92. Jacques SL. Time resolved propagation of ultrashort laser pulses within turbid tissues. *Appl Opt* 1989; **28**:2223-9.

93. Hasegawa Y, Yamada Y, Tamura M, Nomura Y. Monte carlo simulation of light transmission through living tissues. *Appl Opt* 1991; **30**:4515-20.

94. Yoo KM, Alfano RR. Determination of the scattering and absorption lengths from the temporal profile of a backscattered pulse. *Opt Lett* 1990; **15**:276-8.

95. Jacques SL. Time-resolved reflectance spectroscopy in turbid tissues. *IEEE Trans Biomed Engr* 1989; **36**:1155-61.

96. Wilson BC, Jacques SL. Optical reflectance and transmittance of tissues: Principles and applications. *IEEE J Quantum Electron* 1990; **26**:2186-99.

97. Cheong W, Prahl SA, Welch AJ. A review of the optical properties of biological tissues. *IEEE J Quantum Electron* 1990; **26**:2166-85.

98. Pan Y, Birngruber R, Rosperich J, Englehardt R. Low-coherence optical tomography in turbid tissue: theoretical analysis. *Appl Opt* 1995; **34**:6564-74.

99. Parsa P, Jacques SL, Nishioka NS. Optical properties of rat liver between 350 and 2200 nm. *Appl Opt* 1989; **28**:2325-30.

100. Wheater PR, Burkitt HG, Daniels VG. *Functional Histology: A Text and Colour Atlas.* Second ed. New York: Churchill Livingstone; 1987.

101. Puliafito CA, Hee MR, Lin CP, Reichel E, Schuman JS, Duker JS, Izatt JA, Swanson EA, Fujimoto JG. Imaging of macular diseases with optical coherence tomography. *Ophthalmology* 1995; **102**:217-29.

102. Hee MR, Puliafito CA, Wong C, Duker JS, Reichel E, Schuman JS, Swanson EA, Fujimoto JG. Optical coherence tomography of macular holes. *Ophthalmology* 1995; **102**:748-56.

103. Hee MR, Puliafito CA, Wong C, Reichel E, Duker JS, Schuman JS, Swanson EA, Fujimoto JG. Optical coherence tomography of central serous chorioretinopathy. *Am J Ophthalmol* 1995; **120**:65-74.

104. Hee MR, Puliafito CA, Wong C, Duker JS, Reichel E, Rutledge B, Schuman JS, Swanson EA, Fujimoto JG. Quantitative assessment of macular edema with optical coherence tomography. *Arch Ophthalmol* 1995; **113**:1019-29.

105. Hee MR, Baumal CR, Puliafito CA, Duker JS, Reichel E, Wilkins JR, Coker JG, Schuman JS, Swanson EA, Fujimoto JG. Optical coherence tomography of age-related macular degeneration and choroidal neovascularization. *Ophthalmology* 1996; **103**:1260-70.

106. de Bustros S. Early stages of macular holes: to treat or not to treat. *Arch Ophthalmol* 1990; **108**:1085-6.

107. Kelly NE, Wendel RT. Vitreous surgery for idiopathic macular holes: results of a pilot study. *Arch Ophthalmol* 1991; **109**:654-9.

108. Wendel RT, Patel C, Kelly NE, Salzano TC, Wells JW, Novack GD. Vitreous surgery for macular holes. *Ophthalmology* 1993; **100**:1671-6.

109. Ruby AJ, Williams DF, Grand MG, Thomas MA, Meredith TA, Boniuk I, Olk RJ. Pars plana vitrectomy for treatment of stage 2 macular holes. *Arch Ophthalmol* 1994; **112**:359-64.

110. Glaser BM, Michels RG, Kuppermann BD, Sjaarda RN, Pena RA. Transforming growth factor-β2 for the treatment of full-thickness macular holes: a prospective randomized study. *Ophthalmology* 1992; **99**:1162-73.

111. Lansing MB, Glaser BM, Liss H, Hanham A, Thompson JT, Sjaarda RN, Gordon AJ. The effect of pars plana vitrectomy and transforming growth factor-beta2 without epiretinal membrane peeling on full-thickness macular holes. *Ophthalmology* 1993; **100**:868-72.

112. Gass JDM, Joondeph BC. Observations concerning patients with suspected impending macular holes. *Am J Ophthalmol* 1990; **109**:638-46.

113. Fish RH, Anand R, Izbrand DJ. Macular pseudoholes: clinical features and accuracy of diagnosis. *Ophthalmology* 1992; **99**:1665-70.

114. Ogura Y, Shahidi M, Mori MT, Blair NP, Zeimer R. Improved visualization of macular hole lesions with laser biomicroscopy. *Arch Ophthalmol* 1991; **109**:957-61.

115. Fisher YL, Slakter JS, Yannuzzi LA, Guyer DR. A prospective and natural history study and kinetic ultrasound evaluation of idiopathic macular holes. *Ophthalmology* 1994; **101**:5-11.

116. Dugel PU, Smiddy WE, Byrne SF, Hughes JR, Gass JDM. Macular hole syndromes: echographic findings with clinical correlation. *Ophthalmology* 1994; **101**:815-21.

117. Acosta F, Lashkari K, Reynaud X, Jalkh AE, van de Velde F, Chedid N. Characterization of functional changes in macular holes and cysts. *Ophthalmology* 1991; **98**:1820-3.

118. Sjaarda RN, Frank DA, Glaser BM, Thompson JT, Murphy RP. Assessment of vision in idiopathic macular holes with macular microperimetry using the scanning laser ophthalmoscope. *Ophthalmology* 1993; **100**:1513-8.

119. Gass JDM. Idiopathic senile macular hole: Its early stages and pathogenesis. *Arch Ophthalmol* 1988; **106**:629-39.

120. Johnson RN, Gass JDM. Idiopathic macular holes: Observations, stages of formation, and implications for surgical intervention. *Ophthalmology* 1988; **95**:917-24.

121. Gass JDM. Reappraisal of biomicroscopic classification of stages of development of a macular hole. *Am J Ophthalmol* 1995; **119**:752-9.

122. Akiba J, Quiroz MA, Trempe CL. Role of posterior vitreous detachment in idiopathic macular holes. *Ophthalmology* 1990; **97**:1610-13.

123. Akiba J, Kakehashi A, Arzabe CW, Trempe CL. Fellow eyes in idiopathic macular hole cases. *Ophthalmic Surg* 1992; **23**:594-7.

124. Hikichi T, Akiba J, Trempe CL. Effect of the vitreous on the prognosis of full-thickness idiopathic macular hole. *Am J Ophthalmol* 1993; **116**:273-8.

125. Guyer DR, de Bustros S, Diener-West M, Fine SL. Observations of patients with idiopathic macular holes and cysts. *Arch Ophthalmol* 1992; **110**:1264-8.

126. Margherio RR, Trese MT, Margherio AR, K C. Surgical management of vitreomacular traction syndromes. *Ophthalmology* 1989; **96**:1437-45.

127. Madreperla SA, Geiger GL, M F, de la Cruz Z, Green WR. Clinicopathologic correlation of a macular hole treated by cortical vitreous peeling and gas tamponade. *Ophthalmology* 1994; **101**:682-6.

128. Funata M, Wendel RT, de la Cruz Z, Green WR. Clinicopathologic study of bilateral macular holes treated with pars plana vitrectomy and gas tamponade. *Retina* 1992; **12**:289-98.

129. Duker JS, Wendel R, Patel AC, Puliafito CA. Late re-opening of macular holes after initially successful treatment with vitreous surgery. *Ophthalmology* 1994; **101**:1373-8.

130. Guyer DR, Green WR, de Bustros S, Fine SL. Histopathologic features of idiopathic macular holes and cysts. *Ophthalmology* 1990; **97**:1045-51.

131. Gass JDM. Pathogenesis of disciform detachment of the neuroepithelium: II. Idiopathic central serous choroidopathy. *Am J Ophthalmol* 1967; **63**:587-615.

132. Burton TC. Central serous retinopathy. In: Blodi FC, ed. *Current Concepts in Ophthalmology.* St. Louis: CV Mosby; 1972:1-28.

133. Schatz H. Central serous chorioretinopathy and serous detachment of the retinal pigment epithelium. *Int Ophthalmol Clin* 1975; **15**:159-68.

134. Yannuzzi LA, Gitter KA, Schatz H. *The Macula: A Comprehensive Text and Atlas.* Baltimore: Williams & Wilkins; 1982:145-65.

135. Gass JDM. *Stereoscopic Atlas of Macular Diseases: Diagnosis and Treatment.* Third ed. St. Louis: CV Mosby; 1987:46-65.

136. Klein ML, Van Buskirk EM, Friedman E, Gragoudas E, Chandra S. Experience with nontreatment of central serous choroidopathy. *Arch Ophthalmol* 1974; **91**:247-50.

137. Schatz H, Madeira D, Johnson RN, McDonald HR. Central serous chorioretinopathy occurring in patients 60 years of age and older. *Ophthalmology* 1991; **99**:63-7.

138. Nussenblatt RB, Kaufman SC, Palestine AG, Davis MD, Ferris FL. Macular thickening and visual acuity. *Ophthalmology* 1987; **94**:1134-9.

139. Early Treatment Diabetic Retinopathy Study. ETDRS Report Number 7. Early Treatment Diabetic Retinopathy Study Design and Baseline Patient Characteristics. *Ophthalmology* 1991; **98**:741-56.

140. Macular Photocoagulation Study Group. Argon laser photocoagulation for senile macular degeneration. Results of a randomized clinical trial. *Arch Ophthalmol* 1982; **100**:912-8.

141. Macular Photocoagulation Study Group. Argon laser photocoagulation for neovascular maculopathy. Five-year results from randomized clinical trials. *Arch Ophthalmol* 1991; **109**:1109-14.

142. Macular Photocoagulation Study Group. Krypton laser photocoagulation for neovascular lesions of age-related macular degeneration. Results of a randomized clinical trial. *Arch Ophthalmol* 1990; **108**:816-24.

143. Macular Photocoagulation Study Group. Laser photocoagulation of subfoveal recurrent neovascular lesions in age-related macular degeneration. Results of a randomized clinical trial. *Arch Ophthalmol* 1991; **109**:1232-41.

144. Moisseiev J, Alhalel A, Masuri R, Treister G. The impact of the macular photocoagulation study results on the treatment of exudative age-related macular degeneration. *Arch Ophthalmol* 1995; **113**:185-9.

145. Bressler NM, Bressler SB, Gragoudas ES. Clinical characteristics of choroidal neovascular membranes. *Arch Ophthalmol* 1987; **105**:209-13.

146. Macular Photocoagulation Study Group. Subfoveal neovascular lesions in age-related macular degeneration: guidelines for evaluation and treatment in the Macular Photocoagulation Study. *Arch Ophthalmol* 1991; **109**:1242-57.

147. Thomas MA, Dickinson JD, Melberg NS, Ibanez HE, Dhaliwal RS. Visual results after surgical removal of subfoveal choroidal neovascular membranes. *Ophthalmology* 1994; **101**:1384-96.

148. Podgor MJ, Leske MC, Ederer F. Incidence estimates for lens changes, macular changes, open-angle glaucoma, and diabetic retinopathy. *Am J Epidemiology* 1983; **118**:206-12.

149. Tielsch JM, Sommer A, Katz J, Royall RM, Quigley HA, Javitt J. Racial variations in the prevalence of primary open-angle glaucoma. *JAMA* 1991; **266**:369-74.

150. Sommer A. Intraocular pressure and glaucoma. *Am J Opthalmol* 1989; **180**:485-95.

151. Hollows FC, Graham PA. Intraocular pressure, glaucoma and glaucoma suspects in a defined population. *Br J Ophthalmol* 1966; **50**:570-86.

152. Lichter PR. Variability of expert observers in evaluating the optic disc. *Trans Am Ophthalmol Soc* 1976; **74**:532-72.

153. Tielsch JM, Katz J, Quigley HA, Miller NR, Sommer A. Intraobserver and interobserver agreement in measurement of optic disc characteristics. *Ophthalmol* 1988; **95**:350-6.

154. Caprioli J. The contour of the juxtapapillary nerve fiber layer in glaucoma. *Ophthalmology* 1990; **97**:358-65.

155. Quigley HA, Miller NR, George T. Clinical evaluation of nerve fiber layer atrophy as an indicator of glaucomatous optic nerve damage. *Arch Ophthalmol* 1980; **98**:1564-71.

156. Quigley HA, Addicks EM. Quantitative studies of retinal nerve fiber layer defects. *Arch Ophthalmol* 1982; **100**:807-14.

157. Quigley HA, Addicks EM, Green WR. Optic nerve damage in human glaucoma, III: quantitative correlation of nerve fiber loss and visual field defect in glaucoma, ischemic neuropathy, papilledema, and toxic neuropathy. *Arch Ophthalmol* 1982; **100**:135-46.

158. Sommer A, Katz J, Quigley HA, Miller NR, Robin AL, Richter RC, Witt KA. Clinically detectable nerve fiber atrophy precedes the onset of glaucomatous field loss. *Arch Ophthalmol* 1991; **109**:77-83.

159. Schuman JS, Hee MR, Puliafito CA, Wong C, Pedut-Kloizman T, Lin CP, Hertzmark E, Izatt JA, Swanson EA, Fujimoto JG. Quantification of nerve fiber layer thickness in normal and glaucomatous eyes using optical coherence tomography. *Arch Ophthalmol* 1995; **113**:586-96.

160. Schuman JS, Hee MR, Arya AV, T P-K, Puliafito CA, Fujimoto JG, Swanson EA. Optical coherence tomography: a new tool for glaucoma diagnosis. *Curr Opin Ophthalmol* 1995; **6**:89-95.

161. Rice TA, de Bustros S, Michels RG, Thompson JT, Debanne SM, Rowland DY. Prognostic factors in vitrectomy for epiretinal membranes of the macula. *Ophthalmology* 1986; **93**:978-83.

162. Trese MT, Chandler DB, Machemer R. Macular pucker. I. Prognostic criteria. *Graefes Arch Clin Exp Ophthalmol* 1983; **221**:16-26.

163. McDonald HR, Verre WP, Aaberg TM. Surgical management of idiopathic epiretinal membranes. *Ophthalmology* 1986; **93**:978-83.

164. Opremack EM. *Uveitis: A Clinical Manual for Ocular Inflammation.* New York: Springer-Verlag; 1995.

165. Specht CS, Mitchell KT, Bauman AE, Gupta M. Ocular histoplasmosis with retinitis in a patient with acquired immunodeficiency syndrome. *Ophthalmology* 1991; **98**:1356-9.

166. Nussenblatt RB, Belfort R. Ocular toxoplasmosis: An old disease revisited. *JAMA* 1994; **271**:304-7.

167. Jabs DA, Green WR, Fox R, Polk BF, Bartlett JG. Ocular manifestations of acquired immune deficiency syndrome. *Ophthalmology* 1989; **96**:1092-9.

168. Fishman GA, Trimble S, Rabb MF, Fishman M. Pseudovitelliform macular degeneration. *Arch Ophthalmol* 1977; **95**:73-6.

169. Gass JDM. A clinicopathologic study of a peculiar foveomaculr dystrophy. *Trans Am Ophthalmol Soc* 1974; **72**:139.

170. Zimmerman LE, Spencer WH. The pathologic anatomy of retinoschisis. *Arch Ophthalmol* 1960; **63**:10.

171. Kranenberg EW. Creater-like holes in the optic disc and central serous retinopathy. *Arch Ophthalmol* 1960; **64**:912-24.

172. Gass JDM. Serous detachment of the macula secondary to congential pit of the optic nervehead. *Am J Ophthalmol* 1969; **67**:821-41.

173. Lincoff H, Lopez R, Kreisseg I, Yannuzzi L, Cox M, Burton T. Retinoschisis associated with optic nerve pits. *Arch Ophthalmol* 1988; **106**:61-7.

174. Rutledge BK, Puliafito CA, Duker JS, Hee MR, Cox MS. Optical coherence tomography of macular lesions associated with optic nerve head pits. *Ophthalmology* 1996; **103**:1047-53.

175. Krivoy D, Gentile R, Liebmann JM, Stegman Z, Walsh JB, Ritch R. Imaging congenital optic disc pits and associated maculopathy using optical coherence tomography. *Arch Ophthalmol* 1996; **114**:165-70.

176. Moreira H, Campos M, Sawusch MR, McDonnell JM, Sand B, McDonnel PJ. Holmium laser thermokeratoplasty. *Ophthalmology* 1993; **100**:752-61.

177. American National Standards Institute. *American National Standard for Safe Use of Lasers.* ANSI Z136.1-1993. Orlando, Fl; 1993.

178. Knighton RW, Jacobson SG, Kemp CM. The spectral reflectance of the nerve fiber layer of the macaque retina. *Invest Ophthalmol Vis Sci* 1989; **30**:2393-402.

179. Bouma B, Tearney GJ, Boppart SA, Hee MR, Brezinski ME, Fujimoto JG. High-resolution optical coherence tomographic imaging using a mode-locked Ti:Al_2O_3 laser source. *Opt Lett* 1995; **20**:1486-8.

180. Clivaz X, Marquis-Weible F, Salathe RP. Optical low coherence reflectometry with 1.9 μm spatial resolution. *Electron Lett* 1992; **28**:1553-4.

181. Hee MR, Huang D, Swanson EA, Fujimoto JG. Polarization-sensitive low-coherence reflectometer for birefringence characterization and ranging. *J Opt Soc Am B* 1992; **9**:903-8.

6266 - 38